TRANSLATION OF NON-INVASIVE OPTICAL MEASUREMENTS OF HEMODYNAMICS AND OXYGEN METABOLISM TO THE CLINIC

CLAUS LINDNER

Medical Optics
ICFO - Institut de Ciències Fotòniques, The Barcelona Institute of Science and Technology
UPC - Universitat Politècnica de Catalunya
June 2016

Claus Lindner: *Translation of non-invasive optical measurements of hemodynamics and oxygen metabolism to the clinic,* Dissertation, © June 2016

SUPERVISOR:
Turgut Durduran

LOCATION:
Castelldefels (Barcelona), Spain

Für Gerda.
1927 – 2014

ABSTRACT

Several clinical studies for non-invasive estimation of tissue hemodynamics by the combination of two diffuse optical techniques, time-resolved and diffuse correlation spectroscopy, were carried out in collaboration with local hospitals. These led to the first application of hybrid diffuse optics in the characterization of healthy and pathological human thyroid tissue and the initiation of a European Horizon 2020 research project aiming at significantly improving the current thyroid cancer screening process.

The advantages of the hybrid diffuse optical device allowed to gain information on cerebral oxygen metabolism and improved estimation of cerebral blood flow. Data was collected from patients without brain diseases as well as healthy volunteers in clinical and surgical environments. The diffuse optical measurements were shown to correlate with the bispectral index, a widely used anesthesia monitor in the clinic. The optically derived parameters demonstrated the conservation of physiological coupling between cerebral blood flow and oxygen metabolism in patients under propofol-induced anesthesia.

Additional studies focused on the investigation of microvascular cerebral physiology in response to common challenges in surgical procedures. These were simulated on healthy subjects and studied in depth.

Overall, this work pushes the limits of the clinical translation of hybrid diffuse optics paving the way for new applications.

RESUMEN

Varios estudios clínicos para estimar de forma no invasiva los parámetros hemodinámicos del tejido humano han sido realizados gracias a la combinación de dos técnicas de óptica difusa, “time-resolved spectroscopy” y “diffuse correlation spectroscopy”, en un instrumento único, manejable y compacto. Esta combinación ha dado luz a una aplicación única para utilizar dichas técnicas en la diferenciación entre tejido tiroideo sano y patológico. Además, estas mediciones han iniciado un proyecto de investigación dentro del marco “European Horizon 2020”, enfocado en una mejora del procedimiento en la detección y caracterización del cáncer de tiroides.

Las ventajas del uso del dispositivo híbrido de óptica difusa han permitido tanto la obtención de información sobre el metabolismo cerebral, como una mejora en la estimación de su flujo sanguíneo. Se han obtenido datos tanto de pacientes sin patologías cerebrales como de voluntarios sanos en un entorno clínico y durante cirugías. Estas mediciones se han comparado con el índice bispectral, que es un factor importante y frecuentemente usado en la monitorización y control de la administración de anestesia en los hospitales, mostrando una fuerte correlación entre ellos. Las mediciones de óptica difusa han mostrado la conservación del acoplamiento fisiológico entre flujo sanguíneo cerebral y metabolismo de oxígeno en un estado de anestesia inducido por propofol.

Estudios adicionales han investigado la fisiología cerebral microvascular y sus fluctuaciones durante cirugías practicadas con anestesia general. Estos cambios fueron simulados y estudiados meticulosamente con voluntarios sanos.

En resumen, esta tesis amplia los límites de la óptica difusa tanto en la detección de patologías como durante cirugías, y muestra el gran potencial de estos sistemas ópticos para su uso clínico en los hospitales.

PUBLICATIONS

During the time of the work presented in this thesis the following peer-reviewed manuscripts have been published and parts of this thesis appear therein:

Lindner C, Mora M, Farzam P, Squarcia M, Johansson J et al. "*Diffuse Optical Characterization of the Healthy Human Thyroid Tissue and Two Pathological Case Studies*". PLoS One. 2016; 11(1):e0147851.

Sekar SKV, Dalla Mora A, Bargigia I, Martinenghi E, Lindner C et al. "*Broadband (600-1350 nm) Time Resolved Diffuse Optical Spectrometer for Clinical Use*". IEEE Journal of Selected Topics in Quantum Electronics. 2015; PP(99):1-1.

Farzam P, Lindner C, Weigel UM, Suarez M, Urbano-Ispizua A et al. "*Noninvasive characterization of the healthy human manubrium using diffuse optical spectroscopies*". Physiological Measurement. 2014; 35(7):1469.

ACKNOWLEDGMENTS

Translational research requires the collaboration of many people. I can not thank enough the collaborators at Hospital Clínic and Hospital Vall d'Hebron. Without your help and fruitful discussions this work would not have been possible. Thank you Javi, Kike, Ricard, Neus from the Anesthesiology department and Mireia, Mattia, Felicia from the Endocrinology and Radiology department at Hospital Clínic, as well as Ángela, Ivette, Miriam, Juan and colleagues from the Department of Anesthesiology and Neurosurgery at Vall d'Hebron University Hospital.
Of course, on the other side, I thank Prof. Turgut Durduran for his guidance along the many studies conducted and problems faced. Thank you for the opportunity to pursue this work in the Medical Optics group at ICFO. I had the privilege to work with amazing and wonderful people. I can only express my gratitude to you and simply say: Thank you, Peyman, Parisa, Tai, Udo, Paco, Igor, JJ, Claudia, Juan, Clara, Martina, Jordi, Miguel, Marco, Tanja, Kristian, Joe, Luca, ... you guys were colleagues, became friends and made these years a truly unforgettable experience.

Also, many people at ICFO were a big support and I highly appreciate their help. Thank you, José Carlos, Alberto, Òscar and team, as well as Xavi and your team at the mechanical workshop. All of you made so many things possible, I do not even know where to start. Thanks you also, Anne, Manuela, Mery, Cristina, Rob and David for an always open door.

Un "gracias" muy personal esta dirigido a ti, Sara! Tu luz y apoyo incondicional definitivamente esta reflejado en esta tesis y me siento muy agradecido! Te debo mucho y miro adelante, hacia un viaje muy especial!

I also want to thank Stefan, Stefan - that's right, same name, two different people ... amazing people and "bla bla" - Daniel, Chris, Alex, Alex, Alex - yes, even three here - Mena, Agi, Lini ... for simply being there. Danke! David, Nuria, Joan and Marc ... simply thank you, thank you, thank you!

Jürgen and Christa, the following includes you as well: I definitely feel an unimaginable amount of gratitude towards my family, in particular, my mother. I'll never forget everything you have done and made possible. Ich kann dir nicht genug danken! Ausserdem, möchte ich noch einer ganz besonderen Person danken: Oma, es ist unglaublich schade und traurig, dass du das Ende dieser Arbeit nicht mehr miterleben kannst. Du fehlst mir und mir fehlen die Worte die tiefe und ewige Dankbarkeit auszudrücken. Deshalb ist diese Arbeit dir gewidmet!

CONTENTS

LIST OF FIGURES

LIST OF TABLES

ACRONYMS

ACA	anterior cerebral artery
APD	avalanche photodiode
ASL-MRI	arterial spin labeled perfusion magnetic resonance imaging
BMI	body mass index
BIS	bispectral index
BF	blood flow

BFI	blood flow index
BOLD	blood-oxygen-level dependent
BP	blood pressure
BP_{dia}	diastolic blood pressure
BP_{sys}	systolic blood pressure
CAR	cerebral autoregulation
C_a	arterial oxygen concentration
CBF	cerebral blood flow
CBFV	cerebral blood flow velocity
$CBFV_{dia}$	diastolic cerebral blood flow velocity
$CBFV_{mean}$	mean cerebral blood flow velocity
$CBFV_{sys}$	systolic cerebral blood flow velocity
CDE	correlation diffusion equation
$CMRO_2$	cerebral metabolic rate of oxygen
CO	cardiac output
CO_2	carbon-dioxide
CI	cardiac index
CNS	central nervous system
C_p	plasma concentration
CPP	cerebral perfusion pressure
CSF	cerebral spinal fluid
CT	computed tomography
CVR	cerebrovascular resistance
C_t	tissue oxygen concentration
C_v	venous oxygen concentration
CW	continuous wave
DCS	diffuse correlation spectroscopy

DE	diffusion equation
DOS	diffuse optical spectroscopy
DWS	diffusing wave spectroscopy
DTOF	distribution time of flight
EEG	electroencephalogram
ECG	electrocardiogram
ESS	elastic scattering spectroscopy
$EtCO_2$	end-tidal CO_2
$ExpO_2$	exhaled O_2
FiO_2	fraction of inspired oxygen
fMRI	functional magnetic resonance imaging
FNAB	fine-needle aspiration biopsy
Hb	deoxy-hemoglobin
HbO_2	oxy-hemoglobin
HOB	head-of-bed
HR	heart rate
HRC	hypercapnia
HOC	hypocapnia
HO	hyperoxia
HV	hyperventilation
ICP	intracraneal pressure
$InspCO_2$	inhaled CO_2
$InspO_2$	inhaled O_2
IPI	integrated pulmonary index
IQR	interquartile range
IRF	instrument response function
IS	ischemic stroke

LDF	laser Doppler flowmetry
LED	light emitting diode
LSF	laser speckle flowmetry
LME	linear mixed effects
MAP	mean arterial pressure
MCA	middle cerebral artery
mCBF	microvascular cerebral blood flow
MRI	magnetic resonance imaging
NIRS	near-infrared spectroscopy
O_2	oxygen
OEF	oxygen extraction fraction
PCA	posterior cerebral artery
$PaCO_2$	arterial partial pressure of carbon dioxide
PEEP	positive end-expiratory pressure
PET	positron emission tomography
pH	acidity/alkalinity scale for an aqueous solution
PMT	photo multiplier tube
PO_2	partial pressure of oxygen
P_t	tissue permeability
PtO_2	tissue oxygen pressure
RBC	red blood cells
rBIS	relative bispectral index
rCBF	relative cerebral blood flow
$rCMRO_2$	relative cerebral metabolic rate of oxygen
rOEF	relative oxygen extraction fraction
RR	respiration rate
RTE	radiation transport equation

SAH	subarachnoid hemorrhage
SHG	second-harmonic generation
SPECT	single photon emission computed tomography
SO_2	oxygen saturation
SaO_2	arterial oxygen saturation
ScO_2	capillary oxygen saturation
$SjvO_2$	jugular venous oxygen saturation
SpO_2	peripheral arterial oxygen saturation
SrO_2	regional oxygen saturation
StO_2	tissue oxygen saturation
SvO_2	venous oxygen saturation
SPAD	single photon avalanche photodiode
STT	superficial tissue thickness
SV	stroke volume
SVR	systemic vascular resistance
SI	stroke index
SNR	signal-to-noise ratio
SVR	systemic vascular resistance
T	temperature
TBI	traumatic brain injury
TC	thyroid cancer
TCD	transcraneal Doppler
TCSPC	time-correlated single photon counting
THC	total hemoglobin concentration
TIVA	total intravenous anesthesia
TN	thyroid nodule
TOF	time of flight

TPEF	two-photon excited fluorescence
TRS	time-resolved spectroscopy
TT	tissue thickness
TTD	total tissue depth
TTL	transistor-transistor logic
US	ultrasound
VAE	venous air embolism
WHO	World Health Organization
XeCT	Xenon-enhanced computed tomography

SYMBOLS

α	fraction of moving scatterers
β	mode parameter
D	photon diffusion coefficient
D_b	particle Brownian diffusion coefficient
ϵ	extinction coefficient
ζ	chromophore concentration
$FWHM$	full width at half maximum
γ	blood volume percentage in venous compartment
g	scattering anisotropy factor
IQR	inter-quartile range
$\mathbf{J}$	photon flux
λ	wavelength of light
μ_a	absorption coefficient
μ_s	scattering coefficient
μ_s'	reduced scattering coefficient
n	index of refraction
n^*	index of refraction of the turbid/medium tissue
G_1	unnormalized electrical field autocorrelation function
g_1	normalized electrical field autocorrelation function
G_2	unnormalized intensity autocorrelation function
g_2	normalized intensity autocorrelation function
K	electrical field autocorrelation decay factor
L	light radiance

p	scattering phase function
Φ	fluence rate
Q	radiant source power per volume element
ρ	source-detector separation
R	reflectance
$R_{pearson}$	Pearson's product-moment correlation coefficient
$R_{spearman}$	Spearman's rank correlation coefficient
S	radiant source power concentration
τ	correlation time

Part I

INTRODUCTION, THEORY AND EXPERIMENTAL SETUP

1

INTRODUCTION

"Medicine is not only a science; it is also an art. It does not consist of compounding pills and plasters; it deals with the very processes of life, which must be understood before they may be guided." [Paracelsus, 1493-1541]

A large part of today's achievements in patient care and monitoring are the result of clinical research and the investigation of physiological processes of the human body. It is the constant urge to save and improve lives that drives medical research. Physics and the use of light in particular has been able to significantly contribute and will continue to do so as new technologies emerge. The use of light enables physicians and researchers to look inside the human body non-invasively and study physiological processes in both healthy and diseased populations. By monitoring blood flow, blood oxygen contents and oxygen metabolism continuously we can characterize different organs in a healthy or pathological state.

1.1 THE NEED FOR NEW APPROACHES IN THE CLINIC

Information on cell metabolism can enable both monitoring cancer therapy and improvements in cancer diagnosis and therapy. Current techniques are generally either invasive, expensive or require movement of the patient to the device rather than bringing the device to the patient's bedside. A clinical device that allows point-of-care testing and easy integration in existing cancer screening processes could significantly improve therapy outcome by providing information on relevant tissue parameters. Standard thyroid cancer screening, which faces a high prevalence of thyroid nodules, the sensitivity and specificity of the first point-of-care, non-invasive screening method, ultrasound (US), is quite poor. Sensitivity ranges from 17-87 % and specificity from 39-95 % depending on the type of the malignant nodules [205, 215, 287, 223, 10]. Even in combination with a biopsy, sensitivity and specificity are still limited [68]. The poor performance of the

existing screening strategies necessitate improvements in the accurate identification of lesions. Non-invasive methods, enabling the accurate characterisation of lesions, have the potential to both improve therapeutic outcomes as well as reduce the number of unnecessary biopsies or surgeries.

In the case of the brain, we face an autoregulatory mechanism, cerebral autoregulation (CAR) [264], which balances pressures in the brain produced by changes in the mean arterial pressure (MAP) and with the counteracting part, the intracraneal pressure (ICP). This is qualitatively illustrated in Figure 1.1.

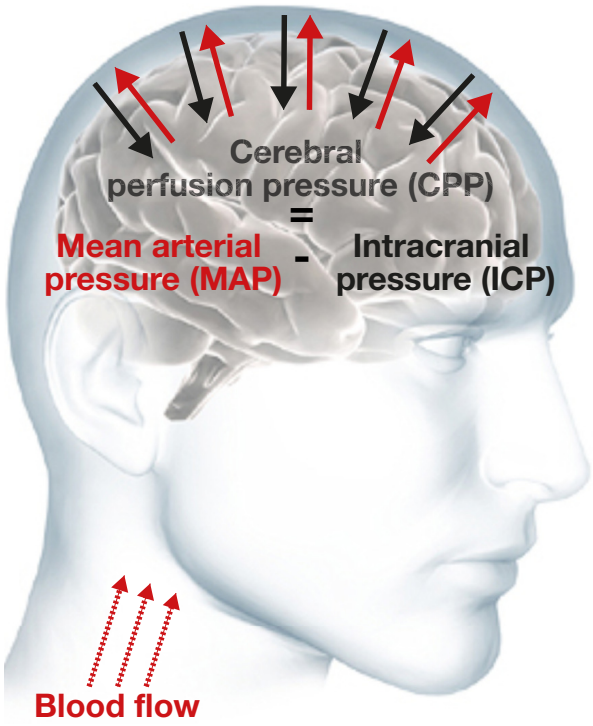

Figure 1.1: The concept of cerebral autoregulation (CAR): Blood pumped from the heart with a certain pressure supplies the brain. The pressure of the cerebral spinal fluid (CSF), acting on the brain from the "outside". The difference between the two pressures is expressed as the cerebral perfusion pressure (CPP). It can vary over a wide range, while maintaining CBF constant by vasodilatation or vasoconstriction.

Blood supplies the brain with an adequate amount of oxygen in order to maintain its functioning. The cerebral blood flow (CBF) is maintained constant over a range of cerebral perfusion pressures by adjusting the blood vessel diameter in the brain [288, 167]. This process is called CAR.

In a non-healthy brain the autoregulation mechanism can be impaired because of blood vessels bursting (hemorrhagic stroke) or brain swelling due to high pressures, both of which can result in an insufficient supply of oxygen. (Traumatic brain injury (TBI) is one major cause of CAR impairment. It has become so prevalent that it is often called the "silent epidemic of the third millennium". Despite from being the first cause of death and disability in the world, it is the number one cause for people under 45 years of age, number seven for disability in the European Union and its relevance in the elderly population is increasing [194]. Approximately 100 per 100.000 inhabitants each year experience severe injuries due to traumatic brain injury (TBI) resulting in hospitalization or death. Although there has been a significant overall mortality reduction in the last 25 years, at the same time there has not been a significant change in the number of TBI survivors suffering from neurological sequelae in TBI [146]. Moreover, the World Health Organization (WHO) has projected that in the year 2020 the major cause of TBI, traffic accidents, will be one of the top three of overall causes of diseases and injuries worldwide.

Ischemic stroke is the leading cause of morbidity and long term disability in the United States and Europe and is among the leading causes of death [189, 110, 194]. In developed countries it is the leading cause of mortality for patients over 75 years of age and the second leading cause of dementia, behind only Alzheimer's disease. Stroke care costs are projected to reach trillions of Euros over the next five decades and the disease is already responsible for about 5 % of total healthcare costs. Stroke accounts for nearly 10 % of deaths in the western hemisphere. While subarachnoid hemorrhage (SAH) represents only 7 % of all strokes, it has a fatality rate of 37.5 % within in 30 days, increasing to 50 % in total. Additionally, 50 % of survivors suffer from a permanent neurological deficit [308].

While a strong ethical exigence to enhance TBI and stroke care exists, the high incidence of stroke and its immense management costs necessitate advances in treatment and diagnosis as well. Advanced multi-modality measurements of cerebral hemodynamics and metabolism have the potential to fill this need. Even modest benefits will lead to a significant improvement of the lives of hundreds of thousands of people and a significant reduction in health care costs.

Optimal management of TBI patients requires advanced, multi-modality neuromonitoring, that is ideally non-invasive and reflects microvascular cerebral hemodynamics as well as metabolism in real time. The latter is not possible with the current modalities. The availability of a safe, non-invasive device, which can be placed at the bed-side in a neurointensive care unit and provides clinicians with this information has the potential to lead to drastic improvements in health-care by allowing a personalized management approach.

Information on (cerebral) hemodynamics can be provided by several methods, each associated with different degrees of cost, portability, localization (macro- versus microvascular level) and invasiveness. A portable non-invasive option is Doppler US and its variations, power Doppler US, color Doppler flowmetry. Making use of the Doppler effect this US technique provides information on blood flow. It widely used in the study of CBF and allows the investigation of CAR. There, it is often called transcraneal Doppler (TCD) and measures the cerebral blood flow velocity (CBFV) [2]. Nonetheless, it only can give information on flow in larger blood vessels (macrovasculature), i. e. CBFV in the middle cerebral artery or anterior cerebral artery [133, 2]. Additionally, it needs insonation windows (thin skull) for proper functioning [199, 180, 24].

Information on blood flow the microvasculature, i. e. the smaller blood vessels, can be gained by utilizing computed tomography (CT), Xenon-enhanced computed tomography, positron emission tomography, single photon emission computed tomography, magnetic resonance imaging and arterial spin labeled perfusion magnetic resonance imaging [247, 334, 261, 85]. There is also blood-oxygen-level dependent (BOLD) contrast imaging, which uses functional magnetic resonance imaging to study vascular reactivity changes based on the oxy- and deoxy-hemoglobin (Hb and HbO_2) levels [233, 232]. BOLD comes with the disadvantage of difficult signal interpretation, low signal-to-noise ratio (SNR) and complex statistical methods. All of the methods mentioned here are either associated with high costs, non-portability, acquire non-continuous measurements, require radiopharmaceuticals or only present information on the macrovasculature.

Optical techniques based on the investigation of tissue absorption and scattering characteristics can be used to study

hemodynamics. These include laser Doppler flowmetry (LDF) and laser speckle flowmetry (LSF) and - compared to the methods mentioned above - offer relatively low costs and portability. Dynamic information about the microvasculature is provided by measuring the Doppler phase shift in LDF or by looking at the speckle profile in LSF. However, these measurements are limited to shallow layers and have not found widespread clinical use [87, 284, 231, 227].

Given the serious limitations of alternative methods as detailed here, diffuse optical techniques represent some of the most promising approaches to non-invasive (neuro-) monitoring.

This thesis is focused on the implementation of two optical modalities - diffuse correlation spectroscopy (DCS) and time-resolved spectroscopy (TRS) - in order to assess microvascular (cerebral) hemodynamics and metabolism in real time in the clinic. These techniques use point-source illumination and can probe several centimeters deep into tissue. In this work, these techniques are used to improve thyroid cancer screening, investigate cerebral hemodynamics and examine CAR. The obtained measures are investigated upon their position dependencies in order to answer questions of increased incidence rates of brain lesions for surgeries carried out in certain positions. Microvascular DCS and TRS-derived CBF and brain metabolism is furthermore validated against established clinical parameters.

1.2 DIFFUSE OPTICS

Near-infrared spectroscopy (NIRS) has evolved around making use of the relatively low tissue absorption in the wavelength range between 650 and 950 nm, which allows the relatively deep non-invasive probing of biological tissue [201, 156]. The probing depth depends on the experimental setup, especially the technique which is used - whether it is pathlength resolved or not. The light of a continuous wave laser can probe $\sim$ 1 - 1.5 cm in the near-infrared spectrum under typical conditions of an adult human brain and the sensitivity of optoeletronics. Other techniques, such as those that use pulsed laser light and time-resolved detection (the topic of this thesis), can provide information from greater depths [201]. In the above-mentioned wavelength range, water and lipid absorption is relatively low enabling photons to travel several

centimeters in tissue and still be detected. Other tissue chromophores, such deoxy-hemoglobin (Hb) and oxy-hemoglobin (HbO_2) become therefore accessible, allowing one to gain information in regards to their concentration within the tissue. Today, widely used standard pulseoximeters make use of this fact by employing light emitting diodes, photodetectors and sophisticated algorithms to determine peripheral arterial oxygen saturation and are a direct application of near-infrared spectroscopy (NIRS) in clinical practice. With relatively low absorption and high scattering, photons are scattered multiple times and those travelling over some minimum distance essentially experience a random walk and can be considered to to have entered the diffusive regime. Photons within this regime can be modelled using the diffusion approximation, which takes into account these two main processes - absorption and scattering.

Different source types can be used with each providing different levels of information per measurement can be used. The basics will be examined here and are illustrated in Figure 1.2.

In the first scenario, continuous wave (CW) laser light is injected into the tissue and the measurement of the associated attenuation can provide information on tissue oxygen saturation [271, 228]. This option is used widely in standard pulseoximeters. By modulating the source intensity, an additional parameter can be measured, the phase shift ($\Delta\varphi$) between the incident and detected light introduced by the medium. The combination of attenuation and $\Delta\varphi$ allows the determination of tissue scattering and absorption properties, i. e. the absorption (μ_a) and reduced scattering coefficients (μ_s') [208, 143, 248, 241]. Absolute scattering and absorption properties can be measured using pulsed lasers together with hybrid photo multiplier tube detectors and sophisticated single photon counting electronics. Due to multiple scattering events inside the tissue, the emitted laser pulse broadens and shifts in time. These time domain measurements are called time-resolved spectroscopy (TRS) and use the distribution of photons travel times to derive the above-mentioned optical properties [311, 66, 306, 310, 240, 153] in order to turn them into tissue chromophore concentrations, such as Hb and HbO_2.

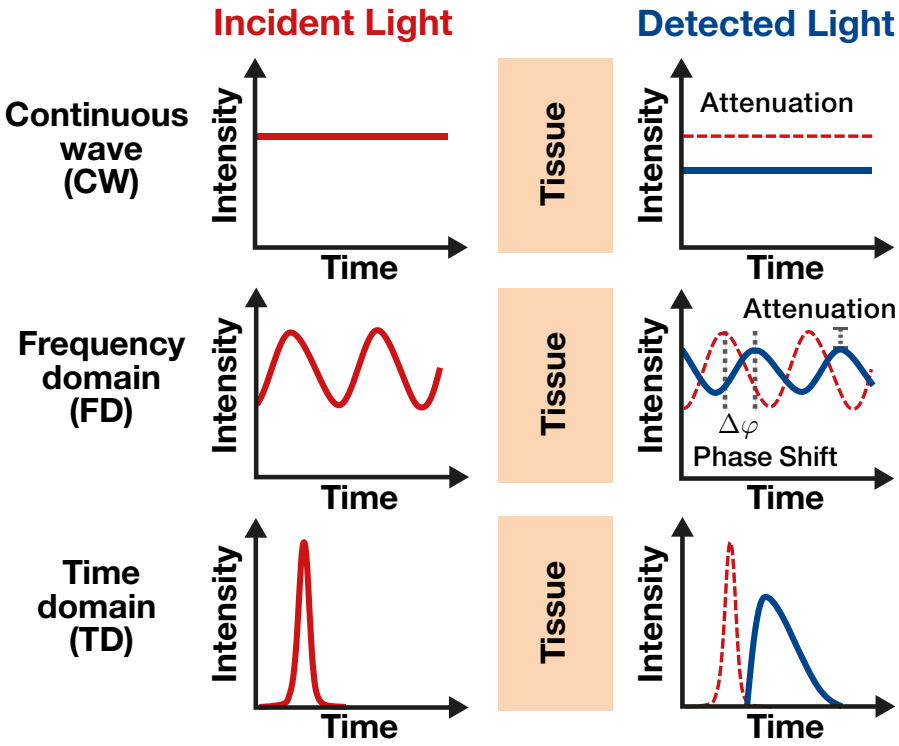

Figure 1.2: NIRS source types: The top graph shows the CW source type and illustrates the light attenuation due to the tissue.; Middle graph: Intensity modulated light source experiences attenuation and a phase shift inside tissue (frequency-domain); Bottom graph: Pulsed light is broadened by the tissue. The time-of-flight information of each photon, which varies depending on the tissue properties, is recorded. Graphs adapted from [26].

1.3 GOALS AND HYPOTHESES

The overall theme of this thesis is the combination of two diffuse optical techniques for the simultaneous, non-invasive and continuous estimation microvascular blood oxygen saturation, blood flow and oxygen metabolism. Followed by its translation into several clinical scenarios With this overall objective in mind, the work presented here is geared towards the following goals and hypotheses:

Goal I: Combination of two diffuse optical techniques into one portable hybrid device.

- Hypothesis I.1: It is possible to combine time-resolved spectroscopy (TRS) and diffuse correlation spectroscopy (DCS) in one portable device for clinical use.

- Hypothesis I.2: Data from TRS and DCS can be obtained in a robust, reliable and stable manner simultaneously under clinical conditions.

Goal II: Employing of diffuse optics on the healthy and pathological human thyroid for the first time.

- Hypothesis II.1: The human thyroid is accessible by diffuse optics and can be differentiated from the surrounding tissues such as the neck muscles.
- Hypothesis II.2: The human thyroid is relatively homogeneous and inter- and intra-individual differences can be characterized by diffuse optics.
- Hypothesis II.3: Thyroid nodules show a detectable contrast in optical properties and in hemodynamic variables.

Goal III: Acquire non-invasive optical data in the clinical and surgical environment using a diffuse optical hybrid device.

- Hypothesis III.1: Hybrid diffuse optics can reliably be employed in the clinical environment and utilized during surgical procedures.

Goal IV: Obtain an estimation of cerebral metabolism and blood flow by hybrid diffuse optics and compare these against the widely used bispectral index.

- Hypothesis IV.1: Cerebral metabolism can be continuously estimated during surgical procedures.
- Hypothesis IV.2: Hybrid diffuse optics data correlates with similar measures of brain activity.
- Hypothesis IV.3: Hybrid diffuse optics can aid in the understanding of brain health, in monitoring depth

of anesthesia and in protecting against anesthesia related injuries.

- Hypothesis IV.4: Hybrid diffuse optics data is useful in the study of cerebral hemodynamics.

Goal V: Investigation of the posture on the cerebral hemodynamics in combination with respiratory challenges.

- Hypothesis V.1: Conditions that challenge cerebral autoregulation during general anesthesia can be mimicked in awake patients in a reproduceable manner.

- Hypothesis V.2: Patient/Volunteer position has an affect on the brain's response to altered levels of gases in the inspired air mixture and/or in response to challenges involving breathing.

Goal VI: Explore the advantages of the hybridization of time-resolved and diffuse correlation spectroscopy in the data analysis.

- Hypothesis VI.1: The knowledge of tissue optical properties retrieved by one modality - here TRS - has a significant influence on the analysis of tissue blood flow data obtained by DCS.

1.4 THESIS OUTLINE

This thesis is organised in three parts. The first one lays the groundwork in terms of background, theory on hemodynamics and diffuse optics and presents the experimental setup. The second part contains all *in-vivo* measurements and the third part summarizes and concludes this work.

Chapter 2 focuses on the light transport in biological tissue, how the diffusion approximation leads to the diffusion equation (DE) and correlation diffusion equation (CDE) and presents the solutions for a semi-infinite geometry, which is used to model the experimental settings used in the measurements presented in this thesis. As a second requisite

for the study and understanding of hemodynamics by diffuse optics, in Chapter 3, after a short explanation of oxygen transport in tissue, based on blood flow and blood oxygenation, we will look at how the human brain is supplied with oxygen and how different oxygen (O_2) and carbon-dioxide (CO_2) concentrations can influence the oxygen affinity of blood and alter CAR. After the theoretical foundations are laid out, the combination of two diffuse optical techniques, TRS and DCS, which can be used to retrieve information on Hb, HbO_2 and total hemoglobin concentration (THC), as well as tissue oxygen saturation (StO_2) and blood flow (BF), into a single hybrid device is explained in Chapter 4. The system is characterized and validated using phantom measurements. This chapter concludes the first part of this work before moving on to *in-vivo* measurements.

Chapter 5 presents *in-vivo* data. Data from the human thyroid is characterised by TRS-derived THC and StO_2 content as well as by BF measurements using DCS. Both, healthy and pathologic tissue data are examined, opening the door towards the potential application of diffuse optics in thyroid cancer screening.

Chapter 6 presents *in-vivo* data focusing on CBF, oxygen extraction fraction (OEF) and cerebral metabolic rate of oxygen ($CMRO_2$) derived from the hybrid TRS/DCS device and references these measurements against the bispectral index (BIS), an electroencephalographic measure of brain activity. The measurements are carried out in the surgical room during propofol-induced anesthesia.

Using the background presented in Chapters 2 and 3, we look at relative cerebral blood flow (rCBF) responses to hyperoxia, hypercapnia and hyperventilation (HV) challenges in Chapter 7. The alterations due to changing O_2 and CO_2 blood concentration on parameters such as CBF, CBFV, MAP, heart rate (HR), cardiac output (CO) and stroke volume (SV) are studied and checked for influences stemming from subject position. As responses to HV in Chapter 7 raise the question as to whether there are two groups showing opposed microvascular cerebral blood flow (mCBF) changes, Chapter 8 will look in more detail at the HV challenge and its implications on mCBF. The HV protocol from Chapter 7 is adopted and TRS data is acquired as well.

Finally, Chapter 9 examines a head-of-bed procedure in order to determine how μ_a and μ_s' from TRS influence the derivation of the blood flow index (BFI) in DCS measurements. Four different analysis methods are compared using BFI and rCBF values. This study concludes the second part of this work.

In the third part, final conclusions are drawn. Additional data related to chapters 5 and 7 is presented in the appendix. The tables include additional pathologic case studies from Chapter 5 as well as full correlation tables from the various number of parameters taken during the study presented in Chapter 7.

2

LIGHT INTERACTIONS WITH BIOLOGICAL TISSUES

Light is used to investigate biological tissue and its hemodynamic properties including blood flow and chromophore concentrations (e. g. deoxyhemoglobin Hb and oxyhemoglobin HbO_2). The underlying theoretical models used here treat photon propagation as a diffusive process and as such are generally referred to as diffuse optics.
This chapter focuses on two basic processes, which affect the light transport in biological tissue: absorption and scattering. The diffusion equation (DE) will be derived and the correlation diffusion equation (CDE) will be introduced. Two diffuse optical techniques - time-resolved spectroscopy (TRS) and diffuse correlation spectroscopy (DCS) - will be presented and shown how their measurements can be related to physiologically important parameters.

First the forward problem will be described. It refers to a setup where the optical properties of the medium are known and are used to calculate the photon density and flux within the medium. The measurements presented in the later chapters refer to the opposite scenario. In the inverse problem the medium's optical characteristics are calculated based on the optical measurements at specific locations. Solving the inverse problem provides information on tissue constituents and dynamics, such as oxygen content and blood flow.

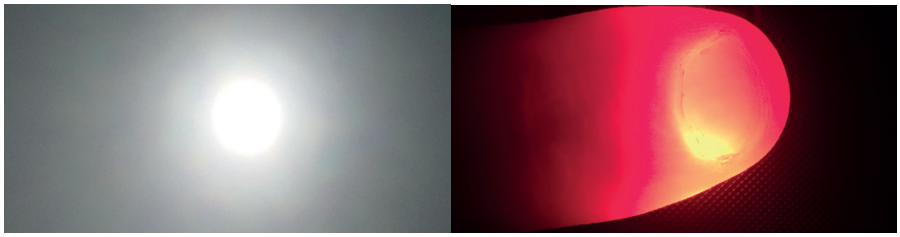

Figure 2.1: Illustrative image: A standard smartphone flashlight (left side) serves as a white light source. Placing a finger on top (right side) illustrates the basis of diffuse optics.

An illustrative example of photon diffusion in biological tissues is given in Figure 2.1. Only red (and near-infrared) photons of a white light source (a standard smartphone flashlight) can be observed after passing through the finger. This photo demonstrates that light in the red region of the spectrum can pass through several cm of biological tissue, but is strongly diffuse after doing so. The fact, that the entire finger cap is illuminated and light can still be observed after several cm is due to the high scattering and relatively low absorption in biological tissue in these wavelengths.

2.1 LIGHT ABSORPTION

The absorption spectrum of the primary chromophores contained in biological tissue are presented in Figure 2.2. The relatively low absorption in the near-infrared (650 - 950 nm) is often referred to as the "physiological window" [156]. It is the relatively low absorption in this range as compared to the rest of the spectrum that explains the red color of the finger in Figure 2.1, which was illuminated using a white (broadband) light source.

In the absorption process the energy from a photon is converted into another form, which in our case is generally thermal energy. This process is wavelength of light (λ) dependent and the extent of absorption will depend on both the molar extinction coefficient of the chromophore (ϵ) [M^{-1} cm^{-1}] as well as its concentration (ζ) [mol/m^3]. The absorption coefficient (μ_a) [cm^{-1}] provides a quantitative measure of absorption and is related to ζ and ϵ for each chromophore (i) and λ by the relation:

$$\mu_a(\lambda) = log(10) \sum_{i}^{n} \epsilon_i(\lambda)\, \zeta_i \tag{2.1}$$

The primary tissue chromophores within biological tissue at the wavelengths of interest (650 - 950 nm) are deoxy- (Hb), oxyhemoglobin (HbO_2), water and lipid. Melanine is nearly constant in this region. At other wavelengths additional chromophores may become important and need to be included. From the derived oxy- and deoxyhemoglobin concentrations one can calculate the total hemoglobin concentration (THC)

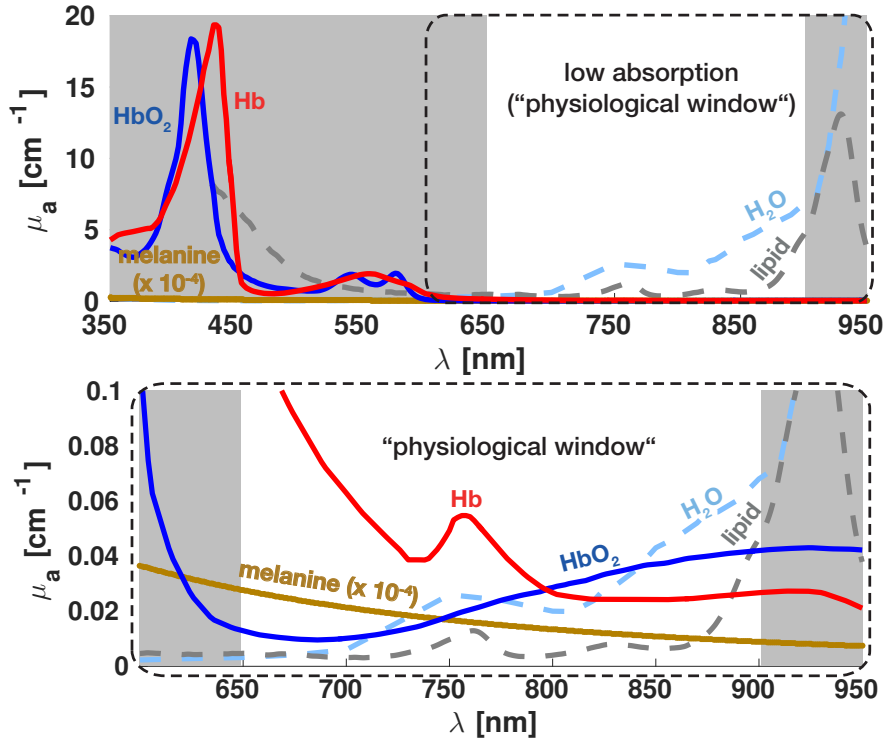

Figure 2.2: Absorption coefficients ($\mu_a(\lambda)$) for deoxy- and oxyhemoglobin (Hb, HbO_2), water, lipid and melanine plotted as a function of wavelength of light (λ). The low absorption between λ = 650 and 950 nm is referred to as the "physiological window".

[M] and tissue oxygen saturation (StO_2) [%], which is a mixture of arterial and venous blood saturation. These parameters provide information on the tissue condition and can be used to calculate oxygen metabolism.

2.2 LIGHT SCATTERING

A light scattering event occurs when a photon hits a target and changes its trajectory. Photon propagation in biological tissues obeys many such events and is therefore a multiple scattering process. In biologic tissue the scattering mean free path of photons - the distance a photon travels freely between two scattering events - is on the scale of hundreds of µm and therefore, in our experimental setups, orders of magnitude smaller than the actual path the photons reaching the detector travel. This leads to a high degree of scattering in when imaging deep *in vivo* tissue and detected photons are

considered multiply scattered.

The scattering process is dependent on the relative size and geometry of the scatterer as compared to the wavelength as well as the difference in refractive indices.

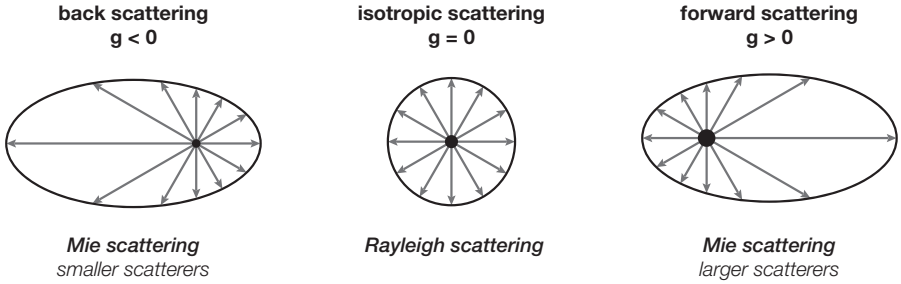

Figure 2.3: Angular distribution of light scattering: The anisotropy factor g defines the scattering nature (g< 0: anistropic back scattering; g = 0: isotropic scattering; g> 0: anistropic forward scattering). Biological tissue is strongly foward scattering (g $\approx$ 0.9)

Two scattering processes - Rayleigh and Mie scattering - are shown in Figure 2.3. While Rayleigh scattering is valid for small particles and is isotropic[1], Mie scattering is capable of describing anisotropic scattering, which is typical in biological tissues. This is due to the size of the scatterers, so that photons experience a strong scattering along the forward direction. A phase function is used to describe the resulting angular distribution of the scattered photons (see also Fig. 2.3). The scattering anisotropy factor (g) is given by the average cosine of the probability distribution of the scattered particles and the scattering angle θ.

It is common to describe scattering by the scattering coefficient (μ_s) [cm^{-1}], which is the inverse of the mean free path. In biological tissue, another parameter is defined, which is the reduced scattering coefficient (μ_s') [cm^{-1}]:

$$\mu_s' = \mu_s \, (1 - g) \tag{2.2}$$

1 Rayleigh scattering allows to describe the interaction of air molecules and visible light and therefore is often used to explain the color of the sky and color effects at sunset. Scattering on larger particles, i. e. water droplets in the air, can no longer be described by the Rayleigh approximation and Mie theory is needed.

Figure 2.4 illustrates the light-tissue interaction process and the mentioned coefficients (μ_a, μ_s and μ_s').

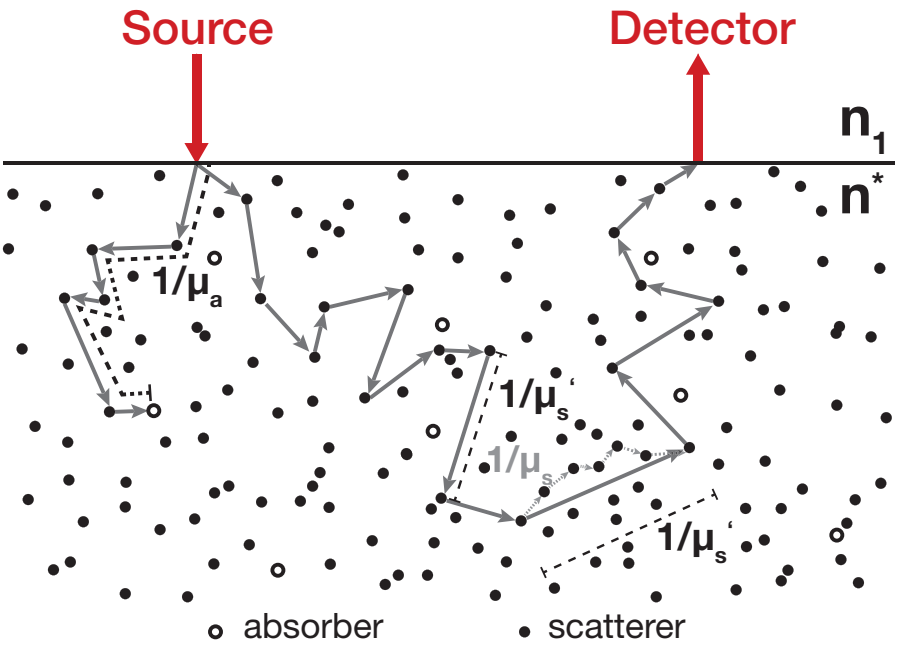

Figure 2.4: Interaction processes between light and a turbid medium: Photons are injected into a turbid medium, i. e. biological tissue, (index of refraction n^*) and interact with scatterers (filled circles) or absorbers (hollow circles) therein. μ_a denotes the absorption coefficient, μ_s and μ_s' the scattering and reduced scattering coefficient.

2.3 RADIATIVE TRANSPORT

Incoherent light transport is described by the radiation transport equation (RTE) [75],

$$\begin{aligned}\frac{1}{v}\frac{\partial L(\mathbf{r},\hat{\Omega},t,\lambda)}{\partial t} = &-\nabla\cdot L(\mathbf{r},\hat{\Omega},t,\lambda)\hat{\Omega} + Q(\mathbf{r},\hat{\Omega},t,\lambda)\\ &-\mu_a(\mathbf{r},\hat{\Omega},t,\lambda)\; L(\mathbf{r},\hat{\Omega},t,\lambda)\\ &-\mu_s(\mathbf{r},\hat{\Omega},t,\lambda)\; L(\mathbf{r},\hat{\Omega},t,\lambda)\\ &+\mu_s(\mathbf{r},\hat{\Omega},t,\lambda)\int_{4\pi} L(\mathbf{r},\hat{\Omega},t)\; p(\hat{\Omega},\hat{\Omega}',\mathbf{r},t,\lambda)\; d\Omega'\end{aligned} \tag{2.3}$$

where the speed of light in the medium is represented by $v = c/n^*$, with the index of refraction of the medium (n^*). The light radiance (L) [W cm^{-2} sr^{-1}] describes the power per area per $\hat{\Omega}$. The RTE relates changes in L travelling in the $\hat{\Omega}$ direction to influences due to absorption and scattering via the corresponding coefficients μ_a and μ_s as well as the scattering phase function (p) [cm^{-1}] and the radiant source power per volume element (Q) [W cm^{-3} sr^{-1}] emerging from a source in $\hat{\Omega}$ direction at $(\mathbf{r}, t)$.

Equation 2.3 ensures energy conservation in each infinitesimal volume element over time. The positive source term is represented by Q. Each absorption event reduces L, which explains the negative sign in front of the $\mu_a L$ term. Scattering can either subtract or add to the signal, so that the $\mu_s L$ term accounts for the loss of a photon due to scattering and the Lp integral describes photons who are added due to scattering happening in the entire solid angle. This becomes more obvious, taking into account that an integration of p over all solid angles Ω results in the scattering coefficient (μ_s).

2.3.1 *Photon diffusion theory*

The RTE can be simplified using the diffusion approximation [90, 325, 94, 27, 53]. Assuming that the photon direction is randomized with only small directional dependence, we can truncate an expansion of the light radiance L by spherical harmonics ($Y_{l,m}(\hat{\Omega})$) from $l = 0$ to $l = N$ with the coefficients $\phi_{l,m}(\mathbf{r}, t)$ [53, 147] at $N = 1$:

$$L(\mathbf{r}, \hat{\Omega}, t) = \frac{1}{4\pi}\Phi(\mathbf{r}, t) + \frac{3}{4\pi}\mathbf{J}(\mathbf{r}, t) \cdot \hat{\Omega} \tag{2.4}$$

Both contributing terms in this P_1 approximation (Equation 2.4) have a physical meaning. The 0^{th} order is defined as the fluence rate (Φ) [W cm^{-2}], which is defined as the light power per area moving radially outward from an infinitesimal volume element at $(\mathbf{r}, t)$

$$\Phi(\mathbf{r}, t) = \int L(\mathbf{r}, \hat{\Omega}, t)\, d\Omega \tag{2.5}$$

and the first order is the photon flux ($\mathbf{J}$) [W cm^{-2}], which is the radiance vector sum with its origin at the infinitesimal volume element at $(\mathbf{r}, t)$:

$$\mathbf{J}(\mathbf{r}, t) = \int L(\mathbf{r}, \hat{\Omega}, t)\hat{\Omega}\, d\Omega \tag{2.6}$$

Substituting this into Equation 2.3, carrying out the integral over all solid angles and assuming that scattering is rotationally symmetric ($p(\hat{\Omega}, \hat{\Omega}', \mathbf{r}, t, \lambda) = p(\hat{\Omega}', \hat{\Omega}, \mathbf{r}, t, \lambda)$) and that it is isotropic ($\mu_a(\mathbf{r}, \hat{\Omega}, t, \lambda) = \mu_a(\mathbf{r}, t, \lambda)$) leads to Equation 2.7, which is also referred to as continuity relation. It describes the transport of Φ through a diffusive medium.

$$\frac{1}{v}\frac{\partial}{\partial t}\Phi(\mathbf{r}, t) + \nabla\mathbf{J}(\mathbf{r}, t) + \mu_a(\mathbf{r}, t)\Phi(\mathbf{r}, t) = S(\mathbf{r}, t) \tag{2.7}$$

with the radiant source power concentration (S) [W cm^{-3}] given by the total power per volume element at position $\mathbf{r}$ and time t propagating radially outwards:

$$S(\mathbf{r}, t) = \int Q(\mathbf{r}, \hat{\Omega}, t)\, d\Omega \tag{2.8}$$

By furthermore considering isotropic light sources as well as slow temporal variations [260], the substitution of Equation 2.4 into Equation 2.3 bears a relation between the photon flux ($\mathbf{J}$) and the photon fluence rate (Φ), also known as Fick's first law of diffusion.

$$\mathbf{J}(\mathbf{r}, t) = -\underbrace{\frac{1}{3(\mu_a + \mu_s')}}_{D(\mathbf{r},t)\cdot v^{-1}} \nabla\Phi(\mathbf{r}, t), \tag{2.9}$$

with the diffusion coefficient $D(\mathbf{r}, t)$ [cm^2/s] [2]. Fick's first law is also used to describe propagations which are not driven by

2 By writing the light radiance as $L(\mathbf{r}, \hat{\Omega}, t) = L_0(\mathbf{r}, \hat{\Omega}, t) \cdot \exp\left[-v\mu_a t\right]$ it was shown that the photon diffusion coefficient (D) could also be simplified to [95] $D = \frac{v}{3(\mu_s' + \mu_a)} \approx \frac{v}{3\mu_s'}$. This transformed absorption-independent diffusion coefficient leads to a better agreement between Monte Carlo results and diffusion theory. This is a result of the P_1 approximation, which requires light isotropy, and the condition $\mu_a \ll \mu_s'$.

external forces, i. e. external electrical fields, such as heat diffusion in a metal.

In the pursuit of an equation, which describes a diffusive process of photons in a medium and allows an analytical solution, we can combine Fick's first law of diffusion (Equation 2.9) and Equation 2.7 in order to reach the diffusion equation (DE):

$$\frac{\partial \Phi(\mathbf{r},t)}{\partial_t} - \nabla \cdot [D(\mathbf{r},t)\nabla\Phi(\mathbf{r},t)] + v\mu_a(\mathbf{r},t)\Phi(\mathbf{r},t) = vS(\mathbf{r},t) \tag{2.10}$$

This equation describes the photon diffusion in diffusive media (i.e. biological tissue) under the above mentioned conditions and assumptions. It relates the radiant source power concentration S to the changes in the photon fluence rate Φ due to absorption, scattering and time variations.

2.3.2 *Boundary conditions*

The solution of the DE in an experimental setting depends on the medium geometry. We are interested in a reflective geometry so we assume the medium to be semi-infinite. This means that the medium spans to infinity along the x-y-plane and from z = 0 to infinity along the z-direction. In the experimental setting the boundary z = 0 then reflects the medium-air boundary. In this case, boundary conditions need to be taken into account. We use the extrapolated-zero boundary condition:

$$\Phi(z) = \Phi(0) + \frac{\partial \Phi}{\partial z} z = \Phi(0) + \frac{\partial \Phi(0)}{\partial z_b} z \xrightarrow{z=z_b} \Phi(z_b) = 0 \tag{2.11}$$

where the zero boundary is set to:

$$z_b = 2\, D \cdot \left(1+R_{eff}/1-R_{eff}\right) \tag{2.12}$$

The effective reflection coefficient R_{eff} is a result of linear least squares fit [134] and given by:

$$R_{eff} \approx -1.440 \cdot (n^*/n_1)^{-2} + 0.701 \cdot (n^*/n_1)^{-1} + \\ + 0.0636 \cdot (n^*/n_1) + 0.668 \tag{2.13}$$

n^* and n_1 represent the refractive indices in- and outside the medium.

The extrapolated-zero boundary condition (Equation 2.11) forces a zero fluence rate at $z = z_b$. This then leads to:

$$\Phi = 2D\frac{1 + R_{eff}}{1 - R_{eff}}\hat{n} \cdot \nabla\Phi \tag{2.14}$$

This approximation is a simple approach in the model for the homogeneous semi-infinite medium and is obtained by a Taylor expansion for the fluence rate around the boundary ($z = 0$) truncated after the first order. Formulating this condition is equal to considering the light source as two isotropic light sources, a positive one located at one transport mean free path inside the medium ($z = l_{tr}$, with $z = 0$ as the air-medium interface) and a negative one located at $z = -(l_{tr} + 2z_b)$ as shown in Figure 2.5.

2.3.3 *Correlation diffusion theory*

The unnormalized electrical field ($\mathbf{E}(\mathbf{r}, t)$) autocorrelation function (G_1 at position $\mathbf{r}$ is defined as

$$G_1(\mathbf{r}, \tau) = \langle \mathbf{E}(\mathbf{r}, t) \cdot \mathbf{E}^*(\mathbf{r}, t + \tau) \rangle . \tag{2.15}$$

$\langle\ \rangle$ denotes the ensemble average. unnormalized electrical field autocorrelation function (G_1) can be interpreted as a "correlation fluence rate".

Similar to the RTE and it's description of Φ, a correlation transport equation can be written [27, 84, 4], which describes the evolution of G_1. Using the diffusion approximation, we then arrive at the correlation diffusion equation (CDE), which

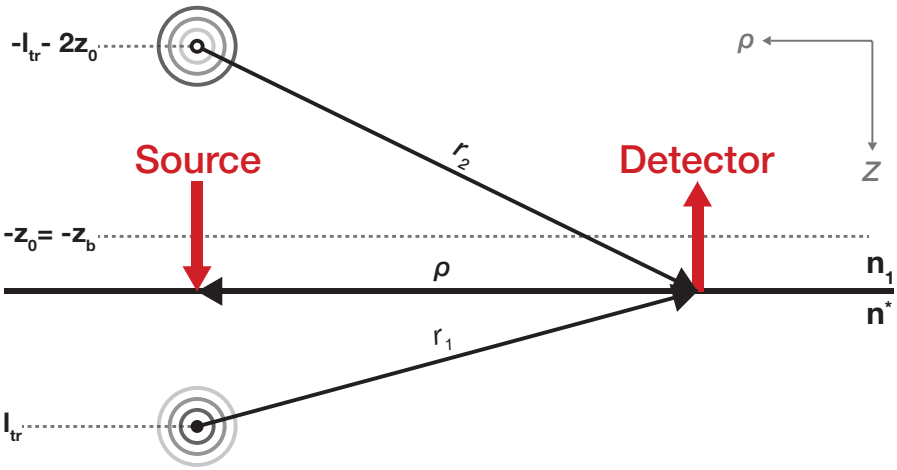

Figure 2.5: Extrapolated zero boundary condition (semi-infinite geometry): The isotropic nature of the source is modeled for a semi-infinite geometry by an isotropic light source at $z = l_{tr}$ inside the medium (refractive index n^*) and a negative isotropic image source at $z = -l_{tr} - 2z_0$ above the medium (refractive index n_1). The source-detector separation is defined as ρ and z=0 is located at the medium interface. This illustration is inspired by [170].

describes the diffusion of the light field autocorrelation [30, 27, 28]:

$$\left[-\nabla \cdot (D\nabla) + v\mu_a + \frac{1}{3} v\mu_s' k_0^2 \alpha \left\langle \Delta r^2(\tau) \right\rangle \right] G_1(\mathbf{r}, \tau) = vS(\mathbf{r}) \tag{2.16}$$

The CDE resembles the diffusion equation, but inherits an additional term with $\langle \Delta r^2(\tau) \rangle$ representing the mean-square displacement of the scatterers over the correlation time (τ), as well as the wavenumber of the light inside the medium $k_0 = 2\pi/\lambda$ and the fraction of moving scatterers (α). That additional term - similarly to the part, which describes the loss of photons due to absorption - accounts for correlation losses due to the dynamics in the medium.

The dynamic term $\langle \Delta r^2(\tau) \rangle$ was found empirically to be expressed best in biological tissue by $\langle \Delta r^2(\tau) \rangle = 6 D_b \tau$ [321, 90, 262, 94, 89, 56, 27], where particle Brownian diffusion coefficient (D_b) [cm^2/s] is the effective diffusion coefficient with the subscripted "b" indicating that the expression originates from the Brownian diffusion model. In comparison to the

thermal Brownian diffusion coefficient of cells in blood given by the Einstein–Smoluchowski relation [99], the diffusion coefficient in the 6 $D_b\ \tau$ - term is a few orders of magnitude larger.

This approach gives rise to diffuse correlation spectroscopy, a technique which provides information about flow inside a medium. The underlying theory originates from diffusing wave spectroscopy (DWS) and the description of diffusing temporal fields [27, 28, 30].

2.4 DIFFUSE CORRELATION SPECTROSCOPY

The CDE can be solved using the famous Green's function approach. We use the same boundary conditions as before (Section 2.3.2). These lead to the semi-infinite medium solution for G_1 [94, 27]:

$$G_1(\rho, z, \tau) = \frac{\nu}{4\pi D}\left(\frac{exp[-K(\tau)r_1]}{r_1} - \frac{exp[-K(\tau)r_2]}{r_2}\right) \quad (2.17)$$

with

$$K(\tau) = \sqrt{3\ \mu_a\ \mu_s' + 6\ k_0^2\ \alpha\ \mu_s'^2\ D_b\ \tau}$$
$$r_1 = \sqrt{\rho^2 + (z - l_{tr})^2}$$
$$r_2 = \sqrt{\rho^2 + (z + 2z_b + l_{tr})^2}.$$

For the definition of r_1 and r_2, please refer also to Figure 2.5. The decay factor from the exponent in Equation 2.17, $K(\tau)$, depends on the correlation time τ. This carries the information about the dynamics in the medium.

2.5 TIME-RESOLVED SPECTROSCOPY

In the time domain, short (picosecond) laser pulses are used and the flight time of diffused photons several mm away from the source is recorded. This technique is called time-resolved spectroscopy (TRS). In this case, the radiant source

power concentration $S(\mathbf{r},t)$ and the photon fluence rate $\Phi(\mathbf{r},t)$ in an infinite homogeneous medium can be written as

$$S(\mathbf{r},t) = S_0\,\delta(\mathbf{r}-\mathbf{r}_0)\,\delta(t-t_0) \tag{2.18}$$

and

$$\Phi(\mathbf{r},t) = S_0\,(4\pi Dt)^{-3/2}\exp\Big[-\frac{\rho^2}{4Dt}-\mu_a ct\Big]. \tag{2.19}$$

In the semi-infinite geometry (see Sec. 2.3.2) and for large source-detector separations compared to the extrapolation distance ($\rho \gg z_b$), the photon fluence rate $\Phi(\mathbf{r},z,t)$ can be written as [240]:

$$\begin{aligned}\Phi(\mathbf{r},t) =& S_0\,(4\pi Dt)^{-3/2}\exp\big[-\mu_a vt\big] \\ &\left[\exp\Big[-\frac{(z-z_b)^2+\rho^2}{4Dt}\Big]-\exp\Big[-\frac{(z+z_b)^2+\rho^2}{4Dt}\Big]\right]\end{aligned} \tag{2.20}$$

Together with Fick's first law of diffusion (Equation 2.9) we obtain the following expression for the reflectance (R) at the medium surface [240]:

$$\begin{aligned}R(\rho,t) &= |\mathbf{J}(\mathbf{r},z=0,t)|^2 \\ &= S_0\cdot(4\pi Dt)^{-3/2}\cdot z_b(t-t_0)^{-5/2} \\ &\quad\cdot\exp\Big[-\frac{\rho^2+z_b^2}{4D(t-t_0)}-\mu_a(t-t_0)\Big]\end{aligned} \tag{2.21}$$

2.6 INVERSE PROBLEM

Based on the solution of the diffusion model the measurements are then linked to the actual biological tissue properties. The wavelengths are chosen from the near-infrared range in the "physiological window" (Figure 2.2) mentioned in Section 2.1. In addition to that we can choose between different source types.

Light from a CW source allows to characterise only the total light attenuation and provides the minimum amount of in-

formation one can retrieve in a diffuse optical measurement. The most complete set of information about the medium is provided by a pulsed light source which allows to build a time-of-flight distribution from the diffused photons. This technique is often referred to as time-resolved spectroscopy or time domain measurements. It acquires distribution time of flight (DTOF) curves for different wavelengths so that the wavelength information can be used to calculate different chromophore concentrations (see Section 2.1).

There are different approaches to the DTOF evaluation. We focus on fitting the solution of the diffusion equation to the measurement. In this process, it is important to correct for the instrument, since the light pulse in theory is described as a delta pulse and we are limited by the available laser pulse widths. Furthermore, optical fibers, detectors and electronics add to the pulse width. The correction is achieved by convolution of the instrument response function (IRF), which accounts for the mentioned instrument characteristics, and the solution for the reflectance (R) from the diffusion approximation for the semi-infinite homogeneous medium [240]. The results is then fitted to the measured DTOF curve. This yields the absorption μ_a and reduced scattering coefficients μ_s'. Both curves, the IRF as well as the DTOF are normalized prior to fitting it to the above-mentioned solution. Typically, the fit range is adjusted based on the diffusion approximation and the nature of absorption [229, 169].

For DCS, it is important to state that detectors can only record the magnitude squared of the electrical field, the irradiance. The unnormalized intensity autocorrelation function (G_2) is defined as

$$G_2(\mathbf{r}, \tau) = \langle I(\mathbf{r}, t) \cdot I(\mathbf{r}, t + \tau) \rangle \,. \tag{2.22}$$

The temporal electric field and intensity autocorrelation functions are related by the Siegert relation [183]:

$$G_2 = \langle I \rangle^2 + \beta \, |G_1|^2 \tag{2.23}$$

The mode parameter (β) depends on the experimental setup and is affected by the number of detected laser modes or

speckles. It can also be affected by laser characteristics such as stability and coherence length but assume this is minimal [21, 254, 198]. The normalized intensity and electrical field autocorrelation functions (g_2 and g_1 respectively) are defined as:

$$g_2(\tau) = \frac{\langle I(t) \cdot I(t+\tau) \rangle}{\langle I(t) \rangle^2} \tag{2.24}$$

$$g_1(\tau) = \frac{\langle E(t) \cdot E^*(t+\tau) \rangle}{\langle E(t) \cdot E^*(t) \rangle} \tag{2.25}$$

With the knowledge of β, the measurement of normalized intensity autocorrelation function (g_2) can be converted in into normalized electrical field autocorrelation function (g_1). The solution of the CDE (Equation 2.17) is then fit to the resulting g_1. As mentioned in Section 2.3.3, the mean square displacement <Δr^2 (τ)> in Equation 2.17 is found to be best approximated by $6D_b\tau$ [60, 90, 46, 262, 50, 346, 94, 96, 44, 341, 340, 92], which gives information about the dynamics in the medium, e. g. blood flow in biological tissue and together with the fraction of moving scatterers (α) is therefore reported often as a blood flow index (BFI).

$$BFI = \alpha \, D_b \tag{2.26}$$

2.7 MODELLING MEDIUM RESPONSE IN THE SEMI-INFINITE MEDIUM APPROACH

Based on the knowledge from photon and correlation diffusion theory (Sections 2.3.1 and 2.3.3) we will explore the expected response for different experimental parameters, such as source-detector separation (ρ), μ_a, μ_s', D_b and the index of refraction of the turbid/medium tissue (n^*).

2.7.1 *Time-resolved spectroscopy*

As explained in Section 2.5, the R of the medium changes with ρ, μ_a and μ_s'. While ρ can be controlled by the experimentalist, μ_a and μ_s' are given by the medium and their knowledge is useful in its characterization. Figures 2.6 and 2.6 illustrate

the changes of R with ρ, μ_a, μ_s' and n^*.

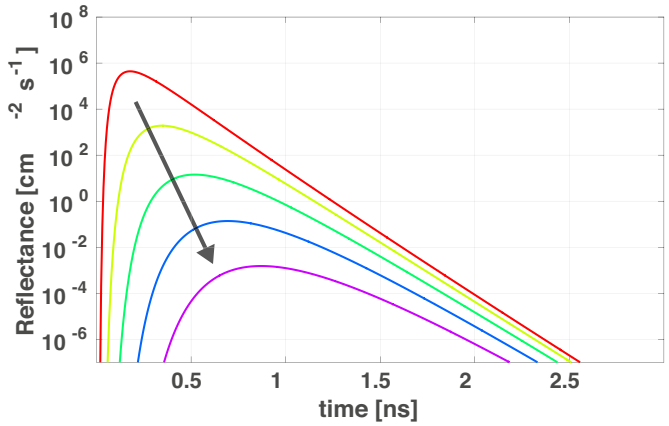

a) Variation of ρ

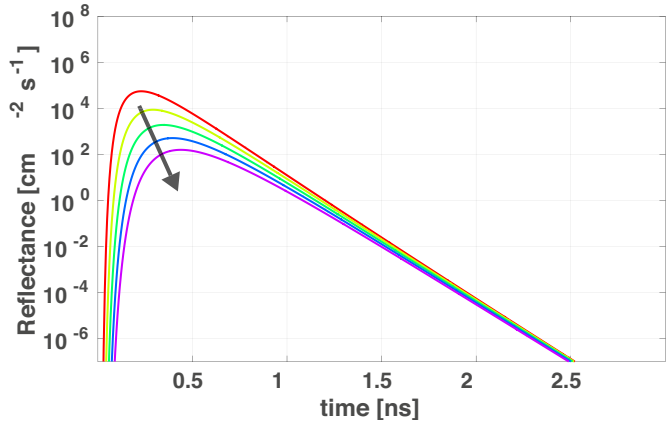

b) Variation of μ_s'

Figure 2.6: Reflectance behaviour under source-detector distance and scattering changes: a) varying ρ between 0.5 cm and 4.5 cm in steps of 1 cm; b) varying μ_s' between 5 cm^{-1} and 15 cm^{-1} in steps of 2.5 cm^{-1}

All three parameters have different influence on the actual shape of the reflectance. The bigger ρ, the more the peak shifts downwards and to the right (Figure 2.6 a). This is expected because the photons need more time to travel to the far distant detector (shift to the right). Along their path more of them get absorbed by the medium since they travel further. A similar behaviour may be observed in variation of μ_s' (Figure 2.6 b)), since a higher degree of scattering results in a shorter transport mean free path l_{tr} and therefore increases the time the photons spent in the tissue. For increasing absorption, e. g. higher μ_a, changes in the decay of R can be

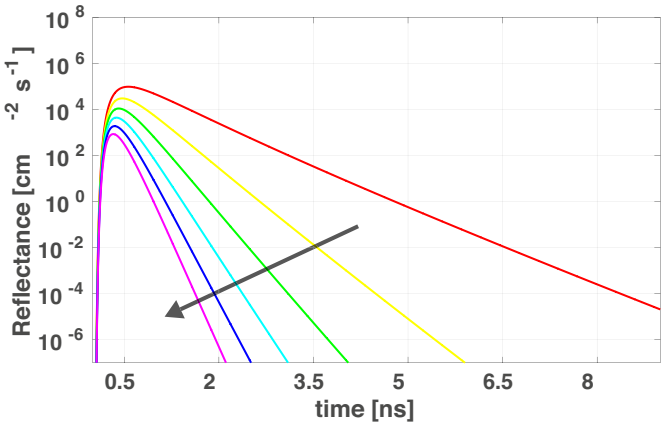

a) Variation of μ_a

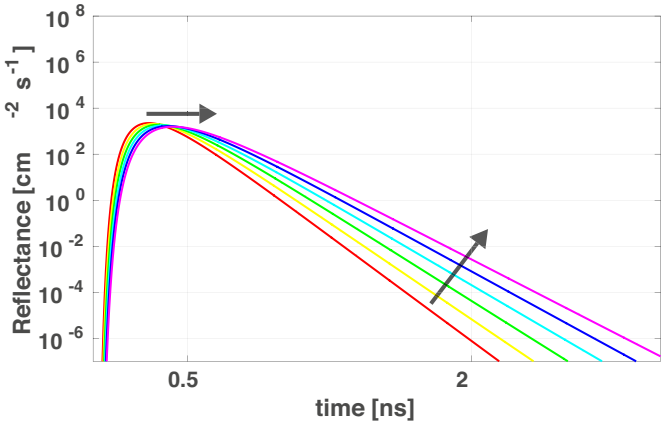

b) Variation of n^*

Figure 2.7: Reflectance behaviour under absorption and refractive index changes: a) varying μ_a between 0.1 cm^{-1} and 0.6 cm^{-1} in steps of 0.1 cm^{-1}; b) varying n^* between 1.14 and 1.64 in steps of 0.1

observed (Figure 2.7 a)). n^* has similar influences on R as μ_s' (Figure 2.7 b)), which related to the fact that scattering is due changes in the index of refraction. Equation 2.21 as a solution of the DE in the time-domain describes this exponential decay behaviour of the reflected signal well.

2.7.2 *Diffuse correlation spectroscopy*

The second diffuse optical technique used in this thesis is DCS. In Section 2.4, the solution for the semi-infinite medium was introduced and here look at the influence of ρ, μ_a, μ_s', n^* and D_b on the correlation curve, i. e. g_1. The according graphs are shown in Figures 2.8 and 2.9.

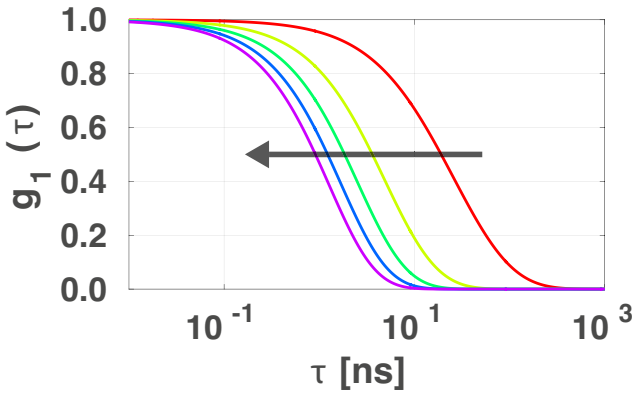

a) Variation of ρ

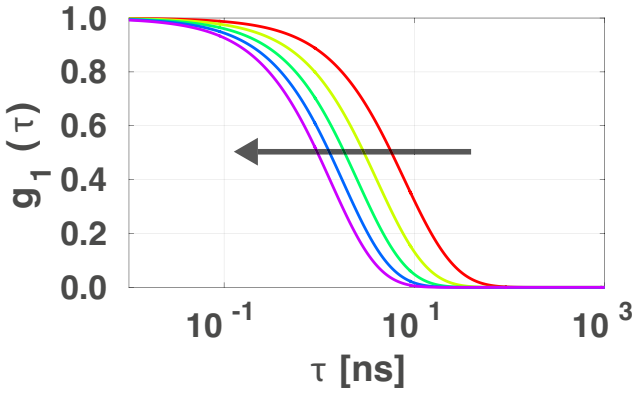

b) Variation of μ_s'

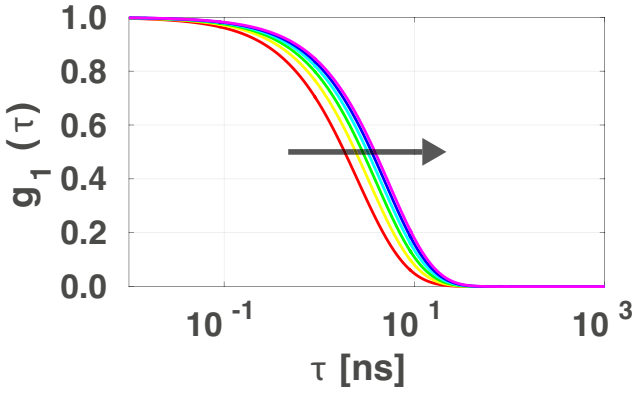

c) Variation of μ_a

Figure 2.8: Autocorrelation g_1 behaviour under changes of ρ, μ_s' and μ_a: a) varying ρ between 0.5 cm and 4.5 cm in steps of 1 cm; b) varying μ_s' between 5 cm^{-1} and 15 cm^{-1} in steps of 2.5 cm^{-1}; c) varying μ_a between 0.1 cm^{-1} and 0.6 cm^{-1} in steps of 0.1 cm^{-1}

With increasing ρ, as shown in Figure 2.8 a), we see that g_1 decays faster, which means that the correlation is lost at ear-

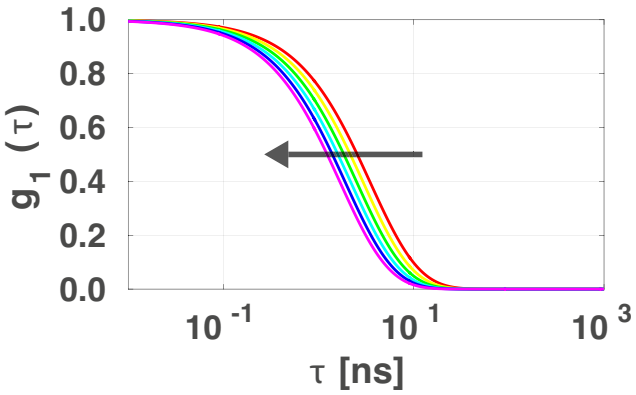

a) Variation of n^*

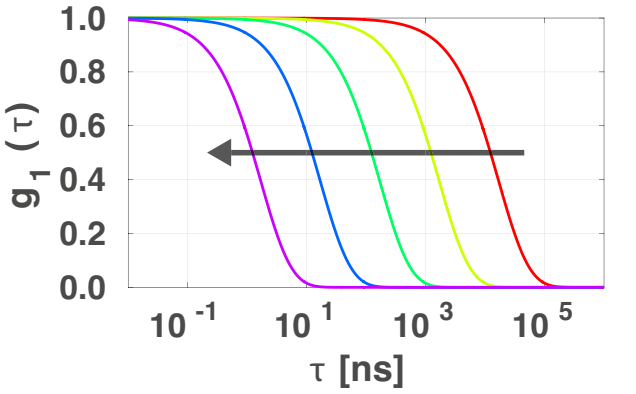

b) Variation of D_b

Figure 2.9: Autocorrelation g_1 behaviour under changes of n^*, and D_b: a) varying n^* between 1.14 and 1.64 in steps of 0.1; b) varying D_b between 1 ×10^{-12} and 1 ×10^{-8}

lier correlation time (τ). Since the photons spent on average more in the medium due to the larger distance they have to travel in order to reach the detector, more scattering events can occur and therefore correlation is lost at earlier τ. This is also true for larger μ_s' as shown in Figure 2.8 b). Changes towards larger μ_s's cause a have a similar effect on the correlation and since the refractive index of the medium (n^*) affects the scattering, we see a related change of g_1 upon increasing n^* (Figure 2.9 a)). With increasing D_b, the g_1 curve decays faster as well (Figure 2.9 b)), which in biological tissues is related a higher blood flow. This parameter together with α is referred to as the blood flow index (BFI) in this thesis.

2.8 CONCLUSION

This chapter only touched the basics of light propagation is tissues and then presented solutions and strategies in a manner relevant to the techniques and data analysis utilized and employed in later chapters. The interested reader can go deeper into the topic by following the references provided here.

3

OXYGEN TRANSPORT, CEREBRAL HEMODYNAMICS AND AUTOREGULATION

In this chapter, the oxygen diffusion in tissue is discussed in a brief and simple manner. The effects of different gas concentrations (CO_2 and O_2) in the blood are presented and how changes in these concentrations affect the blood perfusion. A compartment model is used to understand how oxygen reaches and penetrates biological tissue. Oxygen uptake by hemoglobin as well as how the oxygen saturation (SO_2) at the arterial and venous end of the capillary depends on the arterial partial pressure of carbon dioxide ($PaCO_2$) will also be explained. cerebral autoregulation (CAR) is introduced and alterations in cerebral blood flow (CBF) as well as the causes are examined. The goal is to present the reader with basic principles needed for a non-clinician to understand the relationship between the measurements and the underlying physiology.

3.1 OXYGEN TRANSPORT

The body's vascular system provides the supply of oxygen to tissue and organs and also takes care of part of the clearance of metabolic byproducts. The system can be divided into the macro- and microvasculature [312]. While the blood vessel at the macrovascular levels are large, such as the middle cerebral artery (MCA) in the brain, it is the microvasculature that plays the main role in the oxygen supply and clearance processes: On the arterial side, oxygen saturated red blood cells (RBC) are transported through the macrovasculature then in to the microvasculature from which oxygen is actually transported into tissue. Oxygen is then used to produce energy and the byproducts are then cleared together with the partially oxygen depleted RBC [312].

In order to explain blood oxygen transport in the tissue a compartment model is often used. We consider the main blood components RBC and blood plasma. Compartment models are widely applied in the estimation of drug uptake and delivery. The simple single compartment model for the estimation of oxygen metabolism can be seen as an oxygen mass balance relation [17, 320, 31, 315, 49] as illustrated in Figure 3.1.

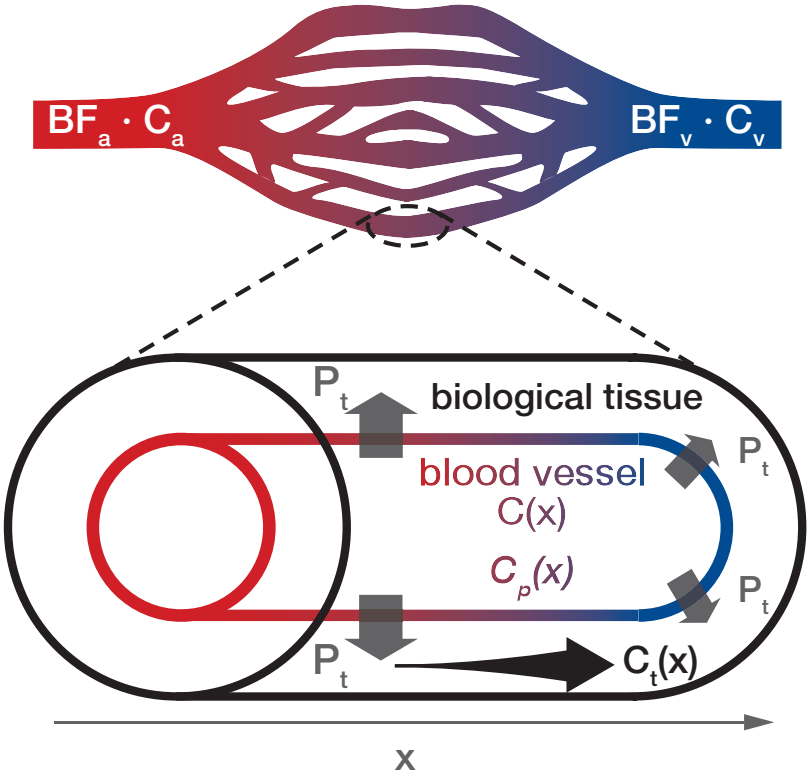

Figure 3.1: Compartment model for blood tissue interaction: The oxygen concentration is abbreviated by C. The plasma concentration (C_p) oxygen represents the O_2 concentration in the blood plasma. The tissue permeability (P_t) leads to a certain tissue oxygen concentration (C_t). All variables are dependent on the distance x each RBC has travelled in the vessel. C_a and BF_a represent the arteriole oxygen concentration and blood flow, C_v and BF_v the venous oxygen concentration and venous blood flow.

Blood with an arterial oxygen concentration C_a on the left passes through the compartment and on the venous side has a venous oxygen concentration (C_v). The total vascular oxygen concentration, which decreases due to the tissue's oxygen demand and the distance the RBC travel in the com-

partment, is described by C(x). The oxygen uptake by the surrounding tissue results in the tissue oxygen concentration (C_t). The plasma concentration (C_p) expresses the amount of oxygen dissolved in the physical solution, i. e. blood plasma. Its oxygen content in the human body is normally about 2 %, while the majority of oxygen - the other 98 % - is taken up by the RBC and attached to a protein called hemoglobin [312]. This molecule contains four separate heme groups each of which can reversibly bind an oxygen molecule [246].

As discussed previously, one can distinguish between oxy- and deoxyhemoglobin (HbO_2 and Hb) based on their absorption spectra and this can be used to determine their concentrations in the blood. This is generally done using near-infrared light and is the basis of the standard pulseoximeter. In this thesis, we employ this same concept with pulsed laser sources and photon counting techniques in a time-resolved spectroscopy (TRS) setup.

Oxygen is released by hemoglobin when a lower partial pressure of oxygen (PO_2) is present in the surrounding tissue [312, 318]. PO_2 in the capillary is higher than in the surrounding biological tissue and it is this condition which drives oxygen diffusion into the tissue. This pressure dependent oxygen dissociation from hemoglobin is shown in Figure 3.2 and is the result of a least-squares fitting to empirical data [318, 162, 280].

The oxygen-hemoglobin dissociation curve is dependent on the temperature (T), the blood's pH and the arterial partial pressure of carbon dioxide ($PaCO_2$) [65, 246, 216, 130, 279, 14, 39]. Changes in these factors can cause a left or right shift to the oxygen-hemoglobin dissociation curve. A smaller value of T and $PaCO_2$ results in a left shift while a larger value results in a shift to the right. The opposite effect is seen with changes in pH. For the description of the oxygen-hemoglobin dissociation curve we need to take into account the Bohr effect. The Bohr effect describes the decreasing oxygen affinity of hemoglobin due to increasing CO_2 blood concentration. As a consequence the acidity/alkalinity scale for an aqueous solution gives a lower pH value. In venous blood this leads to a slight deviation to the right from the plotted oxygen-hemoglobin dissociation curve (Figure 3.2) and for arterial blood it results in a higher pH and lower $PaCO_2$.

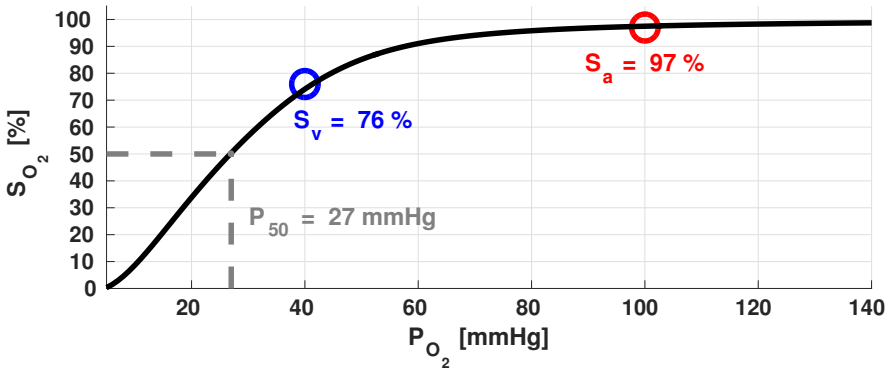

Figure 3.2: Oxygen-hemoglobin dissociation curve: It relates the oxygen saturation (SO_2) to the partial pressure PO_2 under standard conditions T = 37°C, pH = 7.4 and $PaCO_2$ = 40 mmHg. The partial pressure at SO_2 = 50 % (P_{50}), which is used a measure of health condition, is marked in grey. Red and blue markings give an idea of the arterial and venous conditions. The graph is created based on [162].

These have changes further implications for the blood circulation, including flow. The relationships between these parameters can be studied by changing the contents of the inhaled gas mixture, which in turn affect PO_2 and $PaCO_2$ [207, 7, 296, 130, 165, 167, 292, 258, 163].

3.2 CEREBRAL CIRCULATION AND METABOLISM

Since a large part of the measurements presented in this thesis includes information on cerebral hemodynamics, in this Section, some important concepts of brain physiology are presented. These help in the understanding of the measurements presented in the second part of this thesis.

The brain is critical and delicate organ and as such nature has provided a couple of elegant design solutions to protect it. Some of the most important of these solutions are the circle of Willis and cerebral autoregulation (CAR).

3.2.1 *Circle of Willis*

The circle of Willis is part of the macrovasculature in the human brain and can be seen as nature's backup plan to avoid ischemic conditions in the brain [188, 312, 303]. If an artery is occluded or bursts, i. e. a stroke or hemorrhage oc-

curs, sufficient oxygen supply to all brain regions needs to insured or re-established. The macro- and microvasculature are connected, but the structure of the circle of Willis as part of the macrovasculature allows the body to attempt that the brain is sufficiently be supplied by blood and oxygen at microvascular levels although a damage occurs within the circle of Willis. This regulating ability eases sufficient blood supply to all regions of the brain and allows us, to place our fiber optic probes on the human forehead in order to gain information on brain hemodynamics. Here, we discuss the circle of Willis as it is present in humans.

Figure 3.3 a) shows a bottom view sketch of the human brain with arteries and the circle of Willis forming around the optic chiasm and in the middle the pituary gland in front the hypothalamus. The diagram in Figure 3.3 b) gives a closer look at the arteries forming and supplying the circle of Willis (i. e. the arterial circle). The angiogram in Figure 3.3 c) shows this region in an actual brain. This technique relies on the injection of a radio opaque contrast agent and the use of X-rays to show a projection of the vertebrobasilar and posterior cerebral circulation.

Blood supply to the brain is provided by the posterior and anterior circulation. The middle and frontal brain regions are taken care of by the anterior circulation, while the brain stem, the cerebellum and the rear portions of the brain are supplied by the posterior circulation.

The circle of Willis is formed as the internal carotid artery enters the cranial cavity bilaterally and divides into the anterior and middle cerebral artery (ACA and MCA respectively). The anterior cerebral arteries are then united by an *anterior communicating artery*. These connections form the anterior half (anterior circulation) of the circle of Willis. Posteriorly, the basilar artery, formed by the left and right vertebral arteries, branches into a left and right posterior cerebral artery (PCA), forming the posterior circulation. The PCAs complete the circle of Willis by joining the internal carotid system anteriorly via the *posterior communicating arteries*.

This architecture enables the body to supply the brain with sufficient blood even when either the posterior or anterior arteries or their branches are occluded or a hemorrhage occurred. The circle of Willis is therefore a crucial feature in the correct functioning of the brain under adverse conditions.

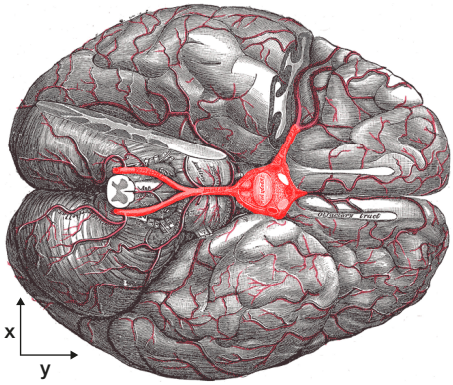

a)

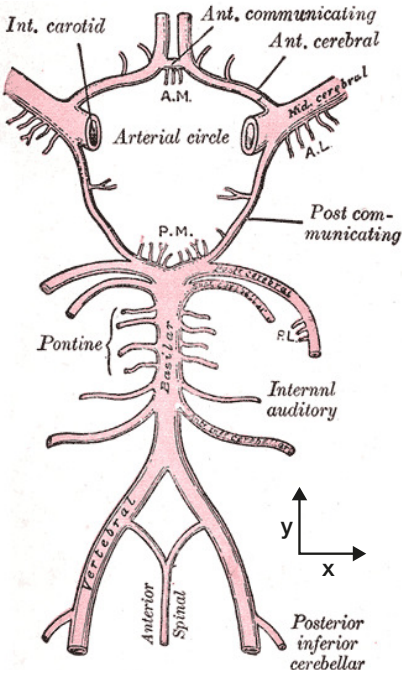

b)

c)

Figure 3.3: Illustration of the circle of Willis: a) shows a depiction of the brain and its basal arteries viewed from the bottom. b) is a schematic illustration only of the arteries feeding and forming the circle of Willis. c) shows a cerebral angiogram of the posterior part of the circle of Willis with a posterior-anterior projection of the vertebrobasilar and posterior cerebral circulation. Figures a) and b) were taken with permission from the Bartleby.com edition of [128] and Figure c) was released by the copyright holder into the public domain and published at [67].

3.2.2 *Blood flow*

Blood flow is defined as the volume of blood which passes through a vessel cross section in given a time interval. It is

influenced by factors such as heart rate (HR),cardiac output, blood pressure (BP) and vessel diameter. Since the heart acts as a pump, we can consider HR as the pumping speed, while BP acts a the pumping force. Imagining the blood vessel as a tube, we know from fluid dynamics (e. g. the Hagen-Poiseuille equation), that the tube diameter has a crucial influence on the flow. In the human body, the blood vessels can dilate and constrict in response to different $PaCO_2$ levels in the blood. As an example, the effect of this vasoconstriction or vasodilatation on CBF due to different $PaCO_2$ blood levels is shown in Figure 3.4.

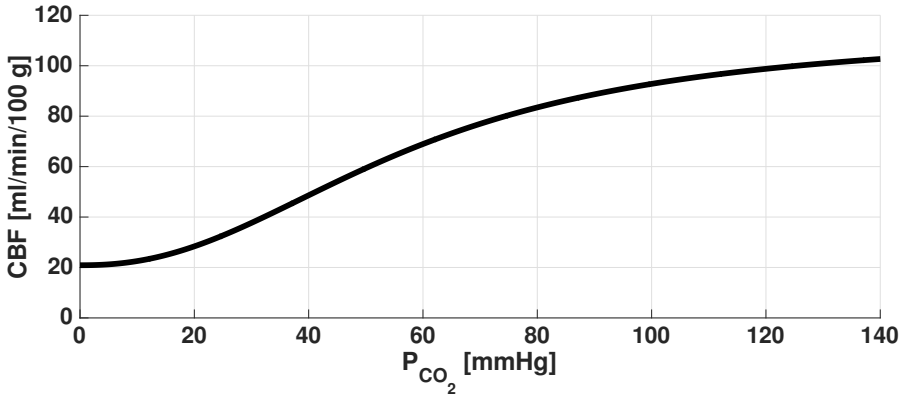

Figure 3.4: CBF dependence on $PaCO_2$. This graph is created based on [258].

3.2.3 *Cerebral autoregulation*

Cerebral autoregulation (CAR) is a physiological regulatory mechanism that acts within the brain and its vascular network to ensure constant blood perfusion - and a constant supply of oxygen - for a broad range of perfusion pressures [181, 297]. This mechanism compensates for changes in the local pressures via the cerebrovascular resistance (CVR) [212]. This process can be interrupted - or impaired - for a number of different reasons, including stroke and traumatic brain injury [122]. The interplay of the cerebral perfusion, the mean arterial and the intracraneal pressure (CPP, MAP and ICP respectively) is described by [135, 297]:

$$CPP = MAP - ICP \tag{3.1}$$

CAR then refers to ability to maintain cerebral blood flow (CBF) constant over a CPP range via the above-mentioned CVR:

$$CBF = \frac{MAP - ICP}{CVR} = \frac{CPP}{CVR} \tag{3.2}$$

A classic graphical representation, commonly used to illustrate the CAR process is shown in Figure 3.5.

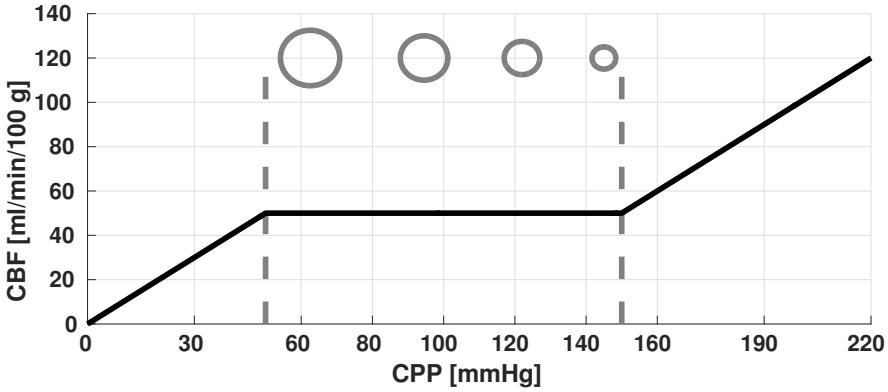

Figure 3.5: Relationship between CBF and CPP: The constant region between CPP = 50 - 150 mmHg illustrates the brain's ability to autoregulate, that is to maintain a constant CBF. This is achieved via vasodilatation or vasoconstriction, as illustrated by the grey circles above the constant region.

An intact CAR process is essential for a healthy brain. In brain injured patients, an invasive pressure probe monitoring ICP can be used to calculate CPP [290]. CPP values are needed in order to assess brain perfusion (see also Figure 3.5) and provide the possibility to study CAR in situations where the process is compromised. On the other hand, combining information on CPP with a non-invasive assessment of CBF provides a simple test of the CAR status. Diffuse optics can provide non-invasive CBF information and are therefore a promising approach to study CAR.

3.2.3.1 *Challenges to cerebral regulation of blood flow*

CBF changes can be induced by altering the concentration of inspired CO_2 concentration while a decreased concentration will act as a vasoconstrictor [207, 242, 196, 305, 257, 7, 64, 296, 216, 289, 114, 3, 256, 130, 167, 258].

In Figure 3.6, the autoregulation curve from Figure 3.5 is presented together with the oxygen-hemoglobin dissociation curve from Figure 3.2 and the relationship between CBF and $PaCO_2$ under normal conditions ("Normocapnia") is shown. It recalls the characteristics of CPP, CBF, $PaCO_2$, PO_2 and SO_2. Non-normocapnic conditions are then discussed in continuation.

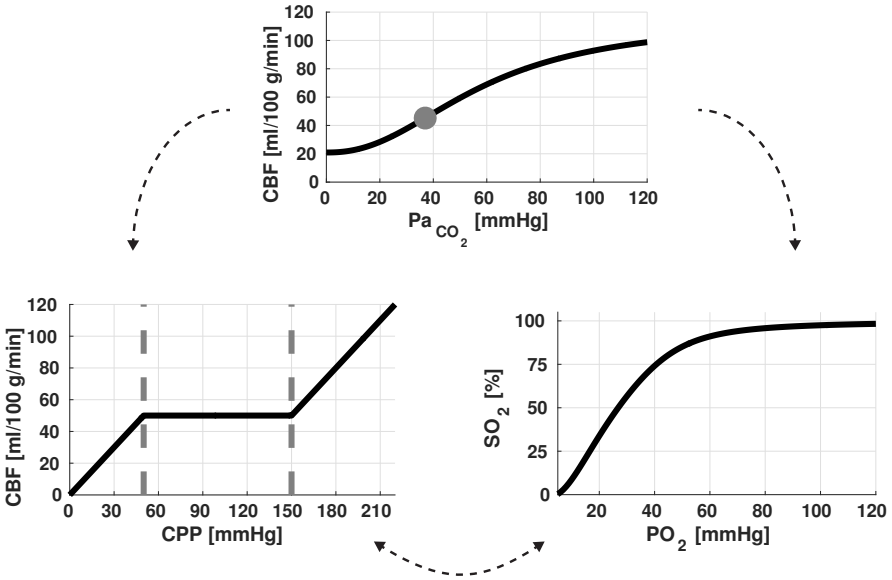

Figure 3.6: Top graph: Effect of $PaCO_2$ on CBF. Left graph: Relationship between CBF and CPP under normocapnic conditions. Right graph: Oxygen hemoglobin dissociation curve.

The grey dot in the $PaCO_2$ - CBF curve shown in the top graph in Figure 3.6 illustrates the pressure and flow that is present in the normocapnic case. As previously shown in Figure 3.5, we see in the bottom left graph the characteristic plateau region between CPP = 50 mmHg and 150 mmHg, where the CBF is kept constant by means of vasodilation (for decreasing CPP) or vasoconstriction (for increasing CPP). The oxygen hemoglobin dissociation curve - plotted on the bottom right in Figure 3.6 - is the standard curve as shown in Figure 3.2 and discussed previously. Changes in $PaCO_2$ result in cases of hypercapnia (HRC) and hypocapnia (HOC) and can be experimentally achieved by altering the CO_2 concentration in the inspired gas mixture. The hypercapnic case is shown in Figure 3.7.

Due to higher $PaCO_2$, the blood vessels dilate and CBF increases to around 70 ml/100 g/min. The increased vessel di-

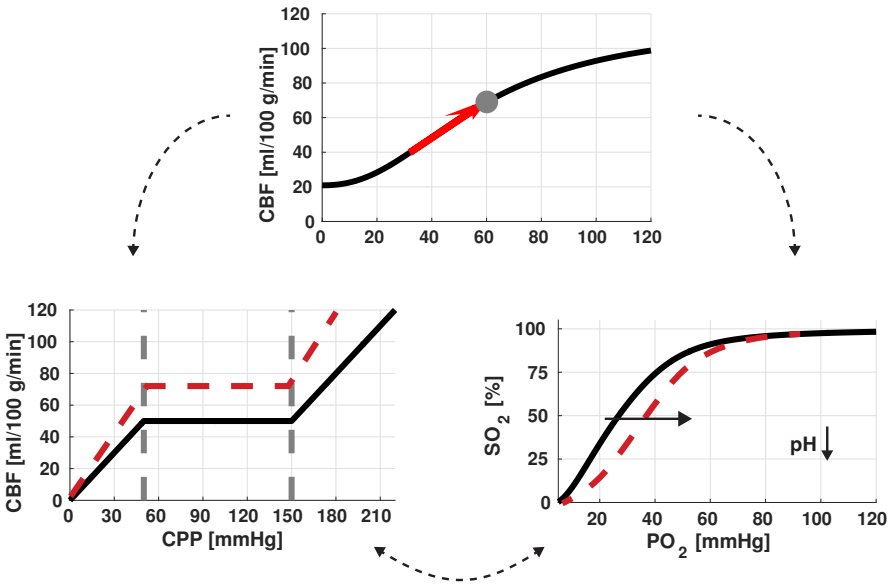

Figure 3.7: Hypercapnic influences cerebral hemodynamics: Top graph: Effect of $PaCO_2$ on CBF. Left graph: Relationship between CBF and CPP under hypercapnic conditions. Right graph: Oxygen-hemoglobin dissociation curve with a shift to the right a indicated by the arrow and caused by a decrease of pH due to an increased CO_2 blood content. Figure partially inspired by [207].

ameter leaves less margin for vessels to account for changes in the CPP, thus shrinking the tolerable pressure range. As a consequence of the $PaCO_2$ increase, the pH decreases and therefore the blood's oxygen affinity is lowered (Bohr effect). This results in a shift to the right of the oxygen-hemoglobin dissociation curve [216]. The above-mentioned CBF increase accounts for the decreased PO_2. In the opposite case, the HOC condition, oxygen affinity is increased due to higher pH and CBF is lowered in consequence of lower $PaCO_2$ (see Figure 3.8).

In this scenario, two possibilities at the rising part of the CAR curve can be thought of. At the endpoint of the region where CPP is kept constant the blood vessel are maximally constricted. Curve number 1 illustrates the case, when the vessel diameters between normo- and hypocapnic conditions at that point are the same. If that the point of maximum vasoconstriction is not the same between normo- and hypocapnia, the plateau region is extended to the right with the endpoint illustrated by the red dot in curve 2 [207]. The exact position of the upper limit of the plateau region still needs to be identified [207].

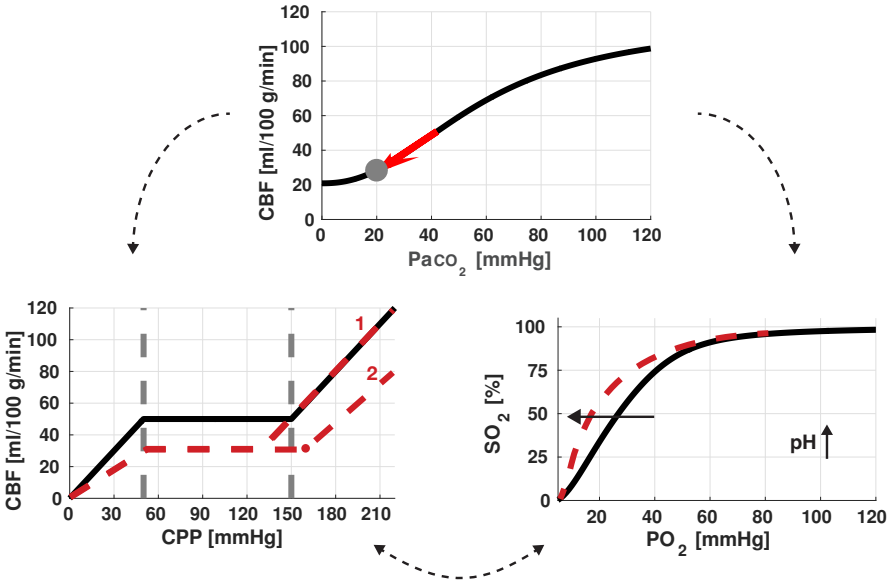

Figure 3.8: Hypocapnic influences cerebral hemodynamics: Top graph: Effect of $PaCO_2$ on CBF. Left graph: Relationship between CBF and CPP under hypocapnic conditions. Right graph: Oxygen-hemoglobin dissociation curve with a shift to the left a indicated by the arrow and caused by an increase of pH due to lower CO_2 blood content. Figure partially inspired by [207].

Another method to manipulate CBF is to change PO_2 by altering the amount of inhaled O_2 ($InspO_2$). While a decrease of O_2 leads to an increase in CBF, an increased O_2 content in the inhaled gas mixture may provoke a decrease in CBF. The latter process is called hyperoxia (HO). All three challenges discussed here (HRC, HOC and HO) may induce changes in CBF in the healthy brain and are utilized in the experiments presented in Chapters 7 and 8.

3.2.4 *Cerebral metabolism*

In the work presented here, we report the tissue oxygen saturation (StO_2). It is calculated based on the Hb and HbO_2 concentrations measured using diffuse optics.

With the tissue compartment model for oxygen metabolism described in Section 3.1, we can express the tissue oxygen saturation (StO_2) as a superposition of arterial oxygen saturation (SaO_2), capillary oxygen saturation (ScO_2) and venous oxygen saturation (SvO_2):

$$StO_2 = k_1 \cdot SaO_2 + k_2 \cdot ScO_2 + k_3 \cdot SvO_2 \tag{3.3}$$
$$ScO_2 = k_4 \cdot SaO_2 + k_5 \cdot SvO_2 \tag{3.4}$$

The respective sum of the weighting factors k_i need to satisfy the condition: $k_1 + k_2 + k_3 = k_4 + k_5 = 1$ [70]. These factors therefore represent the contributions of each compartment to the total blood volume.

The oxygen extraction fraction (OEF) can be defined as the fraction of oxygen released by the RBC and taken up by tissue as the RBC travel from the arterial to the venous side. Assuming a steady-sate balance between the hemoglobin concentration and C_a, OEF can be written as [145]

$$OEF = \frac{SaO_2 - StO_2}{\gamma \cdot SaO_2}, \tag{3.5}$$

with the arterial oxygen saturation (SaO_2), tissue oxygen saturation (StO_2) and blood volume percentage in venous compartment (γ). The parameter γ is defined as:

$$\gamma = k_3 + k_2 \cdot k_5 \tag{3.6}$$

γ has its origin in expressing StO_2 as a superposition of arterial oxygen saturation (SaO_2), capillary oxygen saturation (ScO_2) and venous oxygen saturation (SvO_2).

The cerebral metabolic rate of oxygen ($CMRO_2$) is dependent on CBF, oxygen extraction fraction (OEF), C_a and can be written as [70, 141, 145]:

$$CMRO_2 = CBF \cdot OEF \cdot C_a. \tag{3.7}$$

Together with Equation 3.5 we then can define the relative cerebral metabolic rate of oxygen ($rCMRO_2$) as [90, 33, 209, 94, 70]

$$rCMRO_2 = rCBF \cdot \underbrace{\frac{SaO_2^{ref}(SaO_2 - StO_2)}{SaO_2(SaO_2^{ref} - StO_2^{ref})} \cdot \frac{\gamma}{\gamma'}}_{rOEF}^{1}. \tag{3.8}$$

In a scenario, where the relation between SaO_2, ScO_2 and SvO_2 (Equation 3.4) changes, γ does not stay constant ($\gamma \neq \gamma'$), so that an error is introduced [250], which in our case can be written as

$$\sigma_{rOEF}[\%] = (\frac{\gamma}{\gamma'} - 1) \cdot 100 \tag{3.9}$$

based on the formulation presented above.

3.3 SUMMARY

Since we can use diffuse optics to measure hemodynamics non-invasively, some basic physiological principles are presented here. As shown in Chapter 2, we can gain information on oxy- and deoxyhemoglobin by time-resolved spectroscopy. Here, we have discussed oxygen diffusion in tissue based on a compartment model. This puts our measurements of tissue oxygen saturation (StO_2) in the later chapters into perspective and helps in the interpretation of the results. This also true when we look at the regulation of blood flow, which can be assessed by diffuse correlation spectroscopy (DCS) (see Chapter 2) as well as when we compare micro- and macrovascular circulation. A large part of the measurements presented in this thesis were acquired to gain information on cerebral hemodynamics. These can be different at the micro- and macrovascular levels due to the circle of Willis, as discussed in Section 3.2.1. The process of CAR and the effects on it due to different gas concentrations (CO_2 and O_2) in the blood have been introduced. These are particularly relevant for the understanding and interpretation of the measurements presented in Chapters 7 and 8, where we study the response of cerebral hemodynamics during hypercapnia, hyperoxia and hyperventilation. Furthermore, we will discuss the relevance of diffuse optics to cancer physiology and their importance in the interpretation of diffuse optical data in Chapter 5 for the example application of thyroid cancer.

4

EXPERIMENTAL SETUP AND INSTRUMENTATION

In this chapter, the experimental setup used for the measurements taken throughout this work is presented and characterized. We are interested in the absolute values of the oxy- and deoxyhemoglobin concentrations (Hb and HbO_2) for tissue characterization and so use a time-resolved spectroscopy (TRS) system. In order to obtain information on tissue BF we use a DCS system.

Previous studies have shown the non-practicatility of a simultaneous evaluation of μ_a, μ_s' and D_b from a single g_2 curve [83]. When using multiple small source-detector separations, such an evaluation can work, but fails at larger source-detector separations ($\rho > 2$ cm) [104]. This scenario requires the use of a hybrid TRS/DCS device and that is what is used throughout this work. Another advantage of of a hybrid design is, that the TRS-derived μ_a can be used together with μ_s' to improve analysis of DCS data [149]. This yields a more accurate estimation of the blood flow index (BFI), which is dependent on both parameters. The combination of TRS and DCS is furthermore advantageous in the calculation of the oxygen extraction fraction (OEF) and cerebral metabolic rate of oxygen ($CMRO_2$) [90, 33, 209, 94].

Details of the hybrid TRS/DCS device including the probes and fiber optics are presented here.

4.1 HARDWARE

In the experimental setup, several physical principles for detection of photons are exploited. Since the interest lies on single photon detection and their correlation characteristics, the techniques chosen to reveal information about temporal distribution of photons and intensity correlations will be discussed here.

While in DCS photons are counted by an avalanche photodiode (APD) and fed into a correlator (see Section 4.1.3) for

the autocorrelation calculation, in the TRS modality hybrid photo multiplier tubes (PMTs) are used, due to their large active area (see Section 4.1.1). The output signal from the hybrid PMT is passed to a time-correlated single photon counting (TCSPC) system (see Section 4.1.2), operated by a PC software to build the distribution time of flight (DTOF) curves.

4.1.1 *Hybrid photomultiplier tube*

A photo multiplier tube (PMT) combines two effects in order to amplify the detection of a photon, the photoelectric effect [138, 100] and secondary emission [15]. The idea is similar to an avalanche photodiode (APD), but a PMT has a larger active area. A photocathode at the beginning of the PMT absorbs an incoming photon and emits a free electron, as a consequence of the photoelectric effect [138, 100] (see also Figure 4.1). Due to a line of dynodes with increasing potential (100-1000 V), the free electron is geared towards one dynode after another, provoking an electron avalanche. This avalanche is a result of secondary emission [15], which is the second of the above-mentioned two effects used in a PMT. At the end of the PMT, this avalanche hits the anode and creates a current pulse. As a result of the electron cascade, the current is amplified by several orders of magnitude and therefore easily detectable.

In a standard PMT, electrons can also be absorbed or reflected at the dynode, thus limiting the signal amplification [18]. This effect can be avoided by using a hybrid PMT. These use an avalanche diode for electron multiplication rather than an arrangement of multiple dynodes. Instead of a secondary emission as in a PMT, here, photoelectrons are multiplied by producing many electron-hole pairs within silicon layer of the avalanche diode. The electrons of these pairs create more electron-hole pairs at the p-n-junction in a series of chain reactions. These two steps are the heart of signal amplification in a hybrid PMT.

There are major advantages in the use of a hybrid PMT. While its efficiency is comparable to that of a single photon avalanche photodiode (SPAD), the active area is significantly larger and afterpulsing becomes negligible [20]. Afterpulsing in PMTs is a result of residual gas ionisation from the pre-

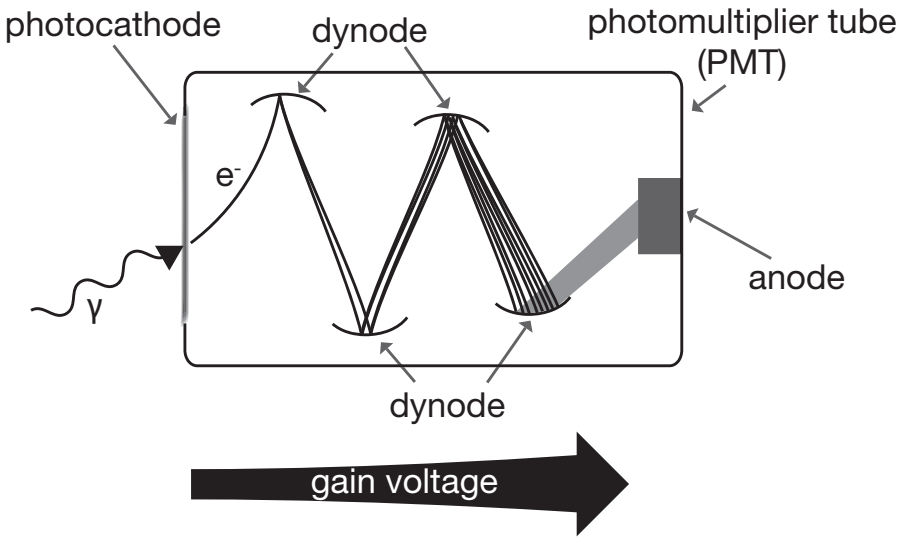

Figure 4.1: Photomultiplier tube: An incoming photon is converted into an electron (photoelectric effect) [138, 100] and due to the increasing gain voltage and secondary emission [15] at each dynode an electron avalanche is created before hitting the anode at the end of the photo multiplier tube (PMT).

vious avalanche within the dynode. When no longer using dynodes rather than an avalanche diode this effect is significantly decreased due to the lower ionisation probability from photoelectrons, which travel in the vacuum inside a hybrid PMT. Moreover, the avalanche diodes used in a hybrid PMT allow for timing resolutions within the picosecond range. This improvement in timing resolution, the reduced afterpulsing and increased signal-to-noise ratio (SNR) - as a result of an increased gain in the first step (1000 versus 5-6 in a standard PMT) - of a hybrid PMT over the conventional PMT makes it suitable for low-level photon detection with picosecond time resolution and is therefore often used in time-correlated single photon counting (TCSPC) in the field of diffuse optics.

As explained earlier, diffuse optics uses light in the near-infrared since it allows for the investigation of tissue hemodynamics. It is therefore crucial to choose a photocathode which has the ability to detect photons within a desired wavelength range. For the setup presented here, a GaAs cathode which is suitable for wavelengths between 400 and 900 nm, is used.

4.1.2 *Time-correlated single photon counter*

The TRS modality records flight times of individual photons and makes use of a technique called time-correlated single photon counting (TCSPC). In this technique, individually detected photons from a periodic low-level light signal can be related to their arrival time. Due to the fact, that the probability of detecting multiple photons per signal period is small, the arrival time can be undoubtedly assigned to a time bin with knowledge of the laser pulse initiation. Based on the periodicity of the light signal, the time bins are filled according to the recorded time of flight (TOF) of each photon. This technique is called TCSPC and its functional principle is illustrated in Figure 4.2.

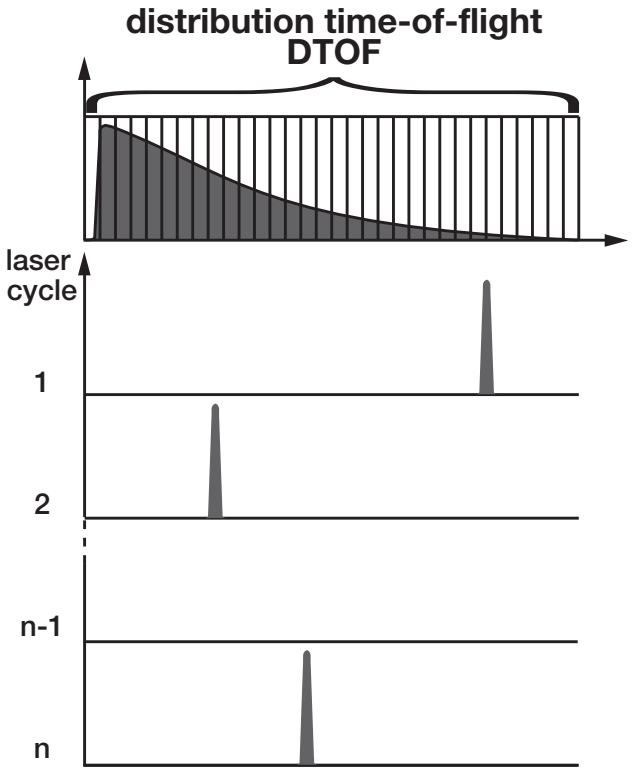

Figure 4.2: The time-correlated single photon counting (TCSPC) functional principle: Each laser cycle photon are emitted, sometimes they are detected. The counted photon pulses are assigned to a time bin and build up the DTOF. Figure adapted from [19].

This technique is described in greater detail in references [18] and [19].

4.1.3 *Autocorrelator*

In DCS measurements, the necessary normalized intensity autocorrelation function (g_2) (see Section 2.6) are calculated in real-time by a digital correlator (Correlator.com, New Jersey, USA). This correlator make use of the transistor-transistor logic (TTL) signal from an APD and time-tags it. Based on a "multi-tau" scheme, the correlator has several tiers each with a set number of registers. While the first tier consists of thirty-two registers, all following tiers have sixteen. The bin width starts at 160 ns in the first tier, 320 ns in the second tier and continues to double for every tier. The correlation time (τ) is the result of an addition of all existing time bins and the time-tagged TTL signal is used to assign the number of photon counts within each binning time. As an additional photon is detected, the existing scheme moves one register, leaving the first one to be occupied by the additional photon (see also Figure 4.3). Prior to each move, a g_2 curve is calculated. Once the acquisition time has passed the calculated g_2 is saved and a new measurement starts.

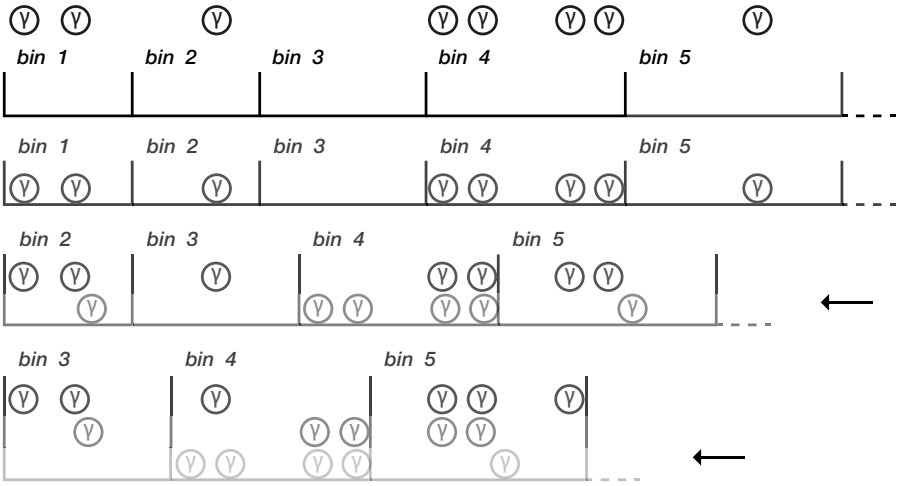

Figure 4.3: The autocorrelator functional principle: Each box is filled with a photon (γ) detected within the according time interval. The boxes are shifted to the left and applied on the photon sequence. Based on the number of photons detected within each time interval the autocorrelation is calculated when the acquisition time has passed.

4.2 HYBRID DIFFUSE OPTICAL DEVICE

The two techniques, TRS and DCS, are combined in a single instrument. Figure 4.4 gives a schematic of the hybrid system. The TRS part consists of pulsed lasers with a repetition rate of 50 Mhz at three wavelengths (690, 785 and 830 nm). The three lasers (BHLP-700, Becker & Hickl GmbH, Berlin, Germany) are connected to two optical switches (3 inputs to 1 output and 1 input to 9 outputs) in order to illuminate tissue separately at either two different source detector separations or locations. The first optical switch is used to choose one out of the three lasers to be put through to the second optical switch which passes the laser light on to either output A or output B. These two outputs allow either two source-detector separations or two separate measurement locations. The collected light is guided to a hybrid photo multiplier detector (HPM-100-50, Becker & Hickl GmbH, Berlin, Germany). Two separate detectors are used in a way that detector A collects the light from output A and accordingly for output B. A single photon counting and a detector control card together with a manufacturer-provided software (SPC-130, DCC-100 and SPCM, respectively, Becker & Hickl GmbH, Berlin, Germany) complete the time-correlated single photon counting (TCSPC) setup. this configuration enables one to acquire the distribution time of flight (DTOF) curves built from the collection of diffuse photons with varying pathlengths (see also Section 4.1.2).

The selection of the wavelength of light (λ) is based on the availability of laser sources as well as the absorption spectra for the various tissue chromophores as discussed in Section 2.1 and shown again Figure 4.5.

The TRS system is multiplexed with two single longitudinal mode lasers and four avalanche photodiodes (APDs) to create the hybrid device. Figure 4.6 illustrates the simultaneous acquisition of TRS and DCS data. The source for DCS measurements requires a laser with a long coherence length - much longer than a typical photon path length - and here we use the DL785-120-SO (CrystaLaser, Reno, NV, USA) laser. For the detection two sets of four single-photon counting avalanche photodiodes (Excelitas, Québec, Canada) are added to the system. Each DCS laser and a set of four single-photon count-

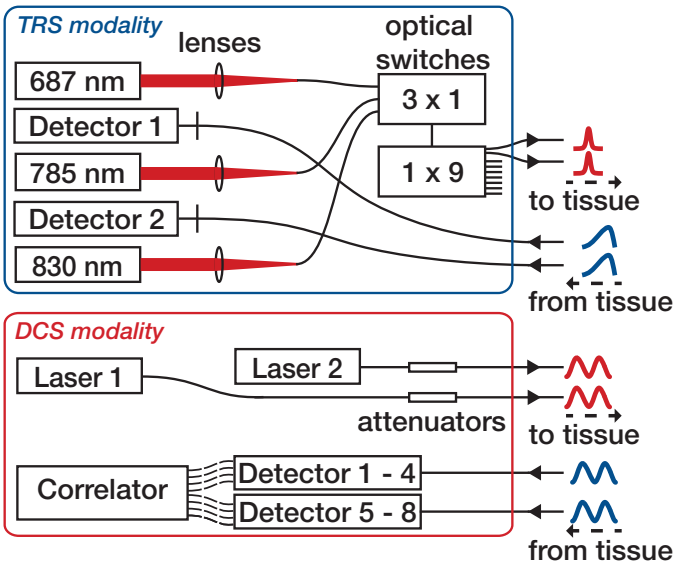

Figure 4.4: Hybrid system schematics showing on the top the time-resolved spectroscopy (TRS) and on the bottom the DCS modality. For TRS, three pulsed picosecond lasers of different wavelengths are coupled into two optical switches before their light is sent to the tissue. Light collection is done by two separate detectors, which are protected from DCS light by individual shutters. For DCS, the light of two CW lasers passes through an attenuator before it reaches the tissue. Two arrays of four single-photon counting avalanche photodiodes detect incoming photons from the tissue and are connected to an eight channel correlator, which calculates intensity autocorrelation functions.

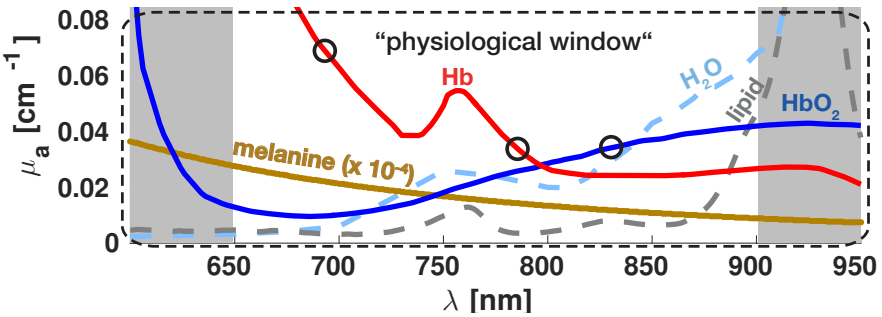

Figure 4.5: Plotted are the absorption curves for different tissue chromophores as in Figure 2.2 in the "Physiological window". The dominant chromophores (Hb and HbO_2) at the selected TRS wavelengths are marked by the black circles.

ing avalanche photodiodes is used to acquire data for either a specific source-detector separation (ρ) or specific probe lo-

cations. This leads to a similar data acquisition as in the TRS implementation, were optical switches together with two hybrid PMT detectors take care of the data recording for different ρ (see also Figure 4.9). For further details on the functional principles of both techniques please refer to Sections 2.4, 2.5, 2.6 and [230, 311, 94, 339].

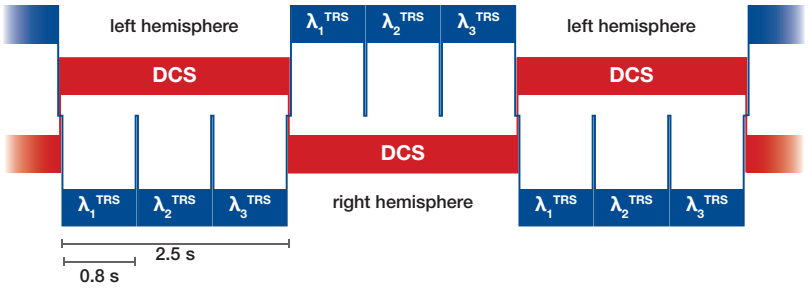

Figure 4.6: TRS and DCS acquire data simultaneously. The intensity autocorrelation curves were calculated with data collected from one hemisphere, while the system switched through all three TRS lasers on the opposite frontal lobe.

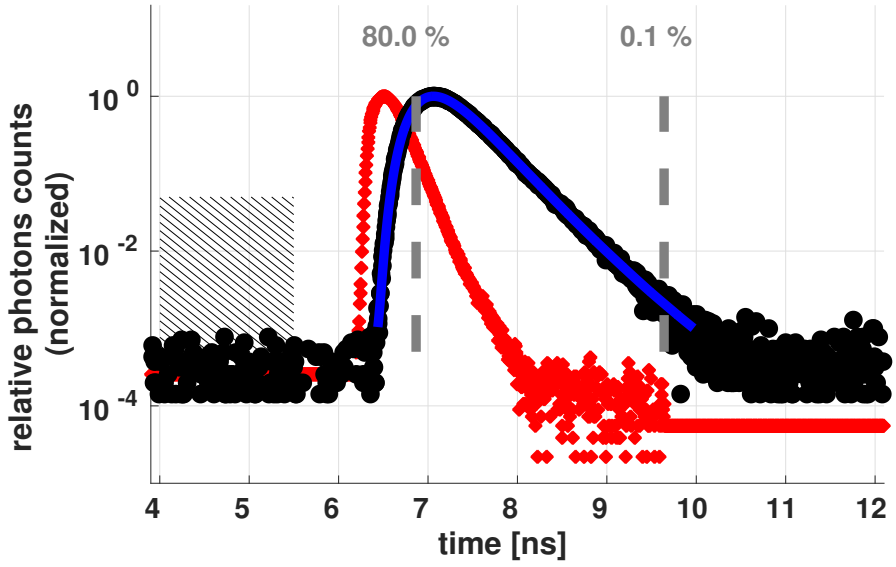

Figure 4.7: Example of a DTOF curve fit by using the IRF input (red) to calculate the theoretical response with given input parameters (μ_a and μ_s') and minimizing the χ^2 between theory and measurement (black). The resulting fitted curve is plotted in blue. Grey dashed lines highlight the fit range and the hatched area symbolizes the region used for background subtraction.

Figure 4.7 shows an example of a fit to TRS acquired data with the device. This data is a sample set from the phantom measurements presented in Section 4.2.2.3. The IRF of the system - plotted in red - is acquired and, as explained in Section 2.6, convoluted with the semi-infinite homogeneous medium solution for the reflectance (R) [240] with initial start parameters of μ_a = 0.1 cm^{-1} and μ_s' = 10 cm^{-1}. This convoluted theoretical DTOF curve is then fitted to the acquired DTOF curve - plotted in black. The final results, the blue curve - yields the final μ_a and μ_s'. Prior to the fit the background - represented by the hatched region - is subtracted and the curves are normalized.

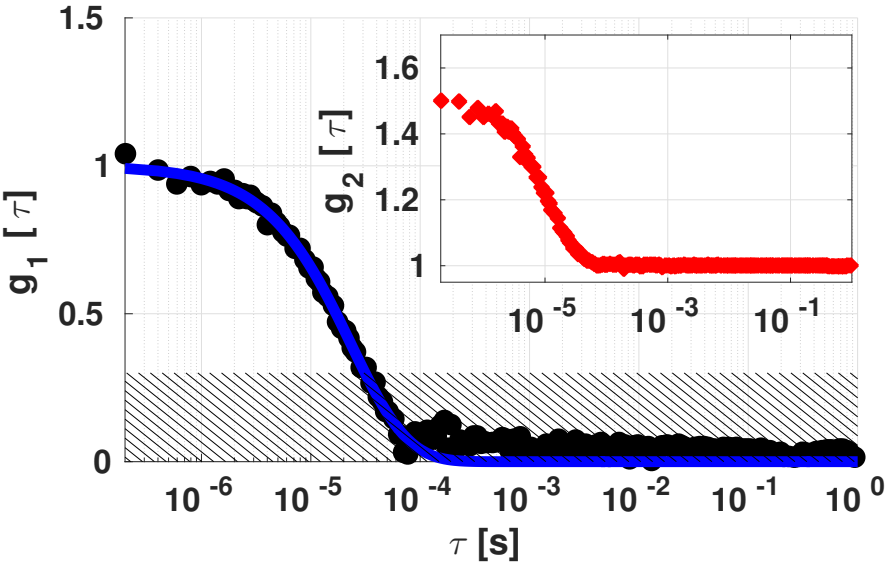

Figure 4.8: Example of a g_2 curve (red), the calculated g_1 curve (black) and the resulting fit to it (blue). Data points within the hatched were excluded from the fit.

Figure 4.8 shows an example of DCS data acquired with this system. The correlator calculated the g_2 points for different correlation times τ - shown in blue. In the data analysis, first β is calculated based on a weighted mean of the first three to five data points and then used to convert $g_2(\tau)$ into $g_1(\tau)$ using the Siegert relation [183]. Based on the semi-infinite medium solution of the correlation diffusion equation (CDE) presented in Section 2.4 and information about μ_a and μ_s' from the TRS modality the fit to the previously calculated g_1 curve is performed - plotted in blue in Figure 4.8.

The entire device is controlled by a PC and custom Visual Basic routines. These also act as a master program in the interaction with the manufacturer provided (and above-mentioned) SPCM software, which records and stores the DTOF acquisitions. An external battery pack (SAI 5160 PRO, NEW-SAI S.L., Badalona, Spain) allows operation of the system without a power cord, when moving it in the hospital environment, which turned out highly useful.

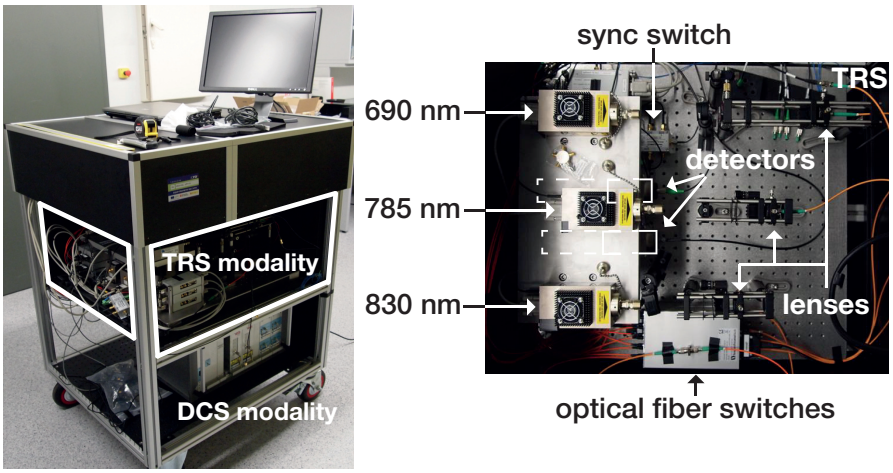

Figure 4.9: Hybrid system illustration: Shown on the left is the entire device with the DCS and TRS part of the system in the bottom and middle part, respectively. A top view onto the TRS part is shown on the right.

This system was first tested on a series of phantoms (INO Biomimic®). Following various refinements, improvements as well as system characterisation it was then employed in the clinical environment. Phantom data was taken alongside hospital measurements. This data is presented in Section 4.2.2.3.

4.2.1 *Fiber probes*

Throughout this thesis several fiber probes have been used to bring the fibers in contact with the medium, of which the optical properties were to be measured. All probes were black and incorporated either 90° bent fiber heads or straight ones. The principle idea of a fiber probe is shown in Figure 4.10.

From chapter 2 we know, that light emitted in the near-infrared can penetrate several centimeters into biological tissue. The emitted photons scatter and some get absorbed

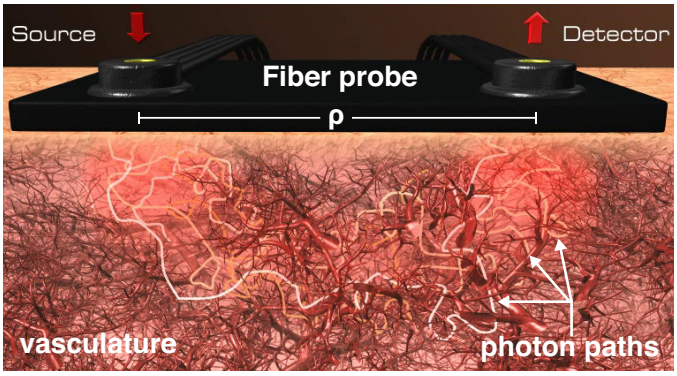

Figure 4.10: Diffuse optical probe schematic for the semi-infinite geometry case.

inside the tissue (see Figure 2.4). Their paths inside the tissue are therefore not straight - illustrated by the white lines in Figure 4.10. The summation over all those paths leads to banana shaped region in the semi-infinite geometry case shown in Figure 4.10, which extends between the source and the detector. The region is hinted by the red shaded region, which expands below the fiber probe and depends on ρ. As a simple rule of thumb, the average penetration depth is approximated by $\rho/2$.

In this thesis moslty two diffuse optical modalities were used. This requires the use of incorporation of several different fibers in the probe. An example, where TRS and DCS were combined in a single probe, which was used to acquire the data presented in the next chapter 5, is shown in Figure 4.11.

The fibers were placed in a cross-geometry, such that the above-mentioned bananas from both modalities probes common region inside the tissue. The 90° fiber heads were incorporated into a black foam pad of 4 cm height and width and the source-detector separation (ρ) was set to 13 mm and 25 mm. Since in the measurements this probe was designed for data was collected from the subject's neck, the pad has a soft surface such that it can adjust slightly to the different neck anatomies of the subjects.

Apart from the human thyroid measurements presented in Chapter 5, the hybrid setup explained above also was used in the collection of data from the human brain by placing the

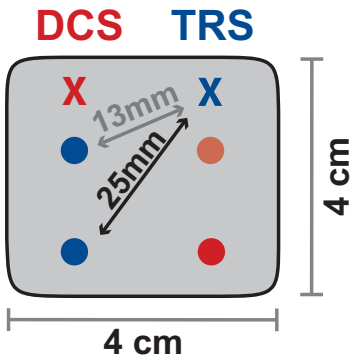

Figure 4.11: Hybrid thyroid probe with cross-geometry: The light emitted by the DCS source on the left (black cross) is collected by single-mode fibers represented by the filled circles to the right. TRS emitted light (hollow cross) is collected by fiber heads placed the hollow circle position.

fiber probes in the subject's forehead. An example of this probe is shown in Figure 4.12.

This probe was designed around an electroencephalogram (EEG) probe (BIS sensor, BIS Vista™, Medtronic plc, IRL), which is also placed on the forehead and whose data needed to be acquired simultaneously. The probe was used in the measurements presented in Chapter 6 and a variation of it without the space for the BIS sensor was placed on the subject's forefront in the studies presented in Chapters 9, 7 and 8. In the top view in Figure 4.12, we see a compact housing for the source and detector fiber heads of both modalities. The TRS fibers are drawn in yellow, while the DCS fibers are colored in green (source) and white (detector). The probe was 3-D printed in TangoBlack shore 27 material and incorporated in a head strap which wrapped around the subject's head. The same head strap provided additional fixation of the fiber after one wrap around the head. The fibers were guided away from the forefront, passing aside the subject's head and then towards the hyrbid device. This is indicated by the red and blue arrow in the bottom view of Figure 4.12, where the standard ρ (25 mm) for the measurements mentioned above is also noted.

4.2.2 *System stability*

An integral part of the hybrid device presented above (Section 4.2) is the use of picosecond pulsed light and TCSPC for

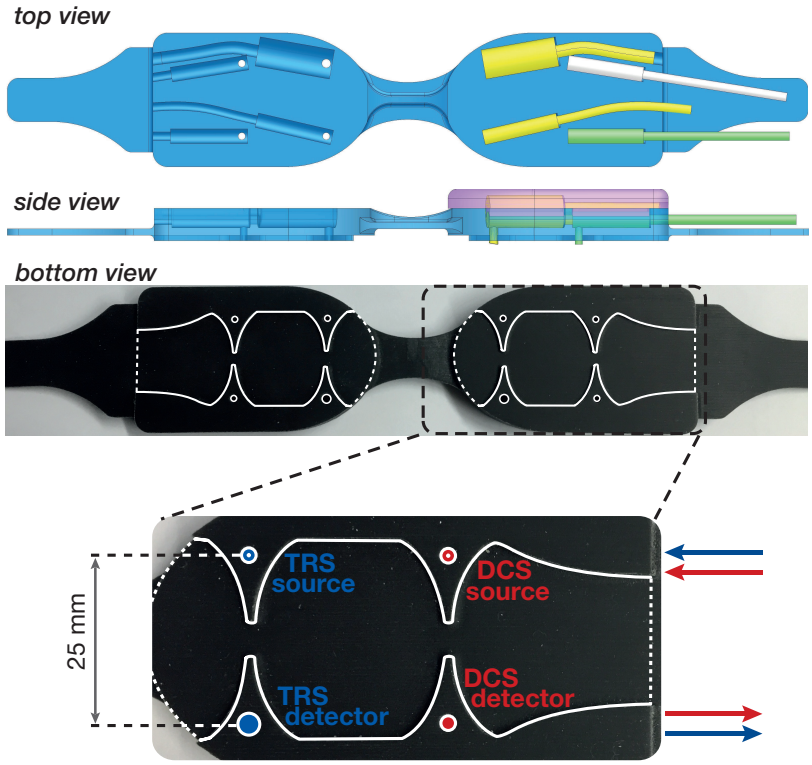

Figure 4.12: Hybrid head probe: The top view shows the TRS source and detector (both yellow), the DCS source (green) and detector (white) 90° fiber heads. The bigger one refers to the TRS detector fiber bundle. The side view shows the fiber protecting cover placed on top and in bottom view the space for the EEG/BIS sensor can be seen. White circle represent fiber tip positions, separated by ρ in both modalites (DCS in red and TRS blue).

constructing the DTOF curves. The accuracy of this TRS part depends on the laser stability - both in peak position and full width at half maximum ($FWHM$) - over time. Only based on this stability it is possible to do longitudinal measurements. Sections 4.2.2.1 and 4.2.2.2 focus on this aspect and Section 4.2.2.3 adds the detector stability to this investigation based on the results of various phantom measurements.

4.2.2.1 *Laser timing*

One important detail in a multi-wavelength TRS setup is the correct knowledge of the instrument response function (IRF), which is the recording of the characteristic photon response due to the materials used in the setup and mainly dependent on the laser itself and PMT. Of course, electronics, fiber optics and simple things, such as actual cable lengths,

have further influence on the IRF shape. As a safety net, each wavelength and each detector in the TRS setup was assigned a specific time delay. This allows to identify the emitting laser wavelength of light and the detector that built the DTOF based on the recorded peak position and therefore tells us which is the corresponding IRF to be used in the data post-processing (see Figure 4.13).

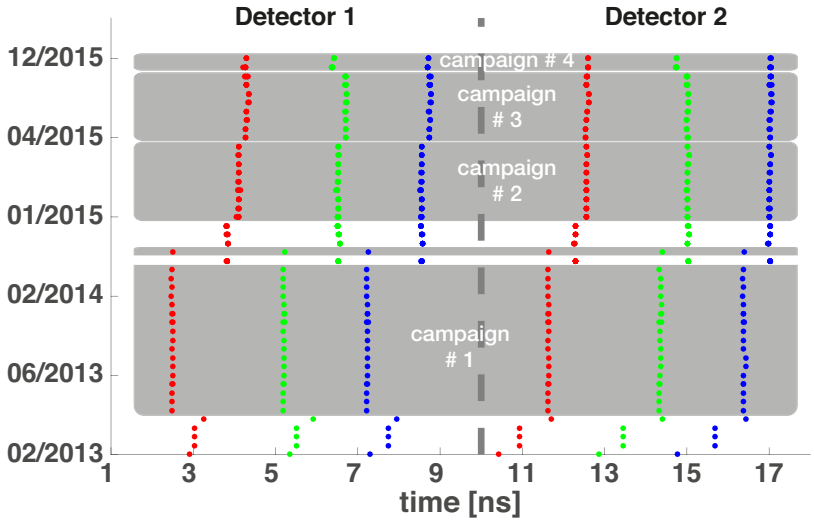

Figure 4.13: Laser peak position for different wavelengths: The calculated barycenter of each peak is plotted over a 3 year period. The three wavelengths $\lambda_{1\text{-}3}$ = 690, 785 and 830 nm are separated by $\sim$ 2 ns. The dashed grey line is set at t = 10 ns and separates curves recorded by detector # 1 (t_1 < 10 ns) and 2 (t_2 > 10 ns). Further details are explained in the text.

In order to fit signals from total of three wavelength of lights (690, 785 and 830 nm) and two hybrid PMT detectors into one 25 ns recording window, each IRF peak is separated by $\sim$ 2 ns. Figure 4.13 illustrates the calculated peak position from the barycenter of each IRF curve and its evolution over time (see also Table 4.1).

Since the setup was adapted various times throughout the curse of this thesis' work, small jumps in the peak positions can be observed. Each measurement campaign (thyroid, 1st brain study, 2nd brain study, etc.) has a specific set of laser pulse peak positions. In Figure 4.13 these are marked by numerating the measurement campaigns (# 1-4). The non-marked regions reflect measurements during maintenance periods and correspond to no specific measurement campaign. The specific setting of the first campaign is related to

campaign #	λ [nm]	peak position [ns]	
		Detector 1	Detector 2
1	690	2.49 ± 0.01	11.63 ± 0.02
	785	5.20 ± 0.02	14.35 ± 0.02
	830	7.22 ± 0.01	16.39 ± 0.02
2	690	4.10 ± 0.01	12.56 ± 0.01
	785	6.52 ± 0.01	15.02 ± 0.01
	830	8.55 ± 0.01	17.01 ± 0.01
3	690	4.30 ± 0.03	12.57 ± 0.01
	785	6.71 ± 0.01	15.01 ± 0.01
	830	8.75 ± 0.01	17.03 ± 0.02
4	785	6.39 ± 0.02	14.74 ± 0.01

Table 4.1: Laser peak position for different wavelengths and detectors: Means and standard deviations for different time delay settings for the three wavelengths (690, 785 and 830 nm) from the presented TRS setup.

the measurements presented in Chapters 5 and 9. Campaign 2 and 3 are linked to the results in Chapter 6 and campaign 4, for which only the 785 nm delay was changed (see Table 4.1), to Chapters 9 and 8. In between campaign, movements to, from and between hospitals took place.

4.2.2.2 *Laser pulse widths*

Similar to the time evolution of the peak position, we can look at the full width at half maximum ($FWHM$) and its behavior over time. Figure 4.14 and Table 4.2 show the $FWHM$ of each laser recorded with two different hybrid PMT detectors.

The system's $FWHM$ varies within less than 10% of its respective average values. Comparing average values and medians we observe only slight variations between them with a maximum value difference of 3.4 ps, which is lies below the standard deviations (4.2 - 10.4 ps) and within the IQRs (4.4 - 15.9 ps). The slightly higher $FWHM$ from detector 1 ($\lambda_1 \sim 405$ ps; $\lambda_2 \sim 345$ ps; $\lambda_3 \sim 448$ ps compared to $\lambda_1 \sim 301$ ps; $\lambda_2 \sim 279$ ps; $\lambda_3 \sim 386$ ps) led to its assignment for measurements

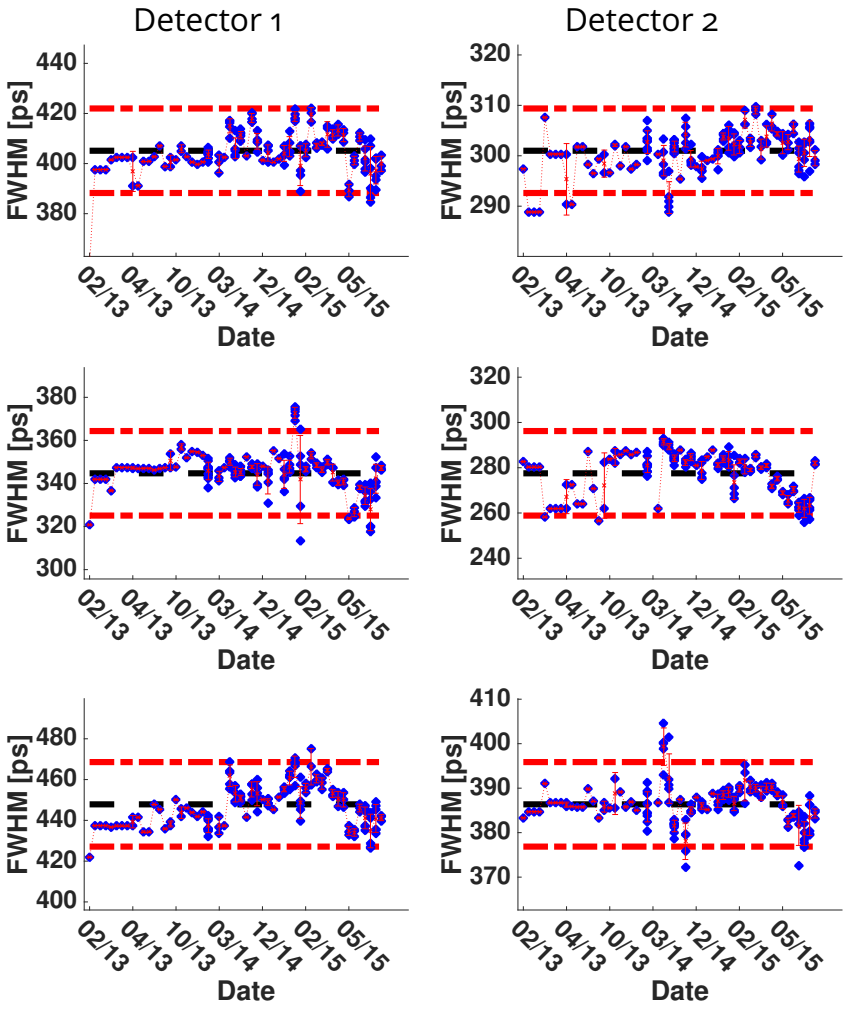

Figure 4.14: Full width half maximum for different wavelengths and detectors: The graphs are ordered from top to bottom by the three wavelengths of the TRS setup (690, 785 and 830 nm), while the left column shows data recorded by the detector # 1 and the right one from detector # 2. The black dashed line represents the mean value and the red dashed lines the ± 2 σ lines.

with a larger source-detector separation (ρ) each time data from different ρ was acquired.

4.2.2.3 *Phantom measurements*

In NIRS measurements one focus lies on the hemoglobin content in *in-vivo* tissue. Its knowledge can improve contrast between healthy and pathologic tissue or aids in the determination of global or local health condition. Information about blood flow and the ability to combine both provides further

λ [nm]	$FWHM$ [ps] Detector 1	Detector 2
	mean ± standard deviation	
690	405.1 ± 8.4	301.0 ± 4.2
785	344.7 ± 9.8	277.5 ± 9.3
830	447.9 ± 10.4	386.4 ± 4.8
	median (IQR)	
690	404.8 (9.7)	301.5 (4.4)
785	346.4 (7.8)	280.9 (14.7
830	448.1 (15.9)	386.4 (5.4)

Table 4.2: Full width half maximum for different wavelengths and detectors: Means and standard deviations as well as medians and inter-quartile ranges (IQRs) for the three wavelengths (690, 785 and 830 nm) from the presented TRS setup.

details on the correct functioning of the area of interest. The blood flow information from the DCS analysis is dependent on the scattering (μ_s') and absorption characteristics (μ_a). It is therefore crucial be able to rely on the correct values derived by diffuse optical methods. These values can be provided in a single acquisition by TRS, but it needs to be insured no offset is introduced. A standard method for this is the use of optical phantoms.

As an integral part of the presented setup, data from all three TRS wavelengths (690, 785 and 830 nm) was taken on two optical phantoms purchased from INO (Québec, Canada) and referenced against the manufacturer provided values. Figure 4.15 shows the results for μ_a from a sequence of those measurements on phantom # 1.

The data was taken prior and/or post a clinical measurement and evaluated in the same way for all dates, convoluting the solution from the diffusion equation with the IRF and then fitted to the acquired DTOF curve. The fitting range was adjusted to span from 80% of the maximum peak height on the rising edge down to 0.1% of the maximum peak height on the falling edge [229, 169]. An example is shown in Figure 4.7. The ranges were chosen based on the fact that we are only interested in the strongly diffused - so-called later - pho-

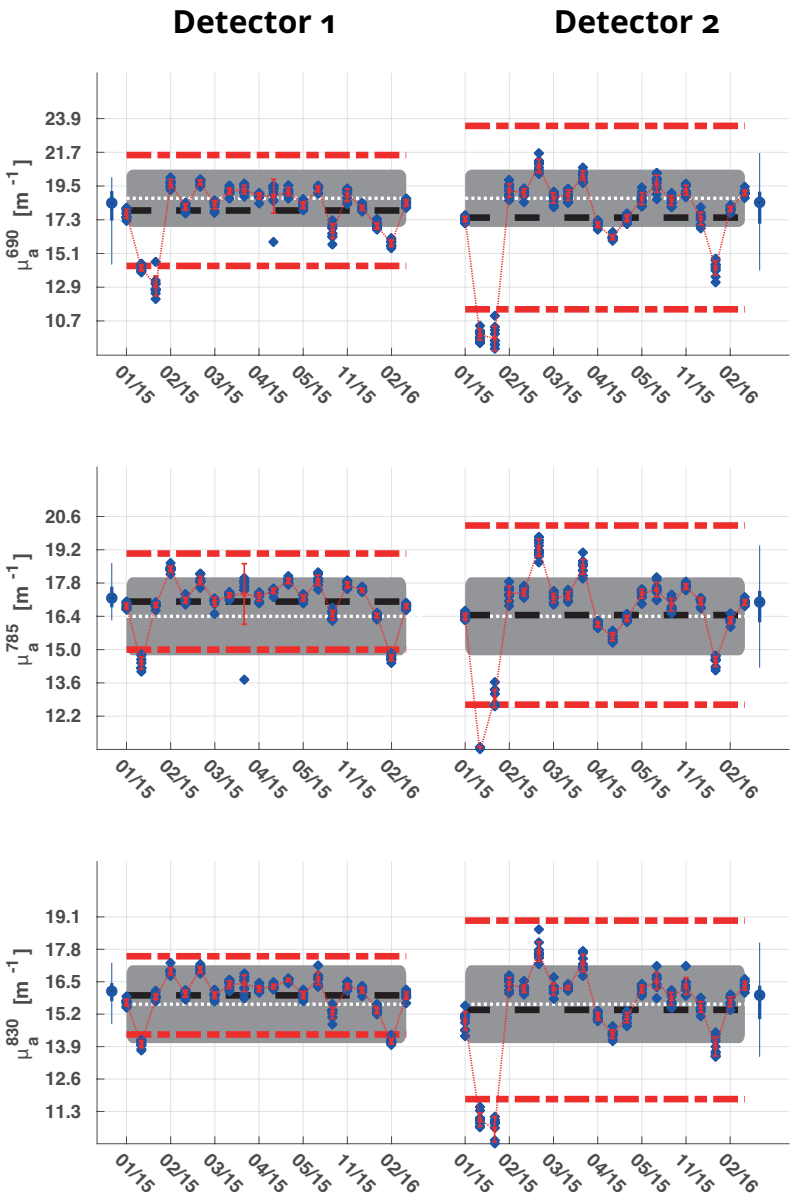

Figure 4.15: Absorption coefficients μ_a for different wavelengths and detectors: The black dashed line represents the mean value, the black dotted line the median and the red dashed lines the ± 2 σ lines. The grey box illustrates the nominal value (white dotted line) and its 2 σ boundaries provided by the manufacturer.

tons, as explained in Section 2.7.1. From the discussion there we know, that the falling edge of the DTOF curve is highly dependent in the actual μ_a of the medium. Further details on TRS data analysis are presented in Sections 2.5, 2.7.1 and 2.6. The shaded grey areas correspond to the nominal values provided by the manufacturer and their respective accuracy

(2 σ confidence intervals) [37]. All averages and medians lie within the nominal value range.

The entire data set for μ_a and μ_s' acquired from both phantoms over the course of eleven months is presented in Tables 4.3 and 4.4. Please note that the presented mean and median values with their respective standard deviations and *IQR*s are the result of measurements over 14 months.

	μ_a [m^{-1}]			
	Detector 1		Detector 2	
λ [nm]	Phantom 1	Phantom 2	Phantom 1	Phantom 2
	mean ± standard deviation			
690	17.59 ± 2.48	9.82 ± 0.63	17.20 ± 3.08	10.13 ± 0.51
785	16.85 ± 1.58	9.14 ± 0.17	16.31 ± 2.01	9.26 ± 0.73
830	15.87 ± 1.06	8.49 ± 0.18	15.24 ± 1.84	8.38 ± 0.30
	median (*IQR*)			
690	18.39 (2.20)	9.97 (0.36)	18.23 (2.97)	10.05 (0.28)
785	17.25 (0.91)	9.16 (0.28)	17.01 (1.78)	9.06 (0.24)
830	16.14 (0.78)	8.47 (0.24)	15.82 (1.85)	8.39 (0.13)

Table 4.3: Phantom results for the absorption coefficient (μ_a) at different wavelengths and detectors: Means and standard deviations as well as medians and inter-quartile ranges (*IQR*s) for the three wavelengths (690, 785 and 830 nm) from the presented TRS setup. Data was acquired on two INO Biomimic® phantoms. Data averaged over from 14 months.

Although we observe differences between the mean and median values, they lie within the standard deviations and *IQR*s. Between both hybrid PMT detectors, values are comparable and show similar trends along the three wavelengths. In Table 4.4 it seems that the order of μ_s' values between 785 nm and 830 nm is disturbed as the lower wavelength shows higher average values than the higher wavelength. Nonetheless, there is no statistically significant difference between these values. This can also be seen by taking the respective standard deviations and values for *IQR* into account. It is assumed that this error is due to the variations over 14 months and since this was not the main goal of the experiment, it

	μ_s' [cm^{-1}]			
	Detector 1		Detector 2	
λ [nm]	Phantom 1	Phantom 2	Phantom 1	Phantom 2
	mean ± standard deviation			
690	8.44± 1.43	5.93± 0.59	7.83± 1.61	5.96± 0.45
785	8.75± 1.04	5.88± 0.38	8.11± 1.28	5.85± 0.45
830	8.31± 0.86	5.60± 0.40	7.72± 1.19	5.51± 0.38
	median (IQR)			
690	8.75 (1.67)	6.03 (0.69)	8.22 (2.16)	6.01 (0.54)
785	8.97 (0.84)	5.82 (0.52)	8.31 (2.10)	5.90 (0.50)
830	8.50 (0.79)	5.54 (0.54)	7.88 (1.89)	5.54 (0.47)

Table 4.4: Phantom results for the reduced scattering coefficient (μ_s') at different wavelengths and detectors: Means and standard deviations as well as medians and interquartile ranges (IQRs) for the three wavelengths (690, 785 and 830 nm) from the presented TRS setup. Data was acquired on two INO Biomimic® phantoms. Data averaged over from 14 months.

was not attempted to acquire a higher signal-to-noise ratio measurement.

Based on the data presented in Figure 4.15 and Tables 4.3, 4.4, we can see that the system provided constant estimation of the phantom properties throughout the curse of one year. This data is the result of equal data acquisition post and/or prior to the use of the hybrid TRS/DCS system on the frontal lobes of brain-healthy patients during surgical procedures. They provide a good measure of stability and furthermore compare well to the manufacturer-provided values.

This chapter concludes the first part of this thesis. After a general introduction (Chapter 1), the theory of light interaction with biological tissue, the forward and inverse problem (Chapter 2) were discussed. This was followed by a description of the transport of oxygen in biological tissue and cerebral hemodynamics/autoregulation (Chapter 3) and this chapter, which explains the functional principles of the hybrid TRS/DCS device, its composition and long term characterization.

The next part focuses on the *in-vivo* measurements and the interpretation of their results based on the knowledge introduced in this first part.

Part II

IN-VIVO MEASUREMENTS

5

EXPLORING THE POTENTIAL TO IMPROVE THYROID CANCER SCREENING WITH DIFFUSE OPTICS

The first of three parts of this thesis has focused - after a general introduction to this thesis' work - on the oxygen transport to and its diffusion into biological tissue, as well as the importance of constant blood perfusion in the human brain and its autoregulatory measures. The theory of diffuse optics and its real world implementation in a hybridization of two techniques, time-resolved spectroscopy (TRS) and diffuse correlation spectroscopy (DCS), was presented. Based on the functional principles, this hybrid TRS/DCS device was characterised in terms of stability and accuracy.

This chapter is the first one of the second part of this thesis, which concentrates on the *in-vivo* application of said hybrid TRS/DCS device. Here, measurements on the human thyroid are presented and referenced against sternocleidmastoid muscle tissue. The optical values (absorption coefficient (μ_a) and reduced scattering coefficient (μ_s')) recorded by the TRS part of the hybrid system are used in the calculation of total hemoglobin concentration (THC), tissue oxygen saturation (StO_2) and the analysis of DCS data, which then provides a more accurate estimation of blood flow (BF) in terms of a blood flow index (BFI). Data from a healthy population (n = 22) was thoroughly analysed and interpreted. Nine pathological cases were studied, but for clarity, only two will be presented in this chapter and data from the lasting seven cases is added in the appendix.

This work is the result of a collaboration with Dr. Mireia Mora, Dr. Felicia Hanzu, Dr. Irene Halperin as well as Dr. Mattia Squarcia and colleagues from the Endocrinology and Radiology Departments at Hospital Clínic and the Institut d'Investigacions Biomèdiques August Pi I Sunyer in Barcelona. The study lays the groundwork for the use of diffuse optics in

thyroid cancer screening and led to a Horizon 2020 project (http://www.luca-project.eu).

5.1 BACKGROUND

A common pathology in endocrinology are thyroid nodules (TNs). They vary in size and statistics show that palpable nodules have a prevalence around 5 % in women and 1 % in men. These numbers increase to 19-76 % [68, 123] when neck US is used for screening in addition to palpation. Approximately 5-15 % of these nodules turn out to be thyroid cancer (TC) [68] which is the most common malignant tumor of the endocrine system. The incidence of thyroid cancer is increasing more rapidly than any other cancer type in the modern world [205].

With exception of the relatively rare poorly differentiated and anaplastic forms, TC prognosis is generally good. The 10-year survival rates - corrected for age and sex - range from 95 % for papillary to 90 % (follicular) and down to 13 % for the anaplastic TC [285]. While TC has a low overall mortality, in specific cases of low conventional treatment response, aggressive behaviour, persistence or recurrence of the disease and no alternative treatment option, the mortality rate is substantially higher.

The initial precise characterization and diagnosis of the thyroid nodule is critical in order to decide on the course of action. The options range from surgical resection to follow-up or - in the case of presumed TC - an extensive initial surgical procedure. Unfortunately, the current sensitivity and specificity of the first point-of-care, non-invasive screening method, ultrasound (US), is quite poor, ranging from 17-87 % in sensitivity and from 39-95 % in specificity depending on the type of the malignant nodules [205, 215, 287, 223, 10]. Unfortunately, an ultrasound-guided fine-needle aspiration biopsy (FNAB) – which follows a positive ultrasound screening result – of the suspicious nodule is also limited in sensitivity and specificity [68].

In addition to various other parameters (e.g. elastography), it has been speculated that the inclusion of the nodule hemodynamics, in particular that of microvascular blood flow, may significantly improve the screening process. In fact, recent studies have observed that papillary carcinomas are richer in microvessels (95.75 %) than adenomas (49 %) and capil-

laries are more frequent in adenomas (9 %) than in carcinomas (1 %) [267]. However, ultrasound has limited sensitivity to microvascular blood flow, and, therefore, complementary modalities are being sought.

In short, the high prevalence of thyroid nodules and the above-mentioned limitations of the existing screening strategies call for improvements in strategies to identify lesions. If successful, these may have an immense socio-economic impact reducing unnecessary FNABs or surgeries and improving the response to therapies.

Several techniques, such as (time-resolved) fluorescence [41, 40, 124, 245], Raman [307, 74], elastic scattering spectroscopy (ESS) [301] spectroscopy and two-photon excited fluorescence (TPEF) [243] in combination with second-harmonic generation (SHG) [142] using light have been suggested for improving the cancer, and, in particular, the thyroid cancer screening process. However, these are invasive techniques focusing on different aspects of light interaction with tissue. ESS, TPEF and SHG suggest an improvement of the thyroid screening process by focusing on the cellular tissue morphology which influences the spatial variations in the refractive index, which in turn result in alterations of photon scattering. Overall, these methods suggest that there is an optical contrast between the healthy and pathologic thyroid tissue.

As near-infrared diffuse optical spectroscopy (DOS) is sensitive to the light scattering characteristics of tissues together with its light absorption spectrum and therefore to the hemodynamics of the tissue microvasculature (see Chapter 2) it plays an important role in the screening and characterization of thyroid nodules for malignancy as well as the overall thyroid characterization [94, 62, 59]. Previous applications of DOS and diffuse correlation spectroscopy in tumor tissue characterization, specially in optical mammography, and for the monitoring of the local tissue response to therapy show the feasibility of these methods in this area [93, 62, 60, 344, 59, 302, 235, 313, 103] . They have, however, not been utilized to characterize the thyroid gland or its pathophysiology. Here we hypothesize that the thyroid gland is accessible to the non-invasive, hand-held DOS/DCS hybrid optical probes (see Figure 5.1 and b) for the illustration of the thyroid gland and its anatomy) and that - in healthy condition - it is relatively homogeneous. Moreover, due to the increased microvasculature in TNs [267], they are expected to present

a measurable contrast, facilitating in the end the use of diffuse optics as an additional tool to improve the limited contrast of the current standard screening process [205, 215, 287, 223, 10, 68]. The ultimate goal is to help classify the nodules as benign or malignant. Here the goal is to test the first part of this hypothesis by characterizing the homogeneity of the thyroid gland and compare the results to the adjacent neck muscles (sternocleidomastoid) using a custom-made time-resolved spectroscopy and DCS hybrid instrument and probe [105]. Furthermore case studies with different thyroid pathologies are presented to begin to address the second part of the hypothesis. Further studies by diffuse optical data on thyroid nodules should allow to establish ranges and relationships between different measurable parameters, indicating the probability of malignancy.

The measurements were guided by ultrasound imaging and its assessment by expert radiologists and endocrinologists. We have quantified the depth and the extent of the thyroid gland and investigated our results to look for correlations between different physical, demographic and clinical parameters. This approach enabled us to establish a range of typical healthy thyroid tissue parameters to serve as a reference for future measurements on thyroid pathologies thus paving the way towards exploring the utility of this method for improved thyroid screening.

5.2 MEASUREMENT PROTOCOL

All procedures and devices of this study were approved by the ethical committee of Hospital Clínic in Barcelona (CEIC - Comité Ético de Investigación Clínica del Hospital Clínic de Barcelona). Each subject signed an informed consent and the study has been conducted according to the principles of the Declaration of Helsinki. The volunteers were screened by ultrasound to evaluate the thyroid condition. The presence of diffuse thyroid diseases, such as hyper- or hypothyroidism, thyroiditis and Graves' disease, as well as benign and/or malign nodules and cervical adenopathies were the main exclusion criteria for the healthy population.

Each subject's tissue dimensions in the marked probe locations (see Figure 5.1) were extracted from the ultrasound images.

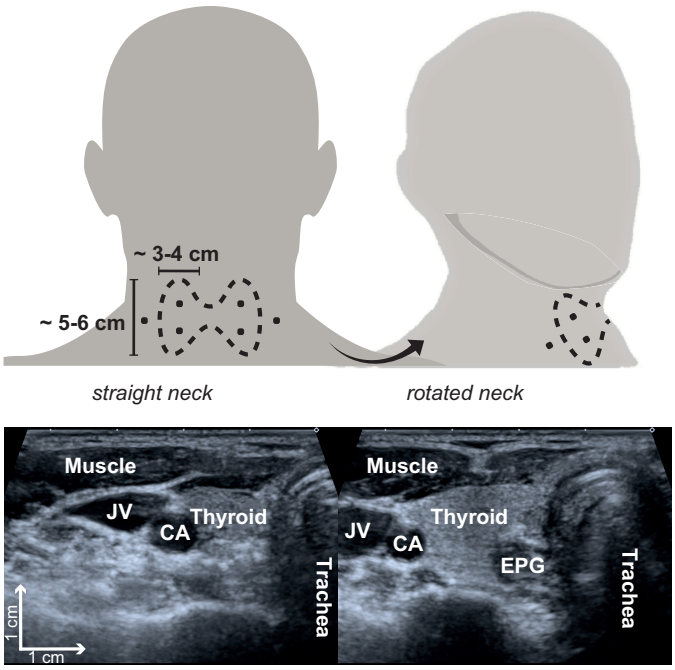

Figure 5.1: Thyroid location and its surroundings: Shown is the location of the thyroid, its dimensions and the defined measurement points. Also shown: Locations of the jugular vein (JV), carotid artery (CA), esophagus (EPG), the (left) thyroid gland, its position and superficial structures (sternocleidomastoid muscle, skin and adipose layers) in normal neck (right) and rotated neck (left) position, used for improved thyroid exposure.

We have defined three representative parameters (see Figure 5.2): the total tissue depth (TTD), superficial tissue thickness (STT) and tissue thickness (TT). The latter is given by the depth extension of the tissue of interest, i.e., muscle or thyroid tissue. This tissue thickness and the superficial tissues (skin and adipose layers) add up to the total tissue depth, which is defined by total distance from the skin surface to the end of the thyroid or muscle tissue.

In order to evaluate the general health condition of subjects, they underwent a basic health screening, which consisted of questions about hypertension, diabetes, hyperlipidemia, arterial fibrillation, congestive heart failure, coronary artery disease, previous myocardial infarction, carotid artery disease, smoking, lung and/or kidney diseases and the list of current medications.

Furthermore, we have noted age, height, weight, body mass index (BMI), heart rate (HR) and arterial oxygen saturation (SaO_2) before the diffuse optical measurement, as well as the

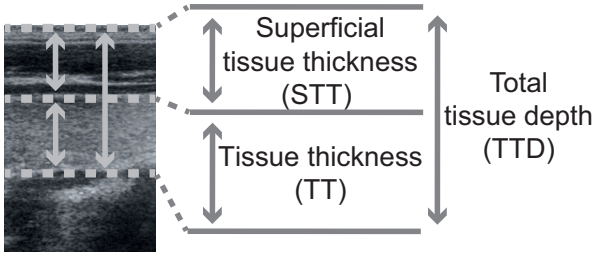

Figure 5.2: Defined tissue dimension parameters: US image excerpt from a thyroid gland. TTD is defined by the sum of the superficial tissues (STT) and the TT. Typical values vary between different tissue types (see Table 5.3).

systolic and diastolic blood pressure (BP_{sys}, BP_{dia}) before and after the data recording procedure. These serve as a check for the subject's general well-being in addition to the above-mentioned basic health screening. Moreover, the blood pressure reading prior and after the measurement procedure provide further information about the global hemodynamic condition over the course of the experiment.

The measurement protocol included of several probe placements on the thyroid and the neck sternocleidomastoid muscle as a reference point as illustrated in Figure 5.1 and 5.3.

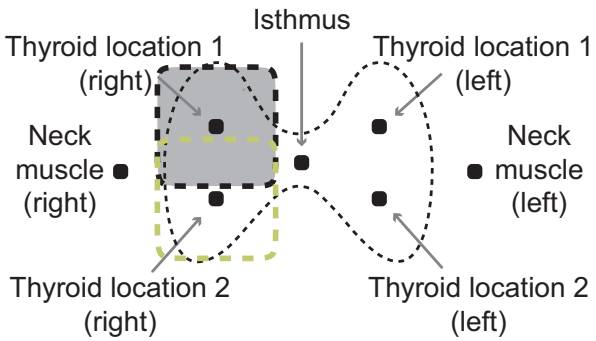

Figure 5.3: US-guided probe placements on the human neck: Three different measurement points per side plus one on top of the isthmus. Probe size and placement are shown in relation to the thyroid gland size.

The subjects were laid down with a slight head tilt backwards to expose the thyroid. Furthermore, we have used ultrasound to explore the optimal way to expose the thyroid and decided to utilize a head turn, thus maximizing the acoustic window. The subjects were asked to turn their head left when we were measuring on right side and vice versa (see Figure 5.1). This procedure was monitored by a high frequency

ultrasound transducer, which, due to its high spatial resolution, allowed to identify the different tissue structures. Two representative ultrasound images are shown in Figure 5.1). The final locations according to Figure 5.1 and c) were chosen depending on the physiology and identification by ultrasound prior to the diffuse optical measurements.

The non-invasive measurements employed diffuse light for two source-detector separations (ρ) - 13 and 25 mm - to probe the tissue properties and the necessary sources and detectors were embedded in a 4 cm x 4 cm soft black foam pad (see Figure 5.4), which was placed directly on the subject's skin. The shorter source-detector separation (ρ) was used in a subset of eleven subjects, which is half of the study population, as well as the two pathology cases. The details are shown in Figures 5.1 - 5.4.

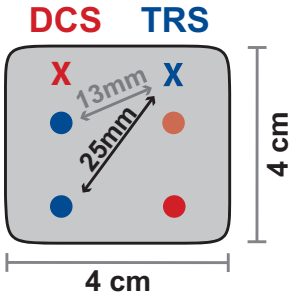

Figure 5.4: Thyroid probe: One source and two different detector locations per modality (DCS and TRS). Cross-geometry lead to overlapping of the probed regions between modalities. A shorter source-detector separation (ρ) was used in a subset of eleven subjects and all pathology cases. This probe was previously shown in Figure 4.11.

The static optical properties (absorption and reduced scattering) were measured with time-resolved spectroscopy (TRS). As presented in Chapter 2, the computed absorption properties at each of the three wavelengths were used to calculate oxy- and deoxy-hemoglobin concentrations using extinction coefficients from the literature [253]. Diffuse correlation spectroscopy (DCS) was used to monitor blood flow. The variations in the correlation decay times from the recorded intensity fluctuations translate into the blood flow index (BFI), which is directly related to microvascular blood flow (see Sections 2.3.3 and 2.6).

One data set consisted of DCS data acquired for both ρ (13 and 25 mm) simultaneously and TRS curves recorded individ-

ually for all wavelengths and ρs with a acquisition time per individual curve of seven seconds (t^{TRS}_{25mm} = 21s; t^{TRS}_{13mm} = 21s; t^{DCS} = 7s). The experimental setup switched automatically between wavelengths and modalities. At each location, we have recorded three complete data sets leading to a total acquisition time of $\sim$ 147 seconds per measurement location.

After one complete scan of the subject's neck - according to the points marked in Figures 5.1 and 5.3 - a second identical scan followed.

All measurements on nodule cases were performed at least 48 days after the FNAB, which is considered to be enough time to avoid contamination of the DOS measurements [304].

All subjects were measured with the hybrid diffuse optics device explained in Section 4.2, using a source-detector separation of 25mm for both, TRS and DCS. Furthermore, for a subset of eleven subjects (six females, five males) additional detectors were introduced for both modalities at a 13 mm distance from the source into our probe to explore whether there are any differences in superficial tissues. The probe is illustrated in Figure 5.4.

Grayscale ultrasound (US) scans were used with the neck in hyperextension both in neutral position and after right and left neck rotation using a real-time ultrasonographic scanner with a 7.5 MHz linear transducer connected to a M7 Mindray US machine (Shenzhen, China). All US examinations were performed by a radiologist and an endocrinologist with extensive experience in thyroid ultrasound (twelve and six years respectively). The US screening consisted of longitudinal and transverse scans from the skull base to the supraclavicular and suprasternal region to identify normal relevant vascular and muscular cervical structures and to evaluate the thyroid gland. As explained above, cases with thyroid nodules, diffuse thyroid disease and cervical adenopathies were excluded from the healthy population. Grayscale US was further utilized to evaluate the thyroid gland position, the common carotid arteries and the jugular veins. Similarly, the sternocleidomastoid muscles were identified bilaterally in neutral position and during right and left lateral rotation. This allowed the evaluation of the normal sternocleidomastoid muscle situation and its displacement over to the deep cervical structures during neck movements (see also Fig 5.1). The distances between the superficial tissue layer and the anterior and posterior border of the muscle belly were recorded.

Moreover, the echo structure and echogenicity of the thyroid parenchyma were analyzed and the thyroid lobes were measured in three different dimensions: craneo-caudal, latero-lateral and antero-posterior. Furthermore, the distances between the superficial tissue layer and the anterior and posterior border of the thyroid gland were measured at the middle third of the right and the left lobe.

For each subject, various other ultrasound images were taken. These images corresponded to the locations of the diffuse optics measurements and provided information on the depth and thickness of the thyroid and the muscle depending on the location. An example US image from the thyroid is shown in Figure 5.2.

5.2.1 *Data analysis*

5.2.1.1 *Time-resolved spectroscopy*

As explained in Section 4.2, the time-resolved spectroscopy setup acquired distribution time of flight curves for three different wavelengths (λ = 690, 785 and 830 nm). Each curve was normalized and the solution for the diffusion approximation for the semi-infinite homogeneous medium (see Section 2.5) was fitted to a range from 80 % of the peak value on the rising edge to 1 % on the tail based on the diffusion approximation and the nature of absorption.

The measured absorption coefficient (μ_a) for each wavelength was used to calculate the oxy- and deoxy-hemoglobin concentrations, since each μ_a relates to the different tissue chromophore concentrations via their respective individual extinction coefficients (ϵ) (Eq.2.1). In case of this study we have considered only three different chromophores, which were the main contributors to the measured signals at the above-mentioned wavelengths. The molar absorption coefficients for oxy- and deoxyhemoglobin were retrieved from [253] and the corresponding ones for water from [132]. The total hemoglobin concentrations and oxygen saturations for each data set have been obtained by assuming a negligible lipid contribution and a water concentration (cH_2O) of 78 % [328].

5.2.1.2 *Diffuse correlation spectroscopy data analysis*

We know that calculating the autocorrelations from random fluctuations in the electric field and the intensity for different delay times yields information on the dynamics in the tissue. By fitting the solution of the correlation diffusion equation for the semi-infinite homogeneous medium to the computed normalized electric field autocorrelation function as described in Section 2.3.3, one can obtain information on the microvascular blood diffusion in the tissue, which is presented here as a blood flow index (BFI) for the probed region.

For each subject and each measurement location the μ_a and μ_s' values from the TRS measurement were used in the DCS analysis.

5.2.2 *Statistical analysis*

All values reported in Tables 5.1 - 5.6 are mean values averaged over all included healthy subjects plus minus the standard deviation. The absorption and scattering coefficients (μ_a, μ_s'), total hemoglobin concentration (THC), tissue oxygen saturation (StO_2) and the blood flow index (BFI) were tested for normality with the "Shapiro-Wilk" test [129] and also cross-checked by quantile-quantile plots. Both tests were in agreement with each other. This normality test serves as a quality check and for the suitability of the methods used for further statistical analysis. The primary method was the linear mixed effects (LME) model. The entire statistical analysis was carried out in R [255]. In general, "p-values" less than 0.05 were considered statistically significant to reject the null hypothesis. Within R, we have used the "nortest" [129] and the "nLME" [244] packages for our evaluation. LME fitted models which did not differ significantly from the null model were rejected. Furthermore, LME fitted values are used to confirm the reported mean values. The differences between genders in the demographical, vital and tissue dimension related parameters were tested using a two-tailed t-test.

The hemodynamic variables (THC, StO_2 and BFI) were investigated using LME models [244] where the subject number was considered as a random effect. These LME models tested for differences between organs, i.e., muscle and thyroid, looked for influences by probe location on the thyroid

("gland location 1" and "gland location 2", see Figure 5.1 and c) or between thyroid lobe sides and checked for dependencies on physiological parameters and tissue dimensions (see Figure 5.2). We fitted each of the LME models with the parameter under investigation (organ, location, side, physiological parameter or tissue dimension) as a fixed effect. We, furthermore, have double checked all our statistically significant findings by a bootstrapping analysis. In the case of eleven healthy subjects that were measured with a second source-detector separation (ρ) of 13 mm, we have used the same LME models to check for dependencies on organs, sides, locations and tissue dimensions for that additional data.

5.3 RESULTS

5.3.1 *Study population*

Twenty-two subjects (ten females and twelve males) out of a total of thirty-four screened ones were included in the analysis as the healthy group for this study. The data of three volunteers was excluded due to technical issues. Nine subjects were diagnosed with pathologies, four of them had a single or multiple malignant thyroid nodule(s) another four were classified as benign or had cells of atypical behaviour, while one patient presented thyroiditis.

The basic health screening confirmed the overall health condition of the subjects. The demographic parameters from the healthy study population, such as age, weight, height and body mass index (BMI) are presented in Table 5.1, while the vital records including heart rate (HR), arterial oxygen saturation (SaO_2), the systolic and diastolic blood pressure (systolic blood pressure (BP_{sys}), diastolic blood pressure (BP_{dia})) prior and post optical measurement are shown in Table 5.2.

	Age [yrs]	Weight* [kg]	Height* [cm]	BMI [kg/m^2]
All	32 ± 5	69 ± 13	171 ± 8	23.5 ± 3.6
Females	*31 ± 4*	*60 ± 11*	*164 ± 6*	*22.2 ± 4.5*
Males	*32 ± 5*	*77 ± 9*	*177 ± 5*	*24.6 ± 2.5*

Table 5.1: Demographic parameters: The demographic parameters of the population given as mean ± their standard deviation. * denotes a statistically significant difference between females and males (t-test, $p < 0.05$).

	HR [bpm]	SaO_2 [%]	BP_{sys} [mmHg]		BP_{dia} [mmHg]	
			prior*	post*	prior*	post
All	73 ± 14	98 ± 1	126 ± 15	127 ± 13	75 ± 10	75 ± 9
Females	*75 ± 13*	*98 ± 1*	*114 ± 9*	*119 ± 10*	*69 ± 9*	*70 ± 4*
Males	*71 ± 14*	*98 ± 1*	*133 ± 14*	*132 ± 12*	*79 ± 8*	*78 ± 11*

Table 5.2: Vital records: The table shows the distribution (mean ± standard deviation) of the vital records: heart rate (HR), arterial oxygen saturation (SaO_2), systolic and diastolic blood pressure (BP_{sys}, BP_{dia}). * denotes a statistical significant difference between females and males (t-test, $p < 0.05$).

The thickness of the superficial and target tissue as well as the total tissue depth were measured by ultrasound. Their values are shown in Table 5.3 and illustrated in Figure 5.2. The whole distance from the skin surface to the deeper border of the target tissue is considered as the TTD, whereas the TT is defined by the difference between the total tissue depth and the corresponding superficial tissue thickness (STT).

		Muscle	
	STT [mm]	TT* [mm]	TTD* [mm]
All	2.9 ± 0.8	7.5 ± 1.9	10.4 ± 2.2
Females	*2.9 ± 0.8*	*6.8 ± 1.7*	*9.7 ± 1.9*
Males	*3.0 ± 0.8*	*8.1 ± 1.8*	*11.1 ± 2.2*
		Thyroid	
	STT* [mm]	TT* [mm]	TTD* [mm]
All	7.6 ± 2.3	12.1 ± 4.1	19.7 ± 4.9
Females	*6.5 ± 2.0*	*10.4 ± 2.8*	*16.9 ± 3.3*
Males	*8.7 ± 2.0*	*13.7 ± 4.5*	*22.4 ± 4.6*

Table 5.3: Tissue dimensions recorded by ultrasound: Means and standard deviations of the tissue dimensions. The definition of these three parameters is illustrated in Figure 5.2. The distance from the probe-skin contact to the deeper end of the target tissue figures as the TTD, whereas the TT is difference between the total tissue depth and the superficial tissue thickness (STT). * denotes a statistical significant difference between females and males (t-test, $p < 0.05$).

5.3.2 *Optical and hemodynamic properties of the healthy population*

On every measurement location, see Figure 5.1 and c), we have obtained the absorption (μ_a) and reduced scattering coefficients (μ_s') at three wavelengths employing time-resolved spectroscopy (TRS) as described in Sections 5.2 and 5.2.1.1. A representation of these values is shown in Table 5.4 and Table 5.5. These mean values and their standard deviations for each location present the healthy population average. Three percent of the initial data was excluded due to a low signal-to-noise ratio.

	$\mu_{a,\,690}$ [cm^{-1}]	$\mu_{a,\,785}$ [cm^{-1}]	$\mu_{a,\,830}$ [cm^{-1}]
Muscle (right)	0.22 ± 0.04	0.21 ± 0.03	0.23 ± 0.03
Gland location 1 (right)	0.30 ± 0.04	0.28 ± 0.04	0.32 ± 0.05
Gland location 2 (right)	0.27 ± 0.04	0.26 ± 0.03	0.30 ± 0.04
Isthmus	0.20 ± 0.02	0.20 ± 0.02	0.22 ± 0.03
Gland location 2 (left)	0.27 ± 0.05	0.26 ± 0.04	0.30 ± 0.05
Gland location 1 (left)	0.28 ± 0.05	0.27 ± 0.04	0.30 ± 0.06
Muscle (left)	0.22 ± 0.04	0.21 ± 0.03	0.24 ± 0.04

Table 5.4: Absorption coefficients (μ_a) from TRS data: Absorption coefficients μ_a (mean ± standard deviation) deducted from the three wavelengths of the time-resolved spectroscopy data. The thyroid gland shows a significantly ($p < 0.05$) higher absorption than the muscle at all locations.

	$\mu_{s,\,690}'$ [cm^{-1}]	$\mu_{s,\,785}'$ [cm^{-1}]	$\mu_{s,\,830}'$[cm^{-1}]
Muscle (right)	9.1 ± 0.9	8.1 ± 1.0	7.3 ± 0.9
Gland location 1 (right)	9.2 ± 1.1	7.9 ± 1.3	7.4 ± 1.1
Gland location 2 (right)	8.6 ± 1.2	7.4 ± 1.3	6.9 ± 1.1
Isthmus	9.6 ± 1.0	8.7 ± 1.1	8.0 ± 1.0
Gland location 2 (left)	8.1 ± 1.2	7.0 ± 1.3	6.5 ± 1.2
Gland location 1 (left)	8.8 ± 1.1	7.6 ± 1.3	7.2 ± 1.2
Muscle (left)	9.1 ± 0.9	8.0 ± 0.9	7.3 ± 0.9

Table 5.5: Reduced scattering coefficients (μ_s') from TRS data: Reduced scattering coefficients μ_s' (mean ± standard deviation) for all three wavelengths obtained by time-resolved spectroscopy. The recorded data reveals statistically significant ($p < 0.05$) differences between the muscle and the thyroid gland.

In order to relate our optical measurements to the tissue hemodynamics, we have assumed the lipid contribution to be negligible and a water content of 78 % [328], which led to THC and StO_2 values as shown in Table 5.6 together with BFI.

	THC [µM]	StO_2 [%]	BFI [cm^2/s] × 10^{-9}
Muscle (right)	100.9 ± 13.7	63.8 ± 3.8	8.1 ± 4.3
Gland location 1 (right)	144.8 ± 21.4	67.4 ± 3.1	13.7 ± 4.5
Gland location 2 (right)	134.7 ± 18.0	68.4 ± 2.7	14.7 ± 6.1
Isthmus	98.0 ± 12.0	67.9 ± 2.0	14.4 ± 7.2
Gland location 2 (left)	131.9 ± 22.2	67.5 ± 2.2	16.0 ± 8.8
Gland location 1 (left)	136.5 ± 26.8	66.6 ± 3.0	15.4 ± 7.3
Muscle (left)	105.7 ± 17.8	65.9 ± 3.4	7.8 ± 1.8

Table 5.6: Calculated hemodynamic parameters: Means and standard deviation for total hemoglobin concentration (THC), tissue oxygen saturation (StO_2) and blood flow index (BFI) are shown here for all six measurement locations according to the study protocol. Rather strong differences ($p < 0.0001$) can be observed in the THC and BFI between the thyroid and the muscle, whereas the StO_2 concentrations show small to almost no variations. Please see the text for details.

On the right neck side, the THC increases from 100.9 ± 13.7 µM in the muscle to 134.7 ± 18.0 µM ("gland location 2 (right)") and 144.8 ± 21.4 µM ("gland location 1 (right)") in the thyroid lobe and on the left side from 105.7 ± 17.8 µM in the muscle to 131.9 ± 22.2 µM ("gland location 2 (left)") and 136.5 ± 26.8 µM ("gland location 1 (left)"), which represents a 33-44 % increase on the right side and a 25-29 % increase on the left side.

The BFI changes from 8.1 ± 4.3 $cm^2/s \times 10^{-9}$ in the right muscle to 13.7 ± 4.5 $cm^2/s \times 10^{-9}$ ("gland location 1 (right)") and 14.7 ± 6.1 $cm^2/s \times 10^{-9}$ ("gland location 2 (right)") in the right thyroid lobe and on the left side from 7.8 ± 1.8 $cm^2/s \times 10^{-9}$ in muscle to 15.4 ± 7.3 $cm^2/s \times 10^{-9}$ ("gland location 1 (left)") and 16.0 ± 8.8 $cm^2/s \times 10^{-9}$ ("gland location 2 (left)"). This is a 70-81 % blood flow increase from muscle to thyroid on the right neck side and a 97-105 % higher blood flow in the left thyroid lobe than the respective muscle.

The StO_2 values increase from 63.8 ± 3.8 % in the muscle to 67.4 ± 3.1 % ("gland location 1 (right)") and 68.4 ± 2.7 % ("gland location 2 (right)") in the thyroid on the right side and

on the left side from 65.9 ± 3.4 % in the muscle to 66.6 ± 3.0 % ("gland location 1 (left)") and 67.5 ± 2.2 % ("gland location 2 (left)") in the thyroid region, which represents a change within the standard deviations.

A full subject-wise representation of the μ_a, μ_s', THC, StO_2 and BFI values can be found in the Tables in A.1, A.2 and A.3.

5.3.2.1 *Normality tests*

As described in Section 5.2.2, all variables (μ_a, μ_s', THC, StO_2 and BFI) have been checked for normality using the "Shapiro-Wilk" test [129] and cross-checked by quantile-quantile plots. According to these tests, the BFI values recorded in "gland location 2 (right and left)", as well as in the "neck muscle (left)" location are not normally distributed ($p \leq 0.01$).

5.3.2.2 *Organ differences*

From the corresponding LME model with the organ as a fixed effect, we have found a statistically significant ($p < 0.0001$) increase over all three wavelengths in the recorded absorption coefficient (μ_a) at the thyroid locations with respect to the sternocleidomastoid muscle. The average μ_a from the thyroid are: $\mu_{a,\,690}$ = 0.28 cm^{-1}; $\mu_{a,\,785}$ = 0.27 cm^{-1}; $\mu_{a,\,830}$ = 0.31 cm^{-1}. In the muscle region we have recorded the following averaged absorption coefficients (μ_a): $\mu_{a,\,690}$ = 0.22 cm^{-1}; $\mu_{a,\,785}$ = 0.21 cm^{-1}; $\mu_{a,\,830}$ = 0.24 cm^{-1}.

The same LME model employed on the scattering characteristics, i.e., the reduced scattering coefficients (μ_s'), leads to statistically significant ($p_{690} < 0.01$; $p_{785} < 0.001$; $p_{830} < 0.05$) differences between organs. In the thyroid the reduced scattering coefficient (μ_s') values are $\mu_{s',\,690}$ = 8.7 cm^{-1}; $\mu_{s',\,785}$ = 7.5 cm^{-1}; $\mu_{s',\,830}$ = 7.0 cm^{-1} and the ones for the muscle are $\mu_{s',\,690}$ = 9.1 cm^{-1}; $\mu_{s',\,785}$ = 8.1 cm^{-1}; $\mu_{s',\,830}$ = 7.3 cm^{-1}.

From the LME model with the organ as a fixed effect we find statistically significant ($p < 0.0001$) differences for THC, StO_2 and BFI with the average thyroid tissue values of: THC = 137.1 µM; StO_2 = 67.5 % and BFI = 15.0 × 10^{-9} cm^2/s. For the muscle tissue we get: THC = 103.3 µM; StO_2 = 64.9 % and BFI = 7.9 × 10^{-9} cm^2/s.

5.3.2.3 *Side and probe location differences*

LME models have been used for further investigation of possible significant differences in the measured values between sides and thyroid probe locations.

In terms of left-right symmetry, we see that StO_2 differs ($p = 0.01$) between the right and the left muscle in contrast to the thyroid glands, where no significant variations were found in none of the recorded values between the opposed sides. Here we have set the side information as a fixed effect and retrieved a fitted value for StO_2 in the left sternocleidomastoid muscle of 65.9 % and on the right side an oxygen saturation of 63.8 %.

Apart from the StO_2 in the muscle, a LME model with the probe location on the thyroid as a fixed effect fitted values which show a statistically significant difference from the zero model for THC ($p < 0.01$) and StO_2 ($p = 0.02$). In the gland location 2 THC and StO_2 are 133.3 µM and 68.0 %, while in gland location 1 they are 125.4 µM and 67.2 %.

5.3.2.4 *Age, gender and BMI influences*

Furthermore, we have investigated influences from the subject demographics, such as body mass index (BMI), age and gender, which revealed a statistically significant dependence on BMI ($p < 0.0001$) for all hemodynamic parameters (THC, StO_2 and BFI) and a significant influence of THC by age ($p < 0.01$) and gender ($p = 0.03$). THC, StO_2, and BFI values decrease with higher BMI, as does THC in older subjects. For female subjects THC is in average 128.2 µM and for the male subjects 144.7 µM.

5.3.2.5 *Dependencies on tissue dimensions*

Additionally, we have looked into possible dependencies of THC, StO_2 and BFI on the different tissue thicknesses (superficial tissue thickness and tissue thickness) and the total tissue depth (see Figure 5.1) and have found a significant decrease in THC with increasing superficial tissue thickness ($p < 0.01$).

5.3.2.6 *Short (13 mm) source-detector separation*

Data for an additional source-detector separation (ρ) of 13 mm has also been recorded for a subset of eleven healthy

subjects (six females, five males) out of the twenty-two in total. The information from the shorter ρ of 13 mm revealed different values and dependencies than the ones from a ρ of 25 mm.
The same statistical tests for organs, sides, locations and the three tissue dimension parameters (superficial tissue thickness, tissue thickness and total tissue depth) were performed on that data subset with this short source-detector separation as before. Similar to the long ρ data, these tests result in significant organ differences ($p < 0.01$) with lower THC, StO_2 and BFI in the muscle locations.

StO_2 shows not only a significant influence by side ($p_{muscle} < 0.01$) in the muscle location as for the ρ of 25 mm, but also depends significantly on the thyroid lobe side ($p_{gland} < 0.01$), showing an increase on the left side. It is also lower with increasing STT ($p < 0.01$) and increases with larger TTD ($p < 0.01$). Also, in this source-detector configuration BFI is increasing with larger TTD ($p < 0.01$) and THC is smaller for larger STT ($p < 0.01$).

Moreover, all hemodynamic variables are still significantly depending on BMI ($p < 0.01$), similar to the data acquired from the large source-detector separation.

As before, a full subject-wise representation for this data subset of 11 subjects for μ_a, μ_s', THC, StO_2 and BFI values can be found in the Tables in A.4, A.5 and A.6.

5.3.2.7 *Summary of dependencies for hemodynamic variables*

For improved clarity, a summary of the statistical results according to the LME models presented in Sections 5.3.2.2 - 5.3.2.6 is given in Tables 5.7 and 5.8. They recollect the dependencies of the three hemodynamic variables total hemoglobin concentration (THC), tissue oxygen saturation (StO_2) and blood flow index (BFI) on either organ, neck side and/or probe location. Also included are influences by the three tissue dimensions as defined in 5.2: superficial tissue thickness (STT), tissue thickness (TT) and total tissue depth (TTD). Dependencies on demographic parameters (body mass index (BMI), age and gender) conclude these tables. A change of a hemodynamic variable with the described parameter is indicated by an arrow. In the "Organ - case", for example, all three hemodynamic variables are higher when retrieved from the thyroid probe locations. For the purpose of a complete overview, cases of non-significance ($p > 0.05$) are listed as well.

	THC	StO_2	BFI
Organ	thyroid ↑	thyroid ↑	thyroid ↑
Side	-	muscle left ↑	-
Location	-	-	-
STT	higher STT ↓	higher STT ↓	-
TT	-	-	-
TTD	-	higher TTD ↑	higher TTD ↑
BMI	higher BMI ↓	higher BMI ↓	higher BMI ↓
Age	-	-	-
Gender	-	-	-

Table 5.7: Results summary of statistical significance ($p < 0.05$) from LME models for a source-detector separation of 13 mm (see Section 5.3.2.6). The table lists of total hemoglobin concentration (THC), tissue oxygen saturation (StO_2) and blood flow index (BFI) and influences by organ, neck side and probe location as well as by tissue dimensions (superficial tissue thickness (STT), tissue thickness (TT) and total tissue depth (TTD)) and by demographic parameters, such as body mass index (BMI), age and gender.

	THC	StO_2	BFI
Organ	thyroid ↑	thyroid ↑	thyroid ↑
Side	-	muscle left ↑	-
Location	gland location 1 ↓	gland location 1 ↓	-
STT	higher STT ↓	-	-
TT	-	-	-
TTD	-	-	-
BMI	higher BMI ↓	higher BMI ↓	higher BMI ↓
Age	higher age ↓	-	-
Gender	females ↓	-	-

Table 5.8: Results summary of statistical significance ($p < 0.05$) from LME models for a source-detector separation of 25 mm (see Sections 5.3.2.2 - 5.3.2.5). The table lists of total hemoglobin concentration (THC), tissue oxygen saturation (StO_2) and blood flow index (BFI) and influences by organ, neck side and probe location as well as by tissue dimensions (superficial tissue thickness (STT), tissue thickness (TT) and total tissue depth (TTD)) and by demographic parameters, such as body mass index (BMI), age and gender.

5.3.3 *Case studies with pathologies*

In addition to the healthy population, nine case studies are included in this study, representing subjects which were previously diagnosed with a pathology. In some cases the measurement protocol was extended by adding probe locations to the existing ones. For simplicity, in this section only two of these cases are shown (*CASE 4* and *CASE 7*). The cases were chosen to illustrate the contrast obtained from the pathologic tissue. Furthermore, they represent a benign and a malignant case. The remaining ones can be found in the appendix (A.2). These cases turned out to be complex, non-representative cases, so that they were excluded from the analysis here. Is it noted, that the numbering is a result of the order the volunteers were recruited.

For the cases presented here, Figures 5.5 and 5.6 show the corresponding thyroid protocol schematics. The shaded regions represent the locations of the thyroid nodules and their approximate size in relation to the complete thyroid. The measurements consisted of the same procedure as for the healthy volunteers, as explained in Section 5.2, but with added measurement locations on the nodule side, i.e. "gland center right" (*CASE 4* and *CASE 7*) and "gland center left" (*CASE 4*).

5.3.3.1 *Pathology case 4 (CASE 4):*

The fourth case was a male (38 years old; weight 71 kg; height 1.64 m; BMI 26.4 kg/m^2) with a thyroid nodule (maximum diameter > 65 mm) affecting the left lobe and extending into the isthmus. The nodule was heterogeneous with necrotic areas. The FNAB examination showed atypical cells suggestive of papillary thyroid cancer and a magnetic resonance imaging (MRI) showed a destructured mass occupying the left thyroid lobe and the isthmus, infiltrating all surrounding thyroid structures (trachea and esophagus) and the skin. Due to the results, the tumor was considered unresectable and radio- and chemotherapy with tyrosine kinase inhibitors ("Sorafenib") was suggested as a neoadjuvant therapy prior to surgery. The radio- and chemotherapy showed an effect and a total thyroidectomy was performed afterwards. Furthermore, the third, fourth and sixth compartment were re-

sected. Histopathology showed a papillary thyroid carcinoma of 65 mm with invasion of the extrathyroidal fibroadipose tissue. Twelve adenopathies were resected with three of them classified as malignant metastatic tissue.

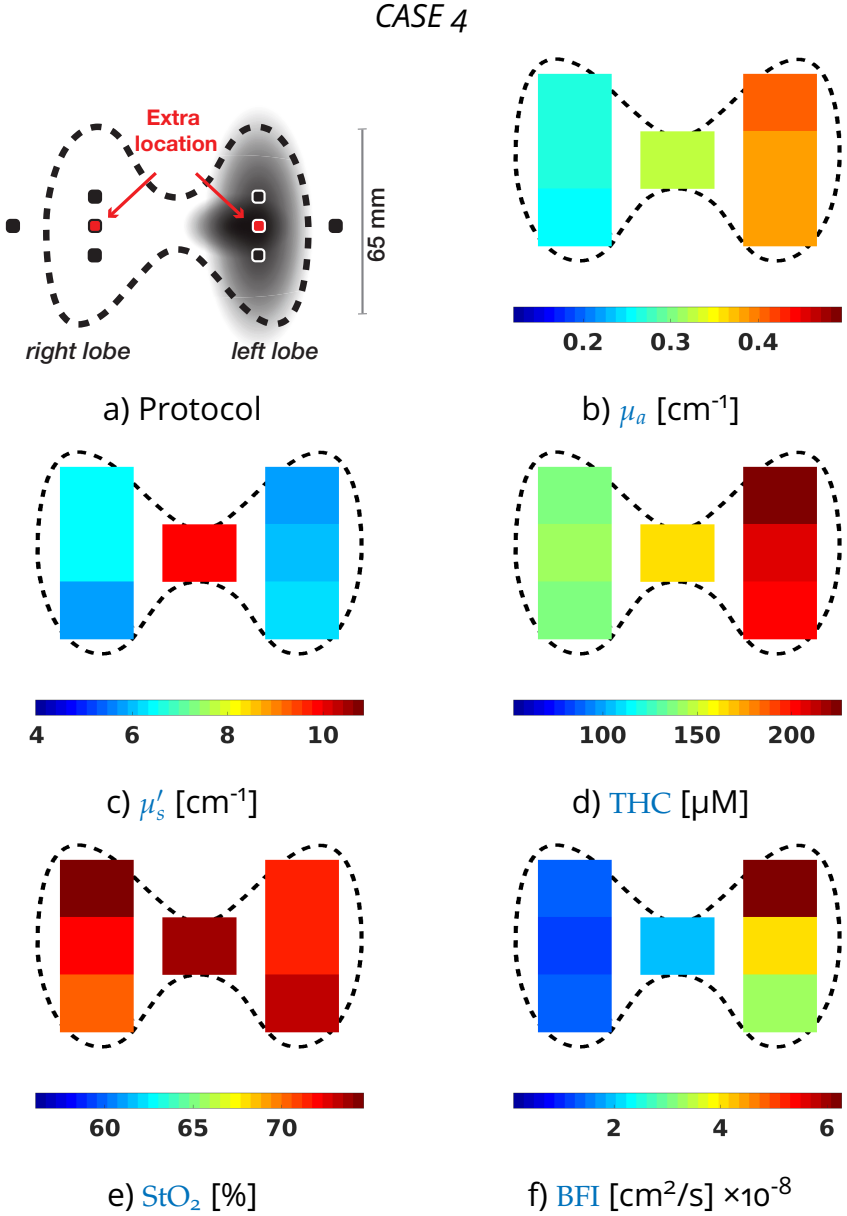

Figure 5.5: Results of the 4th pathology case: The measurement protocol a) consists of nine probe locations. The results are shown for the b) absorption (μ_a) and c) reduced scattering coefficients (μ_s') for 785 nm as well as the d) total hemoglobin concentration (THC), e) tissue oxygen saturation (StO_2) and f) blood flow index (BFI). Note, that these color plots do not include the muscle locations.

	THC [µM]	StO_2 [%]	BFI [cm^2/s] × 10^{-9}
Muscle (right)	82.6 ± 0.8	71.9 ± 1.2	7.3 ± 0.2
Gland location 1 (right)	138.5 ± 1.6	74.1 ± 0.5	12.9 ± 1.2
Gland location 2 (right)	134.7 ± 1.2	70.2 ± 0.5	12.9 ± 1.1
Isthmus	161.39 ± 2.4	73.6 ± 1.2	18.7 ± 2.0
Gland location 2 (left)*	201.3 ± 3.7	72.9 ± 2.2	33.1 ± 3.4
Gland location 1 (left)*	221.1 ± 11.4	71.6 ± 3.3	62.8 ± 6.4
Muscle (left)	92.7 ± 1.5	66.1 ± 3.3	17.8 ± 4.1
Gland center (right)	141.8 ± 2.4	71.8 ± 2.8	12.5 ± 0.5
Gland center (left)*	210.0 ± 6.1	71.6 ± 0.8	40.6 ± 3.01

Table 5.9: Results of *CASE 4*: Means and standard deviations from for total hemoglobin concentration (THC), tissue oxygen saturation (StO_2) and blood flow index (BFI) are shown here for all nine measurement locations according to the study protocol for this patient as presented in Figure 5.5 a). * denotes the nodule locations.

The hybrid diffuse optics probe was applied on a total of nine locations in this case as shown in Figure 5.5 a). The extra locations were added in order to ensure that nodule is measured. The hybrid diffuse optics results are shown in Figures 5.5 b) - f) and Table 5.9[1]. We see that in all three locations on the left lobe the total hemoglobin concentration (THC) and blood flow index (BFI) are higher than the right thyroid side ($p < 0.0001$). We have defined a nodule index which was set positive in all probe location on the left thyroid gland - as opposed to the nodule-free right thyroid gland where that index was set to zero - and fitted a LME model with the nodule index as a fixed effect. The right thyroid lobe values average to THC = 138.3 µM and BFI = 12.8 × 10^{-9} cm^2/s, and, on the nodule, in the left thyroid lobe they increase to THC = 210.8 µM and BFI = 45.5 × 10^{-9} cm^2/s. Additionally, the values show a higher variability with three to nine times higher standard deviations, especially in the gland location 1 on the nodule side, and are distinguishable from the contralateral lobe. The observed standard deviations were: $\sigma_{THC,left}$ = 3.7 - 11.4 µM versus $\sigma_{THC,right}$ = 1.2 - 2.4 µM ; $\sigma_{StO_2,left}$ = 0.8 - 3.3 % versus $\sigma_{StO_2,right}$ = 0.5 - 2.8 %; $\sigma_{BFI,left}$ = (3.0 - 6.4) × 10^{-9} cm^2/s versus $\sigma_{BFI,right}$ = (0.5 - 1.2) × 10^{-9} cm^2/s. Moreover, we observe a

1 Please, refer to Table A.10 for μ_a μ_s' results

relatively high oxygen saturation (StO_2) throughout the whole thyroid (StO_2 = 70.2 - 74.1 % compared to $StO_{2,\,healthy}$ = 66.6 - 68.4 %), while the reduced scattering coefficient (μ_s') in the thyroid turns out lower than the healthy population (μ_s' = 5.2 - 5.7 cm^{-1} compared to $\mu_{s,\,healthy}'$ = 7.0 - 7.9 cm^{-1}). A tabular representation of this case can be found in Table A.10 in Section A.2

5.3.3.2 *Pathology case 7 (CASE 7):*

As *CASE 7* we present results from a female (32 years old; weight 68 kg; height 1.82 m; BMI 20.5 kg/m^2) with a thyroid nodule (40 mm) in the right lobe with foci of colloid degradation and peripheral vascularisation suggestive of a hyperplastic nodule. An additional small nodule of a 3 mm diameter in the right lobe was observed, with no laterocervical adenopathies. Fine needle aspiration biopsy was performed and suggestive of a follicular lesion. Furthermore, the nodule showed microfollicular characteristics and was classified according to the "Bethesda system for reporting thyroid cytopathology" [63], which scales from one to six with increasing malignancy risk as Bethesda 4. After the optical measurements, a total thyroidectomy was performed and histopathology showed multinodular thyroid hyperplasia with a hyperplastic dominant nodule (maximum diameter of 40 m) and regressive changes with adenomatoid nodules. No follicular neoplasms were observed. Finally, the pathology was classified as benign.

Figure 5.6 and Table 5.10 show the diffuse optics results[2]. Similar to the previous cases, a nodule index was defined and set to positive in "gland location 2" and "gland center". With the same LME model as for *CASE 4* we have found a significant difference from the null model ($p < 0.01$) with a THC for a positive nodule index of 206.8 µM in contrast to 147.9 µM for non-nodule locations. The other parameters (StO_2, BFI and μ_s') are not significantly influenced by the two nodule locations. The μ_s' values in three thyroid locations are lower than the ones retrieved from the healthy population (μ_s' = 4.0 - 6.5 cm^{-1} against $\mu_{s,\,healthy}'$ = 7.0 - 7.9 cm^{-1}). A tabular representation of this case can be found in Table A.13 in Section A.2.

2 Please, refer to Table A.13 for μ_a μ_s' results

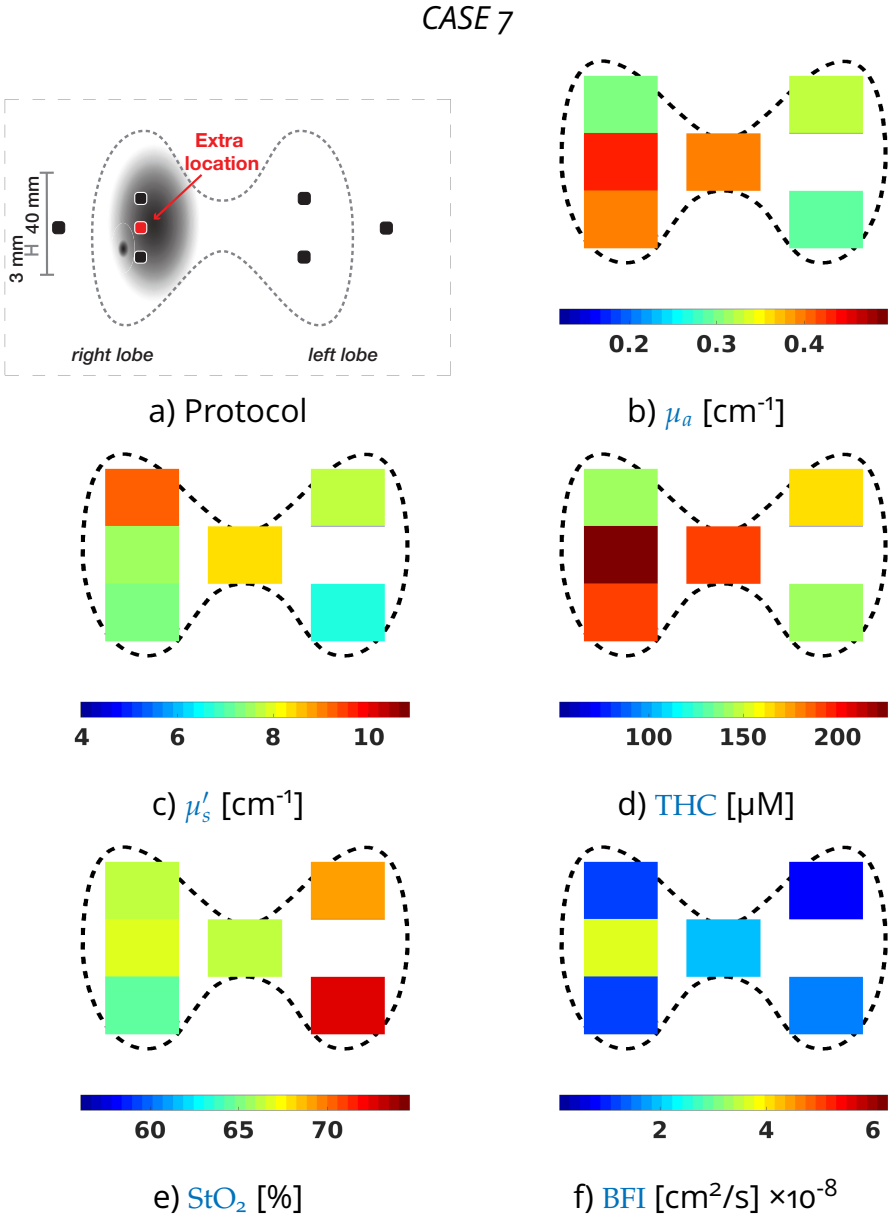

Figure 5.6: Results of the 7th pathology case: The measurement protocol a) consists of eight probe locations. The results are shown for the b) absorption (μ_a) and c) reduced scattering coefficients (μ_s') for 785 nm as well as the d) total hemoglobin concentration (THC), e) tissue oxygen saturation (StO_2) and f) blood flow index (BFI). Note, that these color plots do not include the muscle locations.

5.4 DISCUSSION

After a general reflection of this study's achievements, we separate the discussion into subsections focusing on various aspects in a detailed manner.

	THC [µM]	StO_2 [%]	BFI [cm^2/s] × 10^{-9}
Muscle (right)	108.3 ± 0.8	61.0 ± 1.1	7.5 ± 0.6
Gland location 1 (right)	140.2 ± 2.9	66.2 ± 1.3	12.1 ± 1.3
Gland location 2 (right)*	191.8 ± 1.5	64.7 ± 2.2	11.2 ± 1.8
Isthmus	192.5 ± 4.4	66.0 ± 1.9	20.2 ± 0.9
Gland location 2 (left)	141.8 ± 0.1	72.5 ± 0.1	15.0 ± 1.8
Gland location 1 (left)	164.1 ± 2.5	69.2 ± 0.5	8.7 ± 0.5
Muscle (left)	117.1 ± 1.2	68.0 ± 1.6	8.5 ± 1.1
Gland center (right)*	226.5 ± 8.2	66.9 ± 0.5	37.6 ± 3.9

Table 5.10: Results of *CASE 7*: Means and standard deviations from for total hemoglobin concentration (THC), tissue oxygen saturation (StO_2) and blood flow index (BFI) are shown here for all eight measurement locations according to the study protocol for this patient as presented in Figure 5.6 a). * denotes the nodule locations.

5.4.1 *Overview*

The first result is that the proposed protocol including the positioning of the subject, the neck and the diffuse optics probe placement locations were sufficiently optimized. The measurement protocol that was drawn-up (see Section 5.2) allowed a good signal-to-noise-ratio and a good fitting quality for TRS and DCS, data sets as well as an appropriate and convenient total measurement duration per subject (30 - 45 min). At the end, the optical and hemodynamic parameters of the human thyroid and the sternocleidomastoid muscle tissue from twenty-two healthy (ten females, twelve males) and two subjects with a thyroid pathology were investigated. The overall procedure demonstrates that it is possible to relate the diffuse optical signal to the hemodynamics in the target tissue.

The measurements appear to be robust in terms of repeatability, since there was no perceivable difference between values from the same subject obtained at different times, neither over the time span of the measurement ($\sim$ 30 minutes), nor for a time span of 1½ months (data not shown). For the latter, we rely on data from a subject, who has volunteered twice within 1½ months and during which we have conducted several probe placements per location. The variations were within the obtained standard deviations. Furthermore, it is

noted that male beard growth in the region did not pose any specific influence on our signal, whereas turning the subject's head in order expose the thyroid - as verified by ultrasound - showed a clear positive effect (see also Figure 5.1).

Varying the assumed water content ± 5 % around the 78 % we used in the analysis did not show a noticeable influence and since thyroid and neck muscle tissue are supposed to have a similar water concentrations [328] we did not assume different concentrations for each tissue. In the future, one could expand the wavelength range to determine water and lipid concentrations [277].

The normality tests on the optical and hemodynamic parameters (μ_a, μ_s', THC StO_2 and BFI) resulted in a non-normality for BFI in three locations ("gland location 2 (right and left)" and "neck muscle (left)"). This was observed in previously reported absolute BFI values [105] and may correctly reflect the underlying physiology or may be related to the technique. Moreover, we would like to point out, that while the majority of DCS results reported so far represent relative blood flow changes with respect to a time or tissue reference and the correct estimation of BFI depends on the optical tissue characteristics [90, 209, 94, 149], we have used TRS data in the DCS analysis leading to absolute, more accurate BFI values.

The probe locations were identified by an experienced radiologist and for each location and subject an ultrasound image was taken. Based on these images, we deduce, that the probed region by the diffuse optics device extends below the superficial tissues into the target tissues (muscle and thyroid) and not into the further underlying regions.

The main target tissue was the thyroid gland and its homogeneity, which we have investigated by including two probe locations on each lobe gland. We have also measured the nearby muscles as a comparison. The overall set of locations was exactly the same on both sides of the human neck.

The computed values for the total hemoglobin concentration (THC), tissue oxygen saturation (StO_2) and the blood flow, represented by the blood flow index (BFI), indicate high levels of vascularisation and blood flow (Table 5.6), which is accordance to previous measurements conducted by arterial spin labeled perfusion magnetic resonance imaging [273].

5.4.2 *The extent of the probed regions*

Using ultrasound guidance it is possible to identify different anatomical structures in the neck region. High frequency ultrasound, with frequencies between 7-13 Mhz, and the associated high spatial resolution permits to identify the thyroid gland, the trachea and the esophagus in the anterior compartment of the neck, the common carotid artery and the jugular vein in the lateral compartment of the neck, as well as the muscular structures, both in the central and lateral compartment of the neck. When using ultrasound guidance it is therefore possible to mark the anatomical landmarks of the thyroid and of the other anatomical structures of the neck on the skin and to identify the position of diffuse optics probe to correctly analyze different anatomical structures without their superposition, thus minimizing interferences in the optical analysis. The mentioned slight head tilt and turn implemented in the protocol assisted this minimization further. Representative ultrasound images of this procedure and its effect are shown in Figure 5.1.

The data acquired from the larger source-detector separation, which presumably probes deeper regions of the tissue, showed a significant ($p < 0.0001$) difference between the two organs (muscle vs thyroid) for all parameters. This implies that we are in fact probing the tissues underneath the superficial layers.

To further investigate this point, we have studied the dependence of THC, StO_2 and BFI on the three variables defining the tissue dimensions: STT, TTD and TT (according to Figure 5.2). STT appears to have an influence on the calculated THC in the thyroid lobes ($p < 0.01$). In a bootstrap analysis we have found out that by exclusion of only one subject (ID: 19) the statistical significant dependence of THC on superficial tissue thickness disappears ($p = 0.08$). This strengthens our assumptions that the majority of the detected photons carry information on the tissue of interest. The fact that subject 19 is the one with the lowest BMI (18.3 kg/m^2) in our study population taken together with the general influence of BMI ($p < 0.01$) on the data explains the found effect in the bootstrapping analysis.

For further support to the claim that we are probing the thyroid gland, we note that different dependencies on the tissue dimensions were observed from the shorter ρ of 13 mm,

which has presumably probed shallower regions and was incorporated into our probe for a subset of eleven subjects (six females, five males). The THC and StO_2 values in this case are dependent on the thickness of the superficial layers ($p < 0.01$), i.e. the superficial tissue thickness, thus indicating that this shorter separation was in fact probing a more superficial region. Additionally, there were no significant differences between gland location 1 and 2 in this configuration.

In summary, when looking at the dependence of the three above-mentioned variables for the tissue dimensions, the results indicate that we reach the thyroid tissue and the signal is dominated by that tissue. Nonetheless, we can not entirely rule out possible contamination from other tissues in some subjects, such as the jugular vein and /or the carotid artery. We have done our best to develop a protocol to specifically address this potential problem, including the neck extension for thyroid exposure, as explained in Section 5.2 and Figure 5.1.

5.4.3 *Lobe (Side) differences*

Apart from a significant difference for oxygen saturation (StO_2) in the muscle location, we did not find any side influence on the values. In general, side differences in healthy subjects would be surprising, which is why we suspect the existence of the mentioned StO_2 muscle side variation lies in the systematic way we placed our probe on the different locations and/or is produced by a single subject. We now discuss this further.

In the measurements, we have always started from the muscle location on the right side moving point by point to the left and then repeated the whole procedure. Since the subject was asked to slightly turn the head according to each probe location, the muscle in the last position was probably less relaxed as the one in the starting position. This may explain the slightly higher values - indicating a higher active region - for the left neck muscle location and the significant influence. The fact that the values from the muscle in the short ρ, which is more sensitive to that region, also showed side influences further supports that assumption.

Furthermore, a bootstrap analysis revealed that the significant difference between muscle sides in StO_2 for a ρ of 25 mm ($p = 0.01$) becomes insignificant $p = 0.06$ by excluding sub-

jects 12 and 18. This strong influence by only two subjects can be attributed to the way of recording our data, as explained above and a slight protocol modification can account for this effect. Nevertheless, this finding does not change our main hypothesis that we are able to probe the thyroid gland.

As mentioned above, the thyroid values from different sides were not significantly different (Section 5.3.2), which is expected. At the same time, our results indicated a dependence on probe location for THC ($p < 0.01$) and StO_2 ($p = 0.02$) between gland location 1 and gland location 2. Although, we tried to maximally expose the thyroid by a head tilt and turn, we could see in the ultrasound images that we could not achieve this by 100 %. Due to the dimensions of the thyroid and the two probe locations on the thyroid as defined in our protocol, we may probe the thyroid better in one location than the other, therefore leading to a change in the computed values.

5.4.4 *Influences of the subject demographics*

Further significant influences on the data by the body mass index (BMI) ($p < 0.0001$), by age ($p_{THC,\,age} < 0.01$) and by gender ($p_{THC,\,gender} = 0.03$) were found. Similar to other influences (Section 5.4.2) bootstrapping revealed a rather strong influence by one (female) subject (ID: 7). Its exclusion leads to a statistically non-significant gender relation ($p_{THC,\,gender} = 0.07$) and to a disappearance of the influence on THC by age ($p_{THC,\,age} > 0.05$). Nonetheless, the BMI influence remains significant, which seems reasonable. That diffuse optical measurements are sensitive to BMI has been shown previously in human breast tissue [294, 295, 91] and bone marrow [105]. Since diffuse optics is a non-invasive technique, one always has to deal with superficial tissues such as skin and adipose layers, which in turn make the optical measurements influenceable by BMI. Furthermore, there are indications that the BMI can actually influence the thyroid function [211, 58], which can partially explain the significant BMI dependence in our data. In the future, a multi source-detector probe can investigate this further.

It is noted that, while these bootstrapping analyses have helped to resolve unexpected results, they also indicate that future studies with a larger subject population are important to further investigate any dependencies on subject demo-

graphics, anatomy and physiology. This current study serves as the basis for this and establishes the variability of the results, which is needed for power calculations.

5.4.5 *Pathology cases*

The case studies introduced in Section 5.3.3 show side differences between the glands and clearly higher vascularisation as indicated by elevated THC and BFI values compared to the healthy population. Assuming that the pathologic nodules are in the thyroid gland below the superficial regions, this further proves that we are sensitive to the thyroid's microvasculature and that we are able to resolve differences in the thyroid glands. The data from *CASE 7* even suggests differences within the same gland, which is noteworthy considering the typical thyroid dimensions and the spatial resolution from diffuse optics. Furthermore, we see higher standard variations in the nodule signals in both pathologic cases, which may be due to the abnormal, unstable hemodynamics of the pathologic tissue volumes.

In *CASE 4*, we use THC ($p_{THC} < 0.0001$) and blood flow ($p_{BFI} < 0.0001$) to differentiate the lobe with the 65 mm nodule from the nodule-free side, which according to the FNAB results was suggestive of papillary thyroid carcinoma. This is in accordance to previous studies which have shown an increased microvasculature in papillary thyroid carcinoma [267].

As for *CASE 7* and its 40 mm nodule in the right lobe, we have observed a significant ($p_{THC} < 0.01$) THC increase in the lobe with the nodule. Furthermore, we note higher blood flows in the nodule, in particular from the added location ("gland center right"). The fact that we do not record higher values in all probe locations from the infected lobe are due to the smaller nodule dimensions compared to *CASE 4*.

The oxygen saturations (StO_2) throughout the whole thyroid in *CASE 4* are noticeably higher than in the healthy population and allow for no distinction between the presumably healthy and the nodule side. This is similar to the reduced scattering coefficients (μ_s') which are similar within both thyroid lobes and are relatively low compared to the healthy population.

For *CASE 7*, StO_2 differs between thyroid lobes and tends to be lower on the nodule side, which might be explained by an increased oxygen consumption due to the nodule. This

different behaviour between the two cases, with a StO_2 increase in *CASE 4* and a decrease in *CASE 7*, makes it difficult to use this variable as a discriminator at this point. It seems likely that μ_s' could be helpful in the search for a contrast between tumor types, since the malignant case presents values on the lower end of the scale, while the benign case lies somewhat in between the healthy population and the malignant nodule. This is supported by previous results from a study by Suh et. al. [301] conducted on twenty patients. They have found that elastic scattering spectroscopy (ESS) can help discriminate between benign and malignant thyroid nodules due to its sensitivity to morphologic characteristics. Similar to ESS, DOS is sensitive to index of refraction changes, i. e. changes in nuclear size and density. These cellular arrangements were confirmed to change among different thyroid nodule types by Hung et al. [142] using two-photon excited fluorescence (TPEF) together with second-harmonic generation (SHG). Altogether ,results from ESS and TPEF with SHG support our findings and encourage the use of μ_s' as a further parameter to improve the thyroid screening process.

Apart from changes in the scattering characteristics, higher vascularisation in nodules is expected [345, 93]. The thyroid, in particular, as an already highly vascularised organ is showing even higher degrees of vascularisation when a nodule is developed, thus leading to increase hemoglobin concentrations and blood flows [81, 273]. This can be even more present on the microvascular level [267]. Our findings are in agreement with this on both the general as well as microvascular level and are therefore a promising approach towards an improvement of the thyroid screening procedure.

5.5 CONCLUSION

The goal of this study was to establish a normal range for optical parameters of the healthy thyroid and their possible influences by physiological parameters, so that in the end these measurements can be compared to values obtained in the same way from pathologic thyroid tissues. We have shown that it is feasible to do diffuse optical measurements on the thyroid in-vivo and that the signal we are receiving is giving information on the thyroid vascularisation. This is supported by the different tests on dependencies of tissue di-

mensions and hemodynamic parameters (THC, StO_2, BFI) as well as the contrast between healthy and pathologic tissue.

As expected, the two thyroid lobes do not show any significant difference in healthy subjects, whereas the signal from subjects with thyroid nodules clearly differed between sides. The observed probe location dependence on demonstrates that it is important to use various probe placements on the gland. The fact that we did not record any changes over time (30 min to 1½ months) in the healthy thyroid tissue proves the robustness and repeatability of such a protocol.

The signals from nodule locations result in elevated microvascular THC values, which makes this a promising parameter for improvement in thyroid screening. There are further indications for higher BFI and altered μ_s' from the pathologic data encouraging the use of diffuse optics on thyroid tissue.

Finally, the observations prove that the diffuse optical signal is in fact strongly influenced by the thyroid tissue, that we are able to characterize differences in the nature of this tissue and therefore paving the way of an improvement in sensitivity and specificity in thyroid screening by diffuse optical methods.

5.6 OUTLOOK

In a next step, diffuse optics will be employed on further thyroid nodule cases and other pathologies in order to improve thyroid screening methods and to compare healthy and pathologic distributions.

Moreover, opening the field of thyroid cancer screening to diffuse optics with promising results together with the novelty of this project led to a European Horizon 2020 (H2020) project called “LUCA” - Light and Ultrasound Co-analyzer for Thyroid Nodules. Within LUCA, the combination of TRS, DCS and US aims to provide doctors better information and more specific results in the thyroid cancer screening process thus having a strong socio-economic impact by saving unnecessary surgery costs and improve thyroid healthcare. The LUCA - consortium is formed by eight different European multidisciplinary partners ranging from the clinic to industry and research facilities. In the first phase of the project, the focus lies on the device integration and development of a new combined diffuse optics-US probe. US is part of the standard thy-

roid cancer screening process and will furthermore be used to guide the diffuse optical measurement, similar to the work presented in this Chapter. This Chapter has shown that it is possible to retrieve a measurable contrast between healthy and pathologic thyroid tissue. Therefore the use of the microvascular hemodynamic properties can help to improve contrast in screening. This will be further aided by information on the optical properties (μ_a, μ_s'), as indicated by the data presented here and in Section A.2. Additionally, the use combined probe of US and diffuse optics could be extrapolated to other cancer screening procedures.

6

HYBRID DIFFUSE OPTICS AS A MEASURE OF DEPTH OF ANESTHESIA

This chapter sets out to reference non-invasive optical measurements of cerebral oxygen metabolism to electrical (electroencephalographic) measurements from brain healthy patients undergoing general anesthesia. To that end, the hybrid device presented in Chapter 4 is used in the surgical environment. This serves as a first comparison of diffuse optically derived cerebral metabolism against a typical clinical tool used in this scenario. This procedure has the potential to estimate brain oxygen metabolism also in traumatic brain injury patients, which could have important clinical implications in the future.

This project is a collaboration with Dr. Ivette Chochrón da Prat, Dr. Ángela Sánchez-Guerrero, Dr. Miriam de Nadal and Dr. Juan Sahuquillo and colleagues from the Department of Anesthesiology and the Neurotraumatology and Neurosurgery Research Unit (UNINN) at the Vall d'Hebron University Hospital and it's Research Institute (VHIR) in Barcelona as well as the Universidad Autònoma de Barcelona.

6.1 BACKGROUND

Anesthetic agents suppress the patient's awareness by disrupting the neuron activity and therefore preventing the formation of memory in a dose-dependent manner [239]. Propofol is a non-barbiturate intravenous agent used commonly for the induction and maintenance of anesthesia and for sedation in critical care [57, 206]. Propofol has many pharmacologic advantages over other anesthetic agents such as rapid effect, short action, and fewer side effects [57, 283, 319]. Due to its effect on the central nervous system (CNS), propofol induces a decrease in cerebral metabolic rate of oxygen ($CMRO_2$) and therefore a dose-dependent depression of cerebral blood flow (CBF) while maintaining the physiological cou-

pling between the two [314, 173, 35, 158, 234, 323].

The proprietary bispectral index (BIS) is a processed electroencephalogram (EEG) measure that summarizes brain activity and is used by anesthesiologists during general anesthesia as a measure of depth of anesthesia due to certain anesthetics during the care of patients [283, 164]. The BIS algorithm was developed based on adult EEG data and combines several readings of time, frequency and high order spectral sub-components into the BIS index [43, 161]. This index is a single dimensionless parameter that scales from 0 (isoelectric EEG) to 100 (awake) with increasing brain activity [43, 161, 54, 286]. Awake, unsedated individuals typically have BIS values > 97 and the BIS is progressively reduced by drug-induced sedation [161, 293]. During general anesthesia BIS values between 45 and 60 have been recommended for anesthetic maintenance [157]. BIS provides a real-time feedback of consciousness during surgical procedures [283, 78, 268, 221, 161, 148, 172, 337] and is widely used to evaluate the depth of anesthesia and in particular to obtain real-time pharmacodynamic information during propofol-induced anesthesia [283, 69, 259, 101, 43, 117, 269, 125, 275, 120, 204, 186]. Moreover, it is often considered as a surrogate indicator for $CMRO_2$ during propofol-induced general anesthesia [259, 101, 43, 6, 192, 117, 272, 8].

General anesthesia diminishes neuronal activity. In consequence, $CMRO_2$ is decreased, which has been observed by positron emission tomography (PET) [158, 9, 8]. A combination of time-resolved and diffuse correlation spectroscopy (TRS and DCS, respectively), also called hybrid diffuse optics, can measure microvascular blood dynamics via the tissue oxygen saturation (StO_2) and a blood flow index (BFI) noninvasively. This together with the knowledge of the arterial oxygen saturation (SaO_2) from a standard pulseoximeter allows the calculation of the oxygen extraction fraction (OEF) and the above-mentioned $CMRO_2$ [90, 45, 209, 262, 94, 29], as we have seen also in Section 3.2.4. While TRS can derive the tissue's absorption and reduced scattering coefficients (μ_a and μ_s'), DCS uses information from the intensity autocorrelation decay times to estimate the tissue blood flow (see also Chapter 2). In DCS, the more accurate the knowledge of μ_a and μ_s' is, the better we can estimate the tissue blood flow

and its changes (see Chapter 9). This is where hybrid diffuse optics provides a huge advantage by combining knowledge about the tissue's static and dynamic optical properties [209, 94, 29, 30, 28]. Both diffuse optical techniques have been employed in the investigation of the human brain *in-vivo*, its autoregulatory mechanisms and hemodynamic properties [105, 60, 45, 209, 97, 333, 341, 92, 91], as also shown in Chapters 7 and 8.

Previous studies have shown that there is a need for registration of the patient's awareness during surgical procedures and that it is therefore crucial to monitor continuously the effect of anaesthetics on the patient's brain during surgical procedures [136, 16, 1, 276, 5]. Techniques making use of photon diffusion in human tissue have the potential to aid in this matter and are therefore a promising approach [113, 136, 71, 184, 316, 152, 106, 191]. In the study presented here, the hybridization of newer diffuse optical techniques (TRS and DCS) sets out to show its capability of addressing the patient's awareness via non-invasive assessment of $CMRO_2$.

Moreover, neurocritical patients therapy requires advanced, multi-modality neuro-monitoring and the need to locally and on-line measure microvascular cerebral hemodynamics and metabolism, which is not possible with the current modalities. The optical modalities presented in Chapter 4 can be used as a promising non-invasive and reliable neuromonitoring tool for continuous monitoring of cerebral hemodynamics in neurocritical care patients.

Here, the interest lies in non-invasively measuring the influences on the brain hemodynamics during controlled propofol-induced anesthesia of patients without brain diseases by using diffuse optical methods. These values will be compared to BIS.

6.2 PATIENTS AND METHODS

A prospective study was conducted in patients above eighteen years of age, who underwent general surgical procedures under standard general anesthesia at Vall d'Hebron University Hospital (VHUH), between December 2014 and January 2016. Patients were enrolled in the study based on the following inclusion criteria: 1) absence of previous stroke, cerebral tumor, chronic hydrocephalus, neurodegenerative sick-

ness, or evidence of carotid stenosis; 2) no contraindications for total intravenous anesthesia (TIVA) with propofol; 3) patients needed to undergo a general surgery, excluding laparascopies with extreme patient positions, i. e. Trendelenburg position; 4) class I (healthy) or II (mild systemic disease) in the physical status classification system defined by the American Society of Anesthesiologists (ASA) [266] and 5) written informed consent signed by the patient or next-of-kin. The study was approved by the VHUH Institutional Ethics Committee (protocol AC/U(AT)203/2012[3531]) and the study was conducted in accordance with the Declaration of Helsinki.

6.2.1 *Diffuse optical device*

The hybrid diffuse optical device used the combination of TRS and DCS as presented in Chapter 4. Near-infrared light was sent into the tissue through a set of fibers incorporated into a combined DCS/TRS-BIS probe with a source-detector separation (ρ) of 25 mm for both optical modalities (please refer to Section 4.2 for details). Diffuse optical data was measured bilaterally on the frontal lobes during extracraneal surgical procedures. The BIS signal was retrieved from the left brain hemisphere. The combined DCS/TRS-BIS probe is shown in Figure 6.1. The probe was designed around the BIS sensor while providing a compact housing for the source and detector fiber head of both modalities. It was 3-D printed in TangoBlack shore 27 material and incorporated in a head strap which wrapped around the patient's head. It also covered and protected the entire combined probe against any kind of contamination by the surgical environment.

The data was taken with the hybrid device explained in Chapter 4. It consists of two single longitudinal mode lasers - one for each brain hemisphere - operating at a wavelength of 785 nm for DCS measurements and with pulsed light sources at three different wavelengths (690, 785 and 830 nm) for TRS measurements. A multimode fiber with a core diameter of 200 µm (NA = 0.22) served as the DCS source fiber and TRS light is sent to the tissue through a graded-index fiber with a core diameter of 62.5 µm (NA = 0.275). At the DCS detection site, set of four single mode fibers (core diameter of 5.6 µm) - each one connected to a single-photon counting

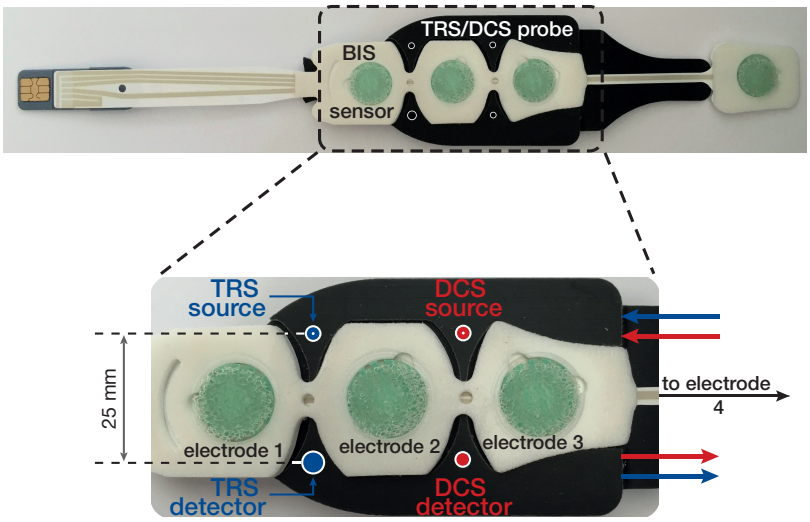

Figure 6.1: Bottom view of the 3-D printed combined BIS-TRS/DCS probe. The first three electrodes of the BIS sensor are placed on the subject's left forehead followed by the black fiber pad which fits around the BIS sensor. The fourth electrode is attached next to the patient's left eye. Source (top) and detector (bottom) fiber tips are placed in between the first and second electrode, surrounded by TangoBlack shore 27 material.

avalanche photodiode - collected the scattered photons. A eighty-five fold graded-index fiber bundle - same fiber properties as the source fiber - collected the TRS light and guided the photons into two hybrid photo multiplier detectors, one for each brain hemisphere. For further details, please refer to Sections 2.4, 2.5, 2.6 and 4.2.

6.2.2 *Clinical data and patient medication*

In addition to the recordings provided by the hybrid diffuse optical setup, information on the arterial oxygen saturation (SaO_2), heart rate (HR), end-tidal CO_2 ($EtCO_2$) and mean arterial pressure (MAP) - measured by an arm cuff - was extracted from an anesthesia monitor (Datex-Ohmeda Aisys™, GE Healthcare, Little Chalfont, United Kingdom) by the open-source VitalSigns capture (VScapture) program [159]. The BIS data was acquired by an unilateral BIS sensor (BIS Vista™, Medtronic plc, IRL) and saved by the Windows™ hyperterminal throughout the entire procedure.

General anesthesia was performed under total intravenous anesthesia with propofol at a concentration of 1 % (Propofol Fresenius®, Fresenius Kabi Deutschland GmbH, Bad Homburg, Germany) using the Schnider model [270] based on age, height, weight and gender of the patient [206, 126] implemented in a TIVA system (Alaris Asena® PK, Becton, Dickinson and Company, Franklin Lakes, NJ, USA). After tracheal intubation pulmonary volume-controlled ventilation was maintained with a fraction of inspired oxygen (FiO_2) of 0.5, a tidal volume of 6-7 mg/kg, a respiration rate (RR) between 12 to 16 breaths per minute and a positive end-expiratory pressure (PEEP) of 4-6 mmHg. The entire anesthesia procedure was carried out by experienced anesthesiologists of the University Hospital Vall d'Hebron.

It should be noted that the patients received further medications, known to influence the cerebral hemodynamics, such as fentanyl [38, 222, 210]. The data presented here does not consider such effects and is focused on the global agreement between rCBF and relative bispectral index (rBIS) in the left brain hemisphere. The reason for the left hemisphere is given by the fact that a unilateral BIS sensor was used and placed on the left forehead.

6.2.3 *Data evaluation*

As explained in Section 2.6, the data is first evaluated by fitting the respective semi-infinite medium solutions (see Sections 2.4 and 2.5) to the measurement. The fitting is done by using the downhill-simplex or Nelder-Mead method in MATLAB™'s implemented "fminsearch" function [179, 226]. Further data analysis is then carried out in R [255]. A wavelet analysis is performed [177] and the figures and tables presented here are generated using packages within R [224, 329, 330, 331]. In all models and statistical tests, "p-values" of less than 0.05 were considered statistically significant to reject the null hypothesis.

The oxy- and deoxyhemoglobin (HbO_2 and Hb) contents were calculated using the absorption information (μ_a) from TRS measurements at different wavelengths (see Section 2.1). Three main tissue constituents (HbO_2, Hb and H_2O) were con-

sidered and tabulated extinction coefficients from [253] and [132] were used. The tissue oxygen saturation (StO_2) was calculated assuming a water concentration of 77 % and a negligible lipid contribution.

As explained in Section 3.2.4, StO_2 can be expressed as a superposition of arterial, capillary and venous oxygen saturations (SaO_2, ScO_2 and SvO_2), which gives rise to blood volume percentage in venous compartment (γ) [70]. Assuming that this quantity does not change ($\gamma_1 = \gamma_2$), the measures of StO_2 were converted into relative OEF (rOEF) and $CMRO_2$ ($rCMRO_2$) changes using the relation from Equation 3.8 [90, 33, 209, 94, 70].

The patient's average value was taken as the reference and defined as zero. The relative changes of the variable of interest throughout the entire surgical procedure was then calculated with respect of the individual subject reference and expressed in percent (%):

$$Y(t)\ [\%] = \left[\frac{X(t)}{\langle X(t)\rangle} - 1\right] \times\ 100 \tag{6.1}$$

Substituting the variable X in Equation 6.1 by BIS yields rBIS (= Y) and for X = OEF results in Y = rOEF. In the calculation of rCBF (= Y), the variable X is set to αD_b, which is often referred to as the blood flow index (BFI) (see Equation 2.26).

Data collected during patient movements in the surgery was excluded from the dataset. Prior to a wavelet denoising, the data was grouped in 5 s bins for each patient in order to match the BIS sample size.

The rCBF and $rCMRO_2$ values from each subject were compared to rBIS for the entire study population using a two-sided Pearson product-moment correlation test with confidence intervals of 95 %. Data was evaluated in three different steps: I, II and III. While in step I all data points were included, step II only considers relative changes in the optically derived parameters ($rCMRO_2$ and rCBF), which are outside the one σ variation around the mean: $|\text{rCBF}| > \sigma_{\text{rCBF}}$ and $|rCMRO_2| > \sigma_{rCMRO_2}$. In step III, this condition was also applied on the rBIS data. The steps are summarised as follows:

Step I: Consider the complete $rCMRO_2$, rCBF and rBIS data set.

Step II: Consider all rBIS data but only significant changes in optical measurements, i. e. changes greater than the standard deviation.

Step III: Consider only changes in $rCMRO_2$, rCBF and rBIS, that are larger than the standard deviation.

Furthermore, the individual intercepts and slopes for each analysis step were computed. Results are presented for the entire study population and for each subject individually. The relative BIS values were calculated for an equal comparison to the derived $rCMRO_2$ and rCBF.

6.3 RESULTS

6.3.1 *Study population*

Seventeen patients (seven females and ten males) were included in the study population out of twenty recruited ones in total. The average age, height, weight and body mass index (BMI) is presented in Table 6.1 for the entire study population, as well as separated by gender.

	Age [yrs]	Weight [kg]	Height* [cm]	BMI [kg/m²]
All	54.5 ± 12.3	81.5 ± 14.1	165.1 ± 11.6	29.8 ± 4.0
Females	*52.9 ± 15.3*	*80 ± 12.9*	*159.4 ± 9.1*	*31.5 ± 4.4*
Males	*55.7 ± 10.5*	*82.4 ± 15.5*	*169.0 ± 11.9*	*28.6 ± 3.3*

Table 6.1: Demographic parameters: Mean ± their standard deviation. * denotes a statistically significant difference between females and males (t-test, $p < 0.05$).

The data from three recruited patients had to be excluded due to the following issues: BIS data capture failed (two cases), the fiber probe was removed during the surgery (one case). All subjects were patients without a brain disease and underwent the following surgical procedures: (para-) thyroidectomy (n = 4), hemithyroidectomy (n = 1), cholecystectomy (n = 5), cholecystomy (n = 1), morbid obesity (n = 1), cystectomy (n = 1), an exploratory laparascopy (n = 1), hemicolectomy (n = 1), a cervical laminectomy (n = 1) and a cervical corpectomy (n = 1).

6.3.2 *Optical data*

Using the wavelet transform and shrinking the wavelet coefficients in order to denoise our data, the combined standard deviations in the rCBF/$rCMRO_2$ and rBIS recordings were reduced from initially around 40 % to about 20 % over stable periods of anesthesia. rBIS, rCBF and $rCMRO_2$ were calculated using Equation 6.1. A representative time evolution of (r)BIS, rCBF and $rCMRO_2$ from the left brain hemisphere in one subject (ID = 5) is shown in Figure 6.2.

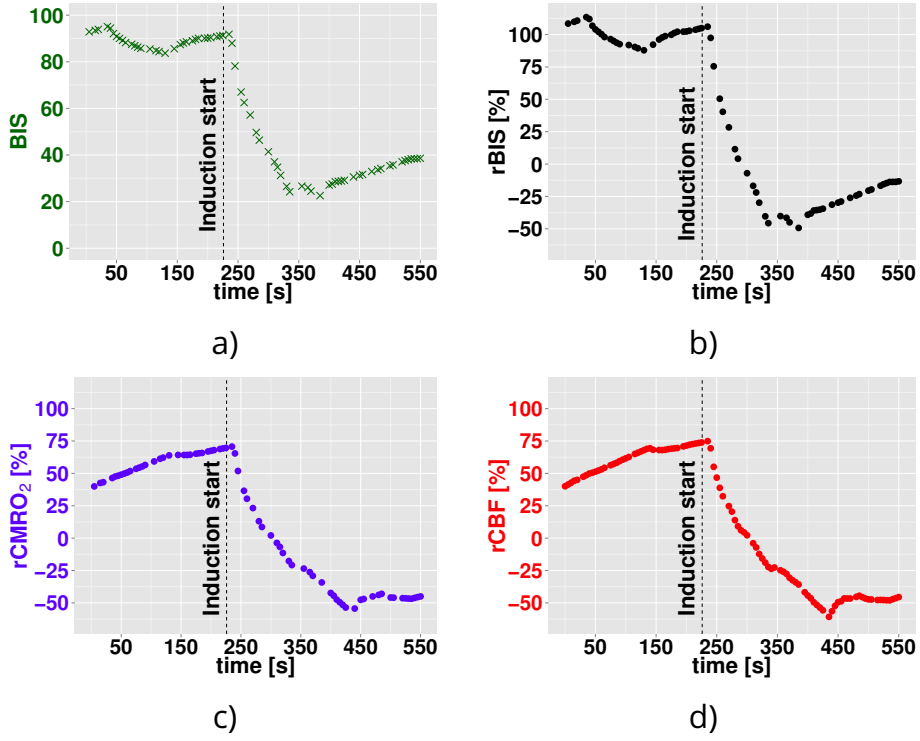

Figure 6.2: Representative time evolution of the a) bispectral index (BIS) and b) rBIS [%]. c) shows the relative cerebral metabolic rate of oxygen extraction change ($rCMRO_2$) [%] and d) the relative cerebral blood flow change (rCBF) [%] during anesthesia induction (t_0 = 175 s) by propofol (1%).

These parameters are plotted around the initiation of general anesthesia by TIVA of propofol (1%). The induction took place at t_0 = 175 s. It is noted, that the graphs presented in Figure 6.2 are excerpts of the entire procedure for the induction phase only.

A clear decrease in BIS (plotted in Figure 6.2 a)) from almost 100 to about 25 represents a characteristic BIS drop due to propofol-induced general anesthesia.

rBIS decreases from around 100 % to about -40 % and the rCBF from around 70 % to approximately -50 % between t = 175 s and t = 375 s. In this anesthesia induction phase the two variables correlate significantly with a $R_{pearson}$ of 0.95 (95 % conf. interval = 0.93 - 0.96) and p-value of less than 0.001.

6.3.3 *Step I: Global agreement between BIS (electrical) and optical data*

Expanding the value range over the entire surgical procedure and analyzing all included subjects leads to a statistically significant ($p < 0.001$) correlation coefficient of $R_{pearson}$ = 0.32 (95 % conf. interval = 0.30 - 0.33) between rBIS and $rCMRO_2$ and $R_{pearson}$ = 0.33 (95 % conf. interval = 0.31 - 0.34) between rBIS and rCBF. The slopes and their standard errors set to $m_{rCMRO_2} = 0.29 \pm 0.01$ and $m_{rCBF} = 0.30 \pm 0.01$.

6.3.4 *Step II: Consideration of only significant changes in optical measurements*

Since we are looking at the changes of rCBF and $rCMRO_2$ with respect to each subject's averaged value defined as 0 % and our one σ variation around this reference is σ_{rCBF} = 22.8 % and σ_{rCMRO_2} = 22.0 %, the second step only considers values that fulfill the following conditions: $|rCBF| > \sigma_{rCBF}$ and $|rCMRO_2| > \sigma_{rCMRO_2}$. Applying this criterion results in significant ($p < 0.001$) correlations with an increased correlation coefficient $R_{pearson\,rBIS \rightarrow rCMRO_2}$ = 0.46 (95 % conf. interval = 0.43 - 0.48) and $R_{pearson\,rBIS \rightarrow rCBF}$ = 0.47 (95 % conf. interval = 0.44 - 0.49).

After evaluation step II[1], the individual subject correlations between rBIS and $rCMRO_2$ are statistically significant ($p < 0.01$ - 0.001) in twelve out of the seventeen patients measured in total. Statistically significant correlation coefficients range from $R_{pearson}$ = 0.14 (ID 5; $p < 0.01$) to $R_{pearson}$ = 0.96 (ID 6; $p < 0.001$). Here, the non-significant cases are IDs 3, 4, 11, 13 and 14.

1 A subject-wise representation of correlation coefficients, intercepts and slopes for step II is given in Tables B.1 and B.2.

For rCBF, ID 13 shows a statistically significant correlation ($R_{pearson}$ = -0.28; p < 0.05) in addition to the same twelve cases as for $rCMRO_2$ (p < 0.001). The correlation coefficients for rCBF and BIS range in this case from $R_{pearson}$ = -0.28 (ID 13; p < 0.05) over $R_{pearson}$ = 0.16 (ID 5; p < 0.001) to $R_{pearson}$ = 0.98 (ID 8; p < 0.01).

6.3.5 *Step III: Consideration of only significant changes in all parameters*

Applying the same condition as in step II (see Sections 6.2.3 and 6.3.4) on the rBIS values (step III), correlation coefficients increase to $R_{pearson, rCMRO_2}$ = 0.67 (95 % conf. interval = 0.64 - 0.70) and $R_{pearson, rCBF}$ = 0.67 (95 % conf. interval = 0.64 - 0.70).

After evaluation step III[2], the individual subject correlations between $rCMRO_2$ and rBIS are statistically significant (p < 0.01 - 0.001) in twelve out of the seventeen patients measured in total. Their correlation coefficients cover a range from $R_{pearson}$ = 0.29 (ID 10; p < 0.01) to $R_{pearson}$ = 0.97 (ID 6; p < 0.001). The non-significant cases are IDs 3, 9, 11 and 13, while ID 8 has no data left after applying the above-mentioned exclusion criteria to perform a correlation test.

In the case of rCBF, the same twelve cases as for $rCMRO_2$ show a statistically significant correlation (p < 0.01 - 0.001). Their correlation coefficients range from $R_{pearson}$ = 0.28 (ID 10; p < 0.01) to $R_{pearson}$ = 0.98 (ID 6; p < 0.001). As for $rCMRO_2$, ID 8 has no data left after the third evaluation step to perform a correlation test. This is due to the fact that data could only be taken while the patient was already anesthesized and no significant changes were recorded during this period.

6.3.6 *Summary of all analysis steps*

Table 6.2 summarizes the retrieved Pearson correlation coefficients, intercepts and slopes from the linear regression analysis[3]. They are shown with their respective standard errors and for the three steps as presented in Section 6.2.3. The slopes of the calculated $rCMRO_2$ and rCBF against the rBIS val-

2 A subject-wise representation of correlation coefficients, intercepts and slopes for step III is given in Tables B.3 and B.4.

3 Data for individual subjects is presented in Tables B.1, B.2, B.3 and B.4.

ues are 0.53 ± 0.02 and 0.54 ± 0.02 respectively. These increase to 0.59 ± 0.02 and 0.60 ± 0.02 in step III of the analysis. In consequence, the intercepts decrease from step II to step III ($m_{CMRO_2, II}$ = -1.74 ± 0.48 to $m_{CMRO_2, III}$ = -6.93 ± 0.90 and $m_{CBF, II}$ = -0.18 ± 0.50 to $m_{CBF, III}$ = -5.09 ± 0.93).

		rCMRO$_2$			
step	R	intercept	slope	N	InD [%]
I	0.32***	-0.04 ± 0.20	0.29 ± 0.01	11913	100
II	0.46***	-1.74 ± 0.48	0.53 ± 0.02	4307	36.15
III	0.67***	-6.93 ± 0.90	0.59 ± 0.02	1408	11.82
		rCBF			
I	0.33***	0.50 ± 0.20	0.30 ± 0.01	11913	100
II	0.47***	-0.18 ± 0.5	0.54 ± 0.02	4183	35.11
III	0.67***	-5.09 ± 0.93	0.60 ± 0.02	1379	11.58

Table 6.2: Pearson correlation coefficients (*** = p < 0.001), intercepts and slopes with their respective standard errors from rCMRO$_2$ and rCBF versus rBIS. Step I represents the bare correlation and linear regression fit analysis results. Step II considers only values outside the ± σ region of rCBF, rCMRO$_2$ (|rCBF|> σ_{rCBF}; |rCMRO$_2$|> σ_{rCMRO_2}). In step III, additionally, only values of |rBIS|> σ_{rBIS} are included. N = total number of used data points; InD = percentage of included data.

Figure 6.3 shows the corresponding three data sets and their linear regression fits for a) rCMRO$_2$ and b) rCBF. The changes associated with a rBIS value of 100 - 150% are due to the patient waking up from the surgery, while the main cloud of data points around 0 % correspond to the phases where the patient was maintained under general anesthesia. These periods lasted between 40 min and 5 h.

6.4 DISCUSSION

In this study, a hybrid diffuse optical device was used to estimate cerebral metabolism [90, 45, 209, 262, 94, 29] during propofol-induced anesthesia. Propofol induced a change in the state of consciousness reflected in the BIS and CMRO$_2$ readings. The correlation between rCBF and rBIS is in agreement with previous observations [314, 173, 158, 112] and, in combination with TRS data, enabled us to link this to the

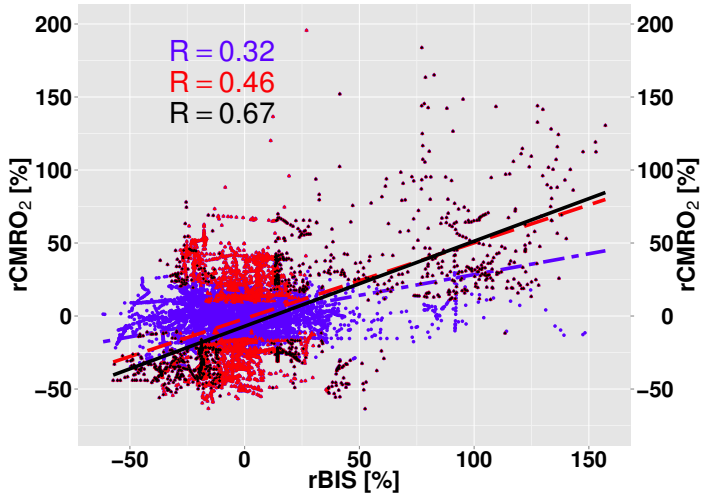

(a)

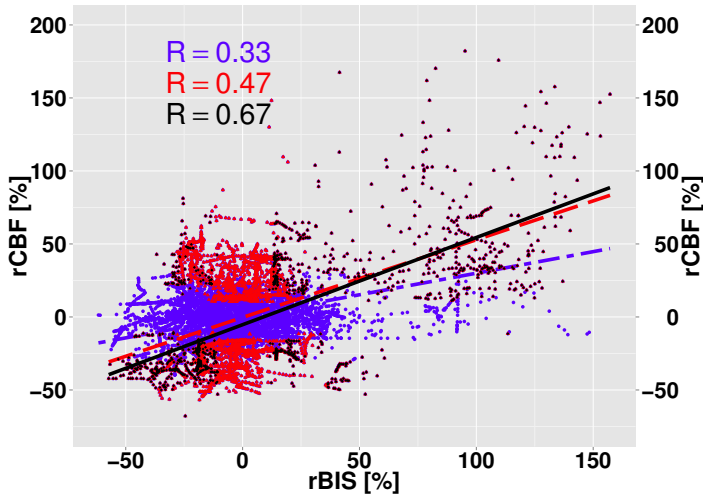

(b)

Figure 6.3: Correlation plots: $rCMRO_2$ against rBIS (a) and rCBF against rBIS (b). Data sets considering all values or only the ones outside the mean ± σ region are plotted in different colors. In blue all values are considered, in red only the ones outside the mean ± σ of rCBF or $rCMRO_2$ respectively, while in black we consider only the values which lie also outside the $\overline{rBIS} \pm \sigma_{rBIS}$.

$rCMRO_2$. The diffuse optical measurements presented here provide information on the microcirculation, while measures of the widely used transcraneal Doppler (TCD) only result in information at the macrovascular level [133, 2]. Moreover, data obtained with TRS and DCS does not require insonation windows like TCD [199, 180, 24], thus providing an advantage over this widely used technique.

Seventeen patients were reported within the defined inclusion criteria over a range of eleven different types of surgeries. In many of the noted cases, various movements of the patient due to the standard procedure for specific surgeries, led to exclusion of those periods in the data. This resulted in only a few patients in which the anesthesia induction phase and the characteristic BIS and $rCMRO_2$ drops during that period could be recorded. An illustrative case was shown in Figure 6.3. The changes are significantly correlated between BIS and $rCMRO_2$ ($R_{pearson}$ = 0.95; p < 0.001). Possible pharmacodynamic interactions between propofol and fentanyl affecting the level of consciousness were seen in the BIS values [222, 210] so that such interactions should not affect the global correlation between optical and BIS data.

Data was denoised using wavelets and shrinking the coefficients in the spectrum, reducing the standard deviation from $\sigma \sim 40$ % to $\sigma \sim 20$ %. Different degrees of changes (step I-III) were used for the correlation investigation. In all steps significant correlations were found (p < 0.001). Surgery durations ranged between 1 h and 6 h, thus producing long periods of time where data was taken without any induced changes in the cerebral activity. This led us to exclude those regions in the correlation analysis. For significant changes in $rCMRO_2$, rCBF and rBIS (step III) strong significant correlations were retrieved ($R_{pearson, rCMRO_2}$ = 0.67 and $R_{pearson, rCBF}$ = 0.67; p < 0.001). In step II, episodes of significant changes in only the optically derived values also correlate significantly with rBIS ($R_{pearson, rCMRO_2}$ = 0.46 and $R_{pearson, rCBF}$ = 0.47; p < 0.001). The data suggests that we are sensitive to changes above the one σ variations around the mean, which is not surprising given the fact that a huge cloud of data points is formed around the reference value as a result of setting it to each subject's average value (Equation 6.1).

In steps II and III, an overall slope ranging from 0.53 ± 0.02 ($m_{rCMRO_2 \rightarrow rBIS, II}$) to 0.59 ± 0.02 ($m_{rCMRO_2 \rightarrow rBIS, III}$) was fitted. The slopes between rCBF and rBIS (0.54 ± 0.02 - 0.60 ± 0.02) do not differ significantly, which supports the assumption that propofol maintains physiological coupling.

The data is consistent over several different types of surgeries and it correlates well for relative changes in both optical data sets. Additional data from a clean anesthesia induction

and emergence from anesthesia could provide further support, since large BIS and $CMRO_2$ are expected in these events. It is however important to state that the data was collected during standard surgical procedures. The surgeries were conducted regarding the patient's health, which is of primary importance. Therefore, movements, medications, patient positioning and the over all surgery process are necessary and in the recording of diffuse optical data we needed to adapt to these circumstances.

6.4.1 *Clinical relevance*

In the study of normal brain physiology as well as in the investigation of neuroprotective drug effects or methods, that target rCBF and $rCMRO_2$, such as induced hypothermia, it is essential to estimate these parameters accurately. The knowledge of the relationship between rCBF and $rCMRO_2$ is a key in defining the viability of the brain following an acute insult and in understanding brain ischemia pathophysiology and ischemic-induced cascades. Most of the invasive methods used in neurocritical care, such as microdialysis, tissue oxygen pressure (PtO_2) probes or jugular bulb oximetry, present only rough estimates of cerebral metabolism and blood flow, the consumption of oxygen or of the repercussions affecting brain metabolism due to a lack in oxygen supply, i. e. hypoxia. Using PtO_2 probes (Licox® or Paratrend/Neurotrend™) one can estimate the local brain tissue oxygenation in a continuously and by jugular bulb oximetry one obtains continuous information on global jugular venous oxygen saturation ($SjvO_2$) and - under constant SaO_2 and PO_2 - information on the relation of CBF to $CMRO_2$ [127, 131, 36, 317]. Microdialysis allows one to monitor cerebral metabolism, to compare it to the systemic level by measures of glucose, lactate and pyrovate and it indicates episodes of hypoxia of hypermetabolism. Nonetheless, these techniques require invasive probes and can not simultaneously provide information on CBF and $CMRO_2$.

Positron emission tomography (PET) using radiotracers such as ^{15}O-labeled H_2O remains the gold standard to assess oxygen levels in brain [217]. PET has been the tool used in most studies to differentiate among the three types of brain tissue that are affected by ischemic stroke: the irreversibly damaged core, the potentially salvageable penumbra and the area

of oligaemia [217]. While PET remains the best tool available, a significant disadvantage is, that measurements can only be performed at specific time-points. This is also true for (arterial spin labeled perfusion) magnetic resonance imaging. Continuous monitoring would be tremendous advantage in clinical practice considering highly variable and dynamic neurocritical patients. The study presented here demonstrates that the above-mentioned parameters can be estimated continuously by hybrid diffuse optical methods in a non-invasive manner and with an acceptable reliability. This technique offers the clinicians as well as the scientific community a unique and powerful tool to improve the understanding of the pathophysiology of the acute injured brain. This tool has the potential to aid the clinicians in the design of therapeutic strategies targeted to the hemodynamic profile of the at risk brain.

6.4.2 *Cases without a significant correlation*

The correlations vary among subjects (see Tables B.1, B.2, B.3 and B.4). Table 6.3 shows a list of the non-significant cases, their types of surgeries and the amount of data used for the correlation analysis.

ID	surgery type	N_{rCMRO_2}		N_{rCBF}	
		step II	step III	step II	step III
3	cholecystectomy	14	8	14	8
4[1]	cholecystectomy	211	31	218	35
9[2]	exploratory laparascopy	63	19	63	19
11	hemithyroidectomy	8	7	9	8
13[3]	cholecystectomy	51	49	51	49
14[4]	cholecystectomy	184	43	186	43

Table 6.3: Surgery and data information of the non-significant correlation cases. The grey areas refer to excluded cases after applying a threshold for N (see text). N = total number of used data points.

For $rCMRO_2$ and rCBF the listed subjects show non-existence of significant correlations with rBIS for either analysis step II or III or both.

1 Case 4 is only significant in the third evaluation step.
2 Case 9 is only significant in the second evaluation step.
3 Case 13 is significant only for rCBF in the second evaluation step.
4 Case 14 is only significant in the third evaluation step.

It is noteworthy, that in total five cholecystectomies were performed throughout the entire study and four of these surgeries appear in the cases listed in Table 6.3. These were laparascopic surgeries and therefore similar to the procedure in ID 9 and known to be able to provoke hyperemia in consequence of elevated arterial partial pressure of carbon dioxide ($PaCO_2$) [324, 185, 144, 76, 118] caused by pneumoperitoneum (abdominal insufflation with CO_2). The effect of elevated arterial partial pressure of carbon dioxide (hypercapnia) has been discussed in Chapter 3 and is studied in Chapter 7 and 8 and could give one explanation for the absence of a significant correlation. Furthermore it was found earlier that cerebral oxygen metabolism can also change under hypercapnic conditions [335, 34], yet not in consequence to the abovementioned pneumoperitoneum [324]. Moreover, the data presented here was taken from intubated and controlled patients connected to a respiratory anesthesia monitor to avoid such alterations. By maintaining normocapnic conditions in this manner the hyperemia effect is reduced and therefore we expect a constant cerebral oxygen metabolism is conserved [178].

In cases without a significant correlation only a few data points for the correlation calculation are available as a result of applying the criterion for steps II and III (see Table 6.3). Based on this, the data was examined using only those cases with some minimum number of data points. This number is set to 60 in step II and 40 in step III, considering that in step III the amount of usable data points is further reduced. Applying this criterion leads to non-consideration of the grey marked subjects in Table 6.3. In step II, this results in a slightly increased $R_{pearson}$ of 0.48 (95 % conf. interval = 0.45 - 0.50) for $rCMRO_2$ and 0.49 (95 % conf. interval = 0.46 - 0.51) for rCBF. Additionally, in step III, further increased correlation coefficients are calculated: 0.69 (95 % conf. interval = 0.66 - 0.72) for $rCMRO_2$ and 0.70 (95 % conf. interval = 0.67 - 0.72) for rCBF.

There are cases in the study population, which are not likely to show significant correlations between $rCMRO_2$/rCBF and rBIS. This may be due to a data sets for specific cases, which do not include sufficient points to ensure that the correlation analysis is not compromised by noise. It is the short surgery duration with many patient - and therefore probe - movements that leads to the reduced size of these data sets. Appli-

cation of the evaluation steps explained in Section 6.2.3 then leads to further data exclusion. These criteria were defined in order to remove periods of stable anesthesia and cerebral activity and therefore noise correlation. Nonetheless, they lead to very few data points in some patients making correlation analysis unreliable. This problem could be addressed in the future using improved probe attachments.

6.4.3 *Confounding factors in optical data*

In the estimation of $CMRO_2$ based on optical data we have to keep in mind that the detected light, has passed through skin, skull and the cerebral spinal fluid (CSF) before it reaches the frontal cortex. The resulting partial volume effects can lead to underestimation of rOEF and rCBF [219, 140, 29, 116, 92, 299, 300, 298, 32]. Since $rCMRO_2$ is derived from these quantities (see Equation 3.8), the possible underestimation translates to the calculated metabolism.

A homogeneous medium was assumed in the analysis of DCS and TRS data. However, this assumption is not entirely correct as the head consists of separate tissue layers with different optical properties. The fraction of moving scatterers (α) in each tissue layer may vary. The blood flow index (BFI) is defined as the product of α times D_b (see Equation 2.26), which means that variations in α will directly affect reported BFI (see Chapter 2). Similarly, the oxygen extraction fraction (OEF), calculated from TRS measurements can be underestimated by not taking a multi-layered medium into consideration. Both parameters, BFI and OEF are needed for the calculation of $CMRO_2$ (Equation 3.8) and possible underestimations could bury some changes.

Apart from partial volume effects, an error might be introduced due to a change in the contribution of arterial, venous and capillary oxygen saturations (SaO_2, SvO_2 and ScO_2, respectively) to the measured tissue oxygen saturation (StO_2) by the hybrid device [219]. $rCMRO_2$ was calculated using Equation 3.8 and considering that the blood volume percentage in venous compartment (γ) did not change. Since the data was averaged over the entire surgery, γ could have changed, leading to an error according to Equation 3.9.

6.5 CONCLUSION

Hybrid diffuse optical data during general surgeries with patients under general anesthesia with target-controlled infusion of propofol was obtained. Cerebral metabolism and blood flow ($CMRO_2$ and CBF) calculated by a combination of TRS and DCS correlate with BIS readings, which provide information on the state of consciousness via EEG measurements of the brain and are widely used in the clinic. This provides the first comparison of non-invasively derived $CMRO_2$ and CBF by hybrid diffuse optics with the established BIS readings and demonstrates the potential of diffuse optical techniques.

Diffuse optical techniques enable the continuous monitoring of patient consciousness during surgical procedures conducted under general anesthesia. The findings presented here relate EEG measures to optically derived $CMRO_2$ and CBF measurements and allow the investigation of the physiological coupling. The results presented here further support previous studies showing that propofol-induced anesthesia maintains physiological coupling between $CMRO_2$ and CBF.

6.6 OUTLOOK

A logical next step would be to use the optical hybrid device in monitoring of neurocritical patients. This would allow studying the hybrid device's applicability in the classification of the pathophysiology in patients who suffer acute brain damage and could provide a promising non-invasive assessment of cerebral hemodynamics and oxygen metabolism and could be used to guide the therapeutic management of these patients. This may prove to be a powerful tool for optimization and monitoring of specific patient treatments, thus improving treatment effectiveness and outcome. In addition, this tool would provide a unique opportunity to compare the temporal profile of many sought-after variables not measurable to date by any single method and correlate them with a long-term evaluation of functional outcome and quality of life.

7

RESPIRATIONAL AND POSTURAL EFFECTS ON CEREBRAL HEMODYNAMICS

In this chapter, we use the information presented in Chapters 2 and 3 to investigate changes in microvascular cerebral blood flow as a consequence of different arterial partial pressures of carbon dioxide and oxygen brought on by changes in inhaled gas contents in two different subject body positions. These positions and alterations in partial pressures are used and can occur in surgery under general anesthesia and may lead to complications. Here, the DCS modality presented in Chapter 4 is used in the clinical environment for the investigation of partial pressure and position influences on the brain's microvasculature in awake volunteers without brain disease.

This study is a result of a collaboration with Dr. Neus Fabregas, Dr. Ricard Valero, Dr Enrique Carrero, Dr. Javier Tercero and colleagues from the Anesthesiology Department at Hospital Clínic in Barcelona.

7.1 BACKGROUND

The positioning of the patient may affect cerebral perfusion pressure (CPP) and intracraneal pressure (ICP) via mean arterial pressure (MAP) and indirectly alter cerebral blood flow (CBF) (see Chapter 9). The alterations in the inclination of the patient's bed in the hospital are referred to as head-of-bed (HOB) manoeuvres. Applications of HOB manoeuvres range from improving brain health in traumatic brain injury (TBI) and (ischemic) stroke patients to evaluation and investigation of cerebral autoregulation (CAR) [23, 109, 171, 12, 170, 11, 97, 332, 274] and cerebrovascular resistance (CVR) health (see Chapter 3). By raising the head above the heart level, the arterial pressure is reduced and the venous drainage increased, thus leading to a CBF decrease. In ischemic stroke (IS) patients one main goal is to maximize the cerebral perfusion, which can be achieved by lowering the HOB angle. HOB ma-

noeuvres are furthermore a common tool in the clinic to aid the surgery.

In the clinical practice, the different positions and bed angles range from head rotation, hyperextension, hyper- or lateral flexion to position adjustments of the whole body, such as supine ("dorsal decubitus"), lateral, (three-quarter) prone and sitting (or "beach chair") position [265]. The sitting position still remains controversial [121, 102, 119], but is widely used [265, 102, 251, 86, 202] in several interventions, such as shoulder surgery [291, 82], posterior fossa and cervical spine surgery since it provides optimum access to midline lesions [251]. It furthermore provides better cerebral venous decompression and favors gravity drainage of blood and cerebral spinal fluid (CSF), thus lowering ICP [121, 102, 251, 25] and is therefore a useful tool in neurosurgery.

There are, however, higher incidence rates of complications associated with general anesthesia in the sitting position, that can alter arterial partial pressure of carbon dioxide ($PaCO_2$) and partial pressure of oxygen (PO_2) and may indirectly affect the brain [238, 225, 22, 281, 107, 213, 265, 137, 251, 86, 187, 236, 190, 338, 203, 139]. Furthermore, cerebral ischemia has also been observed in relation to shoulder surgeries in sitting position [237, 249].

From Chapter 3 we know that changes in the inhaled gas contents alter CBF. Hyperoxia (HO), hypercapnia (HRC) and hyperventilation (HV) and how these manoeuvres affect CBF and indirectly challenge CAR were discussed [193, 52, 242, 278, 196, 154, 305, 336, 257, 96, 200, 322, 7, 309, 72, 48, 51, 296, 176, 88, 77, 61, 141, 289, 197, 297, 3, 24].

By altering the respiratory gas contents, such as inhaled CO_2 ($InspCO_2$) and inhaled O_2 ($InspO_2$) or simply by changing the respiration rate (RR), $PaCO_2$ and PO_2 change thus causing vasoconstriction (HO, HV) or vasodilatation (HRC).

The interplay between the effects caused by HOB angle change and the manipulation of $PaCO_2$ and PO_2 on the cerebral hemodynamics remains a field of interest as HO, HRC and HV may occur during surgical procedures in different positions. In fact, complications such as venous air embolism (VAE) [238, 225, 22, 281, 107, 213, 86, 338, 203], paradoxical air embolism, upper airway obstruction or pneumocephalus

[137, 190] are associated with HO, HRC, HV [252, 291, 225, 107, 213, 251]. In anesthesized and intubated patients pulmonary volume-controlled ventilation is used to account for periods of HO or HRC. Nonetheless, these need to be identified first and this is usually based on the analysis of the exhaled gas mixture and its O_2 and CO_2 contents [55, 249]. The externally controlled patient ventilation can futhermore lead to hyperventilation (HV).

There are indications that near-infrared techniques may help identify the complications mentioned above or could provide an early warning sign [252, 225]. It is the existence of complications and their increased incidence rates in the sitting position that is worrisome. Although no increased mortality rate has been reported [265], there is a need for a clear understanding of influences of the sitting position on cerebral hemodynamics [82] and how these are affected in combination with CBF alterations due to induced vasodilatation and constriction.

Commercial devices, which make use of near-infrared spectroscopy (NIRS) as discussed in Section 2.1, have been utilized to monitor cerebral regional oxygen saturation (SrO_2) in shoulder surgeries in the sitting position [155, 174, 182, 220, 80, 111]. The need for close non-invasive monitoring of cerebral hemodynamics in this scenario has been emphasized earlier [214, 174]. The evolution of CBF has been examined using transcraneal Doppler (TCD) observing no significant influence on CBF by the "beach chair" positioning [291].

These studies either use commercial NIRS devices, such as the INVOS™ (Medtronic plc, IRL) or FORE-SIGHT™ monitor (CAS Medical Systems Inc., Branford, CT, USA), which both use continuous wave near-infrared illumination for the measurement of SO_2 [219], or employ TCD, which only provides information on the blood dynamics at the macrovascular level, for cerebral blood flow velocity (CBFV) measurements.

A more advanced technique providing information on CBF at the microvascular level is diffuse correlation spectroscopy (DCS). A number of DCS measurements have reported the above-mentioned relative CBF (rCBF) changes in response to HOB procedures [90, 109, 171, 170, 98, 44, 97], but not in combination with the respiratory challenges discussed in this chapter .

Recording macrovascular CBFV by TCD, which is associated with CBF [327, 175, 73, 42, 24, 2] and microvascular CBF estimated by DCS at the same time during the mentioned challenges is an approach to investigate CAR and more closely to look at the regional hemodynamic implications of HO, HRC and HV together with the subject's positioning. By combining the investigation of CBF and CVR responses to the above-mentioned respiratory challenges and their response from the subject position we can look for possible differences in the brain's behaviour due to an already changed CBF and therefore an alteration in the ability to regulate blood flow by vasoconstriction or dilatation. The study presented here aims to investigate microvascular cerebral blood flow (mCBF) together with macrovascular CBFV information and additional physiological parameters, such as heart rate (HR), mean arterial pressure (MAP), peripheral arterial oxygen saturation (SpO_2) and SrO_2 upon position changes together with their responses to different respiratory challenges, such as hyperoxia (HO), hypercapnia (HRC) and hyperventilation (HV). To that extent, the respiratory challenges were conducted in two different positions (supine and 50° sitting (or "beach chair") position).

7.2 METHODS

Nineteen volunteers were recruited for this study. The inclusion criteria were absence of pathologies and no use of any nervous system activator in the eight hours prior to the measurement. Additionally, smokers were excluded. The mentioned criteria and exclusion of two cases for protocol elaboration purposes and a technical issue in additional two cases led to the inclusion of fifteen healthy volunteers out of the nineteen recruited ones. Each subject signed an informed consent, which was approved by the ethical committee of Hospital Clínic in Barcelona (CEIC - Comité Ético de Investigación Clínica del Hospital Clínic de Barcelona), as well as all procedures and devices of this study. The measurements were conducted according to the principles of the Declaration of Helsinki.

7.2.1 *Clinical data*

The general health condition of the included volunteers and global physiological parameters, such as HR, BP_{dia}, BP_{sys}, and MAP were recorded by a Nexfin® device (BMEYE, Amsterdam, The Netherlands), which provided further measures, such as cardiac output (CO), cardiac index (CI), stroke volume (SV), stroke index (SI) and systemic vascular resistance (SVR). In addition to SpO_2 - provided by a standard pulseoximeter - the SrO_2 in leg and arm of the subjects was also monitored. This data was taken with an INVOS™ device (Medtronic plc, IRL), which employs infrared-light from a light emitting diode (LED) at wavelengths of 730 and 810 nm to measure the proportion between HbO_2 and THC. The respiratory values ($EtCO_2$, $InspCO_2$, $InspO_2$ and exhaled O_2 ($ExpO_2$)) were recorded using an anesthesia monitor (Julian®, Dräger Medical GmbH, Lübeck, Germany).

The CBFV (systolic and mean) measures were taken with a TCD device (Intraview™, Rimed, Tel Aviv, Israel) for recordings of hemodynamic changes in the macrovasculature. Based on measured $CBFV_{sys}$ and $CBFV_{mean}$ information, the diastolic cerebral blood flow velocity ($CBFV_{dia}$) was calculated using the relation:

$$CBFV_{dia} = \frac{3 \cdot CBFV_{mean} - CBFV_{sys}}{2} \tag{7.1}$$

7.2.2 *Challenge protocols*

Figures 7.1 and 7.2 illustrate the different procedures each volunteer experienced in different two positions (50° sitting and supine). Three challenges were used: hyperoxia (HO), hypercapnia (HRC) and hyperventilation (HV). The initial position and challenge order was randomized. After one complete set of challenges the subject's position was changed. The challenges were defined as follows (see also Figure 7.1):

Challenge I: *Hyperoxia* (HO)
5 min *pre*-baseline, 3 min challenge, 5 min *post*-baseline
$ExpO_2$ > 70 %

Challenge II: *Hypercapnia* (HRC)
5 min *pre*-baseline, 2 min challenge, 8 min *post*-baseline

CO_2 concentration $\sim$ 6.8 - 8 %
O_2 concentration $\sim$ 30 %
$EtCO_2$ $\uparrow$ 20 mmHg

Challenge III: *Hyperventilation* (HV)
5 min *pre*-baseline, 1 min challenge, 5 min *post*-baseline
Metronome rate $\sim$ 40 min^{-1}
$EtCO_2$ $\downarrow$ 15 mmHg

For the HO challenge the subjects were asked inhale pure O_2. Once their exhaled O_2 ($ExpO_2$) rose beyond 70% the patient was considered to be hyperoxic and the mask was kept in place for another three minutes. In total, each subject underwent two hyperoxias, one in a 50° sitting position and one in supine position, while the order of these positions was random between subjects. In a similar manner, each subject performed a HRC maneuver in two positions for two minutes each after they started inhaling an increased content of CO_2 (6.8 - 8 %; see also Figure 7.1 and 7.3) and their $EtCO_2$ increased by at least 20 mmHg. In the illustration in Figure 7.3, we see the white bag, which has a gas mixture of 6.8 - 8 % CO_2, in the back. This gas mixture reaches the volunteer through a plastic tube and a mouthpiece. As above, there was one HRC in a 50° sitting position whereas for a second one the subject was placed in supine position. The order of these positions was randomized for each subject.

In the same randomized way, each subject underwent a HV challenge in both mentioned positions. Here a metronome was held in front of the volunteer and the challenge lasted for one minute after the $EtCO_2$ dropped at least 15 mmHg. All challenges had a preceding baseline of five min and were concluded by a recovery period which lasted another five min, except for the HRC case, where the recovery time was set to eight min.

In addition to the challenge protocols (see Figure 7.2), each subject's position was changed in a defined manner prior to the challenge protocol (supine → 50° → supine → 30° → legs at 45°; see Figure 7.2). After the complete set of challenges, the entire procedure was concluded with an additional baseline in supine position followed by the subject standing up, both for a duration of five minutes (see Figure 7.2).

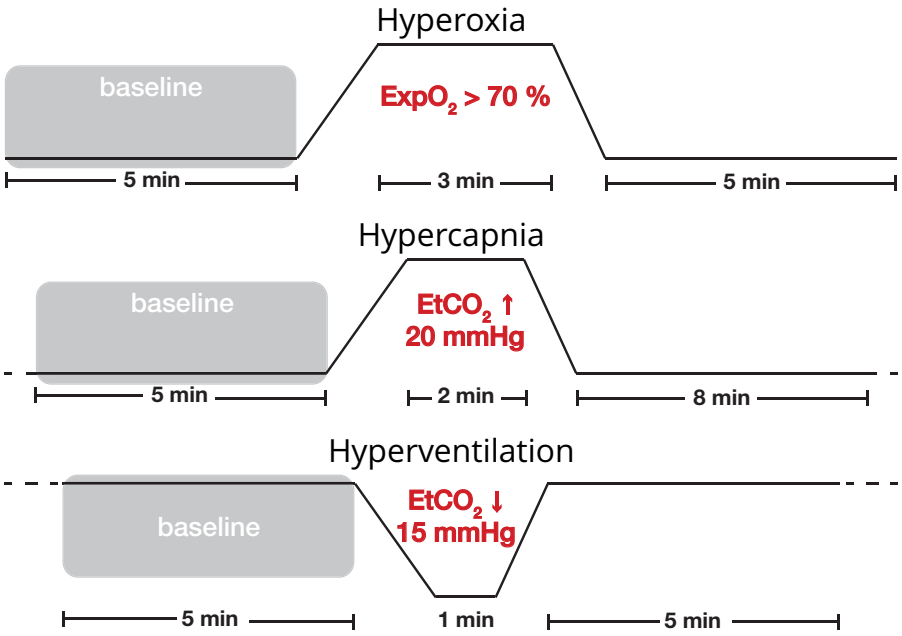

Figure 7.1: Challenge protocols: Hyperoxia required an exhaled O_2 ($ExpO_2$) content of > 70 % and lasted for 3 min. Hypercapnia required an increase of end-tidal CO_2 ($EtCO_2$) by at least 20 mmHg and hyperventilation an $EtCO_2$ decrease of minimum 15 mmHg.

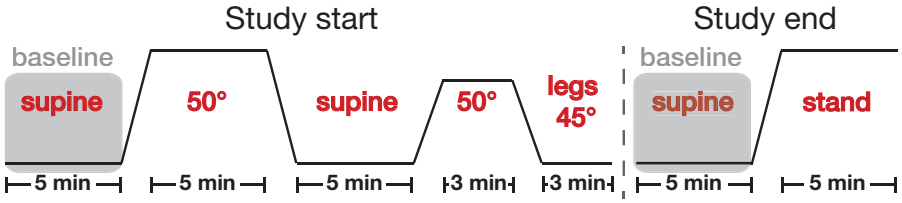

Figure 7.2: Start sequence: The different positions were kept for a duration of five minutes except for the 30° and legs at 45° positions, which lasted three minutes; End sequence: The procedure consisted of a supine baseline for five minutes followed by the subject standing for five minutes.

7.2.3 *Diffuse optical device*

A custom-built research DCS system (one part of the hybrid device presented in Chapter 4) monitored the microvasculatury CBF changes via fiber probes placed on the subject's frontal lobes. The source-detector separation (ρ) was 25 mm and the fiber tips were incorporated into a flexible plastic black head strap.

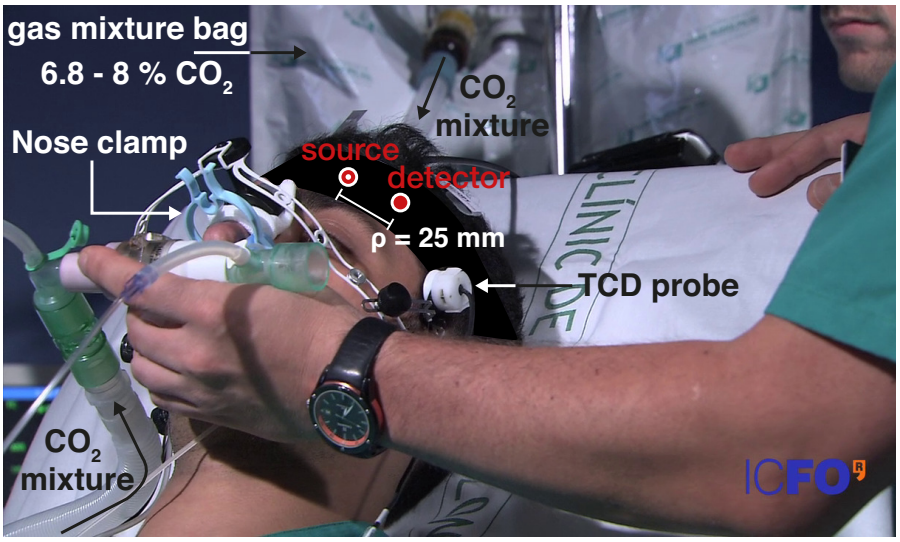

Figure 7.3: Diffuse optics headprobe for respiratory challenges: Image was taken during the HRC procedure. CO_2 bag with a gas mixture of 6.8 - 8 % CO_2 content is seen in the back.

Figure 7.3 shows the headstrap with the incorporated 90° fiber tips schematically together with the holder for the TCD probes. As presented in Chapter 4, the laser were operating at a wavelength of light (λ) of 785 nm and light was sent to the tissue through a multimode fiber with a core diameter of 200 µm (NA = 0.22). A a set of four single mode fibers (core diameter of 5.6 µm; NA = 0.13), each one connected to a single-photon counting avalanche photodiode (Excelitas, Québec, Canada) collected the light and the signal was processed in real-time by a digital correlator (Correlator.com, New Jersey, USA), which calculated the normalized intensity autocorrelation function (g_2) from intensity fluctuations in the recorded light.

7.2.4 *Data analysis*

Non-valid challenges were not considered. For example, if a subject could not withstand the 120 second duration of a hypercapnia the data was discarded. For the detailed definitions of challenge durations and further parameters please refer to Section 7.1.

Based on the calculated the intensity autocorrelations for different delay times $g_2(\tau)$ information on the tissue dynam-

ics, i. e. relative cerebral blood flow (rCBF), was computed. The semi-infinite homogeneous medium solution of the correlation diffusion equation as described in Section 2.3.3 was used in the fitting procedure.

Derivation of the normalized electrical field autocorrelation function (g_1) from g_2 after the determination of the mode parameter (β) is done via the Siegert relation $g_2 = (1 + \beta\, g_1)^{1/2}$ [183] (see also Section 2.6). Using the "fminsearch" function (based on the Nelder-Mead method) within MATLAB (The MathWorks Inc., Natick, MA, USA) [179, 226] and setting $<\Delta r^2(\tau)>$ to 6 $D_b\, \tau$, we have fitted the semi - infinite medium solution of the diffusion approximation [94] to our g_1 derived from the measurement, as described in Section 2.3.3. The result was converted to a measure of relative cerebral blood flow (rCBF) with respect to a baseline (see Section 7.2).

All reported values reflect the respective mean plus minus the standard errors - unless stated otherwise - and the entire statistical analysis was carried out in the statistical software package R [255]. As the primary method for statistical significant influences linear mixed effects (LME) models ("nLME" [244] package in R) were used. Fitted LME models which did not differ significantly from the null model were rejected. The recorded variables were tested for statistical significance among their relative and absolute changes with respect to each challenge's baseline by a Mann-Whitney-Wilcoxon test. The DCS measures of cerebral blood flow on the microvascular level were checked for correlations with the TCD measures, which are related to CBF on the macrovascular level (Spearman rank correlation test). In all models and statistical tests, "p-values" of less than 0.05 were considered statistically significant, enabling rejection of the null hypothesis.

7.3 RESULTS

Fifteen patients (five females and 10 males) were included in the study population. Their average age, height, weight and body mass index (BMI) is presented in Table 7.1 for the study population as a whole and is separated by gender.

Bilaterally collected CBF data - acquired by DCS - was analysed and averaged over both hemispheres for each subject,

	Age* [yrs]	Weight* [kg]	Height* [cm]	BMI* [kg/m²]
All	32.5 ± 6.3	72.2 ± 11.3	173.7 ± 8.6	23.8 ± 2.3
Females	*28.4 ± 2.3*	*61.2 ± 9.3*	*166.6 ± 7.5*	*21.9 ± 1.8*
Males	*34.6 ± 6.7*	*77.7 ± 7.6*	*177.3 ± 6.8*	*24.7 ± 2.0*

Table 7.1: Demographic parameters: The demographic parameters of the population given as mean ± their standard deviation. * denotes a statistically significant difference between females and males (t-test, $p < 0.05$).

since no statistical significant differences between brain hemispheres was observed (LME model with hemisphere as a factor; $p > 0.05$).

7.3.1 *Study start and study end procedure*

The procedure was the same for all subjects. The supine position is used as a baseline and all values for the following positions reflect the changes with respect to this initial baseline. The results are shown in Figure 7.4, where the baseline is represented by the black dashed lines.

Plotted in Figure 7.4 are the relative microvascular cerebral blood flow rCBF and macrovascular cerebral blood flow velocity ($rCBFV_{mean}$, $CBFV_{dia}$ and $rCBFV_{sys}$) changes with one boxplot per position and variable. The four boxes to the left of the grey dashed line correspond to the posture changes at the beginning of the study (supine → 50° → supine → 30° → legs at 45°), while the box on the right shows the results of the "study end" procedure (supine → standing; see Figure 7.2). Additional parameters, ΔHR, ΔMAP, ΔSpO_2, ΔSV, ΔCO and ΔSrO_2 are shown in Figure C.2.

Changes with positions show that rCBF and rCBFV have similar tendencies. The rCBF changes in the 50°, supine, legs at 45° as well as the right after standing up differ significantly ($p < 0.001$) from the baseline (initial supine position; see Figure 7.2). The same holds for all CBFV changes when the volunteers stood up ($p < 0.05$), as well as for the $CBFV_{sys}$ in the 50° position ($p < 0.001$).

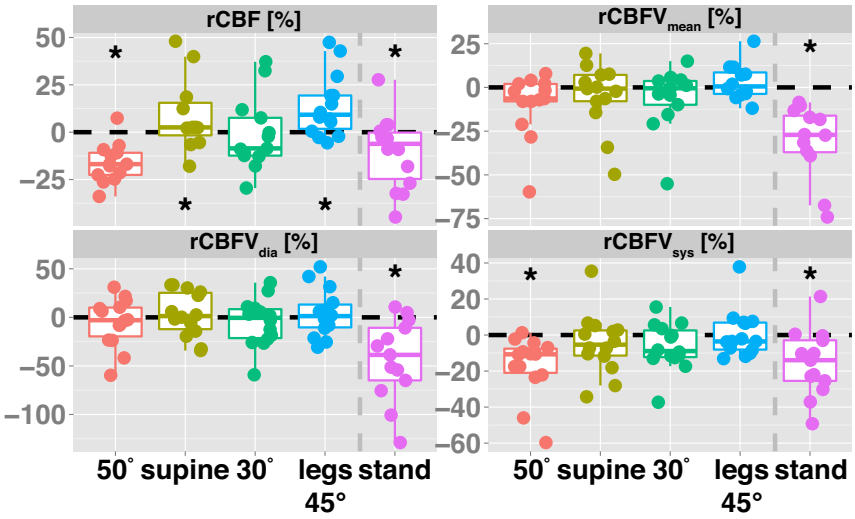

Figure 7.4: Posture changes in the beginning and the end - separated by a dashed grey line - of each case. The changes correspond to the protocols presented in Figure 7.2 and the abbreviations read as follows: rCBF = relative microvascular cerebral blood flow change; rCBFV$_{mean}$, rCBFV$_{dia}$ and rCBFV$_{sys}$ = mean, systolic and diastolic blood flow velocity changes. Statistically significant changes ($p < 0.05$) are marked by *. The dashed lines refer to the baseline taken from each initial supine position values for the beginning and the end of each case.

7.3.2 *Respiratory challenges*

The validity criterion explained in Section 7.2.4 reduced the data sets for the HRC challenge to eleven in the 50° sitting position and twelve for the supine position, while HV and HO data sets are complete.

Representative responses to the respiratory challenges are shown in Figure 7.5.

Each challenge in each position shows statistically significant ($p < 0.05$) changes in rCBF (Table 7.2), with respect to the 5 min baseline prior to the challenge. This is true for both cases:

Case I: no position distinction

Case II: separating supine and 50° position

Microvascular responses to the HO and HRC challenges show the same tendency in both positions, i. e. CBF either

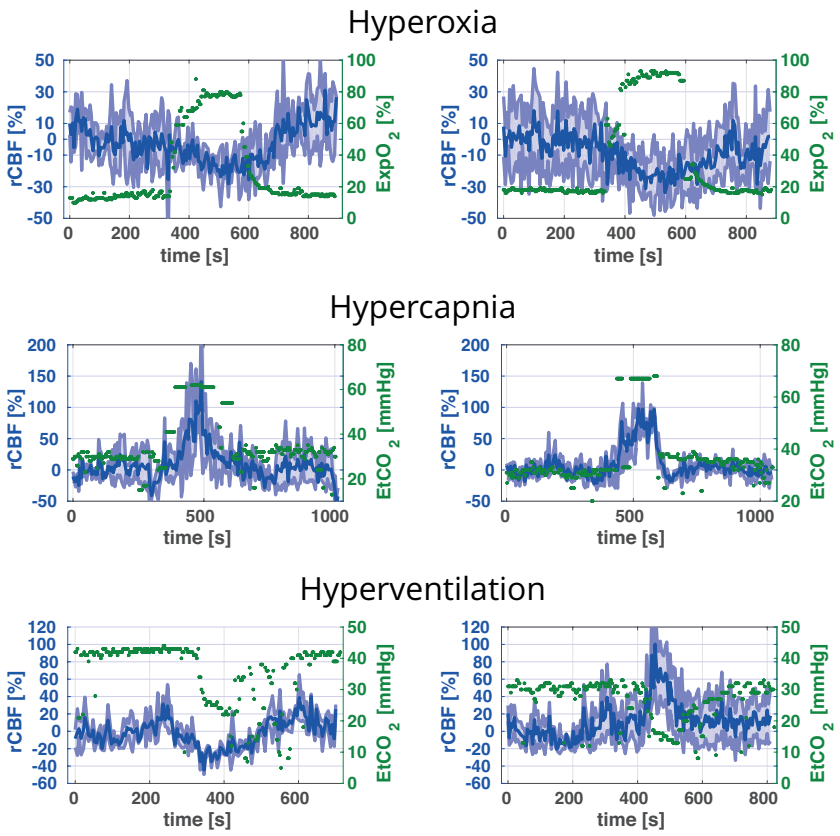

Figure 7.5: Respiratory challenge responses in two positions: The top graphs show the hyperoxia (HO) challenge, the middle graph the hypercapnia (HRC) challenge and the bottom one refers to the hyperventilation (HV). The left graphs correspond to the results from the supine, the ones on the right side to the 50° sitting position. Blue shows the rCBF evolution over time with their standard deviations in light blue and green lines represent the $ExpO_2$ (for the HO challenge) or $EtCO_2$ (in the HRC and HV case).

decreases (HO) or increases (HRC).

A LME mean model and a LME position model was employed in each challenge and fitted to the valid microvascular rCBF data (see Section 7.2.4). These models fitted a microvascular CBF response during HO showed of $\sim$ 9 % decrease ($rCBF_{supine}$ = -9.26 ± 2.53; $rCBF_{50°}$ = -9.11 ± 3.49; $rCBF_{global}$ = -9.18 ± 1.80). In the HRC challenge, the rCBF increases range from 48.71 ± 9.98 % ($rCBF_{supine}$) to 63.70 ± 12.24 % ($rCBF_{50°}$) depending on the position. Without position separation we obtain a rCBF increase of $rCBF_{global}$ = 55.85 ± 8.03 %. In response

	supine	50°	no position distinction
$rCBF^{HO}$ [%]	-9.26 ± 2.53	-9.11 ± 3.49	-9.18 ± 1.80
$rCBF^{HRC}$ [%]	48.71 ± 9.98	63.70 ± 12.24	55.85 ± 8.03
$rCBF^{HV}$ [%]	-4.29 ± 4.23	5.40 ± 5.78	0.56 ± 3.39

Table 7.2: Mean relative cerebral blood flow (rCBF) response, their standard errors and statistical significances for each challenge. The changes are statistically significant ($p < 0.05$) and calculated with respect to each challenge's baseline.

to HV we obtain small rCBF changes when not separating between positions ($rCBF_{global}$ = 0.56 ± 3.39), but a rCBF decrease in the supine position ($rCBF_{supine}$ = -4.29 ± 4.23) and increasing rCBF in the 50° position ($rCBF_{50°}$ = 5.40 ± 5.78). No LME position model revealed statistically significant differences from the null model.

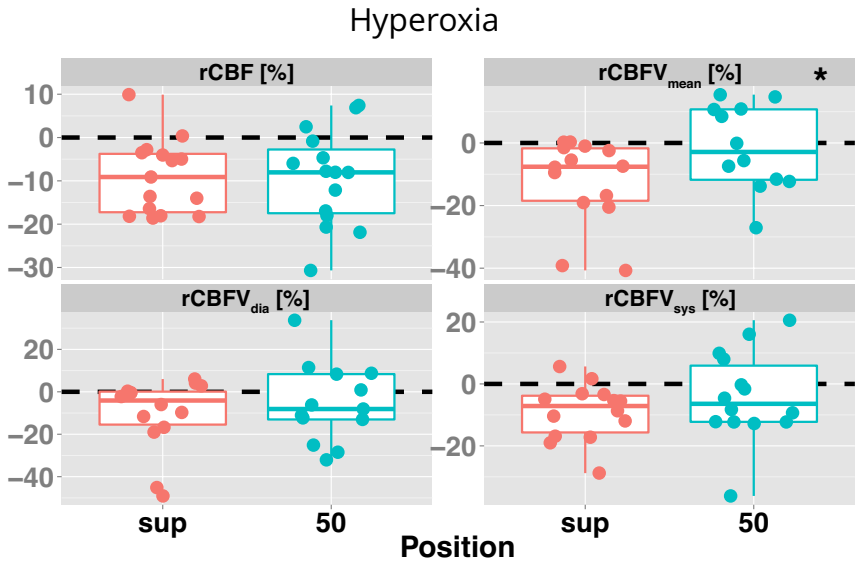

Figure 7.6: Responses to the hyperoxia challenge in two positions: Microvascular rCBF and macrovascular CBFV (mean, diastolic and systolic) change in response to inhalation of 100% O_2. The baseline is marked by the black dashed line. $rCBFV_{mean}$ is statistically significantly ($p < 0.05$) different between positions (marked by *).

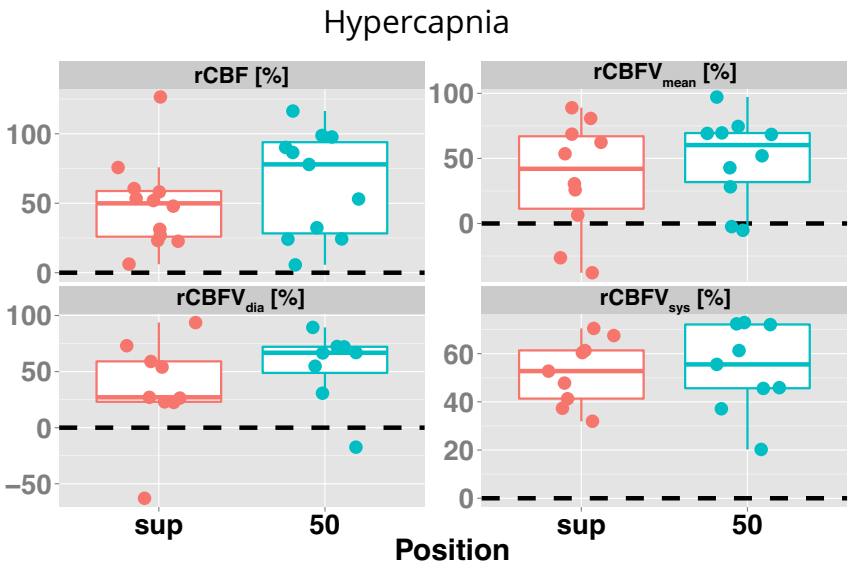

Figure 7.7: Challenge responses to hypercapnia in two positions: Microvascular rCBF and macrovascular CBFV (mean, diastolic and systolic) change during increased $EtCO_2$ ($\Delta EtCO_2$ = +20 mmHg) in response to inhalation of a gas mixture with an increased CO_2 content ($\sim$ 6.8 - 8 %). The baseline is marked by the black dashed line.

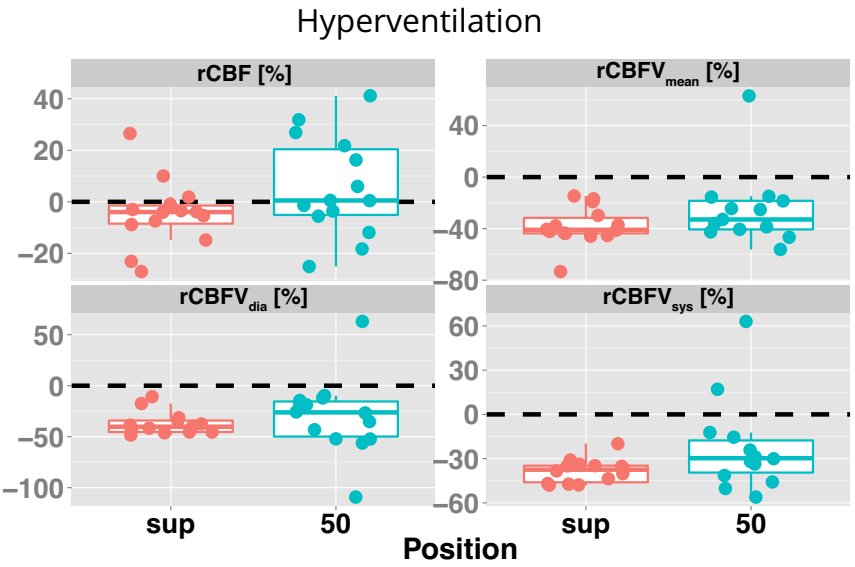

Figure 7.8: Challenge responses to hyperventilation in two positions: Microvascular rCBF and macrovascular CBFV (mean, diastolic and systolic) change during increased RR and therefore decreased $EtCO_2$ ($\Delta EtCO_2$ = -15 mmHg). The baseline is marked by the black dashed line.

7.3.2.1 *Macro- and microvascular hemodynamics*

Based on a Spearman correlation test[1] between microvascular rCBF - estimated by DCS - and macrovascular CBFV - retrieved from TCD - we find, no significant correlations between microvascular CBF and macrovascular $CBFV_{mean}$ and $CBFV_{dia}$ measures, neither in the supine nor the 50° position. Moreover, the macrovascular $CBFV_{sys}$ change was not significantly correlated with the microvascular CBF response during HO and HV nor was HRC in the 50° sitting position. In contrast, CBF in the microvasculature is significantly correlated with the macrovascular $CBFV_{sys}$ in supine position during HRC ($R_{spearman}$ = -0.65; p = 0.01).

1 please refer to Tables C.1, C.2 C.3, C.4, C.5 and C.6 for tabulated results with significance levels

7.3.2.2 *Challenges in detail*

HYPEROXIA Here we look in more detail at the response of other parameters during HO. In Section 7.3.2 and 7.9, we saw the changes of CBF in the microvasculature and CBFV (mean, diastolic and systolic) in the macrovasculature. In this section, we add the $\Delta ExpO_2$, ΔHR, ΔMAP, ΔSpO_2, ΔSV, ΔCO and ΔSrO_2 measures from the arm and look at their absolute changes during the HO maneuver. These parameters in both positions are shown in Figure 7.9. Values cited in the text represent median ± inter-quartile range (IQR).

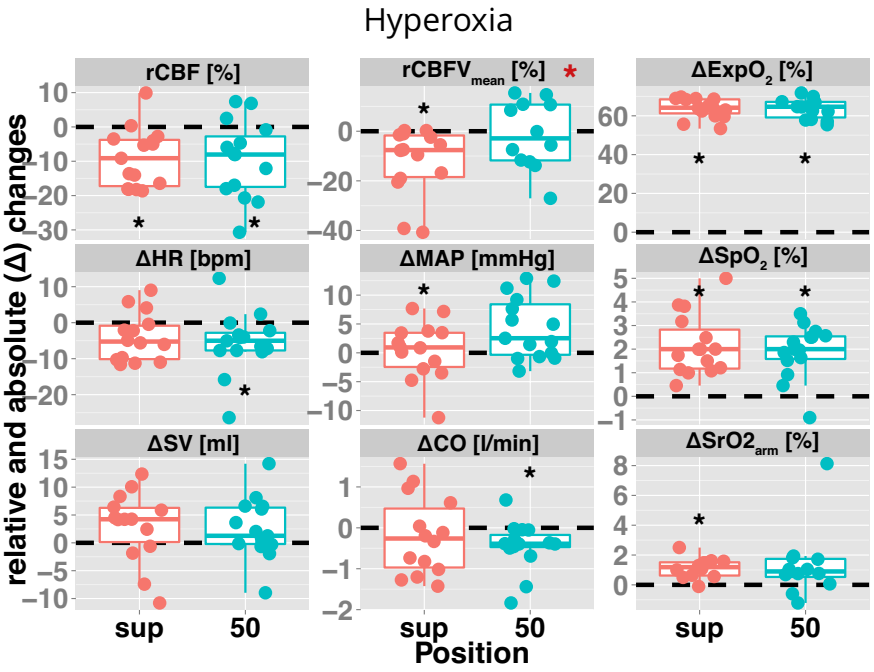

Figure 7.9: Hyperoxia data per position: Relative microvascular cerebral blood flow (rCBF) and macrovascular cerebral blood flow velocity (rCBFV$_{sys}$ and rCBFV$_{mean}$) changes and absolute changes of heart rate (HR), mean arterial pressure (MAP), peripheral arterial oxygen saturation (SpO_2), exhaled O_2 ($ExpO_2$), stroke volume (SV) and cardiac output (CO). Statistically significant changes (Mann-Whitney-Wilcoxon test, $p < 0.05$) in each position are marked by *. The baseline is marked by the black dashed line. rCBFV$_{mean}$ is statistically significantly (LME position model, $p < 0.05$) different between positions (marked by * in red).

We see that $ExpO_2$ increased significantly ($p < 0.001$) with a $\Delta ExpO_{2,\,supine}$ = 64.2 (7.2) % and $\Delta ExpO_{2,\,50°}$ = 64.7 (8.0) %

so that the following total $ExpO_2$ were achieved: $ExpO_{2,\,supine}$ = 80.2 (5.5) % and $ExpO_{2,\,50°}$ = 78.5 (8.0) %. The rCBF and $rCBFV_{mean}$ values set to $rCBF_{supine}$ = -9.1 (13.5) %, $rCBF_{,\,50°}$ = -8.0 (14.7) % and $rCBFV_{mean,\,supine}$ = -7.6 (16.7) % and $rCBFV_{mean,\,50°}$ = -2.9 (22.5) %, respectively. While CBF changed in both positions significantly ($p < 0.01$), the TCD-recorded $CBFV_{mean}$ decreased significantly only the supine position ($p < 0.01$). Decreases in HR and CO were significant in the 50° position ($p < 0.01$), as were MAP increases in the supine position ($p < 0.001$). The oxygen saturations acquired by a standard pulseoximeter placed on one finger and the INVOS® device with one sensor one the subject's arm (see Section 7.2.1) increased by $\Delta SpO_{2,\,supine}$ = 2.0 (1.7) %, $\Delta SpO_{2,\,50°}$ = 2.0 (1.0) %, $\Delta SrO_{2,\,supine}$ = 1.2 (0.9) % and $\Delta SrO_{2,\,50°}$ = 0.9 (1.2) %, respectively. The SpO_2 changes were statistically significantly different from the baseline in both positions ($p < 0.001$), whereas only the SrO_2, which was recorded by the INVOS® device, changed significantly only in the supine position ($p < 0.01$).

According to the LME position model as used in Section 7.3.2 the $CBFV_{mean}$ response to the HO challenge has a statistically significant dependence on the positioning of the volunteer ($p = 0.03$, $rCBFV_{mean,\,supine}$ = -12.2 ± 3.7 % compared to $rCBFV_{mean,\,50°}$ = -3.4 ± 3.4 %; fitted value ± standard error). All other changes showed no significant position dependencies.

As a result of a Spearman correlation test of rCBF with other variables[2], such as the relative cerebral blood flow velocity changes ($rCBFV_{mean}$, $rCBFV_{dia}$ and $rCBFV_{dia}$) and the absolute changes of HR, MAP, SpO_2, $ExpO_2$, SV and CO, we find that the rCBF changes correlate significantly in the supine position with ΔHR (Spearman's rank correlation coefficient ($R_{spearman}$) = 0.64, $p = 0.01$), SV ($R_{spearman}$ = 0.67, $p < 0.01$) and CO ($R_{spearman}$ = 0.68, $p < 0.01$), while none of the other above-mentioned parameters revealed statistically significant correlations with rCBF.

HYPERCAPNIA The obtained relative and absolute changes of recorded and relevant parameters during this challenge are shown in Figure 7.10. Please note that only data from subjects that underwent the entire 2 minute challenge, was

2 please see Tables C.1 and C.2 for a set of correlation results from the HO data set

considered for the evaluation.

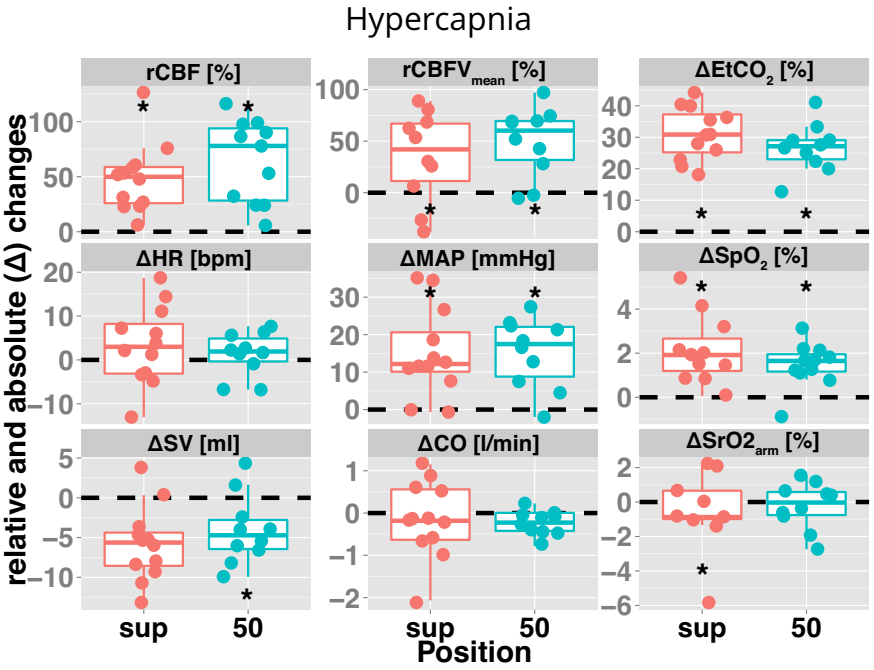

Figure 7.10: Hypercapnia data per position: Relative microvascular cerebral blood flow (rCBF) and macrovascular cerebral blood flow velocity changes (rCBFV$_{sys}$ and rCBFV$_{mean}$) and absolute changes of heart rate (HR), mean arterial pressure (MAP), peripheral arterial oxygen saturation (SpO$_2$), end-tidal CO$_2$ (EtCO$_2$), stroke volume (SV) and cardiac output (CO). Statistically significant changes (Mann-Whitney-Wilcoxon test, $p < 0.05$) in each position are marked by *. The baseline is marked by the black dashed line.

In this challenge, EtCO$_2$ increased significantly ($p < 0.01$) with ΔEtCO$_{2,\,supine}$ = 30.9 (12.1) mmHg and ΔEtCO$_{2,\,50°}$ = 27.1 (6.1) mmHg. The relative CBF showed significant ($p < 0.001$) increases (rCBF$_{supine}$ = 49.9 (32.9) %, rCBF$_{50°}$ = 78.0 (65.6) %). The relative CBFV$_{mean}$ in supine (rCBFV$_{mean}$ = 42.0 (55.7) %) and 50° sitting position (rCBFV$_{mean}$ = 60.2 (37.7) %) increased significantly ($p < 0.01$) as well. Furthermore, a significant ($p < 0.001$) increase of MAP with ΔMAP$_{supine}$ = 12.2 (10.5) mmHg and ΔMAP$_{50°}$ = 17.5 (13.3) mmHg was recorded, as well as decreases in SV with ΔSV$_{supine}$ = -5.6 (4.2) ml and ΔSV$_{50°}$ = -4.7 (3.7) ml. The latter decrease was statically significant ($p = 0.03$). HR and CO did not show significant changes ($p > 0.05$) in none of the positions. The oxygen saturations ac-

quired by a standard pulseoximeter placed on one finger increased significantly ($p < 0.01$) with $\Delta SpO_{2,\,supine} = 1.9\ (1.5)$ % and $\Delta SpO_{2,\,50°} = 1.6\ (0.8)$ %, while the ones acquired by the INVOS® device with one sensor on the subject's arm (see Section 7.2.1) decreased with $\Delta SrO_{2,\,supine} = -0.9\ (1.6)$ % and $\Delta SrO_{2,\,50°} = -0.1\ (1.3)$ %. According to a Mann-Whitney-Wilcoxon test, the change in the supine position was statistically significant ($p = 0.02$)

As in Section 7.3.2, we employed a LME position model on these variables and found no significant position dependencies. We also performed a Spearman rank correlation test[3]. As mentioned above, there is a significant correlation in our data between the rCBF change and the $CBFV_{sys}$ change in the supine position ($R_{spearman} = -0.65$, $p = 0.03$). In the 50° position, there is a significant correlation between rCBF and ΔMAP ($R_{spearman} = 0.75$, $p = 0.01$).

HYPERVENTILATION Figure 7.11 shows the relative and absolute changes of relevant parameters during the one minute long challenge described in Section 7.2.

In this challenge $EtCO_2$ increased significantly ($p < 0.001$) with $\Delta EtCO_{2,\,supine} = 16.6\ (2.4)$ mmHg and $\Delta EtCO_{2,\,50°} = 16.2\ (3.7)$ mmHg. The relative CBF shows positive and negative changes ($rCBF_{supine} = -4.0\ (7.0)$ % and $rCBF_{50°} = 0.5\ (25.5)$ %). Macrovascular relative $CBFV_{mean}$ decreases significantly ($p < 0.01$) in both positions with $rCBFV_{mean,\,supine} = -40.9\ (12.1)$ % and $rCBFV_{mean,\,50°} = -32.9\ (21.8)$ %. A significant ($p < 0.001$) HR increase with $\Delta HR_{supine} = 17.9\ (13.6)$ bpm and $\Delta HR_{50°} = 17.5\ (9.7)$ bpm was observed. Furthermore, a significant ($p = 0.03$) decrease of MAP in the supine position with $\Delta MAP_{supine} = -2.2\ (12.1)$ mmHg and a decrease of $\Delta MAP_{50°} = -4.4\ (9.4)$ mmHg in the 50° position. Also, significant ($p < 0.001$) increases in CO with 1.5 (1.3) l/min (supine) and 1.8 (0.8) l/min (50°) were observed. The oxygen saturations acquired using a standard pulseoximeter placed on one finger increased signifcantly ($p < 0.001$) with $\Delta SpO_{2,\,supine} = 1.7\ (1.4)$ % and $\Delta SpO_{2,\,50°} = 1.9\ (1.1)$ %, as well as those acquired with one sensor on the subject's arm (INVOS®, see Section 7.2.1), which also increased significantly ($p < 0.01$) with $\Delta SrO_{2,\,supine} = 1.2\ (1.2)$ % and $\Delta SrO_{2,\,50°} =$

3 please refer to Tables C.3 and C.4 for tabulated correlation results from the HRC data set

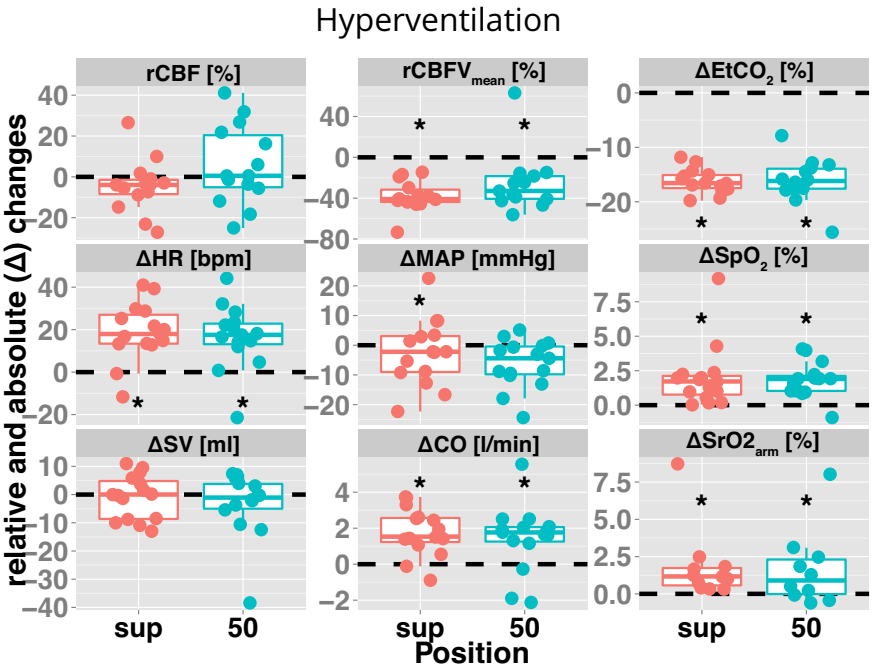

Figure 7.11: Hyperventilation data per position: Relative microvascular cerebral blood flow (rCBF) and macrovascular cerebral blood flow velocity changes (rCBFV$_{sys}$ and rCBFV$_{mean}$) and absolute changes of heart rate (HR), mean arterial pressure (MAP), peripheral arterial oxygen saturation (SpO$_2$), end-tidal CO$_2$ (EtCO$_2$), stroke volume (SV) and cardiac output (CO). Statistically significant changes (Mann-Whitney-Wilcoxon test, $p < 0.05$) in each position are marked by *. The baseline is marked by the black dashed line.

4.7 (2.8) %.

After fitting a LME model with the position factor, we obtain no significant position dependencies.

A Spearman rank correlation test was also conducted[4]. In HV, changes of microvascular CBF in the supine position correlate significantly with ΔMAP ($R_{spearman}$ = 0.67, $p < 0.01$) and ΔEtCO$_2$ ($R_{spearman}$ = 0.57, $p = 0.03$). In the 50° position, we found correlations of rCBF with rCBFV$_{mean}$ ($R_{spearman}$ = 0.57, $p = 0.04$).

4 for tabulated results of the correlation test for the HV challenge please refer to Tables C.5 and C.6

7.4 DISCUSSION

Optically measured cerebral blood flow (CBF) responses due to hyperoxia (HO) and hypercapnia (HRC) compare to similar measurements collected using (functional) magnetic resonance imaging (MRI) [336, 47, 176, 326, 46, 96, 160], arterial spin labeled perfusion magnetic resonance imaging (ASL-MRI) [342] and positron emission tomography (PET) [151, 263]. Here a number of aspects of the data presented above are examined more closely. We start with the bare position changes in the beginning and end of the study. These served as quality check on the brain's response. The protocol and how the desired conditions could be achieved and maintained are discussed and we also focus on the micro- and macrovascular levels and the respiratory challenges in detail. Finally, the postural effect on the manoeuver response are discussed.

7.4.1 *Study start and end procedures*

The responses to the initial position changes (see Section 7.3.1) were observed as expected, thus providing a valid check for the CBF changes observed in the respiratory challenges (Section 7.3.2). A decrease of rCBF in healthy subjects with increasing the HOB angle has been previously observed and reported [171, 170].

7.4.2 *Challenge validity*

All challenges in both positions met the criteria defined in Section 7.2. This is expected as the presented values are a result of an average of the challenge taken over its respective duration once the specific challenge criterion (increase or decreased $EtCO_2$ or $ExpO_2$) has been met. The fact that all average values are in accordance with the defined criteria shows that the desired conditions could be maintained over the necessary durations. This serves as an additional positive validity check. Moreover, four (50° position) and three (supine position) data sets from subjects undergoing the HRC challenge had to be excluded due to the subject not withstanding the manoeuvre for the desired period of 2 min. This is a notable number considering the total of fifteen volunteers and has to be kept in mind when looking at the HRC data.

7.4.3 *Micro- and macrovascular levels*

Mirco- and macrovasculature correlate only in the supine position during HRC ($R_{spearman}$ = -0.65). In this case, CBF measured at the microvascular level and CBFV recordings from the macrovessels show increases of comparable nature. Accordingly, a possible correlation between rCBF and $CBFV_{sys}$ might be expected from the boxes plotted in Figure 7.10 but the negative correlation in this case seems surprising. The other respiratory challenges did not show any significant correlations between the two vascular levels. The fact that no significant positive correlation was found, could reveal that the blood vessel's in the brain may respond differently depending on the vasculatory level.

7.4.4 *Hypercapnia*

Due to the strong HRC with a CO_2 concentration of 6.8 - 8 % the rCBF changes are much larger than in the HO or HV case ($rCBF_{supine}$ = 45.49 ± 8.99 % compared to $rCBF_{50°}$ 65.03 ± 12.86 %). A similar tendency is seen at the macrovascular level ($rCBFV_{mean,\ supine}$ = 42.0 (55.7) % compared to $rCBFV_{mean,\ 50°}$ = 60.2 (37.7) %), yet this difference is not significant. This could be related to the large IQR and may at least indicate a difference in response to hypercapnic conditions depending on the two investigated positions. In general, a CBF increase is expected since HRC increases the arterial partial pressure of carbon dioxide which leads the vessels to dilate (see Chapter 3) [181, 166, 165]. The increases in $EtCO_2$ levels show that the desired hypercapnic conditions could be maintained well during the HRC duration.

Readings from pulse oximetry can be influenced by alterations in the arterial partial pressure of carbon dioxide, leading to an impairment between peripheral arterial and the actual arterial oxygen saturation, especially during hypercapnia [218]. On the other hand, the Bohr effect, as discussed in Chapter 3, influences the oxygen-hemoglobin dissociation due to a lower pH value in hypercapnic conditions. Furthermore, the SpO_2 increase seems surprising compared to the small, non-significant changes around the baseline of SrO_2 in the 50° position or even the statistically significant SrO_2 decrease in the supine position. The latter significance is likely

to be produced by an outlier, resulting in a median close to the lower quartile and thus a significant SrO_2 change in the supine position. The INVOS™ device used for the recording of SrO_2 employs the same principles of absorption in near-infrared spectroscopy as presented in Chapter 2 and is using continuous wave light (see also Section 1.2). It is therefore important to keep in mind, that, while both parameters (SpO_2 and SrO_2) express oxygen saturation, SpO_2 provides information about the arterial oxygen saturation and SrO_2 is a measurement of the regional tissue oxygenation. The latter is therefore the result of a mixture of arterial, capillary and venous oxygen saturation, similar to the tissue oxygen saturation retrieved from the hybrid device presented in Chapter 4[5]. The differences between the recorded SpO_2 and SrO_2 therefore point towards a possible change in the transfer constants k_1, k_2 and k_3, e. g. changes in the blood volume percentages in the different compartments (arterial, capillary and venous).

The increased blood pressure and heart rate (HR) readings during hypercapnia are expected [96, 166]. The latter - in combination with the stroke volume changes - explains the non-significant changes in the cardiac output. Nonetheless, the fact that the HR changes are non-significant and no significant cardiac output increases were seen on average is not expected. During hypercapnia the body tries to compensate for the increased CO_2 content in the inhaled air by incrementing the heart's activity, e. g. increased cardiac output [168]. The fact that the heart rate and cardiac output changes are non-significant is not surprising since these readings - together with the stroke volume - were all recorded with the same Nexfin® device.

To address this further the presented HR readings are compared with the ones obtained from ECG data in Figure 7.12. Although these readings show slight differences, e. g. a median HR decrease in the 50° position, these changes are not statistically significant with respect to the baseline and the IQRs are overlapping between both devices. In total, the HR averages support each other.

5 Please refer also to Section 3.2.4 and [70] for further details.

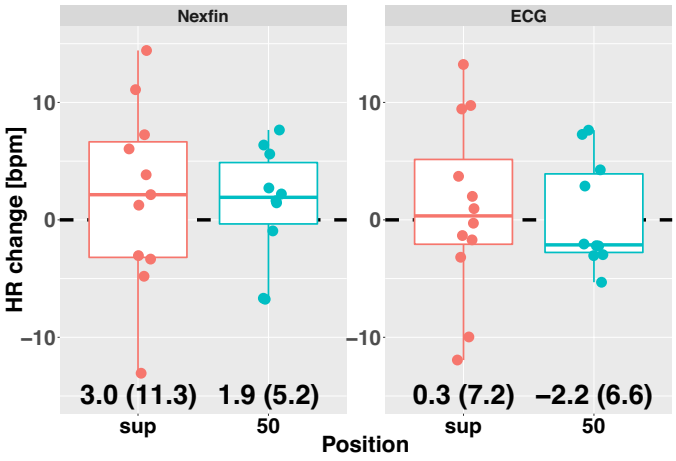

Figure 7.12: Heart rate changes during hypercapnia in two subject positions taken with the Nexfin® device and from ECG recordings. The baseline is marked by the black dashed line.

7.4.5 *Hyperventilation*

The rCBF values in both positions increase in response to HV. The challenges in both positions were valid for all subjects, maintaining the $EtCO_2$ below the desired individual drop of 15 mmHg throughout the challenge. This supports the validity of the acquired data from the physiological point of view. The data does not point towards a significant position influence in this manoeuver. Nonetheless, it is noteworthy, that the supine value ($rCBF_{supine}$ = 8.01 ± 6.75 %) is only half of the recorded rCBF at 50° ($rCBF_{50°}$ 15.20 ± 8.56 %). There might still be a position dependence in HV, but due to its observed adverse effect on the rCBF and the rather strong variation in readings, this could be unobservable in this population.

The increased HR during HV, observable in both positions, leads to an increased CO, while maintaining the SV around the baseline values. The HR increase might furthermore indicate a possible exercising condition for the volunteer related to the active hyperventilation they were asked to carry out.

Changes in the HR as recorded by ECG do not show statistically significant changes with respect to the baseline, as such these readings do not support the exercising hypothesis. Nonetheless, on an individual subject basis HR increases are seen as well, which might still show a subject-dependent response to the active hyperventilation.

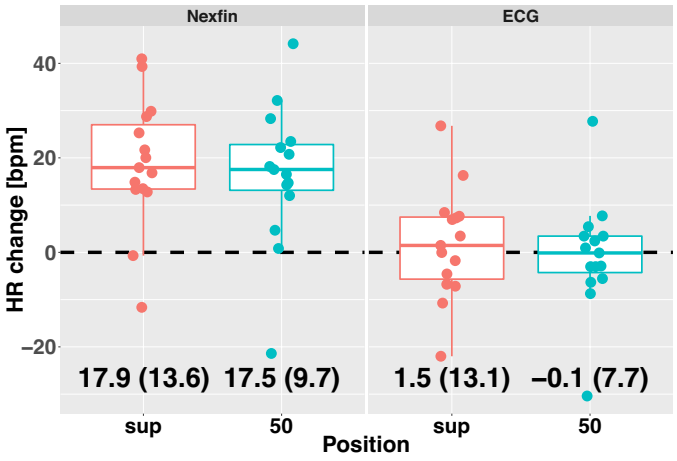

Figure 7.13: Heart rate changes during hyperventilation in two subject positions taken with the Nexfin® device and from ECG recordings. The baseline is marked by the black dashed line.

The observable slight increases in both oxygen saturation values (SpO_2 and $SrO_{2,\,arm}$) are intelligible by a shift in the oxygen-hemoglobin dissociation curve to the left, as it was described in Chapter 3. The blood's pH increases due to the lower $PaCO_2$ leading to the mentioned shift. In consequence, higher oxygen saturation levels can be reached.

We do not expect to see an increase in CBF in response to HV, as the reduced arterial partial pressure of carbon dioxide ($PaCO_2$), which is intended by this challenge, leads to vasoconstriction [305, 257, 48, 343, 256, 130, 181]. A condition under which $PaCO_2$ is reduced is also referred to as hypocapnia - as opposed to HRC - and is provoked by HV. Differences between active and passive HV were observed previously, showing stronger CBF decreases when the volunteer performed a passive HV [165]. The data acquired according to the measurement protocol for HV of this study is either the result of a hypocapnia and an additional effect, such as imposed exercise, which causes CBF to increase in some cases or subject to motion or activation artefacts induced by head movements or increased concentration of the volunteer to correctly execute the manoeuver. Such effects on the hypocapnic CBF might explain the above-mentioned differences between actively and passively conducted HV and have been discussed previously [150, 176]. For these aspects please refer to Chapter 8, which investigates these unexpected results in a more detailed manner.

It shall be noted, that there are indications of CBF increases being related to a non-intact coupling between $PaCO_2$ in the body and in the brain [108]. Previous data obtained with a combined NIRS/US device for non-invasive monitoring of the capillary oxygen saturation and CBF (CerOx®, Ornim Medical Ltd, Israel) also revealed an increasing CBF during HV [193].

7.4.6 *Hyperoxia*

The CBF changes in the microvasculature during HO are similar between positions ($rCBF_{supine}$ = -9.98 ± 2.17 % compared to $rCBF_{50°}$ = -9.24 ± 2.79) and do not indicate any position dependence. The statistically significant difference for $CBFV_{mean}$ between the supine and 50° position in response to HO is likely to be caused by the subjects with a $CBFV_{mean}$ increase in the 50° sitting position. This is surprising, but might be related to the operator dependence of TCD, i. e. the correct placement of the probe at the insonation window and the angle the ultrasound waves enter the tissue. In consequence, this might also explain the non-existence of significant correlations between micro- and macrovasculature, i. e. rCBF and relative CBFV. In general, a CBF decreasing effect in HO caused by a direct vasoconstricting effect of the partial pressure of oxygen and an indirect one caused by the altered arterial partial pressure of carbon dioxide [176] due to an increased $InspO_2$ is expected and was discussed in Sections 3.1 and 3.2.3.

High O_2 levels could be reached as confirmed by the significant changes in $ExpO_2$. Non-significant SV changes are expected due to the non-exercising nature compared to the other two respiratory manoeuvres. In fact, the heart rate in 50° even decreases significantly during hyperoxia, illustrating the relaxing effect of this manoeuvre. The peripheral arterial oxygen saturation (SpO_2) increases significantly in both positions as does the regional oxygen saturation (SrO_2) in the supine position, which is directly related to the increased PO_2 as seen in the oxygen-hemoglobin dissociation curve (3.2). Moreover, SrO_2 in the 50° position increased in response to hyperoxia, although this was not statistically significant.

7.4.7 *Effect of subject positioning*

Notable differences between positions in response to the respiratory challenges were seen, however these differences were not statistically significant. It is likely that the sitting position is not a confounding factor in these awake volunteers, however, this can not be concluded definitively. This is noteworthy since the complications associated with general anesthesia in the sitting position, which have been reported can cause the alteration in the partial pressure of oxygen and CO_2. This suggests that the reported increased incidence rates of venous air embolism (VAE), upper airway obstruction or paradoxical air embolism associated with general anesthesia in the sitting position [238, 22, 281, 137, 86, 338, 190, 203] can not be explained by the bare usage of the respiratory manoeuvres presented here. A possible explanation could be combination of these manoeuvres with general anesthesia.

7.5 CONCLUSION

Although the fitted mean responses to HRC and HV appear to be different in each position, no significant influences of position on the CBF response to HO, HRC and HV were found. This would mean, that the bare effect of change in arterial partial pressure of carbon dioxide and/or oxygen is stronger than any influence induced by position.

This chapter has shown that an optical device is able to measure CBF changes due to position changes and manoeuvers, that these compare to previous findings and that subject positioning in unanesthesized subjects does not seem to have an effect, although we know that head-of-bed position affects CBF. The results from the HV challenges showing some CBF increases require further investigation (see Chapter 8). However, it is worth noting that other studies have found positive rCBF changes during hyperventilation [193, 108].

It is possible that conducting the same study with subjects under general anesthesia and pulmonary volume-controlled ventilation would reveal a significant position dependence on CBF. Information on brain metabolism would provide further insight on the underlying physiology and in Chapter 6, we have shown that brain metabolism ($CMRO_2$) during general anesthesia can be estimated by the presented hybrid device.

8

CEREBRAL HEMODYNAMIC RESPONSES TO HYPERVENTILATION

In Chapter 7 we used diffuse correlation spectroscopy (DCS) to measure cerebral blood flow (CBF) and saw different rCBF responses to the hyperventilation (HV) challenge. There are some subjects, which respond in the expected way with a decrease in relative cerebral blood flow (rCBF), and other subjects whose response is just the opposite, a rCBF increase. It appears that there are two subgroups in our subject population, "positive" and "negative" responders. In this chapter this phenomena will be further investigated by comparing the rCBF results to the cerebral blood flow velocity (CBFV) obtained using transcraneal Doppler (TCD) and presenting data from sixteen additional subjects who underwent a hyperventilation (HV) challenge.

8.0.1 *Background: Why does cerebral blood flow increase during hyperventilation?*

There are different rCBF responses to HV observed in Section 7.3.2.2. We saw rCBF decreases as well as increases during HV (see also Figure 7.11). In Figure 8.1 representative evolutions of rCBF are shown in blue. The rCBF changes, which are representatively shown in Figure 7.11 (ID # 4 from the population presented in Chapter 7) are unexpected, since HV is used with the intention of reducing arterial partial pressure of carbon dioxide ($PaCO_2$), thus leading to a vasoconstriction and therefore a reduction in cerebral blood flow (CBF) (see 3.8). This is why the HV challenge is often considered as the counterpart to hypercapnia (HRC) and therefore referred to as hypocapnia (HOC).

For further investigation of this phenomenon, the HV challenge was conducted on additional healthy volunteers, who

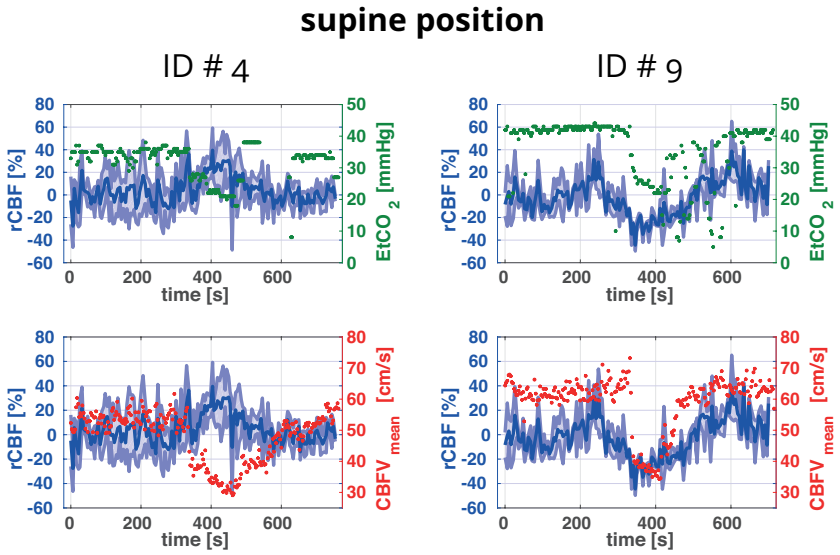

Figure 8.1: **Hyperventilation response groups:** The rCBF changes in blue with their standard deviations represented by the shaded areas together with the absolute $EtCO_2$ (top graph) and mean CBFV (bottom) evolution over time. Graphs on the left show a subject with rCBF increases during the HV and the ones on the right refer to a subject which shows rCBF decreases in response to HV.

were measured using the hybrid TRS/DCS device, presented in Chapter 4.

8.1 PROTOCOL

In total, thirty-one subjects are included in the presented dataset. Based on the exclusion criteria (non-smokers, absence of pathologies, no nervous system activator in the measurement preceding eight hours), fifteen volunteers (referred to as cohort 1) signed an informed consent and were recruited under the protocol approved by the ethical committee of Hospital Clínic in Barcelona (CEIC - Comité Ético de Investigación Clínica del Hospital Clínic de Barcelona). These volunteers are the same ones as presented in Chapter 7. The additional sixteen subjects (cohort 2) were measured at ICFO. These signed an informed consent which was approved by the ethical committee of Hospital Clínic in Barcelona (CEIC - Comité Ético de Investigación Clínica del Hospital Clínic de Barcelona). The measurements were conducted according to the principles of the Declaration of Helsinki.
In addition to the thirty-one subjects, additional subjects were

recruited under the same protocol as cohort 2 to qualitatively address questions, which arose from our data. These results are presented in the discussion (Section 8.3.1).

8.1.1 *Clinical data*

The measured parameters - apart from the blood flow index (BFI) - were heart rate (HR), diastolic, systolic and mean arterial blood pressure (BP_{dia}, BP_{sys}, and MAP, respectively). These were recorded by a Nexfin device (BMEYE®, Amsterdam, The Netherlands) for cohort 1 and a FINAPRES monitor (FINAPRES®, Amsterdam, The Netherlands) for cohort 2. A standard pulseoximeter provided measurements of the peripheral arterial oxygen saturation (SpO_2). The $EtCO_2$ recordings were provided by a respiratory monitor (Julian®, Dräger Medical, Lübeck, Germany or Capnostream 20®, Medtronic, Dublin, Ireland; cohort 1 and 2 respectively). Similar to the HV results presented in Chapter 7, the data for the first cohort of volunteers (n = 15) contains further parameters which are listed in Section 7.2.1.7.2. In this cohort, the macrovasculatory CBFV (diastolic, systolic and mean) measures were taken by a TCD device (Intraview®, Rimed, Tel Aviv, Israel) and calculated using the relation 7.1.

8.1.2 *Diffuse optical device*

The DCS monitor recorded the BF in the microvasculature on frontal lobes of subjects in cohort 1 and 2. On the latter, TRS acquired absorption and scattering data (μ_a and μ_s'), which was used to calculate THC and StO_2. The fiber tips were incorporated in a black head strap (see Figure 7.3) at a source-detector separation of 25 mm.

8.1.3 *Hyperventilation protocol*

As mentioned in Section 7.2, the HV challenge was defined to consist of a pre- and post-baseline and HV was supposed to be carried out at respiration rate (RR) of 20 min^{-1} for 1 min (see Fig 8.2).

There was a slight difference between protocols for cohorts 1 and 2 in regards to the duration of the post-baseline:

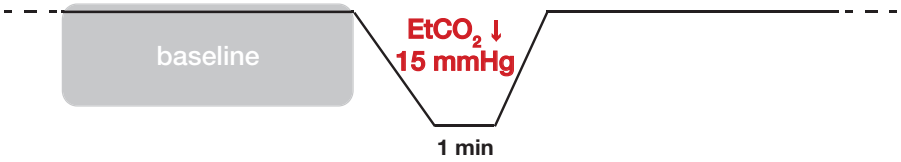

Figure 8.2: Protocol for hyperventilation (HV)

Cohort I: 5 min *pre*-baseline, 1 min challenge, **5 min** *post*-baseline
Metronome rate ∼ 40 min^{-1}
$EtCO_2$ ↓ 15 mmHg

Cohort II: 5 min *pre*-baseline, 1 min challenge, **3 min** *post*-baseline
Metronome rate ∼ 40 min^{-1}
$EtCO_2$ ↓ 15 mmHg

Since the measurements of the second cohort of volunteers were carried out in supine position, only the results from the HV challenge in that position presented in Chapter 7 (cohort 1) are included in the analysis here.

8.1.4 *Data analysis*

From the calculated intensity autocorrelations for different delay times $g_2(\tau)$ we determined the mode parameter (β) and calculated the normalized electrical field autocorrelation function (g_1) using the Siegert relation $g_2 = (1 + \beta\, g_1)^{1/2}$ [183] (see also Section 2.6). The semi-infinite homogeneous medium solution of the correlation diffusion equation as described in Section 2.3.3 and [94] was fitted to the calculated g_1 in order retrieve the particle Brownian diffusion coefficient (D_b) from each curve. Data from different detectors placed at the same forefront was averaged and the αD_b is reported as a BFI. The according semi-infinite medium solution for the reflectance [240] was convoluted with the instrument response function (IRF) and fitted to the recorded distribution time of flight (DTOF) curve in order to retrieve the μ_a and μ_s' values. For details please refer to Chapter 2.

Assuming a water content of 77 % and a negligible lipid content, the derived μ_a and μ_s' values were turned into THC and StO_2 using the extinction coefficients for Hb, HbO_2 and

water from [253, 132].

The values during the initial baseline (see Figure 8.2) were taken as a reference used for the calculation of relative and absolute changes. The entire study population, including both cohorts is separated into two groups based on their rCBF response and Mann-Whitney-Wilcoxon tests on the difference between these groups were performed within R [255]. All reported values reflect the respective median and inter-quartile range (IQR), unless stated otherwise. In all statistical tests, "p-values" of less than 0.05 were considered statistically significant to reject the null hypothesis.

8.2 RESULTS

Thirty-one subjects (eleven females and twenty males) were included in the study population. These consist of the fifteen subjects from the measurements presented in Chapter 7 (cohort 1) and sixteen additional volunteers (cohort 2). The entire population's average age, height, weight and body mass index (BMI) is presented in Table 8.1.

	Age [yrs]	Weight* [kg]	Height* [cm]	BMI* [kg/m²]
All	34.2 ± 8.3	72.3 ± 12.2	173.1 ± 8.7	24.0 ± 2.9
Females	*31.2 ± 8.5*	*60.5 ± 8.3*	*164.4 ± 5.5*	*22.4 ± 2.4*
Males	*35.9 ± 7.9*	*78.8 ± 8.6*	*178.0 ± 5.9*	*24.9 ± 2.8*

Table 8.1: Demographic parameters: The demographic parameters of the population given as mean ± their standard deviation. * denotes a statistically significant difference between females and males (t-test, $p < 0.05$).

Since no significant differences between brain hemispheres were observed ($p > 0.05$), only the results of the left hemisphere are presented here for clarity. Based on the rCBF responses, the data is separated into the two possible groups ("rCBF increasers" and "rCBF decreasers") and plotted accordingly for parameters recorded in the two cohorts. This division into two groups is based only on the positive and negative rCBF changes during the challenge in each position. The (grouped) boxplot representations are presented in the same way as in Chapter 7 and can be seen in Figure 8.3 for rCBF, $rCBFV_{mean}$, total hemoglobin concentration (rTHC) and tissue

oxygen saturation (ΔStO_2). It must be noted, that CBFV was only measured in cohort 1, while in cohort 2 also the microvascular THC and StO_2 changes were recorded.

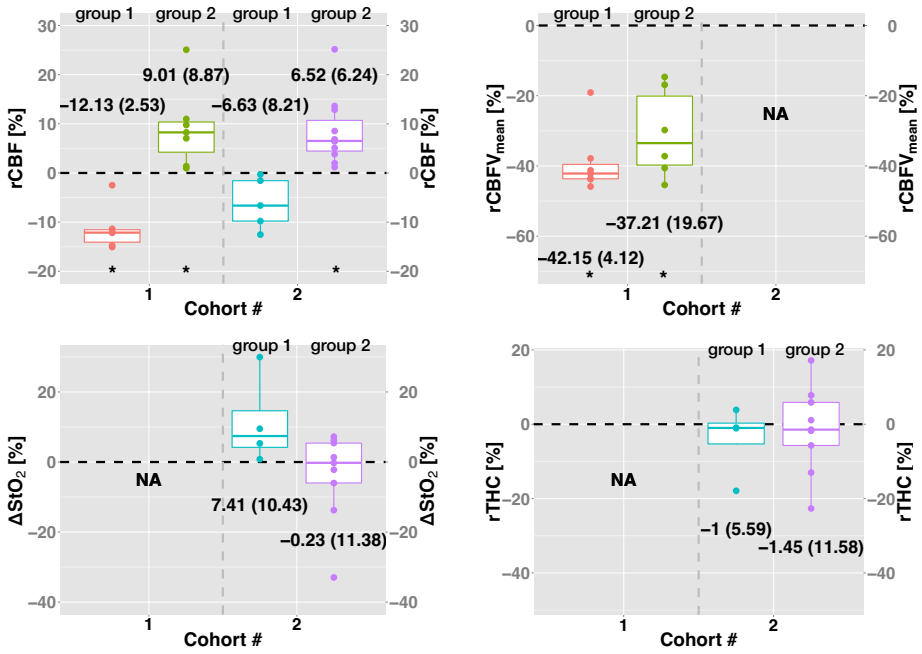

Figure 8.3: Shown are the relative microvascular cerebral blood flow (CBF), total hemoglobin concentration (THC) and absolute tissue oxygen saturation (StO_2) changes together with the relative mean macrovascular cerebral blood flow velocity ($CBFV_{mean}$) change. Data is separated by challenge response. Group 1 represents the subjects with a rCBF decrease, while group 2 refers to subjects with a rCBF increase during HV. Statistically significant changes (Mann-Whitney-Wilcoxon test, $p < 0.05$) are marked by *. The baseline is marked by the black dashed line.

The subjects with rCBF decreases have a median (IQR) of -12.13 (2.53) % in cohort 1 and -6.63 (8.21) % in cohort 2, while the second group shows rCBF increases of 9.01 (8.87) % and 6.52 (6.24) % for respective cohorts. The $CBFV_{mean}$ changes recorded in the first cohort in both groups are negative with -42.15 (4.12) % for group 1 and -37.21 (19.67) % for group 2. From the TRS data analysis extracted StO_2 and THC changes in the second cohort set to ΔStO_2 = 7.41 (10.43) % (group 1), ΔStO_2 = -0.23 (11.38) % (group 2), rTHC = -1.00 (5.59) % and rTHC = -1.45 (11.58) %. Apart from the rCBF values, there is no significant difference between groups according to a Mann-

Whitney-Wilcoxon test.

The ΔHR, ΔMAP, ΔSpO_2 and ΔCO values during the HV challenge with respect to the baseline (see Section 8.1) are shown in Figure 8.4.

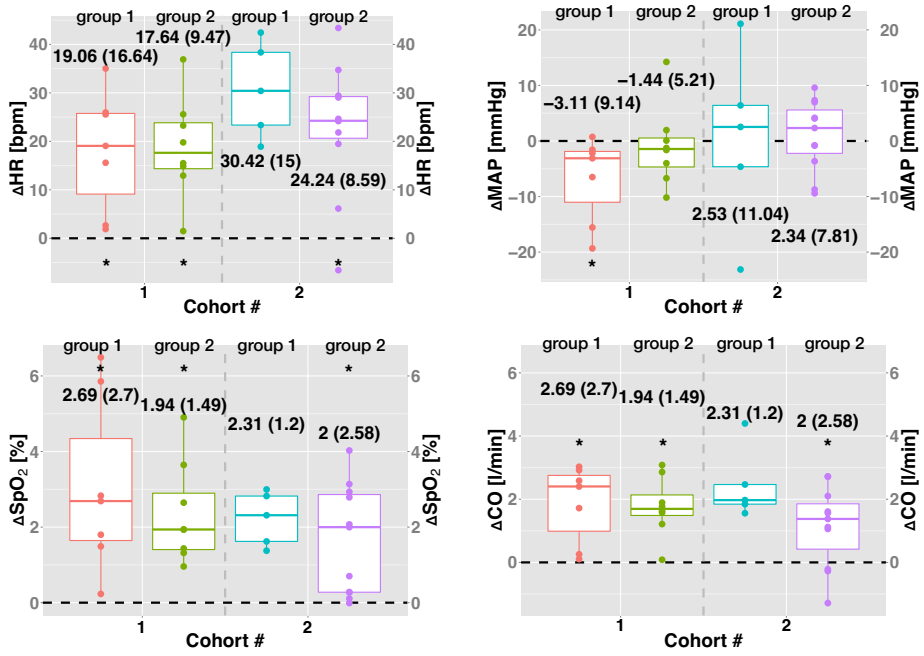

Figure 8.4: Absolute changes of heart rate (HR), mean arterial pressure (MAP), peripheral arterial oxygen saturation (SpO_2) and cardiac output (CO) separated by subject positions and challenge response. Group 1 represents the subjects with a rCBF increase, while group 2 contains subjects with rCBF decrease during HV. Statistically significant changes (Mann-Whitney-Wilcoxon test, $p < 0.05$) are marked by *. The baseline is marked by the black dashed line.

As before, the data is separated by cohorts and based on rCBF response. The boxes to the left of each cohort refer to subjects with a rCBF increase during HV (group 1), while the boxes to the left of each cohort contain subjects with rCBF decrease (group 2). Apart from MAP, all changes are positive with an increase in HR of 19.06 (16.64) bpm in group 1 and 17.64 (9.47) bpm in group 2 for the first cohort of volunteers. In the second cohort, HR increases of 30.42 (15.0) bpm in group 1 and of 24.24 (8.59) bpm in group 2 were recorded. The MAP changes in the first cohort are negative with -3.11 (9.14) mmHg and -1.44 (5.21) mmHg for groups 1 and 2 respectively, while in the second cohort MAP increases by 2.53

(11.04) mmHg in group 1 and by 2.34 (7.81) mmHg in group 2. The ΔSpO_2 values in cohort 1 range from 2.69 (2.70) % (group 1) to 1.94 (1.49) % (group 2) and in the second cohort from 2.31 (1.20) % (group 1) to 2.00 (2.58) %. Groups 1 and 2 also show increases in CO in both cohorts. These values are 2.69 (2.70) l/min (group 1, cohort 1), 1.94 (1.49) l/min (group 1, cohort 1), 2.31 (1.20) l/min (group 1, cohort 2) and 2.00 (2.58) l/min (group 2, cohort 2). A Mann-Whitney-Wilcoxon test was used and showed no significant difference between groups in any of the variables presented here.

8.3 DISCUSSION

Adding further microvascular CBF data recorded from hyperventilating subjects to the existing data set presented in chapter 7 allowed also to check the reproducibility of our previous results and served to increase the total study population. An additional sixteen subjects were included and responses to HV were measured. Further information could be collected by adding the TRS modality and thus estimating hemoglobin concentrations in the brain during the challenge. Unfortunately, CBFV data could not be recorded in the second cohort of volunteers due to the lack of a TCD device. The drop in $PaCO_2$ was induced by having each volunteer increase their RR to a specific metronome frequency. The goal was to decrease $EtCO_2$ by 15 mmHg and to continue in this condition for 1 min.

The results from chapter 7 were able to be reproduced as the presence of two distinct groups in response to HV were also observed in the second cohort of healthy volunteers. The rCBF decreases range from -12.13 (2.53) % in cohort 1 to -6.63 (8.21) % in cohort 2. Group number 2 shows rCBF increases of 9.01 (8.87) % (cohort 1) and 6.52 (6.24) % (cohort 2), which are comparable between cohorts (no statistically significant difference was found).

None of the other physiological parameters (macrovascular CBFV, HR, MAP, SpO_2 or CO) suggested the existence of distinct subject groups. Furthermore, tendencies in these parameters are similar, i. e. HRs, SpO_2s and COs all increase during active HV and are comparable to reported changes in the literature [193]. The observed HR increase might also

include a possible exercising effect, which could have been introduced by the active hyperventilation. The recorded CO increase gives further support to this point. The CBFV in group 1 ($CBFV_{mean}$ = -42.15 (4.12) %) shows a slightly larger decrease as compared to group 2 ($CBFV_{mean}$ = -37.21 (19.67) %), but this difference was not found to be statistically significant ($p > 0.05$). Nonetheless, this might point towards the existence of two groups in active HV and additional CBFV measurements could provide further information.

In general, a decrease in CBF is expected due to the HOC effect of HV. The reduction of $PaCO_2$ induced by an increased RR leads a lower blood pH, which in turn causes the oxygen-hemoglobin dissociation curve to shift to the left, thus increasing the oxygen affinity. Furthermore, the blood vessels constrict which causes a decrease in CBF [305, 7, 48, 343, 256, 130, 181]. This was discussed in Chapter 3 and HV is used in the clinic during general anesthesia for that purpose.

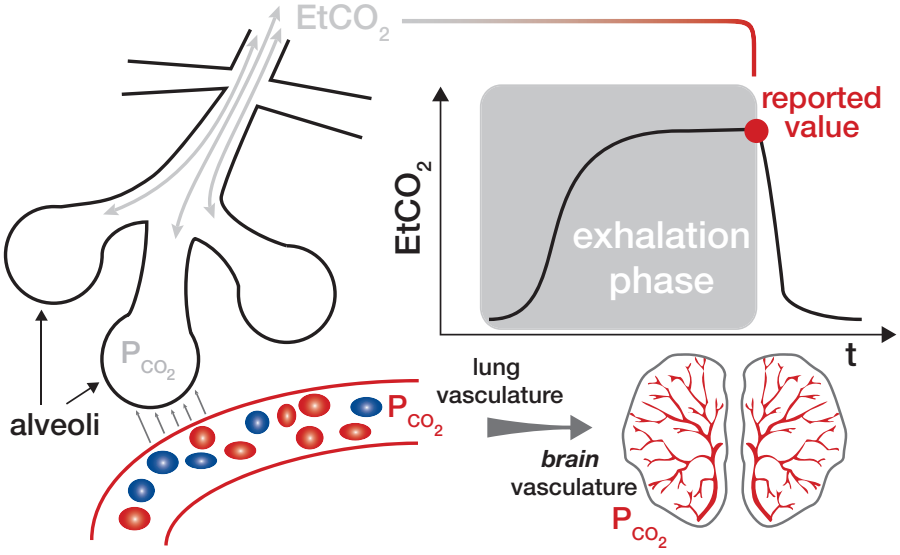

Figure 8.5: Inhaled air reaches the lungs and the alveoli. Gas exchange between them and the blood happens through diffusion along a gradient in partial pressures. The $PaCO_2$ in the blood depends on the $PaCO_2$ in the alveolus. Partial pressure differences between different locations in the body could lead to different $PaCO_2$s between the lung and brain blood vasculature.

However, there are reports of CBF increases in response to increased RR. Lund et al. [193] used a CerOx® monitor

(Ornim Medical Ltd, Israel), which combines NIRS and US for non-invasive monitoring of ScO_2 and CBF, and observed a 9 % (median) increase in the CBF index. In a study of cerebrovascular response during rowing Faull et al. [108] state that the observed CBF increases in response to the higher RR could be explained by a mismatch between the measured $EtCO_2$ and the actual $PaCO_2$ in the brain. While the $EtCO_2$ drops during short frequent breaths, $PaCO_2$ might not be affected and therefore may lead to an unexpected response to HV.

In the measurements presented in this and the preceding chapter, we rely on the $EtCO_2$ readings in order to initiate the 1 min duration once the volunteer has reached the desired $EtCO_2$ level, e. g. after a 15 mmHg drop in $EtCO_2$ has occurred, thus assuming that the volunteer is purely hypocapnic. In fact, we are measuring $EtCO_2$, which only can give a rough estimation of the blood's $PaCO_2$. This point is schematically illustrated in Figure 8.5. It gives an idea of the relation between $EtCO_2$ and $PaCO_2$ in the blood. The $EtCO_2$ reading is the maximum peak of the exhalation curve. Depending on the depth of the respiration, this might not entirely reflect the lung gas mixture. If there is a difference between $PaCO_2$ in the blood and the lung alveoli this will present an additional confounding factor. Furthermore, we measure the cerebral response, which is a result of changes in $PaCO_2$ in the brain and could be different from the changes in $PaCO_2$ in the blood near the lungs [108]. Nonetheless, it seems that in our measurements the microvasculature reacts differently from the macrovasculature.

Two confounding factors that could be influencing our data are motion artefacts and the patient concentration needed to adjust breathing to the metronome rhythm. We qualitatively address these points in the next section.

8.3.1 *Clicking task and motion artefacts*

The data may suggest, that the adjustment of RR to the rate of the metronome causes the blood vessels to dilate at the microvascular level in the brain in some subjects to react differently than at the macrovascular level. The effect of an imposed (motor) exercise could counteract the vasoconstricting effect and therefore lead to a CBF increase [150, 176]. In order to test this, we conducted further measurements on an additional five subjects (ID # 32 - 36). These measurements were

conducted under the same protocols and the subjects signed the same informed consent as the second cohort presented in Section 8.1. The volunteers were asked to concentrate on a rhythmic sound similar to the one from the metronome. The rhythm was set to 40 tones per minute with ± 0.5 second variations to avoid habituation of the subject to the signal. With each sound the volunteer was asked to click a keyboard button in order to mimic to the action chain (listen → act). DCS was used to record CBF changes during this procedure.

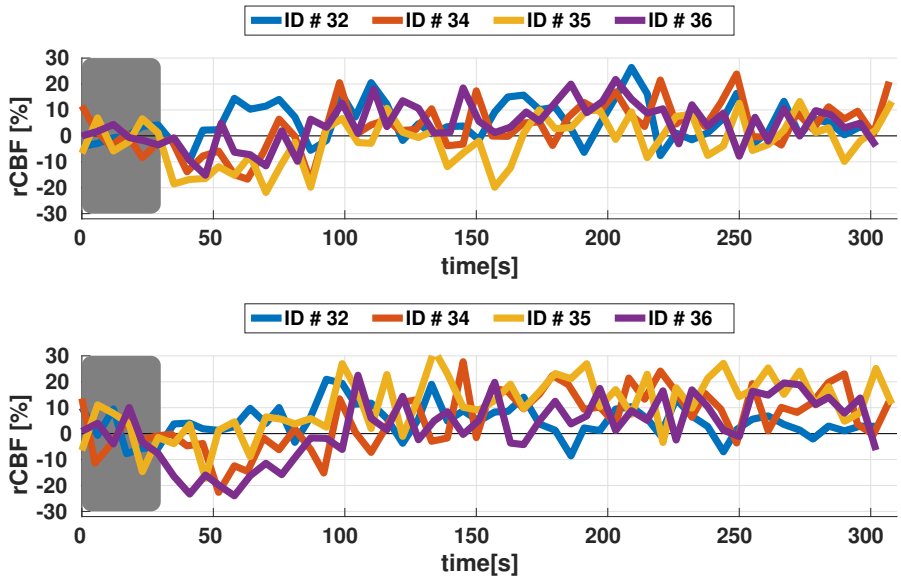

Figure 8.6: rCBF response to a simple clicking task. Top graph: left brain hemisphere, bottom graph: right brain hemisphere. The grey region represents the baseline (first 30 s).

The exercise started after a 30 s baseline and lasted 3 min. In Figure 8.6 the data is shown for four subjects. The volunteer ID # 33 was excluded due to not completing the task according to the protocol. We observe slight increases between 10 - 20 % after approximately 80 s of exercise, after an initial decrease (5 - 20 %). This suggests that there was no corruption of our signal due to concentration-induced microvascular CBF changes as a result of the subject acting on the marked rhythm by metronome.

As an additional check for motion artefacts, which may introduce rCBF increases, we asked the additional volunteers who performed the clicking task to nod their head for 1 min after an initial baseline. The timing was chosen in order to

replicate the HV duration as presented in Section 8.1. The head nod did not show any changes, effectively eliminating motion artefacts as the possible cause of the adverse rCBF results during HV.

8.3.2 *Altered hyperventilation*

A milder HV was conducted on a further six subjects (ID # 37 - 42) with the same RR as in the standard HV (20 min^{-1}), as well as with twice the RR (40 min^{-1}) in two of them (ID # 41 - 42). Here, the volunteers were asked to simply adjust their RR to the metronome and not to focus on reaching a specific $EtCO_2$ drop. This aims to remove a possible effect associated with the patient's effort by focusing on achieving the defined $EtCO_2$ drop and therefore the forced usage of the entire lung volume. For that reason, we did not control the $EtCO_2$, but only focused on having the subject adjust RR to the metronome. Only DCS data was acquired in these subjects. The rCBF responses of ID # 41 and 42 - the subjects with the doubled RR - are presented in Figure 8.7.

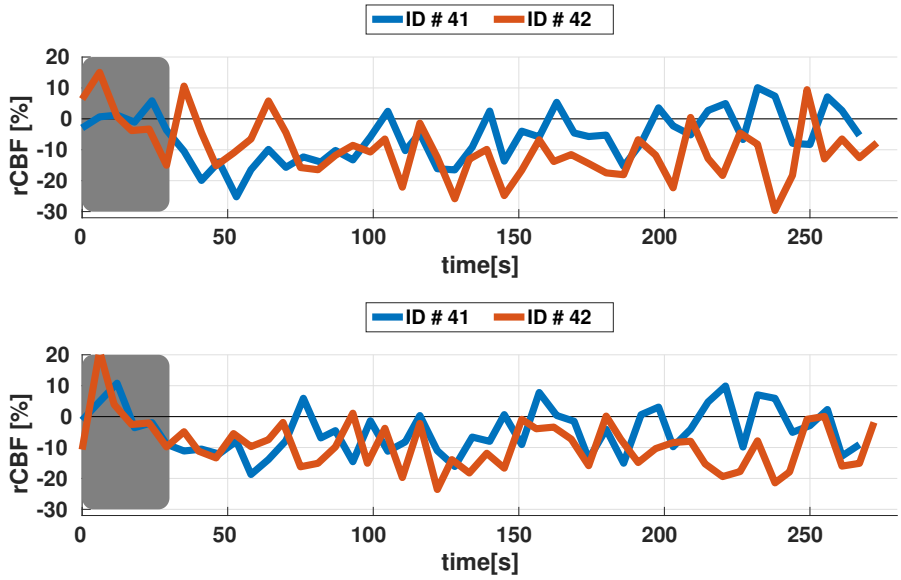

Figure 8.7: rCBF response from two subjects to HV at twice the RR as presented in Section 8.1.3. Top graph: left brain hemisphere, bottom graph: right brain hemisphere. The grey region represents the baseline (first 30 s).

While the first HV in these volunteers at the RR as presented in Section 8.1.3 without the use of the $EtCO_2$ criterion did not show any notable changes in CBF, in the two sub-

jects (ID # 41 and 42), who were also asked to hyperventilate at a further increased RR (twice the rate as before), CBF decreases could be observed. It should be noted, that these measurements only provide a qualitative check to address the questions of whether the task and/or exercise of adjusting your RR to a sound you hear and to reach a specific $EtCO_2$ threshold ($\Delta EtCO_2$ = -15 mmHg) could provoke a CBF increase, whose effect is stronger than the HV effect.

8.4 CONCLUSION

The additional CBF measurements recorded here also support the existence of two groups. Other physiological parameters did not show two groups. Further measurements, recording CBF with a DCS device during milder HV, as well as the clicking task in order to simulate a possible activation of the frontal lobe regions, do not suggest that either one or the other acts as a confounding factor. Data from an active HV with a doubled RR points towards an influence of the HV level, i. e. if the subjects are asked to reach the defined $EtCO_2$ level ($\Delta EtCO_2$ = -15 mmHg from the baseline), this invokes an exercising effect which is stronger than the one intended by the HV. This effect might be stronger in some (less-trained) volunteers, thus causing the recorded microvascular CBF increase in response to active HV. It is nonetheless noteworthy that in the first cohort we saw significant CBFV decreases in all subjects, while the microvascular rCBF only showed this in some (group 1). None of the other clinical parameters indicate a possible systemic effect. The fact that we were able to reproduce the microvascular changes in CBF recorded by DCS in a second cohort strongly supports the validity of the measurements. The work presented here gives further support to the existence of two groups in terms of microvascular CBF changes. However, varying the level of active HV (smaller and bigger $EtCO_2$ drops) and varying the RR while simultaneously recording macrovascular CBFV data may be interesting for further investigation of cerebrovascular resistance in active HV.

9

IS IT A MAJOR MISTAKE TO CALCULATE CEREBRAL BLOOD FLOW IN RESPONSE TO HEAD-OF-BED WITHOUT A HYBRID DEVICE?

This chapter focuses on one possible advantage, that can come out an hybridization of the two diffuse optical modalities TRS and DCS in *in-vivo* measurements. The assumption here is, that through a better estimation of optical properties by TRS the DCS analysis can more accurately estimate the information on blood flow. The work presented here is made possible by Hospital Clínic in Barcelona and the correspondent ethical committee in collaboration with ICFO.

9.1 INTRODUCTION

It is known that relative cerebral blood flow (rCBF) derived from diffuse correlation spectroscopy (DCS) measurements changes by so-called head-of-bed (HOB) manoeuvres [90, 109, 171, 170, 98, 44, 97]. These manoeuvres consist of an alteration of the subject's bed inclination. In healthy patients a lowering of the HOB angle leads to an increase in microvascular cerebral blood flow (CBF) [98]. HOB angle changes are used to evaluate cerebrovascular resistance (CVR) and brain health in traumatic brain injury (TBI) and stroke patients [23, 109, 171, 12, 170, 11, 97, 332, 274].

From DCS measurements a so-called blood flow index (BFI) is reported. It is a result of calculating the normalized electrical field autocorrelation function (g_1) from the normalized intensity autocorrelation function (g_2) (see Equation 2.23) and fitting a Brownian diffusion model ($<\Delta r^2(\tau)> = 6\ D_b\ \tau$) to the calculated normalized electrical field autocorrelation function (g_1) (see Equations 2.17 and 2.25)). The details are explained in

Sections 2.4, 2.6 and 4.1.3. The electrical field autocorrelation decay factor (K) in Equation 2.17 is defined as:

$$K(\tau) = \sqrt{3\,\mu_a\,\mu_s' + k_0^2\,\alpha\,\mu_s'^2\,\underbrace{\langle \Delta r^2(\tau)\rangle}_{6\,D_b\,\tau}} \tag{9.1}$$

For the mean-square displacement $<\Delta r^2(\tau)>$, it was found empirically to be best expressed by $<\Delta r^2(\tau)> = 6\,D_b\,\tau$ [321, 90, 262, 94, 89, 56, 27]. BFI is then defined as $BFI = \alpha D_b$, with α representing the fraction of moving scatterers and D_b the particle Brownian diffusion coefficient. In HOB manoeuvres these are often reported as relative values with respect to a baseline [90, 109, 171, 170, 98, 44, 94, 97]. From Equation 9.1 we see that the model we fit to our DCS data is dependent on the absorption coefficient (μ_a) and reduced scattering coefficient (μ_s'). Their values need to be specified in order to evaluate the data acquired with a DCS system (see Sections 2.3.3 and 2.7.2). A common guess for them is $\mu_a = 0.1\ cm^{-1}$ and $\mu_s' = 10\ cm^{-1}$.

The advantage of combining DCS with time-resolved spectroscopy (TRS) into a hybrid device - as presented in Chapter 4 - is the simultaneous acquisition of μ_a, μ_s' and D_b, which allows a more accurate estimation of the BFI with the TRS-derived μ_a and μ_s' values [149].

One could think of various ways for using μ_a and μ_s' for the DCS evaluation. These range from a general guess over population or subject averaged values to either averaged values over certain episodes of the measurement or even the usage of TRS-derived optical properties for each individual data point taken per subject. It is furthermore an open question, whether the actual relative CBF change due to a HOB sequence depends on the knowledge of the correct μ_a and μ_s'. In this chapter, we aim at answering this question by comparing five different evaluation methods against each other. The comparison is done on the BFI basis as well with the rCBF values in consequence of a HOB angle change in healthy volunteers.

9.2 PROTOCOL

This study, all including procedures and devices were employed according to the protocol ICFO_HCP/2012/1 and each

subject signed an informed consent, both approved by the ethical committee of Hospital Clínic in Barcelona (CEIC - Comité Ético de Investigación Clínica del Hospital Clínic de Barcelona). Moreover, all measurements were carried out in compliance with the principles specified in the Declaration of Helsinki. The exclusion criteria were absence of pathologies, smoking and no diagnosed blood pressure alteration. In consequence, sixteen volunteers were recruited and included in this study. Two hybrid TRS/DCS sensors with a fixed source-detector separation (ρ) of 25 mm were placed on the subject's forehead, one on the left hemisphere and one the right one. Each sensor consists of two source-detector pairs, one for each modality. The TRS setup uses picosecond pulsed laser light at three different wavelengths (λ_1 = 690 nm; λ_2 = 785 nm;λ_3 = 830 nm) and its evaluation yields the absorption (μ_a) and reduced scattering (μ_s') coefficients (for details see Sections 2.5 and 4.2).

While DCS data was recorded for 1800 ms on one hemisphere, each TRS wavelength acquired data for 600 ms on the opposite one. This led to total acquisition time of 3600 ms for all full data set of TRS and DCS data from both hemispheres.

A standard pulseoximeter and a capnograph (Capnostream 20®, Medtronic, Dublin, Ireland) were used to monitor the following parameters: peripheral arterial oxygen saturation (SpO_2), heart rate (HR), RR, $EtCO_2$ and integrated pulmonary index (IPI), which gives a simple indication about the subject's respiratory status in real time. These values were taken for monitoring the volunteer's general health condition throughout the procedure, so that any general potential physiological influence on our data could be ruled out. For the same purpose, the subject's blood pressure (BP_{dia}, BP_{sys} and MAP) was recorded as well (FINAPRES®, Amsterdam, The Netherlands).

The following simple HOB angle change was chosen: 30°→ 0° (or "supine") (see Fig. 9.1).

Each position was kept for five minutes. The interest lies in the resulting BFI values for each position, their relation to one another and behaviour between different evaluation types.

Figure 9.1: HOB protocol sequence: 30°→ 0° (supine).

To that end, the DCS data was evaluated in five different ways. These are:

Method I: fix μ_a at 0.1 cm^{-1} and μ_s' at 10 cm^{-1}

Method II: population (n = 10) average of μ_a and μ_s'

Method III: subject average of μ_a and μ_s' (entire sequence)

Method IV: subject position average of μ_a and μ_s'

Method V: subject individual μ_a and μ_s' per acquisition ("one-to-one")

The first method is a results of the standard guess for μ_a and μ_s' used in the diffuse optics community. Starting with method II we use the TRS information in the DCS analysis and move to subject individualised values for μ_a and μ_s' (method III-V). As the method number increases, we move closer to the real-time μ_a and μ_s' for each subject.

The entire statistical analysis was carried out in R [255]. In order to compare the five analysis methods and their influence on the computed CBF changes LME ("nLME" [244] package in R) models for the subject's HOB angle and different evaluation methods were defined. For the calculation of rCBF, the first HOB (30°) position was set as a baseline (rCBF = 0 %). Fitted values from the LME models are reported as means plus minus their standard errors and models which did not differ significantly from the null model were rejected. Other reported values are median values and their respective interquartile ranges (IQRs). In all models and statistical tests, "p-values" of less than 0.05 were considered statistically significant to reject the null hypothesis.

9.3 RESULTS

A total of sixteen subjects (six females, ten males), whose blood pressures did not change significantly throughout the procedure, were evaluated in five different ways. These differ from each other in the way μ_a and μ_s' are fed into the DCS analysis, as explained in Section 9.2. Table 9.1 shows the study population demographics.

	Age [yrs]	Weight* [kg]	Height* [cm]	BMI [kg/m²]
All	35,8 ± 9.7	72.4 ± 13,4	172.6 ± 9.1	24.2 ± 3.4
Females	*33.5 ± 11.3*	*60.0 ± 8.2*	*162.5 ± 2.5*	*22.7 ± 3.0*
Males	*37.2 ± 9.0*	*79.9 ± 9.9*	*178.6 ± 5.2*	*25.1 ± 3.5*

Table 9.1: Demographic parameters: The demographic parameters of the population given as mean ± their standard deviation. * denotes a statistically significant difference between females and males (t-test, $p < 0.05$).

DCS recorded data did not show significant differences between brain hemispheres, so that for clarity only the results of the left hemisphere are presented here. All statistically significant results are comparable to the right hemisphere, whose results are presented in Section D.

9.3.1 *Blood flow indices upon different usage of optical properties*

The BFI values calculated using the methods explained in Section 9.2 are presented in Figure 9.2. Their median (IQR) values are shown in Table 9.2.

According to Table 9.2, BFI values in the left brain hemisphere obtained with μ_a and μ_s' values of 0.1 cm^{-1} and 10 cm^{-1} (method I) set to median (IQR) values of $BFI_{30°,\,I}$ = 7.19 (2.51) × 10^{-9} cm^2/s and $BFI_{supine,\,I}$ = 9.54 (3.19) × 10^{-9} cm^2/s and the ones for the study averaged μ_a and μ_s' values (method II) to $BFI_{30°,\,II}$ = 6.89 (2.41) × 10^{-9} cm^2/s and $BFI_{supine,\,II}$ = 9.13 (3.08) × 10^{-9} cm^2/s.

For method III, where we used the individualised μ_a and μ_s' values from each subject, the BFI median (IQR) values result in $BFI_{30°,\,III}$ = 6.28 (2.62) × 10^{-9} cm^2/s and $BFI_{supine,\,III}$ = 7.43 (2.74) × 10^{-9} cm^2/s. In methods IV and V we obtain me-

Figure 9.2: Comparing evaluation methods I-V against each other by looking at the BFI.

method #	position	Median BFI (IQR) [cm²/s] × 10^{-9}
I	+30°	7.19 (2.51)
	supine	9.54 (3.19)
II	+30°	6.89 (2.41)
	supine	9.13 (3.08)
III	+30°	6.28 (2.62)
	supine	7.43 (2.74)
IV	+30°	6.19 (3.01)
	supine	7.43 (2.74)
V	+30°	6.23 (2.82)
	supine	7.38 (2.78)

Table 9.2: Medians (and IQR) for the absolute BFI values taken from the left brain hemisphere separated by methods and positions. Data was taken in two positions according to measurement protocol.

dian (IQR) values of $BFI_{30°,\,IV}$ = 6.19 (3.01) × 10^{-9} cm²/s and $BFI_{supine,\,IV}$ = 7.43 (2.74) × 10^{-9} cm²/s and $BFI_{30°,\,V}$ = 6.23 (2.82) × 10^{-9} cm²/s and $BFI_{supine,\,V}$ = 7.38 (2.78) × 10^{-9} cm²/s.

A LME model on method influence[1] revealed a significant difference between the first two methods (I and II) and meth-

1 The fitted intercepts and their slopes are presented in Table D.5.

ods III-V ($p \leq 0.05$). The according p-values are presented in Table 9.3. For better visibility, statistically significant differences between methods are marked by a grey background.

	30° position			
method	I	II	III	IV
II	p > 0.05	-		
III	p < 0.001	p < 0.001	-	
IV	p < 0.001	p < 0.001	p > 0.05	-
V	p < 0.001	p < 0.001	p > 0.05	p > 0.05
	supine position			
II	p > 0.05	-		
III	p < 0.001	p < 0.001	-	
IV	p < 0.001	p < 0.001	p > 0.05	-
V	p < 0.001	p < 0.001	p > 0.05	p > 0.05

Table 9.3: Results (p-values) from a LME model with the method factor for the absolute BFI values. Statistically significance is marked by a grey background.

The top part of Table 9.3 shows the resulting p-values for the comparison of BFI values from the 30° position between methods. The bottom part refers to the same test, but conducting it on the BFI values taken while the volunteers was in the supine position.

All values between positions differ significantly ($p < 0.001$) independently of the used analysis method. The BFIs calculated based on methods I and II differ significantly ($p < 0.05$) from the ones evaluated with method III, IV and V. Between the latter three, no significant difference was found.

9.3.2 *Influence of optical properties on estimated relative cerebral blood flow*

After evaluating BFI according to the five methods as presented in Section 9.2, for each volunteer the 30° position average was taken as a baseline and the CBF change with the HOB angle calculated for each method individually. The resulting rCBF values are shown in Figure 9.3. The graph compares all five methods (I:"fixed"; II: "study average"; III: "subject average"; IV:"subject position average" and V: "one-to-

one" usage of μ_a and μ_s').

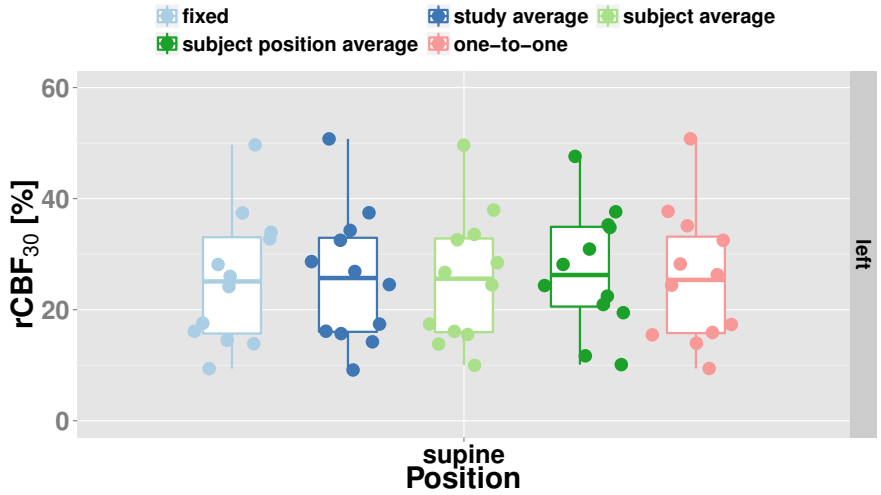

Figure 9.3: Comparing evaluation methods 1-4 against each other by looking at the CBF changes with respect to the 30° position (starting position). The dashed line represents zero CBF change and "left" and "right" label the respective brain hemispheres.

method #	Median $\mathrm{rCBF}_{30°}$ (IQR) %
I	28.14 (26.72)
II	28.67 (27.35)
III	28.47 (27.03)
IV	30.91 (20.94)
V	28.23 (27.63)

Table 9.4: Medians (and IQR) for the relative CBF changes with respect to initial 30° position separated by methods.

Table 9.4 shows the rCBF values in terms of a median and its respective IQR after the change from 30° to supine position for each analysis method and hemisphere. These values set for method I to $\mathrm{rCBF}_{\mathrm{left,\ I}}$ = 28.14 (26.72) % and the ones for the study averaged μ_a and μ_s' values (method II) to $\mathrm{rCBF}_{\mathrm{left,\ II}}$ = 28.67 (27.35) %.

In the case of method III, where we used the individualised μ_a and μ_s' values from each subject, the rCBF median (IQR) values result in $\mathrm{rCBF}_{\mathrm{left,\ III}}$ = 28.47 (27.03) %. In methods IV and V we obtain median (IQR) values of $\mathrm{rCBF}_{\mathrm{left,\ IV}}$ = 30.91 (20.94) %

and $rCBF_{left,\,V}$ = 28.23 (27.63) %.

Similar to the analysis of the BFI values (Section 9.3.1), we employ a LME model to investigate differences between rCBF values among different analysis methods[2]. Here we only compare rCBF in the supine position between the above-presented different analysis methods. The p-values of this investigation are shown in Table 9.5. As before, statistically significant differences between methods are marked by a grey background for better visibility.

method	I	II	III	IV
II	p > 0.05	-		
III	p > 0.05	p > 0.05	-	
IV	p = 0.01	p < 0.05	p < 0.05	-
V	p > 0.05	p > 0.05	p > 0.05	p < 0.05

Table 9.5: Results (p-values) from a LME model with the method factor for the relative CBF values with respect to the initial 30° position. Statistically significance is marked by a grey background.

According to Table 9.5, the rCBF calculated based on method I-III does not differ significantly. Method IV differs significantly ($p \leq 0.05$) from all other ones in the resulting rCBF for a change from 30° to supine position. Values obtained from method V are comparable to method I-III.

9.4 DISCUSSION

The blood flow index (BFI) changes not only with position but also dependent on the analysis method used. The first point has its origin in the orthostatic challenge by changing the head-of-bed (HOB) angle and was reported previously in DCS measurements [90, 109, 171, 170, 98, 44, 97]. Since BFI depends on the optical properties μ_a and μ_s' (see Equation 9.1) and it is not feasible to evaluate all three parameters at the same time from a single measurement [83], we used TRS to gain information on μ_a and μ_s'. Based on the different methods used in analysing DCS data in this Chapter, we obtain BFI values ranging from 6.19 - 7.19 × 10^{-9} cm^2/s in the initial 30° sitting position. In supine these range from 7.38 × 10^{-9}

2 The fitted intercepts and their slopes are presented in Tables D.7 and D.8

cm^2/s to 9.54×10^{-9} cm^2/s. Since these values are dependent on the optical properties, they also vary between study populations. This is reflected in the statistically significant differences found between analysis methods I and II on one side and methods III, IV and V on the other side. Since the later three use subject-specific μ_a and μ_s' values they lead to differences in the BFI compared to methods I and II, where either a general guess of μ_a and μ_s' or their population average was taken.

The majority of DCS work reports relative blood flow measures in terms of rCBF [90, 109, 171, 170, 98, 44, 97]. The data presented here shows rCBF increases of around 28 - 30 % with a HOB angle change from 30° position to supine. Previous work reports changes between 18 % and 25 % [109, 171, 98, 97], with significantly higher responses in male subjects (rCBF = 27.1 %) [98].

This chapter aimed at giving an answer to the specific question whether the previously reported changes in CBF under- or overestimated the actual microvascular rCBF response. The LME models employed to investigate this, found method IV to be significantly different from the other ones. It is the method with the usage of μ_a and μ_s' position averages per subject and therefore taking into account absolute changes in μ_a and μ_s', when moving to the supine position. As mentioned before, μ_a and μ_s' influence BFI. In healthy volunteers only μ_a is imagined to change due to changes in the blood volume, not μ_s'. Along this line, method V should even reflect physiology more correctly, but it is likely that it propagates variations in the optical properties to strongly, thus burying a possibly effect in this crosstalk. Method IV looks therefore like the cleanest and the one closest to physiology. It shall be noted that several studies [195, 278, 46, 98, 346, 97, 282, 92, 300, 115] using DOS estimate μ_a changes using the differential pathlength method, which assumes that the variations in optical properties are small compared to the baseline value [13, 79]. Assuming furthermore a homogeneous distribution across the medium the temporal changes in the optical density can then be related to changes in chromophore concentrations and therefore to variations in Hb and HbO_2. Nonetheless, this method can lead to underestimations similarly to the confounding factors discussed in Section 6.4.3.

9.5 CONCLUSION

A combination time-resolved spectroscopy (TRS) and diffuse correlation spectroscopy (DCS) does not only allow an estimation of cerebral metabolism ($CMRO_2$), but also improves the DCS-derived blood flow index (BFI). The work in this chapter has shown that hybridization of TRS and DCS is advantageous in the estimation of the derived blood flow index (BFI) during a simple head-of-bed (HOB) procedure. Previous work did not rely on a TRS-derived absolute absorption (μ_a) and reduced scattering coefficient (μ_s'). Since BFI is dependent on the optical properties μ_a and μ_s', the absolute, subject specific values should be used in the analysis of DCS data, thus retrieving a BFI which closer reflects physiology. This is expressed by the statistically significant difference of BFI values resulting from method III, IV and V, which used individual subject optical properties, compared to the first two.

In HOB procedures, it appears to be sufficient to use an average of subject specific μ_a and μ_s' independent of HOB angle in order to estimate BFI.

Relative CBF changes are also significantly influenced by the absolute μ_a and μ_s' calculation. Using these values for specific measurement periods leads to a significantly improved rCBF estimation, as expressed by the significant difference of the fourth method. The highest degree of integrating both techniques (DCS and TRS), is the evaluation of BFI with simultaneously acquired μ_a and μ_s' values, as done in analysis method V in this chapter. Improving the SNR in the TRS measurements could reduced a possibly introduced cross-talk in the fifth method and therefore reveal also a significant difference for that method.

Although CBF measures presented in this Chapter lie on the upper range of previously reported values [109, 171, 98, 97], they are within or close to the respective standard errors or standard deviations.

Part III

CONCLUSION

10

SUMMARY

After a general introduction, I discussed the oxygen delivery in the human body, how hemoglobin takes in oxygen and deploys it in the destination region due to different partial pressures of oxygen (PO_2) between the blood and the surrounding tissue. The compartment model was introduced as well as the dependence of oxygen saturation on PO_2 and how their relation is affected by CO_2 via a change in pH. The role of blood flow in oxygen supply to the brain, the differences between the macrovasculature (Circle of Willis) and microvasculature were discussed. I furthermore introduced the concept of cerebral autoregulation, which is the interplay of mean arterial pressure, cerebral perfusion pressure and intracraneal pressure, and their relation to cerebrovascular resistance and cerebral blood flow (CBF). How changes on the arterial partial pressure of carbon dioxide affect these parameters were also introduced and therefore lay the groundwork for the respiratory challenges in Chapters 7 and 8.

How hybrid diffuse optics, whose concepts have been discussed in Chapter 3, can be used to estimate the cerebral metabolism was explained. In Chapter 6, this was shown using a constructed hybrid setup. This instrument was explained and characterised in Chapter 4 and the physical basics for this device were introduced in Chapter 2.

The mentioned hybrid setup was also used in further measurements with probes placed on the human forehead brain, similar to the study presented in Chapter 6, in order to investigate the responses of CBF to changes in the inhaled gas contents (Chapter 7). For this purpose the volunteer's end-tidal CO_2 was either in- or decreased by a specific amount. These effects where achieved by challenges called hypercapnia or hyperventilation and either in- or decreased CBF. A third one consisted of an increasing the amount of exhaled O_2 and thus decreasing CBF. All three challenges were conducted in two positions (supine and 50°) in order investigate possible microvascular position dependencies in order to help understand increased incidence rates of complications during surgeries associated with the sitting position.

Since the response to hyperventilation showed unexpected positive changes in CBF, which only few people reported earlier [193, 108], this challenge was repeated in additional subjects and the results could be reproduced (see Chapter 8). Based on their relative rCBF change, the subjects were separated into two groups ("CBF decreasers" and "CBF increasers") in order look for possible group correlation in other clinical parameters, such as heart rate, mean arterial pressure, cardiac output, etc.. Additional measurements with clicking tasks and head nods could rule out motion artefacts and strong concentration influences, suggesting that the answer lies in the way the hyperventilation was performed. By increasing the breathing rate, the expected negative CBF change could be observed in two further recruited subjects, for which the protocol was changed by doubling the respiration rate. Using the same hybrid device, measurements were conducted on the human neck with the goal of improving thyroid cancer screening (Chapter 5). As a first step, values of the absorption and reduced scattering coefficient at three wavelengths according to the presented device, as well as the total hemoglobin concentration, tissue oxygen saturation and the blood flow index in a healthy population were reported. Moreover, data from pathological cases was taken. This study led to a European Horizon 2020 (H2020) project called Light and Ultrasound Co-analyzer for Thyroid Nodules ("LUCA"; for further information see http://www.luca-project.eu).

11

CONCLUSION

Two relatively new techniques, time-resolved spectroscopy (TRS) and diffuse correlation spectroscopy (DCS), employing low intensity light in the near-infrared and diffuse optical concepts were combined in a single hybrid instrument. The system provides reproducible measurements of tissue optical properties and allows both techniques to be used simultaneously. It provides non-invasive information about (cerebral) hemodynamics and metabolism. The advantages of the hybridization of TRS and DCS were shown throughout the studies presented in Chapters 5 - 9.

In Chapter 5, I showed, for the first time, that it is feasible to do diffuse optical measurements on the thyroid in-vivo. The hybrid device was used with the ultimate goal of testing the feasibility of improving thyroid cancer screening. Several challenges, from the adequate probe design to elimination of possible confounding factors such as repeatability, shielding of the signal by muscle tissue, correct probe placement and the elaboration of a feasible measurement protocol were tackled. Moreover, it was crucial to decide on the adequate subject recruitment, a sensible integration with ultrasound (US) measurements and their use in the analysis. With the US information and the noted tissue dimensions, I was able to conclude that the hemodynamic parameters (THC, StO_2, BFI) derived from diffuse optical measurements reflect thyroid vascularisation. Pathologic contrast was observed with elevated microvascular THC values, making it a promising parameter for improvement in thyroid screening. Further indications of elevated BFI and altered μ_s' in pathologic areas - reflecting the proliferation of cells - encourage the use of diffuse optics on thyroid tissue. Further results from pathological cases are promising. This project opened the door for diffuse optics in thyroid cancer screening and led to a European Horizon 2020 (H2020) project called "LUCA" - Light and Ultrasound Co-analyzer for Thyroid Nodules. LUCA will continue this work by developing a new combined diffuse optics TRS/DCS-US probe and is a collaboration between clinical (Hospital Clínic and IDIBAPS - Institut d'Investigacions

Biomèdiques August Pi I Sunyer) and research entities (ICFO, Politecnico de Milano, University of Birmingham and EIBIR - European Institute for Biomedical Research), as well as industry partners (ECM - Echo Control Medical, Vermon SA and Hemophotonics SL).

The data I presented in Chapter 6 showed that optically derived brain metabolism ($CMRO_2$) during general anesthesia correlated significantly with the widely used bispectral index (BIS) readings, which provides information about the state of consciousness via EEG readings of the brain, and are widely used and accepted in the clinic. The presented data set is one of the few DCS - and even fewer in combination with TRS - to have been acquired during surgeries under general anesthesia. This non-invasively collected optical data from patients under propofol-induced general anesthesia relates to EEG measures. This brings diffuse optical techniques closer to applications in the clinic. It furthermore shows that the hybridization of TRS and DCS is powerful tool that has the potential to continuously monitor patient consciousness during general anesthesia surgeries as well as cerebral hemodynamics in neurocritical care patients, thus improving neuromonitoring. Furthermore, additional support was given to the point that propofol-induced anesthesia maintains physiological coupling between $CMRO_2$ and CBF. Moreover, the acquisition of this data required the design of fiber probes around existing sensors in the clinic, such as the BIS sensor, as well as a close integration and adaptation to the clinical environment of the constructed TRS/DCS hybrid device.

As another potential impact of DCS - and in the future TRS - in the area of general anesthesia, I used diffuse optically derived microvascular cerebral blood flow (mCBF) for the investigation of possible position dependencies of brain hemodynamics in response to respiratory challenges in the study presented in Chapter 7. These challenges were hyperoxia (HO), hypercapnia (HRC) and hyperventilation (HV) and can occur during surgical procedures under general anesthesia. No significant subject position influences were identified, thus suggesting that the reported increased incidence rates of complications, such as venous air embolism (VAE), upper airway obstruction or paradoxical air embolism, which can lead to the above-mentioned conditions (HO, HRC and HV), associated

with general anesthesia in the sitting position, are not related to the respiratory manoeuvres alone, but to a combination with general anesthesia. Additional information about brain metabolism can further help in understanding this problem. This is where the hybrid device presented in Chapter 4 and used in the studies in Chapters 5 and 6 has proven itself to be capable of such measurements in the clinic. This emphasizes again its potential in answering questions on the cerebral hemodynamical behaviour in the clinal environment and the area of general anesthesia.

Furthermore, the hybrid system was utilized to investigate various data analysis methods and physiological confounders of certain challenges as shown in Chapters 8 and 9. I found support to the hypothesis that active hyperventilation can impose an exercise, which is stronger that actual hyperventilation influences on other cerebral hemodynamics. Moreover, I showed that the use of TRS-derived values - averaged for specific measurement periods - led to significantly improved rCBF estimation. Improvements in the SNR from TRS measurements are likely to more closely reflect physiology.

The work presented in this thesis has advanced the field of diffuse optics by validating it against clinical monitors, thus bringing these techniques closer to the application in the continuous patient (neuro-) monitoring, as well incorporating diffuse optics in existing clinical processes such as cancer screening with the potential to significantly improve specificity and sensitivity. Moreover, the combination of TRS and DCS for their simultaneous data acquisition as well as the advantages of such a hybridization were presented. This allows improved information gain on cerebral hemodynamics by better reflecting physiology and estimating brain health.

Part IV

APPENDICES

A

THYROID CHARACTERISATION BY DIFFUSE OPTICS

In Chapter 5 the combination of time-resolved spectroscopy (TRS) and diffuse correlation spectroscopy (DCS) was used to characterize the human thyroid tissue with a final goal of optimizing current thyroid cancer screening procedures. This work led to a European Horizon 2020 project called Light and Ultrasound Co-analyzer for Thyroid Nodules (`http://www.luca-project.eu`) and in this first part of the appendix, individual subject data as well as further case studies with pathologies are shown in addition to the data presented in Chapter 5.

A.1 OPTICAL AND HEMODYNAMIC VALUES PER SUBJECT

Here the absorption coefficient (μ_a), reduced scattering coefficient (μ_s'), total hemoglobin concentration (THC), tissue oxygen saturation (StO_2) and blood flow index (BFI) values for each subject are added. The measurement protocol was explained in detail in Chapter 5. A schematic showing the probe locations is shown in Figure A.1.

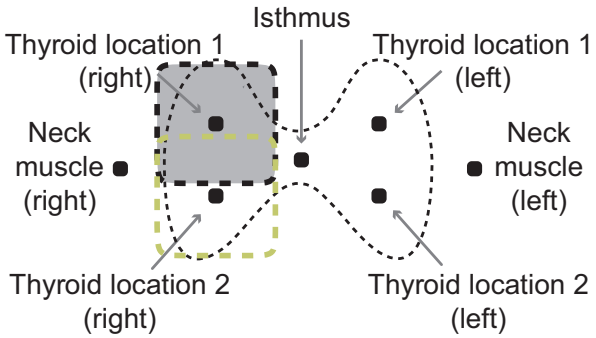

Figure A.1: US-guided probe placements on the human neck: Seven different probe locations were defined in the measurements protocol. Probe size and placement are shown in relation to the thyroid gland size.

Tables A.1, A.2 and A.3 show the data for a source-detector separation (ρ) of 25 mm and Tables A.4, A.5 and A.6 do so for the subset with ρ of 13 mm [1].

1 The numbers shown are mean values with their respective standard deviations. Although IDs 11 (gland location 2, 25 mm), 12 (gland location 1, 25 mm) and 16 (gland location 1, 13 mm) show a non-decreasing μ_s' behaviour with a wavelength increase, the ranges of their respective standard deviations still allow an actual value decrease with increasing wavelength. In other words, the variation is higher than the apparent differences of the means

ID	$\mu_{a,690}$ [cm^{-1}]	$\mu_{a,785}$ [cm^{-1}]	$\mu_{a,830}$ [cm^{-1}]	$\mu'_{s,690}$ [cm^{-1}]	$\mu'_{s,785}$ [cm^{-1}]	$\mu'_{s,830}$ [cm^{-1}]	THC [µM]	StO_2 [%]	BFI [cm^2/s] × 10^{-9}
1	0.25 ± 0.01	0.24 ± 0.01	0.27 ± 0.01	9.8 ± 0.2	9.0 ± 0.2	7.9 ± 0.2	119.6 ± 3.9	66.7 ± 1.4	10.7 ± 1.9
2	0.24 ± 0.01	0.20 ± 0.01	0.22 ± 0.01	9.0 ± 0.3	8.1 ± 0.2	7.4 ± 0.2	97.8 ± 3.0	57.9 ± 2.1	7.3 ± 1.4
3	0.24 ± 0.01	0.22 ± 0.01	0.24 ± 0.01	9.0 ± 0.6	8.2 ± 0.5	7.1 ± 0.4	109.5 ± 3.3	63.7 ± 1.9	7.1 ± 0.6
4	0.23 ± 0.01	0.21 ± 0.01	0.24 ± 0.01	9.0 ± 0.2	8.2 ± 0.1	7.6 ± 0.3	104.9 ± 5.3	64.8 ± 1.6	8.2 ± 1.0
5	0.22 ± 0.01	0.22 ± 0.01	0.24 ± 0.02	10.1 ± 0.2	9.1 ± 0.2	8.1 ± 0.2	107.1 ± 6.9	66.8 ± 1.9	13.4 ± 3.0
6	0.22 ± 0.02	0.23 ± 0.01	0.26 ± 0.01	8.8 ± 0.2	7.5 ± 0.2	6.7 ± 0.3	115.9 ± 5.1	70.0 ± 2.7	11.0 ± 1.3
7	0.19 ± 0.01	0.19 ± 0.01	0.20 ± 0.01	10.0 ± 0.2	9.4 ± 0.2	8.3 ± 0.2	88.4 ± 3.3	64.0 ± 1.4	5.8 ± 0.8
8	0.31 ± 0.03	0.26 ± 0.01	0.29 ± 0.01	7.9 ± 0.4	6.5 ± 0.3	5.8 ± 0.2	131.8 ± 5.4	60.4 ± 2.9	13.8 ± 2.3
9	0.21 ± 0.01	0.19 ± 0.01	0.21 ± 0.01	9.8 ± 0.3	8.6 ± 0.3	7.7 ± 0.2	92.7 ± 3.4	63.5 ± 1.2	11.2 ± 1.7
10	0.20 ± 0.01	0.19 ± 0.01	0.22 ± 0.01	7.4 ± 0.1	6.2 ± 0.1	5.7 ± 0.1	94.3 ± 2.0	66.6 ± 1.2	9.8 ± 1.5
11	0.18 ± 0.01	0.17 ± 0.01	0.19 ± 0.01	8.7 ± 0.2	7.5 ± 0.1	6.9 ± 0.2	80.2 ± 2.5	63.6 ± 1.9	6.0 ± 0.7
12	0.27 ± 0.01	0.26 ± 0.01	0.28 ± 0.01	11.5 ± 0.6	10.3 ± 0.5	9.6 ± 0.5	127.0 ± 3.2	64.7 ± 1.7	4.8 ± 1.1
13	0.23 ± 0.01	0.20 ± 0.01	0.22 ± 0.01	8.8 ± 0.1	7.3 ± 0.1	6.8 ± 0.1	97.9 ± 3.3	61.3 ± 1.8	9.2 ± 2.8
14	0.17 ± 0.01	0.17 ± 0.01	0.19 ± 0.01	8.7 ± 0.2	7.7 ± 0.2	7.1 ± 0.2	80.4 ± 2.8	66.8 ± 2.2	8.6 ± 1.5
15	0.26 ± 0.01	0.23 ± 0.01	0.26 ± 0.01	8.0 ± 0.1	7.2 ± 0.1	6.4 ± 0.1	115.2 ± 1.9	62.6 ± 1.2	6.6 ± 2.1
16	0.17 ± 0.01	0.19 ± 0.01	0.21 ± 0.01	8.4 ± 0.2	8.0 ± 0.2	7.1 ± 0.2	92.1 ± 6.6	70.8 ± 1.5	5.6 ± 1.2
17	0.20 ± 0.01	0.20 ± 0.01	0.22 ± 0.01	9.4 ± 0.1	8.2 ± 0.1	7.6 ± 0.1	98.6 ± 1.4	67.3 ± 2.1	7.0 ± 2.0
18	0.20 ± 0.01	0.18 ± 0.01	0.21 ± 0.01	8.9 ± 0.1	7.7 ± 0.1	7.3 ± 0.1	90.1 ± 3.1	62.6 ± 1.9	5.7 ± 0.6
19	0.23 ± 0.01	0.21 ± 0.01	0.23 ± 0.01	9.3 ± 0.3	8.2 ± 0.2	7.8 ± 0.2	104.0 ± 5.7	64.4 ± 1.6	4.3 ± 0.6
20	0.26 ± 0.01	0.24 ± 0.01	0.29 ± 0.01	8.9 ± 0.1	7.6 ± 0.1	7.5 ± 0.1	126.6 ± 3.0	67.6 ± 1.1	4.3 ± 0.4
21	0.21 ± 0.01	0.19 ± 0.01	0.21 ± 0.01	9.1 ± 0.2	8.1 ± 0.1	7.5 ± 0.1	94.0 ± 3.0	62.9 ± 1.4	5.9 ± 1.3
22	0.19 ± 0.01	0.19 ± 0.01	0.21 ± 0.01	9.8 ± 0.1	8.8 ± 0.1	8.1 ± 0.2	93.2 ± 3.4	67.7 ± 1.4	7.9 ± 1.6

Table A.1: Muscle location data: Means and standard deviations for the absorption coefficient (μ_a) and reduced scattering coefficient (μ'_s) per wavelength as well as total hemoglobin concentration (THC), tissue oxygen saturation (StO_2) and blood flow index (BFI) for a source-detector separation (ρ) of 25 mm (n = 22).

ID	$\mu_{a,690}$ [cm^{-1}]	$\mu_{a,785}$ [cm^{-1}]	$\mu_{a,830}$ [cm^{-1}]	$\mu'_{s,690}$ [cm^{-1}]	$\mu'_{s,785}$ [cm^{-1}]	$\mu'_{s,830}$ [cm^{-1}]	THC [µM]	StO_2 [%]	BFI [cm^2/s] × 10^{-9}
1	0.24 ± 0.01	0.22 ± 0.01	0.23 ± 0.01	10.4 ± 0.2	9.8 ± 0.2	8.4 ± 0.3	104.2 ± 4.5	61.0 ± 2.0	9.4 ± 2.0
2	0.31 ± 0.01	0.29 ± 0.01	0.34 ± 0.02	9.9 ± 0.4	8.7 ± 0.2	8.3 ± 0.4	153.6 ± 4.7	68.5 ± 2.4	22.5 ± 5.6
3	0.27 ± 0.01	0.25 ± 0.01	0.27 ± 0.02	9.2 ± 0.4	8.3 ± 0.4	7.2 ± 0.3	122.1 ± 8.3	63.9 ± 1.8	12.2 ± 2.3
4	0.29 ± 0.02	0.29 ± 0.01	0.34 ± 0.02	10.0 ± 0.3	9.4 ± 0.1	9.0 ± 0.4	152.9 ± 5.5	70.6 ± 2.9	16.5 ± 2.1
5	0.31 ± 0.01	0.30 ± 0.01	0.33 ± 0.01	8.3 ± 0.3	6.9 ± 0.4	6.2 ± 0.3	150.4 ± 2.5	66.5 ± 1.6	15.1 ± 3.1
6	0.31 ± 0.02	0.31 ± 0.01	0.37 ± 0.03	8.3 ± 0.3	6.7 ± 0.2	6.6 ± 0.4	164.1 ± 6.6	73.7 ± 3.2	22.8 ± 2.7
7	0.16 ± 0.01	0.17 ± 0.01	0.17 ± 0.01	10.5 ± 0.2	10.2 ± 0.2	9.2 ± 0.2	76.8 ± 4.6	64.8 ± 1.6	7.33 ± 2.0
8	0.33 ± 0.01	0.30 ± 0.01	0.34 ± 0.01	8.8 ± 0.4	7.2 ± 0.4	6.5 ± 0.4	154.2 ± 3.6	65.3 ± 1.9	22.3 ± 6.1
9	0.33 ± 0.01	0.31 ± 0.01	0.34 ± 0.01	10.2 ± 0.3	8.7 ± 0.2	8.0 ± 0.4	156.0 ± 4.2	65.8 ± 2.2	26.0 ± 5.6
10	0.34 ± 0.02	0.32 ± 0.02	0.37 ± 0.03	7.4 ± 0.3	6.0 ± 0.1	5.8 ± 0.2	167.6 ± 13.0	68.0 ± 2.2	19.4 ± 2.6
11	0.27 ± 0.01	0.26 ± 0.01	0.31 ± 0.01	8.1 ± 0.7	6.7 ± 0.8	6.5 ± 0.8	135.7 ± 5.2	68.4 ± 2.6	11.7 ± 2.4
12	0.30 ± 0.02	0.26 ± 0.02	0.31 ± 0.03	7.2 ± 0.1	5.7 ± 0.1	5.7 ± 0.1	138.0 ± 11.7	65.1 ± 2.7	17.7 ± 3.3
13	0.36 ± 0.01	0.31 ± 0.01	0.36 ± 0.03	8.5 ± 0.2	6.5 ± 0.1	6.4 ± 0.3	163.7 ± 10.4	63.3 ± 3.6	13.9 ± 2.0
14	0.27 ± 0.01	0.28 ± 0.01	0.33 ± 0.01	8.5 ± 0.3	7.1 ± 0.2	6.9 ± 0.3	145.0 ± 3	71.6 ± 1.4	13.2 ± 1.9
15	0.34 ± 0.01	0.31 ± 0.01	0.35 ± 0.02	8.4 ± 0.3	7.4 ± 0.1	6.6 ± 0.2	161.6 ± 5.9	65.9 ± 2.1	14.1 ± 2.6
16	0.23 ± 0.01	0.25 ± 0.01	0.27 ± 0.01	8.8 ± 0.1	8.2 ± 0.1	7.2 ± 0.1	122.4 ± 3.9	71.4 ± 1.9	9.6 ± 2.0
17	0.21 ± 0.01	0.22 ± 0.01	0.24 ± 0.01	10.1 ± 0.2	9.0 ± 0.3	8.3 ± 0.2	107.3 ± 3.0	68.9 ± 1.3	8.9 ± 1.4
18	0.30 ± 0.01	0.28 ± 0.01	0.33 ± 0.01	9.5 ± 0.2	7.9 ± 0.2	7.9 ± 0.2	146.5 ± 3.7	67.9 ± 1.3	15.4 ± 1.9
19	0.27 ± 0.02	0.25 ± 0.01	0.30 ± 0.02	9.8 ± 0.4	8.5 ± 0.3	8.3 ± 0.4	131.5 ± 7.2	67.2 ± 0.8	15.7 ± 3.9
20	0.30 ± 0.01	0.26 ± 0.01	0.31 ± 0.01	7.9 ± 0.2	6.3 ± 0.1	6.2 ± 0.1	136.9 ± 2.4	64.9 ± 0.6	6.9 ± 1.3
21	0.29 ± 0.01	0.28 ± 0.01	0.32 ± 0.01	8.9 ± 0.4	7.7 ± 0.4	7.4 ± 0.4	142.3 ± 5.2	67.2 ± 1.5	8.4 ± 1.4
22	0.34 ± 0.01	0.32 ± 0.01	0.37 ± 0.01	9.1 ± 0.1	7.4 ± 0.1	7.2 ± 0.2	165.9 ± 1.9	67.6 ± 1.1	12.3 ± 1.6

Table A.2: Gland location 1 data: Means and standard deviations for the absorption coefficient (μ_a) and reduced scattering coefficient (μ'_s) per wavelength as well as total hemoglobin concentration (THC), tissue oxygen saturation (StO_2) and blood flow index (BFI) for a source-detector separation (ρ) of 25 mm (n = 22).

ID	$\mu_{a,690}$ [cm^{-1}]	$\mu_{a,785}$ [cm^{-1}]	$\mu_{a,830}$ [cm^{-1}]	$\mu'_{s,690}$ [cm^{-1}]	$\mu'_{s,785}$ [cm^{-1}]	$\mu'_{s,830}$ [cm^{-1}]	THC [µM]	StO_2 [%]	BFI [cm^2/s] × 10^{-9}
1	0.26 ± 0.01	0.25 ± 0.01	0.27 ± 0.02	9.6 ± 0.4	8.8 ± 0.4	7.7 ± 0.4	123.0 ± 8.8	65.2 ± 1.8	12.7 ± 2.2
2	0.28 ± 0.03	0.28 ± 0.02	0.32 ± 0.03	8.9 ± 0.6	8.0 ± 0.4	7.6 ± 0.6	142.6 ± 12.7	68.6 ± 2.9	14.8 ± 4.9
3	0.26 ± 0.03	0.25 ± 0.03	0.28 ± 0.03	8.6 ± 0.4	8.0 ± 0.4	7.0 ± 0.4	125.8 ± 14.8	67.1 ± 1.3	16.1 ± 4.8
4	0.29 ± 0.01	0.29 ± 0.01	0.34 ± 0.01	9.1 ± 0.1	8.3 ± 0.2	8.0 ± 0.3	151.0 ± 5.2	69.9 ± 3.2	14.7 ± 3.6
5	0.29 ± 0.01	0.28 ± 0.01	0.32 ± 0.01	8.6 ± 0.5	7.4 ± 0.3	6.6 ± 0.2	142.8 ± 3.4	68.3 ± 2.7	11.3 ± 2.1
6	0.29 ± 0.01	0.30 ± 0.01	0.36 ± 0.03	7.7 ± 0.3	6.3 ± 0.2	5.7 ± 0.5	157.8 ± 8.8	71.8 ± 2.0	21.0 ± 4.5
7	0.18 ± 0.01	0.19 ± 0.01	0.20 ± 0.01	10.3 ± 0.1	9.9 ± 0.2	8.9 ± 0.1	88.0 ± 3.5	66.3 ± 0.9	7.2 ± 1.8
8	0.33 ± 0.02	0.29 ± 0.01	0.34 ± 0.01	8.5 ± 0.3	6.7 ± 0.2	6.2 ± 0.2	152.2 ± 3.4	64.8 ± 2.7	13.8 ± 1.5
9	0.25 ± 0.02	0.24 ± 0.01	0.26 ± 0.01	7.8 ± 0.3	6.9 ± 0.4	6.2 ± 0.3	117.4 ± 4.0	66.1 ± 2.3	20.8 ± 6.4
10	0.25 ± 0.03	0.26 ± 0.02	0.30 ± 0.04	6.2 ± 0.1	5.2 ± 0.1	4.9 ± 0.2	133.6 ± 15.6	71.7 ± 1.1	36.1 ± 8.0
11	0.29 ± 0.01	0.27 ± 0.01	0.32 ± 0.01	7.4 ± 0.4	5.9 ± 0.3	5.7 ± 0.3	140.2 ± 3.3	66.3 ± 1.7	11.7 ± 1.7
12	0.29 ± 0.02	0.26 ± 0.01	0.32 ± 0.01	6.2 ± 0.1	4.8 ± 0.1	4.9 ± 0.1	140.5 ± 3.4	68.3 ± 2.3	29.3 ± 9.9
13	0.33 ± 0.03	0.29 ± 0.01	0.34 ± 0.01	8.0 ± 0.3	6.4 ± 0.2	6.3 ± 0.2	151.7 ± 4.4	65.4 ± 3	21.4 ± 5.5
14	0.26 ± 0.01	0.26 ± 0.01	0.31 ± 0.02	7.6 ± 0.1	6.3 ± 0.1	6.2 ± 0.2	138.2 ± 7.7	70.6 ± 1.5	16.2 ± 2.4
15	0.29 ± 0.02	0.28 ± 0.02	0.32 ± 0.02	7.3 ± 0.7	6.4 ± 0.6	5.7 ± 0.5	143.2 ± 10.2	67.5 ± 2.3	16.9 ± 3.4
16	0.24 ± 0.01	0.25 ± 0.01	0.28 ± 0.01	7.4 ± 0.1	6.7 ± 0.1	5.9 ± 0.1	124.2 ± 2.1	70.6 ± 1.1	10.8 ± 1.3
17	0.20 ± 0.01	0.21 ± 0.01	0.23 ± 0.01	9.7 ± 0.5	8.5 ± 0.5	7.9 ± 0.5	102.7 ± 4.0	69.9 ± 0.9	10.8 ± 1.9
18	0.27 ± 0.01	0.26 ± 0.01	0.30 ± 0.01	9.9 ± 0.4	8.6 ± 0.4	8.3 ± 0.3	132.7 ± 3.3	68.3 ± 1.7	10.0 ± 1.8
19	0.21 ± 0.01	0.21 ± 0.01	0.23 ± 0.02	10.0 ± 0.3	8.9 ± 0.4	8.4 ± 0.3	103.1 ± 9.5	66.6 ± 1.6	12.9 ± 1.8
20	0.28 ± 0.01	0.25 ± 0.01	0.29 ± 0.01	8.1 ± 0.1	6.6 ± 0.2	6.5 ± 0.2	129.1 ± 4.7	64.8 ± 1.0	7.1 ± 0.9
21	0.26 ± 0.02	0.26 ± 0.01	0.30 ± 0.01	8.1 ± 0.1	7.1 ± 0.1	6.8 ± 0.1	132.4 ± 7.3	69.3 ± 1.0	11.8 ± 2.7
22	0.33 ± 0.01	0.31 ± 0.01	0.36 ± 0.01	8.8 ± 0.4	7.1 ± 0.3	6.8 ± 0.5	163.7 ± 4.5	67.5 ± 1.5	11.6 ± 1.7

Table A.3: Gland location 2 data: Means and standard deviations for the absorption coefficient (μ_a) and reduced scattering coefficient (μ'_s) per wavelength as well as total hemoglobin concentration (THC), tissue oxygen saturation (StO_2) and blood flow index (BFI) for a source-detector separation (ρ) of 25 mm (n = 22).

ID	$\mu_{a,\,690}$ [cm^{-1}]	$\mu_{a,\,785}$ [cm^{-1}]	$\mu_{a,\,830}$ [cm^{-1}]	$\mu'_{s,\,690}$ [cm^{-1}]	$\mu'_{s,\,785}$ [cm^{-1}]	$\mu'_{s,\,830}$ [cm^{-1}]	THC [µM]	StO_2 [%]	BFI [cm^2/s] × 10^{-9}
3	0.21 ± 0.01	0.20 ± 0.01	0.20 ± 0.01	10.1 ± 1.2	9.5 ± 1.1	7.6 ± 1	92.3 ± 3.4	60.9 ± 2.3	9.4 ± 1.5e
13	0.23 ± 0.01	0.21 ± 0.01	0.21 ± 0.01	13.2 ± 0.3	11.0 ± 0.2	9.9 ± 0.2	97.3 ± 4.5	60.0 ± 1.9	8.5 ± 3.2
14	0.17 ± 0.01	0.17 ± 0.01	0.18 ± 0.01	11.6 ± 0.2	10.1 ± 0.2	9.4 ± 0.2	77.8 ± 2.4	64.7 ± 2.9	7.8 ± 1.6
15	0.25 ± 0.01	0.23 ± 0.01	0.23 ± 0.01	10.6 ± 0.6	9.9 ± 0.5	8.1 ± 0.5	108.6 ± 2.7	60.4 ± 1.9	8.3 ± 2.7
16	0.16 ± 0.01	0.18 ± 0.01	0.19 ± 0.01	8.9 ± 0.2	8.9 ± 0.1	7.3 ± 0.2	84.9 ± 6.5	70.3 ± 1.0	5.6 ± 0.8
17	0.18 ± 0.01	0.17 ± 0.01	0.20 ± 0.01	10.9 ± 0.1	9.1 ± 0.2	8.8 ± 0.1	85.5 ± 1.9	65.4 ± 2.3	13.6 ± 1.9
18	0.19 ± 0.01	0.17 ± 0.01	0.19 ± 0.01	11.7 ± 0.3	9.6 ± 0.3	9.4 ± 0.3	81.7 ± 2.8	60.9 ± 2.6	7.3 ± 1.7
19	0.22 ± 0.01	0.19 ± 0.01	0.21 ± 0.01	12.4 ± 0.4	10.5 ± 0.3	10.4 ± 0.2	93.6 ± 4.4	61.5 ± 2.4	8.2 ± 1.4
20	0.26 ± 0.01	0.24 ± 0.01	0.27 ± 0.01	12.8 ± 0.3	10.5 ± 0.2	10.4 ± 0.2	122.2 ± 3.5	64.9 ± 1.1	8.6 ± 1.0
21	0.20 ± 0.01	0.18 ± 0.01	0.19 ± 0.01	11.2 ± 0.3	9.7 ± 0.3	8.9 ± 0.3	83.6 ± 3.4	60.1 ± 2.4	7.5 ± 1.1
22	0.21 ± 0.01	0.21 ± 0.01	0.22 ± 0.01	12.9 ± 0.4	11.1 ± 0.3	10.2 ± 0.3	99.9 ± 5.3	66.4 ± 1.1	8.7 ± 1.7

Table A.4: Muscle location data: Means and standard deviations for the absorption coefficient (μ_a) and reduced scattering coefficient (μ'_s) per wavelength as well as total hemoglobin concentration (THC), tissue oxygen saturation (StO_2) and blood flow index (BFI) for a source-detector separation (ρ) of 13 mm for a study population subset (n = 11).

ID	$\mu_{a,690}$ [cm^{-1}]	$\mu_{a,785}$ [cm^{-1}]	$\mu_{a,830}$ [cm^{-1}]	$\mu'_{s,690}$ [cm^{-1}]	$\mu'_{s,785}$ [cm^{-1}]	$\mu'_{s,830}$ [cm^{-1}]	THC [µM]	StO_2 [%]	BFI [cm^2/s] × 10^{-9}
3	0.27 ± 0.02	0.26 ± 0.02	0.26 ± 0.02	12.4 ± 0.5	12.0 ± 0.4	9.8 ± 0.4	123.6 ± 9.0	64.1 ± 1.3	8.9 ± 2.1
13	0.40 ± 0.02	0.41 ± 0.02	0.36 ± 0.01	12.1 ± 0.2	10.4 ± 0.2	8.4 ± 0.1	183.6 ± 7.0	62.4 ± 3.2	13.3 ± 2.9
14	0.27 ± 0.01	0.30 ± 0.01	0.30 ± 0.01	12.0 ± 0.3	10.7 ± 0.3	9.4 ± 0.3	142.4 ± 3.9	70.7 ± 1.1	10.1 ± 1.89
15	0.34 ± 0.02	0.33 ± 0.01	0.32 ± 0.01	10.1 ± 0.4	9.7 ± 0.3	7.5 ± 0.3	155.5 ± 3.3	63.9 ± 1.6	15.9 ± 2.9
16	0.19 ± 0.01	0.22 ± 0.01	0.23 ± 0.01	10.0 ± 0.5	10.0 ± 0.4	8.1 ± 0.5	104.9 ± 4.5	71.4 ± 1.7	11.8 ± 3.1
17	0.18 ± 0.01	0.17 ± 0.01	0.19 ± 0.01	11.2 ± 0.3	9.4 ± 0.2	9.1 ± 0.3	83.4 ± 2.5	66.4 ± 1.6	9.9 ± 1.1
18	0.30 ± 0.01	0.28 ± 0.01	0.31 ± 0.01	12.5 ± 0.2	10.0 ± 0.2	9.8 ± 0.2	141.5 ± 4.9	66.2 ± 1.2	20.4 ± 3.4
19	0.29 ± 0.03	0.27 ± 0.02	0.30 ± 0.02	12.9 ± 0.7	10.6 ± 0.7	10.5 ± 0.7	137.7 ± 11.1	65.1 ± 1.8	33.4 ± 3.5
20	0.29 ± 0.01	0.25 ± 0.01	0.29 ± 0.01	10.4 ± 0.3	8.1 ± 0.2	8.0 ± 0.2	131.0 ± 2.5	63.6 ± 0.7	9.6 ± 2.0
21	0.30 ± 0.01	0.29 ± 0.01	0.30 ± 0.01	10.8 ± 0.4	9.5 ± 0.4	8.5 ± 0.3	140.3 ± 3.2	64.5 ± 1.8	14.6 ± 3.0
22	0.34 ± 0.01	0.34 ± 0.01	0.35 ± 0.01	12.4 ± 0.6	10.6 ± 0.5	9.3 ± 0.5	165.7 ± 3.4	66.4 ± 0.9	17.1 ± 2.7

Table A.5: Gland location 1 data: Means and standard deviations for the absorption coefficient (μ_a) and reduced scattering coefficient (μ'_s) per wavelength as well as total hemoglobin concentration (THC), tissue oxygen saturation (StO_2) and blood flow index (BFI) for a source-detector separation (ρ) of 13 mm for a study population subset (n = 11).

ID	$\mu_{a,\,690}$ [cm^{-1}]	$\mu_{a,\,785}$ [cm^{-1}]	$\mu_{a,\,830}$ [cm^{-1}]	$\mu'_{s,\,690}$ [cm^{-1}]	$\mu'_{s,\,785}$ [cm^{-1}]	$\mu'_{s,\,830}$ [cm^{-1}]	THC [µM]	StO_2 [%]	BFI [cm^2/s] × 10^{-9}
3	0.29 ± 0.01	0.28 ± 0.01	0.29 ± 0.01	11.1 ± 0.1	10.8 ± 0.2	8.7 ± 0.1	135.1 ± 5.6	64.9 ± 1.7	12.5 ± 1.7
13	0.35 ± 0.02	0.33 ± 0.01	0.32 ± 0.01	12.4 ± 0.3	10.5 ± 0.4	9.1 ± 0.3	156.3 ± 3.8	62.4 ± 2.0	12.8 ± 3.3
14	0.28 ± 0.01	0.30 ± 0.01	0.30 ± 0.01	11.9 ± 0.3	10.6 ± 0.2	9.3 ± 0.3	142.6 ± 3.5	68.1 ± 1.2	8.1 ± 1.0
15	0.35 ± 0.03	0.35 ± 0.02	0.34 ± 0.02	9.5 ± 0.5	9.0 ± 0.4	6.9 ± 0.3	165.5 ± 8.1	64.7 ± 2.9	19.1 ± 2.5
16	0.21 ± 0.01	0.24 ± 0.01	0.25 ± 0.01	8.4 ± 0.3	8.4 ± 0.2	6.6 ± 0.3	112.9 ± 2.8	70.1 ± 1.4	11.1 ± 1.3
17	0.19 ± 0.01	0.19 ± 0.01	0.22 ± 0.01	10.9 ± 0.9	9.1 ± 0.8	8.8 ± 0.8	93.3 ± 4.1	68.5 ± 1.5	12.8 ± 1.7
18	0.29 ± 0.01	0.27 ± 0.01	0.30 ± 0.01	12.8 ± 0.2	10.4 ± 0.1	10.2 ± 0.2	134.5 ± 3.4	65.6 ± 1.4	13.9 ± 1.8
19	0.25 ± 0.01	0.24 ± 0.01	0.26 ± 0.01	12.1 ± 0.3	10.2 ± 0.2	10.0 ± 0.2	118.2 ± 4.7	64.6 ± 2.3	23.3 ± 3.5
20	0.28 ± 0.01	0.25 ± 0.01	0.28 ± 0.01	11.4 ± 0.3	8.9 ± 0.2	8.8 ± 0.2	124.7 ± 1.7	62.4 ± 1.7	8.6 ± 1.0
21	0.27 ± 0.01	0.27 ± 0.01	0.29 ± 0.01	9.8 ± 0.3	8.6 ± 0.3	7.8 ± 0.3	130.8 ± 3.1	66.5 ± 1.8	21.1 ± 7.2
22	0.35 ± 0.01	0.34 ± 0.01	0.36 ± 0.01	11.6 ± 0.7	9.8 ± 0.7	8.6 ± 0.6	168.0 ± 4.3	66.0 ± 1.5	17.3 ± 2.0

Table A.6: Gland location 2 data: Means and standard deviations for the absorption coefficient (μ_a) and reduced scattering coefficient (μ'_s) per wavelength as well as total hemoglobin concentration (THC), tissue oxygen saturation (StO_2) and blood flow index (BFI) for a source-detector separation (ρ) of 13 mm for a study population subset (n = 11).

A.2 PATHOLOGY CASES

In Section 5.3.3, data from two thyroid pathologies was presented, but nine cases were included in the study. Here the data from the other seven cases is presented. Figures A.2 - A.9 show the corresponding thyroid protocol schematics with the shaded regions representing the thyroid nodule location(s) and their approximate size(s) in relation to the complete thyroid. The measurements consisted of the same procedure as for the healthy volunteers, explained in Section 5.2 but with added measurement locations on the nodule side. These locations are:

I: "gland center right" (*CASE 2, 3, 4, 6* and *CASE 7*)

II: "gland center left" (*CASE 3, 4* and *CASE 8*)

III: "isthmus b" (*CASE 6*)

IV: "adenopathy" (*CASE 2*)

A.2.1 *Pathology case 1 (CASE 1):*

This case is a 58 year old woman (weight 75 kg, height 1.60 m, BMI 29.3 kg/m^2) presenting a left thyroid nodule, which was characterized as solid, iso-hypoechoic and well defined with peripheral vascularization and a size of 22 x 18 x 33 mm. The fine-needle aspiration biopsy (FNAB) showed atypical cells suggestive of papillary thyroid carcinoma. The patient underwent a total thyroidectomy. Histopathology showed a follicular lesion of 34 mm, which was well differentiated with uncertain malignant potential. Due to the results, the lesion was considered as malignant and was treated with radioiodine ablation.

The results in pseudo-color scale are presented in Fig. A.2 including the measurement protocol in Fig. A.2 b). The tabulated values are shown in Table A.7. *CASE 1* shows generally lower total hemoglobin concentrations and blood flow indices for all locations. The oxygen saturation in the thyroid is comparable to the healthy population, while the muscles show lower saturations.

The nodule was located on the left thyroid side in the "gland location 2" (marked with * in Table A.7), where the blood flow index (BFI) is lower than the in rest of the thyroid locations, yet higher than the muscle. Moreover, the reduced scattering coefficient (μ_s') reveal here lower scattering characteristics than the healthy tissue. In the left "gland location 2" we see up to 21 % lower reduced scattering coefficient (μ_s') values than on the healthy right side, which is a difference three times bigger than in the "gland location 1". Also the BFI value in the starred nodule location is rather low compared to the healthy and active thyroid tissue and therefore closer to the muscle tissue.

In *CASE 1* the rather large nodule size of 33 mm suggests already that photons emitted from at least one probe position on the left thyroid gland should reach the pathologic tissue. In fact, the location probing the nodule is the gland location 2. The reduced scattering coefficient (μ_s') for all three wavelengths show clear differences between sides (Tab. A.7) with a 21 % lower value for the nodule location in this case. Since the thyroid is already an very active organ, cancerous tissue, while also possessing a high activity, can actually reveal inferior hemodynamic values than its surrounding healthy tissue.

	$\mu_{a,\,785}$ [cm^{-1}]	$\mu'_{s,\,785}$ [cm^{-1}]	THC [µM]	StO_2 [%]	BFI [cm^2/s] ×10^{-9}
Muscle (right)	0.13 ± 0.01	8.83 ± 0.07	57.1 ± 0.2	62.3 ± 0.8	1.29 ± 0.09
Gland location 1 (right)	0.15 ± 0.01	9.40 ± 0.09	70.5 ± 0.2	65.6 ± 0.7	3.44 ± 0.27
Gland location 2 (right)	0.17 ± 0.01	9.95 ± 0.08	78.3 ± 0.4	67.6 ± 0.3	5.02 ± 0.25
Isthmus	0.16 ± 0.01	9.28 ± 0.03	74.4 ± 1.0	66.3 ± 0.3	3.62 ± 0.16
Gland location 2 (left)*	0.16 ± 0.01	7.88 ± 0.03	74.4 ± 0.4	68.0 ± 0.2	2.46 ± 0.64
Gland location 1 (left)	0.17 ± 0.01	8.71 ± 0.07	79.4 ± 0.2	68.1 ± 0.2	6.35 ± 0.41
Muscle (left)	0.12 ± 0.01	10.21 ± 0.05	52.6 ± 0.8	61.9 ± 0.2	1.14 ± 0.10

Table A.7: Results of *CASE 1*: Means and standard deviations from for the absorption coefficient (μ_a), reduced scattering coefficient (μ'_s), total hemoglobin concentration (THC), tissue oxygen saturation (StO_2) and theBFI are shown here for all seven measurement locations according to the study protocol for this patient as shown in Figure A.2 a). * denotes the nodule locations.

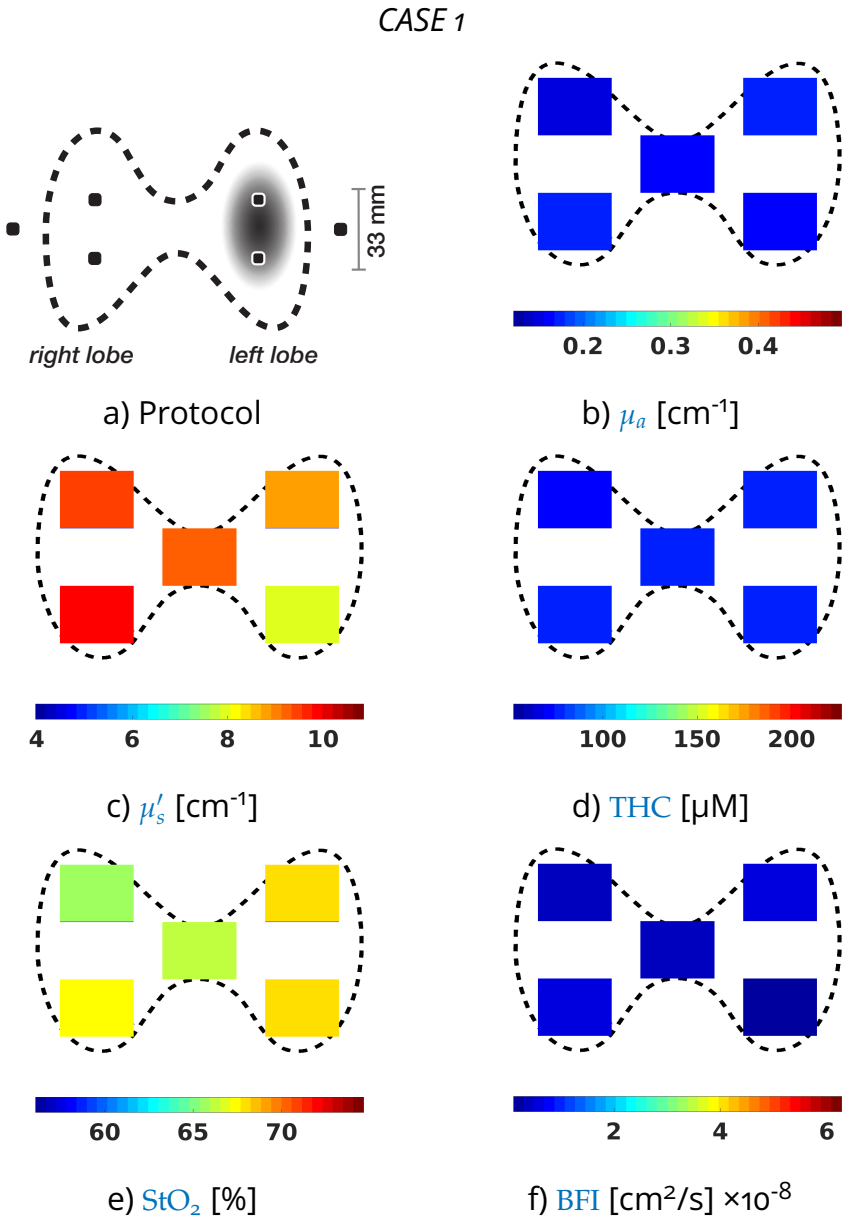

Figure A.2: Results of the 1st pathology case: The measurement protocol a) consists of seven probe locations. The results are shown for the b) absorption (μ_a) and c) reduced scattering coefficients (μ_s') for 785 nm as well as the d) total hemoglobin concentration (THC), e) tissue oxygen saturation (StO_2) and f) blood flow index (BFI). Note, that these color plots do not include the muscle locations.

This can explain the low BFI in the starred probe location of this case.

A.2.2 *Pathology case 2 (CASE 2):*

The second case was a 24 year old woman (weight 52 kg; height 1.53 cm; BMI 22.2 kg/m^2) who presented a right thyroid nodule with a maximum diameter of 8 mm and an adenopathy of 20 mm next to the right thyroid gland. The nodule was characterized as solid, hypoechoic, with irregular borders and microcalcifications. The adenopathy was characterized as a nodular heterogeneous solid lesion including a abundant central vascularisation and microcalcifications. The FNAB of the thyroid nodule was non diagnostic due to a insufficient sample, while the FNAB result of the adenopathy showed atypical cells compatible with a metastasis of a papillary thyroid carcinoma. A total thyroidectomy was performed, with central node dissection and modified right lateral neck and right supraclavicular dissections. The histopathology revealed a right papillary thyroid microcarcinoma (7 mm) and one adenopathy in the lateral section of 19 mm consistent with the ultrasound diagnosis. Due to the results, the nodule as well as the adenopathy was considered as malignant the patient was treated with radioiodine ablation.

The results in pseudo-color representation are shown in Fig. A.3. In this case the nodule was located within the right thyroid gland and the measurement protocol was extended with two additional probe placement (“thyroid gland center” and “adenopathy”). Note that the nodule was rather small with a maximum diameter of 8 mm.

We can see here, that the patient showed generally higher oxygen saturations throughout the whole thyroid and especially in the right gland 2 position a noticeable lower (~ 24 % compared to the non-starred locations) total hemoglobin concentration (THC), which is here more similar to the respective muscle probe location. Also a lower THC value from the added location (“gland center right”) than from the other non-pathologic ones was recorded. The μ_s' values from starred probe locations - gland location 2 and gland center on the right side - are higher. The BFI has an up to 56 % higher value in the right gland location 2 compared to the other side and in the right gland center position the BFI value is the highest for this subject.

	$\mu_{a,\,785}$ [cm^{-1}]	$\mu'_{s,\,785}$ [cm^{-1}]	THC [µM]	StO_2 [%]	BFI [cm^2/s] ×10^{-9}
Muscle (right)	0.21 ± 0.01	7.11 ± 0.08	104.4 ± 0.9	68.5 ± 0.6	17.67 ± 2.18
Gland location 1 (right)	0.27 ± 0.01	6.72 ± 0.07	141.1 ± 1.1	72.1 ± 1.3	15.91 ± 4.25
Gland location 2 (right)*	0.21 ± 0.01	8.42 ± 0.02	105.1 ± 1.5	71.3 ± 0.3	12.35 ± 0.46
Isthmus	0.20 ± 0.01	8.06 ± 0.02	100.1 ± 0.9	70.3 ± 1.4	38.85 ± 4.27
Gland location 2 (left)	0.25 ± 0.01	6.79 ± 0.07	126.9 ± 0.6	69.8 ± 0.7	11.30 ± 0.28
Gland location 1 (left)	0.28 ± 0.01	7.39 ± 0.04	145.5 ± 1.2	71.3 ± 0.4	14.00 ± 1.53
Muscle (left)	0.19 ± 0.01	7.91 ± 0.02	96.0 ± 1.8	71.8 ± 1.1	9.74 ± 0.35
Gland center (right)*	0.23 ± 0.01	7.88 ± 0.08	117.5 ± 0.2	72.1 ± 0.5	16.57 ± 3.70
Adenopathy	0.28 ± 0.01	6.75 ± 0.06	147.1 ± 3.7	69.2 ± 0.9	16.11 ± 1.58

Table A.8: Results of *CASE 2*: Means and standard deviations from for the absorption coefficient (μ_a), reduced scattering coefficient (μ'_s), total hemoglobin concentration (THC), tissue oxygen saturation (StO_2) and theBFI are shown here for all nine measurement locations according to the study protocol for this patient as shown in Figure A.3 a). * denotes the nodule locations.

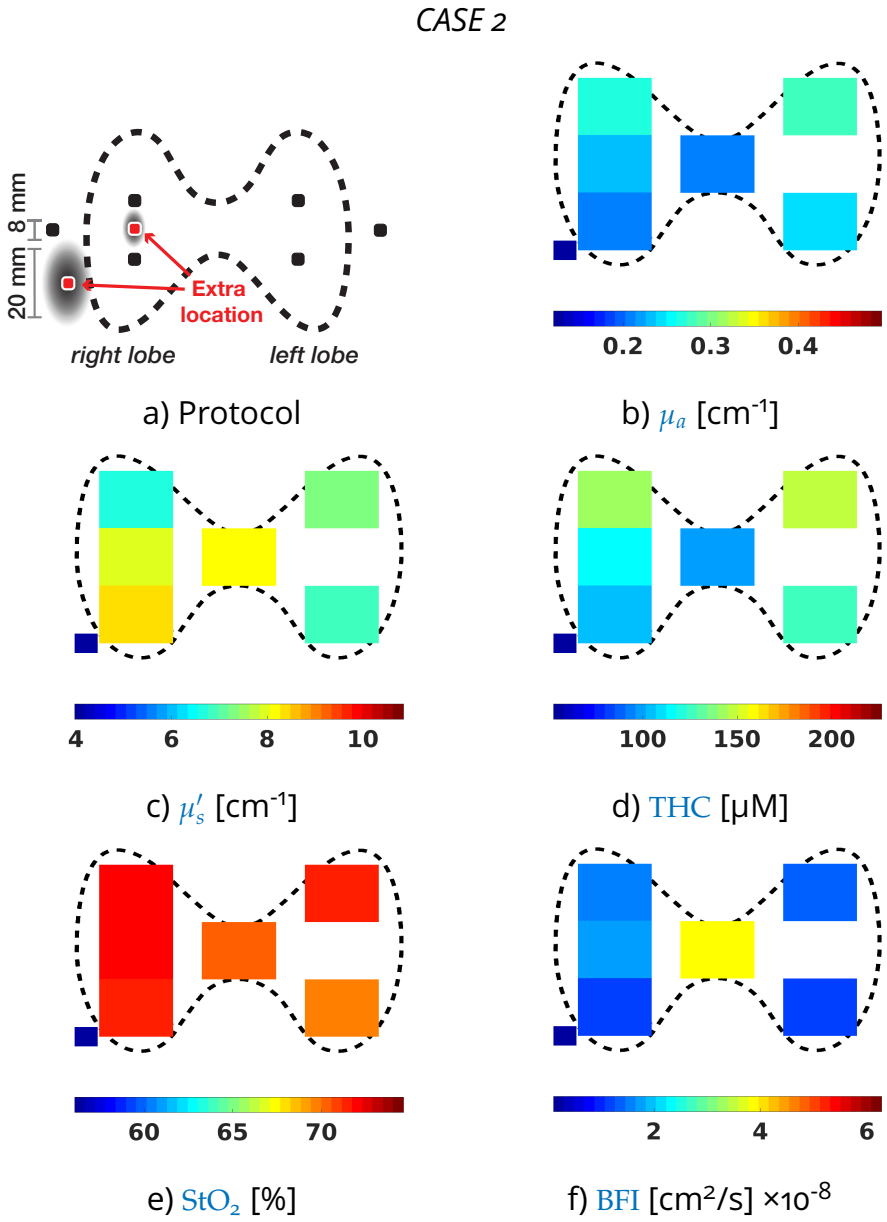

Figure A.3: Results of the 2nd pathology case: The measurement protocol a) consists of nine probe locations. The results are shown for the b) absorption (μ_a) and c) reduced scattering coefficients (μ_s') for 785 nm as well as the d) total hemoglobin concentration (THC), e) tissue oxygen saturation (StO_2) and f) blood flow index (BFI). Note, that these color plots do not include the muscle locations.

Similar to the first case, μ_s' side variations in *CASE 2* identify the "pathologic positions" as the right gland 2 probe location and gland center position, which is further supported by the low total hemoglobin concentration (THC) and high (up to 56 % higher) BFI values. This increase in the BFI might be

explained with previous observations of increased microvasculature in papillary thyroid carcinomas and the sensitivity of TRS/DCS to this vasculature part. Nonetheless, we note that this case presented a microcarcinoma with a maximum diameter of 8 mm, which is small compared to the total thyroid size. Similar to the 1st case, the reduced scattering coefficient (μ_s') serves as a further discriminator between pathologic and non-pathologic tissues - especially their differences between corresponding locations on opposite sites.

A.2.3 *Pathology case 3 (CASE 3):*

A 23 years old man (weight 74 kg; height 1.81 m; BMI 22.6 kg/m^2) who presented two right cystic nodules, one with a size of 27 x 17 mm and solid content and the other one with a maximum diameter of 14 mm was included as the 3rd case. The patient also presented a left thyroid nodule with a maximum diameter of 14 mm. The FNAB examination of the solid content from the bigger right thyroid nodule showed atypical follicular cells. A total thyroidectomy was performed and histopathology showed a extensive regressive cystic lesion with a size of 20 mm and the presence of atypical cells. The cells were suspicious for papillary thyroid carcinoma but the sample was insufficient for a diagnosis. The lesion was CK19 positive and BRAF negative. Due to the results, the lesion was considered as malignant and was treated with radioiodine ablation.

The thyroid scheme with the nodules as black shadowed regions can be seen in Figure A.4 b) and the results from the measurement on *CASE 3* are presented in pseudo-color scale in Fig. A.4 b) to f).

Since the patient had three different thyroid nodules, two of which located on the right side and one on the left side, we added two probe locations ("thyroid gland center right" and "thyroid gland center left") in this case. Note that, on the right side the gland carried one cystic nodule with a maximum diameter of 27 mm in addition to 14 mm nodule.

On the right side we see the center position (marked by * in Tab. A.9) clearly sticking out in the total hemoglobin concentration (THC) with the highest value in general for this case, while at the same time presenting the lowest oxygen saturation on this thyroid side. Apart from the center position, information about the nodule was also retrieved in the gland location 1 (marked with * in Tab. A.9) showing a similar trend. This position presents also the highest reduced scattering coefficient (μ_s') for this case. The blood flow indices (BFI) recorded at the nodule locations are on the higher end of the BFI range for this subject. All starred locations show consistently lower oxygen saturations than the rest of the thyroid tissue and blood flow indices for these locations are at the lower end of thyroid range for this subject.

	$\mu_{a,\,785}$ [cm^{-1}]	$\mu'_{s,\,785}$ [cm^{-1}]	THC [µM]	StO_2 [%]	BFI [cm^2/s] ×10^{-9}
Muscle (right)	0.23 ± 0.01	5.97 ± 0.02	114.2 ± 0.7	60.0 ± 1.3	10.55 ± 0.85
Gland location 1 (right)*	0.28 ± 0.01	9.22 ± 0.07	143.4 ± 1.4	66.5 ± 0.3	9.84 ± 0.46
Gland location 2 (right)	0.26 ± 0.01	5.09 ± 0.05	137.1 ± 0.7	68.1 ± 0.7	22.64 ± 1.41
Isthmus	0.22 ± 0.01	9.02 ± 0.08	108.9 ± 0.5	71.5 ± 0.5	13.44 ± 1.50
Gland location 2 (left)	0.25 ± 0.01	7.83 ± 0.06	129.7 ± 2.5	69.4 ± 1.1	21.08 ± 2.83
Gland location 1 (left)	0.24 ± 0.01	8.72 ± 0.08	125.0 ± 0.1	70.0 ± 1.2	13.54 ± 1.61
Muscle (left)	0.21 ± 0.01	7.25 ± 0.07	106.3 ± 2.1	67.2 ± 0.5	13.39 ± 2.22
Gland center (right)*	0.29 ± 0.01	7.43 ± 0.08	150.4 ± 2.8	63.8 ± 0.7	14.58 ± 1.87
Gland center (left)	0.24 ± 0.01	8.40 ± 0.10	121.5 ± 1.8	70.3 ± 0.4	12.18 ± 0.66

Table A.9: Results of *CASE 3*: Means and standard deviations from for the absorption coefficient (μ_a), reduced scattering coefficient (μ'_s), total hemoglobin concentration (THC), tissue oxygen saturation (StO_2) and theBFI are shown here for all nine measurement locations according to the study protocol for this patient as shown in Figure A.4 a). * denotes the nodule locations.

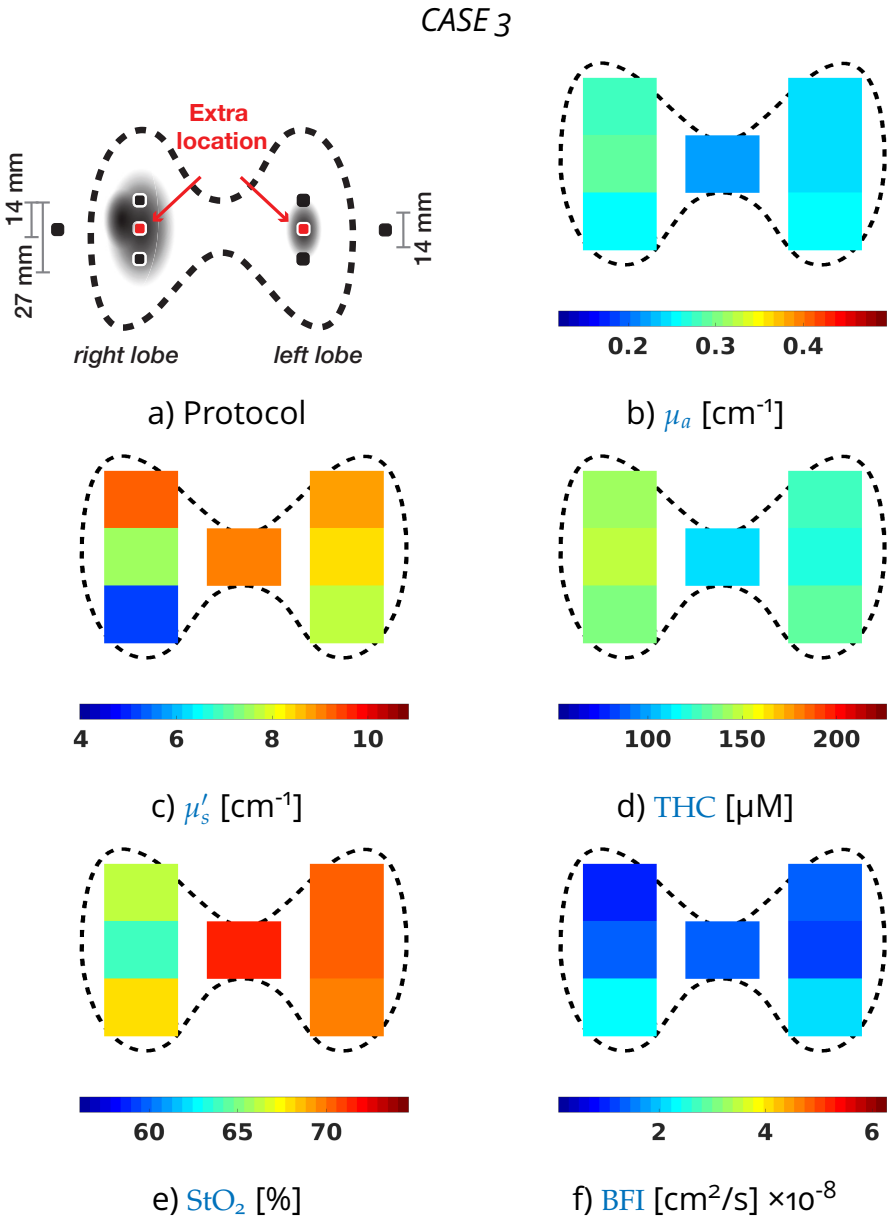

Figure A.4: Results of the 3rd pathology case: The measurement protocol a) consists of nine probe locations. The results are shown for the b) absorption (μ_a) and c) reduced scattering coefficients (μ_s') for 785 nm as well as the d) total hemoglobin concentration (THC), e) tissue oxygen saturation (StO_2) and f) blood flow index (BFI). Note, that these color plots do not include the muscle locations.

The 3rd case furthermore presented clear differences in the added probe locations as well as in the right gland location 1 (marked by * in Tab. A.9). Although, it is difficult to assign the values on the right side to a specific nodule out of the two located here, the high total hemoglobin concentra-

tions, lower oxygen saturations and changed scattering characteristics indicate clearly differences in the nature of the tissue.

A.2.4 *Pathology case 4 (CASE 4):*

This case was presented in Chapter 5 and its condition and protocol is just briefly repeated here, so that the tabulated results, which contain more details than in Section 5.3.3.1 can be better understood.

The fourth case was a male (38 years old; weight 71 kg; height 1.64 m; BMI 26.4 kg/m^2) with a thyroid nodule (maximum diameter > 65 mm) affecting the left lobe and extending into the isthmus. The nodule was heterogeneous with necrotic areas. The FNAB examination showed atypical cells suggestive of papillary thyroid cancer and MRI showed a destructured mass occupying the left thyroid lobe and the isthmus, infiltrating all surrounding thyroid structures (trachea and esophagus) and the skin. Due to the results, the tumor was considered unresectable and a radio- and a chemotherapy with tyrosine kinase inhibitors ("Sorafenib") was suggested as a neoadjuvant therapy prior to a possible surgery. The radio- and chemotherapy showed an effect and a total thyroidectomy was performed afterwards. Moreover, the third, fourth and sixth compartment were resected. The histopathology showed a papillary thyroid carcinoma of 65 mm with invasion of the extrathyroidal fibroadipose tissue. Twelve adenopathies were resected. Out of these twelve, three were classified as malignant metastatic tissue.

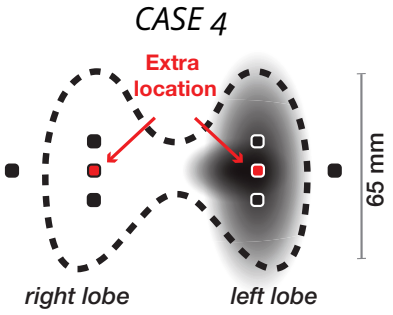

Figure A.5: The protocol for the 4th pathology case consists of nine probe locations.

	$\mu_{a,785}$ [cm^{-1}]	$\mu'_{s,785}$ [cm^{-1}]	THC [µM]	StO_2 [%]	BFI [cm^2/s] ×10^{-9}
Muscle (right)	0.17 ± 0.01	7.79 ± 0.08	82.6 ± 0.8	71.9 ± 1.2	7.3 ± 0.22
Gland location 1 (right)	0.27 ± 0.01	6.51 ± 0.12	138.5 ± 1.6	74.1 ± 0.5	12.9 ± 1.2
Gland location 2 (right)	0.26 ± 0.01	5.81 ± 0.06	134.7 ± 1.2	70.2 ± 0.5	12.9 ± 1.1
Isthmus	0.33 ± 0.01	9.90 ± 0.15	161.4 ± 2.4	73.6 ± 1.2	18.7 ± 2.0
Gland location 2 (left)*	0.38 ± 0.01	6.24 ± 0.04	201.3 ± 3.7	72.9 ± 2.2	33.1 ± 3.4
Gland location 1 (left)*	0.40 ± 0.01	5.89 ± 0.21	221.2 ± 11.4	71.6 ± 3.3	62.8 ± 6.4
Muscle (left)	0.19 ± 0.01	8.18 ± 0.16	92.7 ± 1.5	66.1 ± 3.3	17.9 ± 4.1
Gland center (right)	0.27 ± 0.01	6.40 ± 0.04	141.8 ± 2.4	71.8 ± 2.8	12.5 ± 0.5
Gland center (left)*	0.39 ± 0.02	6.06 ± 0.30	210.0 ± 6.1	71.6 ± 0.8	40.6 ± 3.0

Table A.10: Results of *CASE 4*: Means and standard deviations from for the absorption coefficient (μ_a), reduced scattering coefficient (μ'_s), total hemoglobin concentration (THC), tissue oxygen saturation (StO_2) and theBFI are shown here for all nine measurement locations according to the study protocol for this patient as shown in Figure A.5. * denotes the nodule locations.

A.2.5 *Pathology case 5 (CASE 5):*

CASE 5, a 33 years old woman (weight 49 kg; height 1.59 m; BMI 19.4 kg/m^2) was diagnosed of a multinodular goiter with two left solid thyroid nodules of 40 and 20 mm. FNAB examination was performed in the biggest nodule, showing a follicular lesion with uncertain significance. The right thyroid lobule showed no atypical behaviour. First a hemithyroidectomy of the left thyroid lobe was performed and the corresponding histopathology showed a follicular carcinoma of 50 mm. In continuation the right thyroid lobe was resected aswell, thus completing the thyroidectomy with a negative histopathology for malignancy.

	$\mu_{a,\,785}$ [cm^{-1}]	$\mu'_{s,\,785}$ [cm^{-1}]	THC [µM]	StO_2 [%]	BFI [cm^2/s] ×10^{-9}
Muscle (right)	0.21 ± 0.01	8.65 ± 0.06	101.2 ± 1.2	70.8 ± 1.1	8.98 ± 0.78
Gland location 1 (right)	0.30 ± 0.01	8.64 ± 0.07	142.7 ± 1.4	74.6 ± 4.3	8.27 ± 0.78
Gland location 2 (right)	0.28 ± 0.01	8.67 ± 0.09	133.0 ± 2.4	74.6 ± 1.4	6.54 ± 1.46
Isthmus	0.23 ± 0.01	9.25 ± 0.16	109.5 ± 1.2	73.9 ± 2.2	5.44 ± 0.27
Gland location 2 (left)*	0.31 ± 0.01	7.49 ± 0.15	148.9 ± 3.4	73.4 ± 1.4	6.78 ± 0.47
Gland location 1 (left)*	0.32 ± 0.01	8.43 ± 0.12	155.0 ± 1.7	74.3 ± 0.3	11.37 ± 1.84
Muscle (left)	0.22 ± 0.01	7.86 ± 0.14	101.9 ± 0.8	72.0 ± 2.4	10.25 ± 0.25

Table A.11: Results of *CASE 5*: Means and standard deviations from for the absorption coefficient (μ_a), reduced scattering coefficient (μ'_s), total hemoglobin concentration (THC), tissue oxygen saturation (StO_2) and theBFI are shown here for all eight measurement locations according to the study protocol for this patient as shown in Figure A.6 a). * denotes the nodule locations.

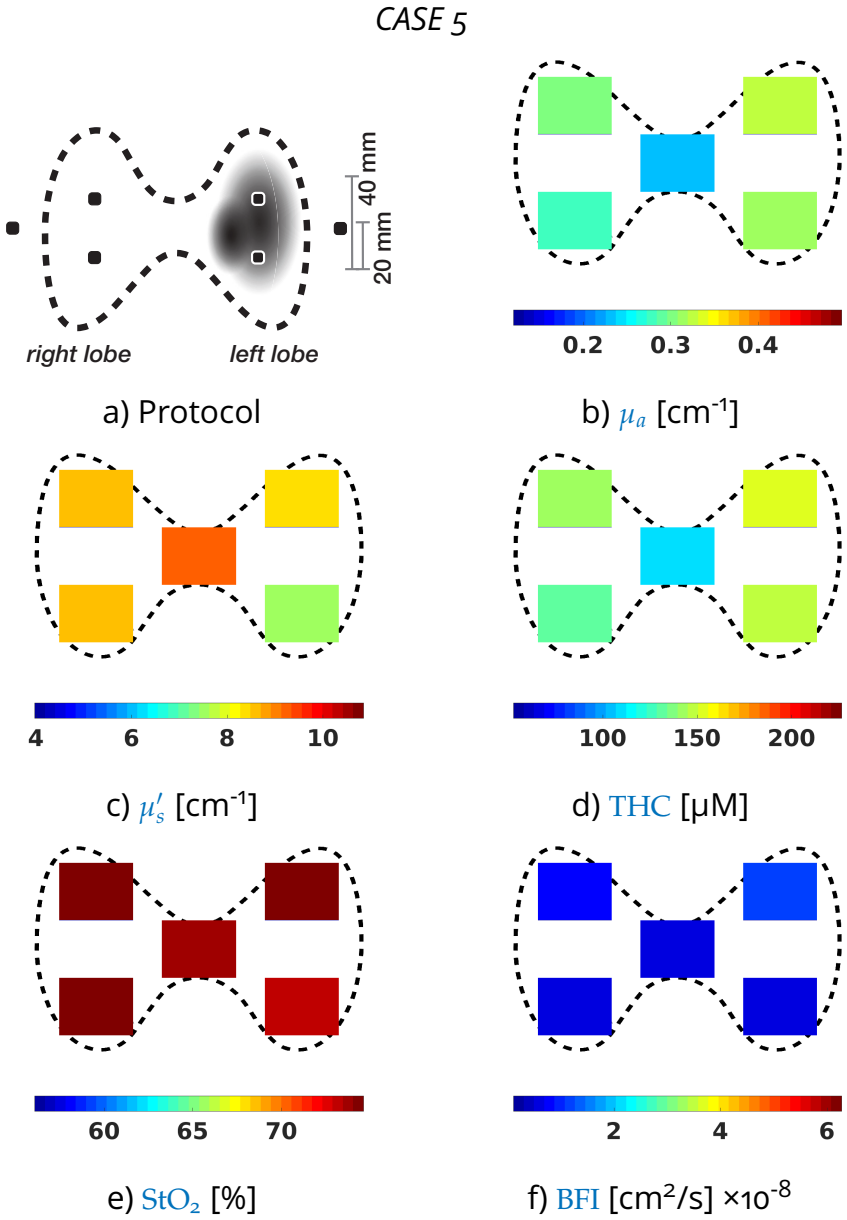

Figure A.6: Results of the 5th pathology case: The measurement protocol a) consists of seven probe locations. The results are shown for the b) absorption (μ_a) and c) reduced scattering coefficients (μ_s') for 785 nm as well as the d) total hemoglobin concentration (THC), e) tissue oxygen saturation (StO_2) and f) blood flow index (BFI). Note, that these color plots do not include the muscle locations.

A.2.6 *Pathology case 6 (CASE 6):*

The sixth case was a 48 years old woman (weight 50 kg; height 1.60 m; BMI 19.5 kg/m^2) presenting a multinodular goiter with several macronodules in both lobes, the biggest one of 44 mm in the right lobe. FNAB examination was performed and was suggestive of multinodular goiter with follicular cells and colloid, with no atypical cells. The isthmus also presented a nodule of 9 mm and in the left lobe a nodule of 14 mm was also observed. Total thyroidectomy was performed and histopathology showed a thyroid hyperplasia with regressive changes a no evidence of malignancy.

	$\mu_{a,\,785}$ [cm^{-1}]	$\mu'_{s,\,785}$ [cm^{-1}]	THC [µM]	StO_2 [%]	BFI [cm^2/s] ×10^{-9}
Muscle (right)	0.21 ± 0.01	8.36 ± 0.02	96.8 ± 0.8	56.1 ± 1.0	5.49 ± 0.66
Gland location 1 (right)	0.33 ± 0.01	6.24 ± 0.10	169.6 ± 1.1	67.4 ± 2.0	16.28 ± 0.55
Gland location 2 (right)	0.35 ± 0.01	6.95 ± 0.06	175.6 ± 5.2	71.5 ± 2.4	16.66 ± 0.44
Isthmus	0.38 ± 0.01	7.99 ± 0.09	182.9 ± 1.8	68.1 ± 0.7	31.76 ± 2.64
Gland location 2 (left)*	0.40 ± 0.01	6.82 ± 0.07	203.5 ± 2.5	66.6 ± 1.1	13.13 ± 2.19
Gland location 1 (left)	0.38 ± 0.01	8.49 ± 0.06	184.3 ± 9.8	62.7 ± 6.7	15.51 ± 1.07
Muscle (left)	0.25 ± 0.01	8.84 ± 0.11	116.7 ± 1.5	61.2 ± 1.6	7.63 ± 0.61
Gland center (right)*	0.37 ± 0.01	7.08 ± 0.03	189.3 ± 0.7	69.9 ± 0.9	15.82 ± 0.44
Isthmus bottom*	0.39 ± 0.01	8.81 ± 0.07	188.8 ± 2.7	68.9 ± 0.9	12.01 ± 0.40

Table A.12: Results of *CASE 6*: Means and standard deviations from for the absorption coefficient (μ_a), reduced scattering coefficient (μ'_s), total hemoglobin concentration (THC), tissue oxygen saturation (StO_2) and theBFI are shown here for all nine measurement locations according to the study protocol for this patient as shown in Figure A.7 a). * denotes the nodule locations.

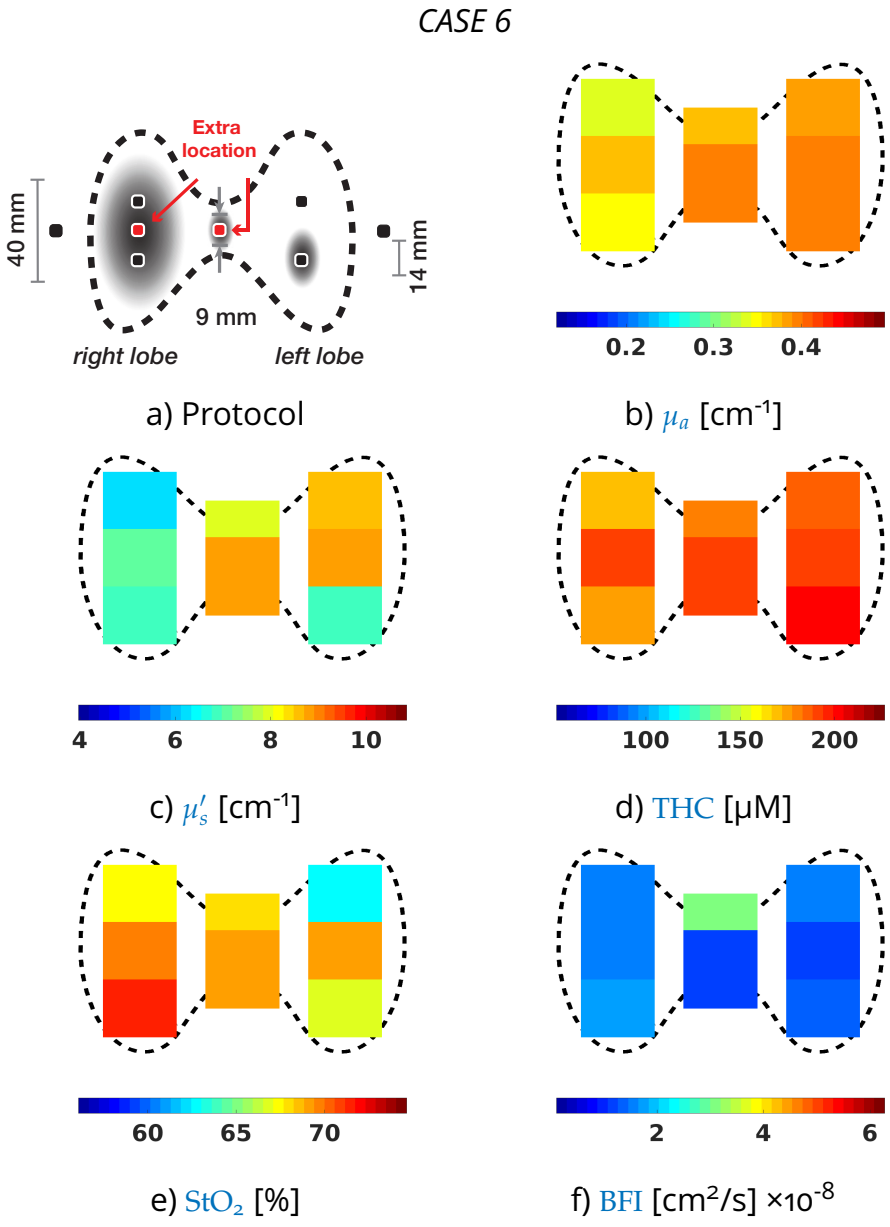

Figure A.7: Results of the 6th pathology case: The measurement protocol a) consists of nine probe locations. The results are shown for the b) absorption (μ_a) and c) reduced scattering coefficients (μ_s') for 785 nm as well as the d) total hemoglobin concentration (THC), e) tissue oxygen saturation (StO_2) and f) blood flow index (BFI). Note, that these color plots do not include the muscle locations.

A.2.7 *Pathology case 7 (CASE 7):*

This case was presented in Chapter 5 and its condition and protocol is just briefly repeated here, so that the tabulated reults, which contain more details than in Section 5.3.3.2 can be better understood.

As *CASE 7* results from a female (32 years old; weight 68 kg; height 1.82 m; BMI 20.5 kg/m^2) with a thyroid nodule (40 mm) in the right lobe are presented. The nodule showed foci of colloid degradation and peripheral vascularisation suggestive of a hyperplastic nodule. An additional small nodule of a 3 mm diameter in the right lobe was observed, with no laterocervical adenopathies. Fine needle aspiration biopsy was performed and suggestive of a follicular lesion. Furthermore, the nodule showed microfollicular characteristics and was classified according to the "Bethesda system for reporting thyroid cytopathology" [63] which scales from one to six with increasing malignancy risk as Bethesda 4. After the optical measurements, a total thyroidectomy was performed and histopathology showed multinodular thyroid hyperplasia with a hyperplastic dominant nodule (maximum diameter of 40 m) and regressive changes with adenomatoid nodules. No follicular neoplasms were observed. Finally, the pathology was classified as benign.

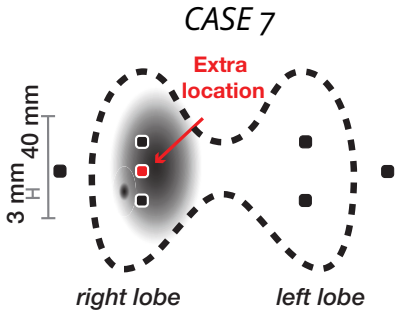

Figure A.8: The protocol for the 7th pathology case consists of seven probe locations.

	$\mu_{a,\,785}$ [cm^{-1}]	$\mu'_{s,\,785}$ [cm^{-1}]	THC [µM]	StO_2 [%]	BFI [cm^2/s] ×10^{-9}
Muscle (right)	0.23 ± 0.01	6.63 ± 0.08	108.3 ± 0.8	61.0 ± 1.1	7.5 ± 0.6
Gland location 1 (right)	0.30 ± 0.01	9.29 ± 0.12	140.2 ± 2.9	66.2 ± 1.3	12.1 ± 1.3
Gland location 2 (right)*	0.39 ± 0.01	7.40 ± 0.03	191.8 ± 1.5	64.7 ± 2.2	11.2 ± 1.8
Isthmus	0.39 ± 0.01	8.45 ± 0.14	192.5 ± 4.4	66.0 ± 1.9	20.2 ± 0.9
Gland location 2 (left)	0.28 ± 0.01	6.69 ± 0.01	141.8 ± 0.1	72.5 ± 0.1	15.0 ± 1.8
Gland location 1 (left)	0.33 ± 0.01	7.80 ± 0.08	164.1 ± 2.5	69.2 ± 0.5	8.7 ± 0.5
Muscle (left)	0.24 ± 0.01	8.68 ± 0.08	117.1 ± 1.2	68.0 ± 1.6	8.5 ± 1.1
Gland center (right)*	0.44 ± 0.02	7.54 ± 0.39	226.5 ± 8.2	66.9 ± 0.5	37.6 ± 3.9

Table A.13: Results of *CASE 7*: Means and standard deviations from for the absorption coefficient (μ_a), reduced scattering coefficient (μ'_s), total hemoglobin concentration (THC), tissue oxygen saturation (StO_2) and theBFI are shown here for all eight measurement locations according to the study protocol for this patient as shown in Figure A.8. * denotes the nodule locations.

A.2.8 *Pathology case 8 (CASE 8):*

CASE 8 is a 67 years old man (weight 98 kg; height 1.66 m; BMI 35.6 kg/m^2) presented a left thyroid nodule with a diameter of 23 mm and subclinical hypothyroidism. FNAB examination was performed and was suggestive of follicular carcinoma. The right thyroid lobe was very destructured. A total thyroidectomy was performed and histopathology showed adenomatoid thyroid hyperplasia with oncocystic changes and no evidence of malignancy.

	$\mu_{a,\,785}$ [cm^{-1}]	$\mu'_{s,\,785}$ [cm^{-1}]	THC [µM]	StO_2 [%]	BFI [cm^2/s] ×10^{-9}
Muscle (right)	0.16 ± 0.01	8.99 ± 0.02	75.8 ± 0.9	65.5 ± 0.6	12.65 ± 0.29
Gland location 1 (right)	0.20 ± 0.01	8.84 ± 0.14	97.0 ± 3.3	66.8 ± 0.6	15.97 ± 2.99
Gland location 2 (right)	0.23 ± 0.01	9.05 ± 0.09	113.5 ± 2.1	66.6 ± 0.6	10.05 ± 2.11
Isthmus	0.15 ± 0.01	9.07 ± 0.04	72.7 ± 1.2	65.4 ± 2.9	10.61 ± 0.68
Gland location 2 (left)	0.23 ± 0.01	7.86 ± 0.24	113.4 ± 2.7	63.0 ± 1.3	12.86 ± 0.76
Gland location 1 (left)	0.20 ± 0.01	8.56 ± 0.09	93.0 ± 1.1	64.6 ± 1.1	16.30 ± 0.25
Muscle (left)	0.16 ± 0.01	8.01 ± 0.15	76.0 ± 2.3	65.5 ± 1.2	8.62 ± 1.57
Gland center (left)	0.24 ± 0.01	8.34 ± 0.02			19.85 ± 0.97

Table A.14: Results of *CASE 8*: Means and standard deviations from for the absorption coefficient (μ_a), reduced scattering coefficient (μ'_s), total hemoglobin concentration (THC), tissue oxygen saturation (StO_2) and theBFI are shown here for all eight measurement locations according to the study protocol for this patient as shown in Figure A.9 a).

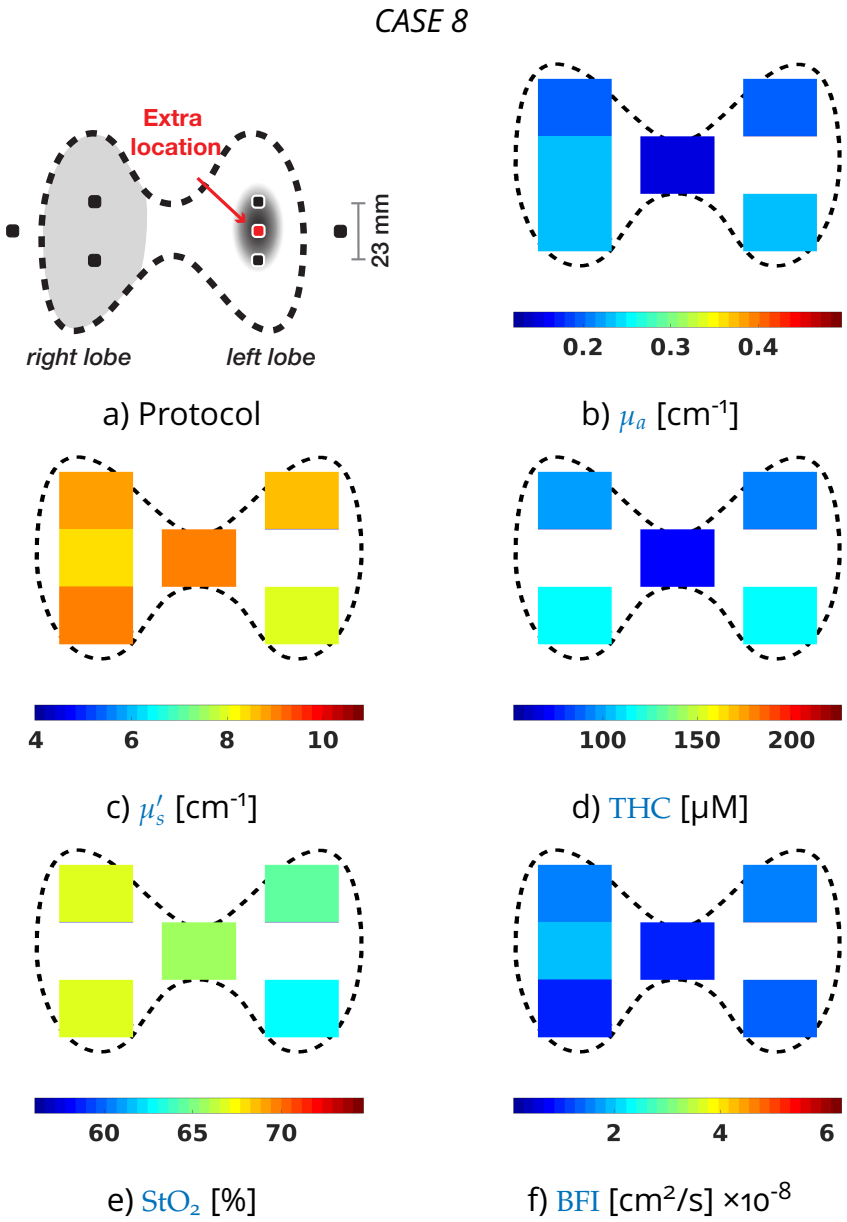

Figure A.9: Results of the 8th pathology case: The measurement protocol a) consists of eight probe locations. The results are shown for the b) absorption (μ_a) and c) reduced scattering coefficients (μ_s') for 785 nm as well as the d) total hemoglobin concentration (THC), e) tissue oxygen saturation (StO_2) and f) blood flow index (BFI). Note, that these color plots do not include the muscle locations.

B

CEREBRAL BLOOD FLOW, METABOLISM AND BRAIN EEG CORRELATIONS

In Chapter 6 a combination of TRS and DCS was used to estimate cerebral metabolism and blood flow ($CMRO_2$ and CBF) in patients under general anesthesia with target-controlled infusion of propofol. These optically derived parameters were shown to correlate with BIS readings, which are widely used in the clinic and are relate to the state of consciousness via EEG measurements of the brain. In the correlation analysis the data was examined in three steps (for further details please refer to Section 6.2.3):

Step I: Consider the complete $rCMRO_2$, rCBF and rBIS data set.

Step II: Consider all rBIS data but only significant changes in optical measurements, i. e. changes greater than the standard deviation.

Step III: Consider only changes in $rCMRO_2$, rCBF and rBIS, that are larger than the standard deviation.

Here the subject individual Pearson's product-moment correlation coefficients from Steps II and III are presented, which were not included in the Chapter for clarity reasons.

ID	$R_{pearson}$	intercept	slope	N	InD [%]
1	0.47***	37.05 ± 2.32	0.72 ± 0.13	108	19.89
2	0.32***	-16.24 ± 1.79	0.63 ± 0.13	204	29.39
3	0.29	34.76 ± 5.20	0.23 ± 0.21	14	40.00
4	-0.12	17.01 ± 2.42	-0.24 ± 0.14	211	29.84
5	0.14**	8.48 ± 2.09	0.14 ± 0.05	425	41.50
6	0.96***	-6.87 ± 2.26	1.61 ± 0.05	78	23.64
7	0.46***	-6.45 ± 0.91	1.14 ± 0.07	1026	35.64
8	0.88***	17.40 ± 0.95	0.40 ± 0.04	32	59.26
9	0.64***	25.36 ± 3.92	0.52 ± 0.08	63	19.87
10	0.32***	-18.89 ± 3.21	0.67 ± 0.16	145	68.40
11	0.16	-34.97 ± 17.00	0.38 ± 0.95	8	24.24
12	0.62***	2.24 ± 3.14	0.98 ± 0.10	156	28.84
13	-0.18	127.85 ± 17.96	-0.20 ± 0.15	51	16.14
14	0.06	9.20 ± 1.61	0.03 ± 0.03	184	33.03
15	0.48***	10.58 ± 1.46	0.30 ± 0.03	267	29.15
16	0.66***	10.53 ± 0.45	0.20 ± 0.01	418	35.70
17	0.48***	-16.76 ± 0.48	0.49 ± 0.03	917	57.89

Table B.1: Pearson correlation coefficients, intercepts and slopes of $rCMRO_2$ versus rBIS considering values outside the mean ± σregion (step II: $|rCMRO_2| > \pm\sigma_{rCMRO_2}$). Results are shown individually per subject. N = total number of used data points; InD = percentage of included data. The levels of significance are defined as follows: *** for $p < 0.001$; ** for $p < 0.01$; * for $p < 0.05$.

ID	$R_{pearson}$	intercept	slope	N	InD [%]
1	0.48***	38.33 ± 2.42	0.70 ± 0.13	97	17.86
2	0.36***	-13.69 ± 1.81	0.67 ± 0.12	197	28.39
3	0.31	35.08 ± 5.09	0.24 ± 0.21	14	40.00
4	-0.13	19.48 ± 2.36	-0.25 ± 0.13	218	30.83
5	0.16***	8.86 ± 2.06	0.17 ± 0.05	426	41.60
6	0.96***	-3.64 ± 2.27	1.52 ± 0.05	72	21.81
7	0.44***	-4.17 ± 0.91	1.09 ± 0.07	1022	35.50
8	0.98**	26.24 ± 2.18	0.37 ± 0.04	5	9.26
9	0.61***	24.52 ± 3.77	0.47 ± 0.08	63	19.87
10	0.31***	-17.35 ± 4.03	0.66 ± 0.19	116	54.72
11	0.03	-33.48 ± 14.46	0.06 ± 0.81	9	27.27
12	0.66***	6.63 ± 3.88	1.15 ± 0.12	122	22.55
13	-0.28*	167.08 ± 23.50	-0.40 ± 0.20	51	16.14
14	0.05	9.35 ± 1.57	0.02 ± 0.03	186	33.39
15	0.44***	14.74 ± 1.50	0.26 ± 0.03	256	27.95
16	0.72***	11.43 ± 0.47	0.24 ± 0.01	400	34.16
17	0.48***	-15.68 ± 0.47	0.49 ± 0.03	929	58.65

Table B.2: Pearson correlation coefficients, intercepts and slopes of rCBF versus rBIS considering values outside the mean ± σregion (step III: $|\text{rCBF}| > \pm\sigma_{\text{rCBF}}$). Results are shown individually per subject. N = total number of used data points; InD = percentage of included data. The levels of significance are defined as follows: *** for $p < 0.001$; ** for $p < 0.01$; * for $p < 0.05$.

ID	$R_{pearson}$	intercept	slope	N	InD [%]
1	0.70***	38.90 ± 2.19	0.75 ± 0.01	63	11.60
2	0.78***	-12.14 ± 2.03	0.85 ± 0.01	64	9.22
3	0.44	27.24 ± 7.65	0.30 ± 0.01	8	22.86
4	-0.68***	17.72 ± 6.21	-0.88 ± 0.01	31	4.83
5	0.80***	-30.27 ± 3.01	0.66 ± 0.01	126	12.30
6	0.97***	2.84 ± 2.82	1.52 ± 0.01	46	13.94
7	0.40***	-2.24 ± 1.62	0.62 ± 0.01	327	11.36
8				1	1.85
9	0.30	8.23 ± 48.87	0.79 ± 0.01	19	5.99
10	0.29**	-21.10 ± 3.91	0.57 ± 0.01	113	53.30
11	0.13	-35.55 ± 21.93	0.35 ± 0.01	7	21.21
12	0.84***	9.62 ± 2.96	1.00 ± 0.01	82	15.16
13	-0.12	121.84 ± 21.33	-0.15 ± 0.01	49	15.51
14	0.80***	-22.80 ± 4.46	0.39 ± 0.01	43	7.72
15	0.58***	10.21 ± 5.20	0.30 ± 0.01	58	6.33
16	0.89***	-0.56 ± 1.38	0.29 ± 0.01	90	7.69
17	0.48***	-15.80 ± 1.12	0.43 ± 0.01	281	17.74

Table B.3: Pearson correlation coefficients, intercepts and slopes of $rCMRO_2$ versus rBIS considering values outside the mean $\pm\sigma$region of $rCMRO_2$ and rBIS ($|rBIS| > \pm\sigma_{rBIS}$ and $|rCMRO_2| > \pm\sigma_{rCMRO_2}$). Results are shown individually per subject and the criteria led to absence of sufficient data points for ID = 8. N = total number of used data points; InD = percentage of included data. The levels of significance are defined as follows: *** for $p < 0.001$; ** for $p < 0.01$; * for $p < 0.05$.

ID	$R_{pearson}$	intercept	slope	N	InD [%]
1	0.71***	38.49 ± 2.22	0.75 ± 0.01	60	11.05
2	0.80***	-10.99 ± 1.92	0.85 ± 0.01	65	9.37
3	0.43	28.10 ± 7.81	0.30 ± 0.01	8	22.86
4	-0.68***	18.00 ± 5.11	-0.79 ± 0.01	35	4.95
5	0.80***	-28.23 ± 2.98	0.66 ± 0.01	129	12.60
6	0.98***	6.57 ± 2.78	1.43 ± 0.01	42	12.73
7	0.41***	0.59 ± 1.64	0.63 ± 0.01	319	11.08
8				1	1.85
9	0.17	39.18 ± 40.13	0.34 ± 0.01	19	5.99
10	0.28**	-19.54 ± 4.32	0.56 ± 0.01	100	47.17
11	0.06	-31.62 ± 18.19	0.15 ± 0.01	8	24.24
12	0.88***	12.87 ± 3.31	1.16 ± 0.01	64	11.83
13	-0.14	144.66 ± 27.00	-0.22 ± 0.01	49	15.51
14	0.80***	-22.52 ± 4.33	0.38 ± 0.01	43	7.72
15	0.53***	16.97 ± 4.71	0.23 ± 0.01	57	6.22
16	0.88***	0.69 ± 1.65	0.33 ± 0.01	90	7.69
17	0.49***	-14.3 ± 1.09	0.44 ± 0.01	290	18.31

Table B.4: Pearson correlation coefficients, intercepts and slopes of rCBF versus rBIS considering values outside the mean ±σregion of rCBF and rBIS (|rBIS|> $\pm\sigma_{rBIS}$ and |rCBF|> $\pm\sigma_{rCBF}$). Results are shown individually per subject and the criteria led to absence of sufficient data points for ID = 8. N = total number of used data points; InD = percentage of included data. The levels of significance are defined as follows: *** for p < 0.001; ** for p < 0.01; * for p < 0.05.

C

MICROVASCULAR CEREBRAL BLOOD FLOW RESPONSES TO RESPIRATORY CHALLENGES

In Chapter 7 we looked at responses of CBF to respiratory challenges in two positions (50° and supine). These challenges were HO, HRC and HV and their protocols were presented in Figure 7.1.

Here additional data is presented, which were not included in the Chapter for clarity reasons.

C.1 POSITION CHANGES

Apart from the challenge protocols presented in Chapter 7, each subject's position was changed in a defined manner prior to the challenge protocol (supine → 50° → supine → 30° → legs at 45°). After the complete set of challenges, the entire procedure was concluded with an additional baseline in supine position followed by the subject standing up, both for a duration of five minutes. The sequences - as shown in Section 7.2.2 - are again illustrated in Figure 7.2 (see Figure 7.2).

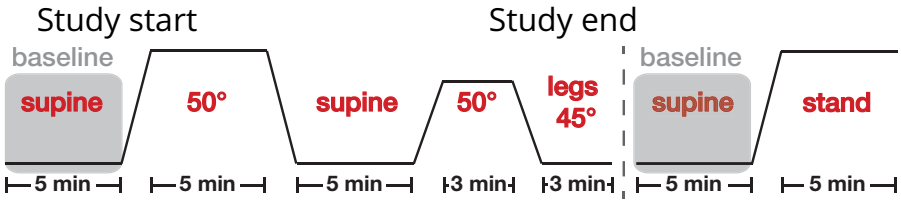

Figure C.1: Start sequence: The different positions were kept for a duration of five minutes except for the 30° and legs at 45° positions, which lasted three minutes; End sequence: The procedure consisted of a supine baseline for five minutes followed by the subject standing for five minutes.

Similar to 7.4, here the relative microvascular cerebral blood flow (rCBF) and blood flow velocity changes ($rCBFV_{mean}$) are

shown. Additionally, also plotted are: absolute heart rate (ΔHR), mean arterial blood pressure (ΔMAP), peripheral oxygen saturation change (ΔSpO_2), stroke volume (ΔSV), cardiac output (ΔCO) and regional oxygen saturation (ΔSrO_2) change. The preceding supine position was used as a baseline (represented by the black dashed lines). The grey dashed lines separate the study start and end procedure from one another.

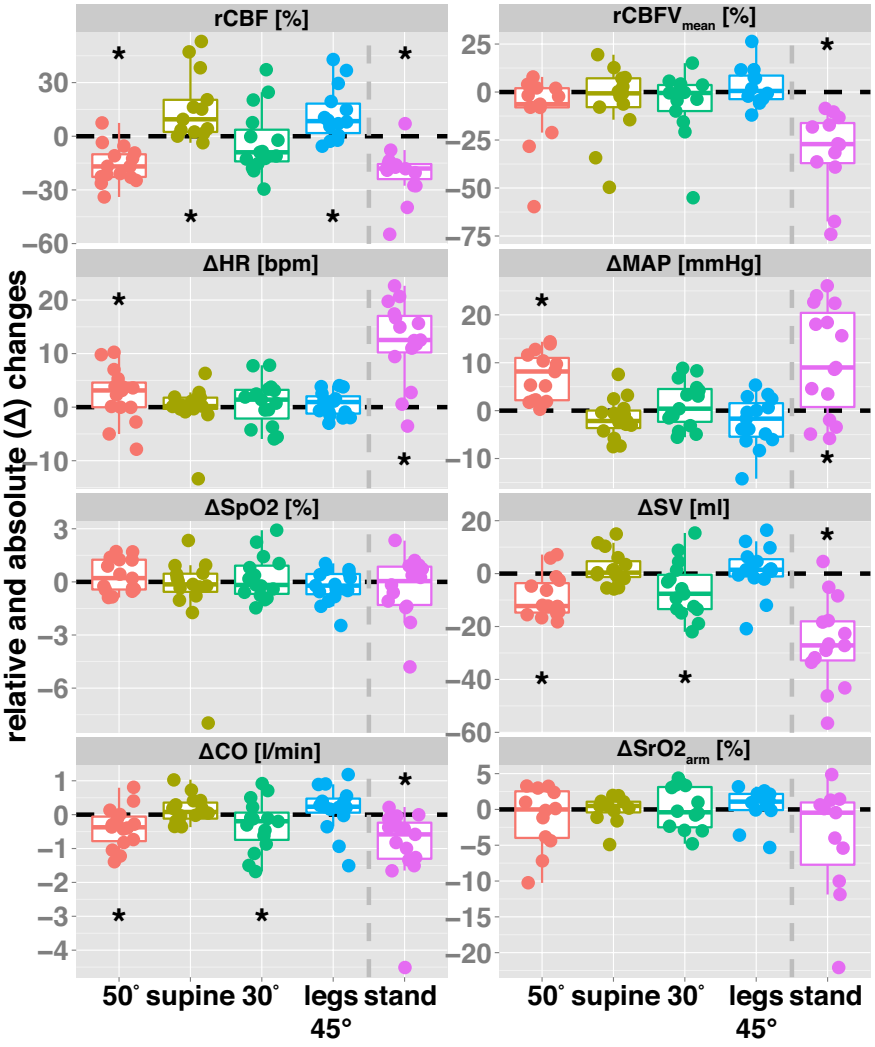

Figure C.2: Posture changes at study start and end - separated by a dashed grey line. The changes correspond to the protocols presented in Figure C.1 and the abbreviations read as follows: rCBF = relative microvascular cerebral blood flow change; r$CBFV_{mean}$ = blood flow velocity changes; ΔHR = absolute heart rate changes; ΔMAP = mean arterial blood pressure change; ΔSpO_2 = peripheral oxygen saturation change; ΔSV = stroke volume change; ΔCO = cardiac output change; ΔSrO_2 = regional oxygen saturation change in the arm. Statistically significant changes ($p < 0.05$) are marked by * and black dashed lines represent the baseline (preceding supine position).

C.2 CORRELATION TABLES

Additional correlation tables to the study presented in Chapter 7 are added here (Tables C.1, C.2, C.3, C.4, C.5 and C.6).

These are separated by manoeuvres, which include hyperoxia (HO), hypercapnia (HRC) and hyperventilation (HV) and positions (supine and 50°). For details on protocols etc. please refer to Section 7.2.

C.2.1 *Hyperoxia*

Tables C.1 and C.2 represent the Spearman correlations for values obtained during hyperoxia (HO) in two different positions. Table C.1 refers to the supine and Table C.2 to the 50° position. For the details on the protocol for this challenge please refer to Figure C.3.

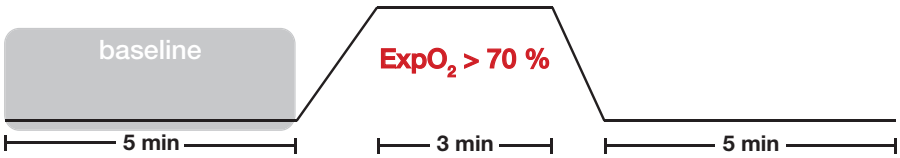

Figure C.3: Hyperoxia protocol. This illustration was previously shown as part of Figure 7.1.

	rCBF	$rCBFV_{sys}$	$rCBFV_{mean}$	$rCBFV_{dia}$	ΔBP_{sys}	ΔBP_{dia}	ΔMAP	ΔHR
$rCBFV_{sys}$	0.06							
$rCBFV_{mean}$	-0.03	0.30						
$rCBFV_{dia}$	-0.14	0.43	0.17					
ΔBP_{sys}	0.22	-0.12	-0.07	-0.16				
ΔBP_{dia}	0.07	-0.36	-0.09	-0.22	0.79^{***}			
ΔMAP	0.19	-0.30	-0.14	-0.21	0.93^{***}	0.94^{***}		
ΔHR	0.64^{*}	-0.12	-0.18	-0.19	0.67^{**}	0.66^{*}	0.68^{**}	
ΔSpO_2	-0.19	0.00	0.38	-0.15	0.47	0.10	0.26	-0.10

	rCBF	ΔSrO_{2arm}	ΔSrO_{2leg}	$\Delta ExpO_2$	ΔSV	ΔCO	ΔSVR	ΔSI
ΔSrO_{2arm}	0.24							
ΔSrO_{2leg}	0.37	-0.14						
$\Delta ExpO_2$	-0.18	-0.25	-0.28					
ΔSV	0.67^{**}	-0.03	0.11	-0.40				
ΔCO	0.68^{**}	0.35	0.10	-0.09	0.55^{*}			
ΔSVR	-0.81^{***}	-0.15	-0.51	0.42	-0.77^{**}	-0.71^{**}		
ΔSI	0.60^{*}	-0.05	0.09	-0.40	0.96^{***}	0.52	-0.76^{**}	
ΔCI	0.66^{**}	0.34	0.08	-0.09	0.55^{*}	0.99^{***}	-0.68^{**}	0.51

Table C.1: Spearman correlation test results during hyperoxia (HO) in supine position. The levels of significance are defined as follows: *** for $p < 0.001$; ** for $p < 0.01$; * for $p < 0.05$.

	rCBF	$rCBFV_{sys}$	$rCBFV_{mean}$	$rCBFV_{dia}$	ΔBP_{sys}	ΔBP_{dia}	ΔMAP	ΔHR
$rCBFV_{sys}$	-0.08							
$rCBFV_{mean}$	0.21	0.21						
$rCBFV_{dia}$	0.13	0.22	0.64*					
ΔBP_{sys}	0.18	0.12	0.70**	0.27				
ΔBP_{dia}	0.03	0.04	0.79***	0.45	0.89***			
ΔMAP	0.12	0.07	0.78***	0.40	0.94***	0.96***		
ΔHR	-0.22	-0.39	-0.45	-0.31	-0.29	-0.17	-0.32	
ΔSpO_2	-0.31	0.32	-0.09	0.36	-0.16	-0.20	-0.14	-0.32

	rCBF	ΔSrO_{2arm}	ΔSrO_{2leg}	$\Delta ExpO_2$	ΔSV	ΔCO	ΔSVR	ΔSI
ΔSrO_{2arm}	0.34							
ΔSrO_{2leg}	-0.25	0.31						
$\Delta ExpO_2$	-0.29	-0.34	-0.24					
ΔSV	0.07	-0.39	-0.02	0.04				
ΔCO	-0.27	0.20	-0.15	0.05	-0.42			
ΔSVR	0.22	0.03	0.02	-0.45	0.16	-0.74**		
ΔSI	0.12	-0.30	0.01	-0.01	0.98***	-0.34	0.10	
ΔCI	-0.10	0.26	-0.16	-0.02	-0.40	0.94***	-0.66**	-0.31

Table C.2: Spearman correlation test results during hyperoxia (HO) in 50° sitting position. The levels of significance are defined as follows: *** for $p < 0.001$; ** for $p < 0.01$; * for $p < 0.05$.

C.2.2 *Hypercapnia*

Tables C.3 and C.4 represent the Spearman correlations for values obtained during hypercapnia (HRC) in two different positions. Table C.3 refers to the supine and Table C.4 to the 50° position. For the details on the protocol for this challenge please refer to Figure C.4.

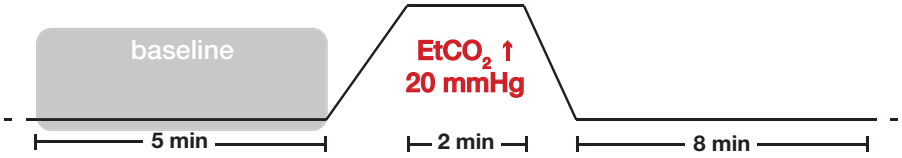

Figure C.4: Hypercapnia protocol. This illustration was previously shown as part of Figure 7.1.

	rCBF	$rCBFV_{sys}$	$rCBFV_{mean}$	$rCBFV_{dia}$	ΔBP_{sys}	ΔBP_{dia}	ΔMAP	ΔHR
$rCBFV_{sys}$	-0.65*							
$rCBFV_{mean}$	0.07	0.29						
$rCBFV_{dia}$	-0.35	0.57	0.29					
ΔBP_{sys}	0.23	0.09	0.00	0.24				
ΔBP_{dia}	0.30	-0.04	-0.13	0.17	0.80**			
ΔMAP	0.21	0.17	0.13	0.43	0.84***	0.91***		
ΔHR	0.23	-0.54	0.01	-0.16	-0.30	0.11	-0.07	
ΔSpO_2	0.55	-0.73*	-0.66*	-0.62	0.09	-0.07	-0.08	-0.11
	rCBF	ΔSrO_{2arm}	ΔSrO_{2leg}	$\Delta EtCO_2$	ΔSV	ΔCO	ΔSVR	ΔSI
ΔSrO_{2arm}	0.18							
ΔSrO_{2leg}	0.36	-0.55						
$\Delta EtCO_2$	-0.07	0.22	-0.47					
ΔSV	0.36	0.70*	-0.41	0.19				
ΔCO	0.42	0.33	0.19	-0.13	0.16			
ΔSVR	-0.14	-0.57	0.25	-0.16	-0.35	-0.48		
ΔSI	0.31	0.70*	-0.43	0.10	0.99***	0.12	-0.31	
ΔCI	0.42	0.33	0.19	-0.13	0.16	1.00***	-0.48	0.12

Table C.3: Spearman correlation test results during hypercapnia (HRC) in supine position. The levels of significance are defined as follows: *** for $p < 0.001$; ** for $p < 0.01$; * for $p < 0.05$.

	rCBF	$rCBFV_{sys}$	$rCBFV_{mean}$	$rCBFV_{dia}$	ΔBP_{sys}	ΔBP_{dia}	ΔMAP	ΔHR
$rCBFV_{sys}$	-0.37							
$rCBFV_{mean}$	-0.38	0.08						
$rCBFV_{dia}$	-0.14	0.15	0.41					
ΔBP_{sys}	0.65*	-0.27	0.08	0.50				
ΔBP_{dia}	0.75*	-0.17	-0.23	0.25	0.93***			
ΔMAP	0.75*	-0.17	-0.23	0.25	0.93***	1.00***		
ΔHR	0.27	0.10	-0.12	0.15	0.07	0.22	0.22	
ΔSpO_2	-0.02	-0.18	-0.15	-0.02	-0.05	0.01	0.01	-0.25
	rCBF	ΔSrO_{2arm}	ΔSrO_{2leg}	$\Delta EtCO_2$	ΔSV	ΔCO	ΔSVR	ΔSI
ΔSrO_{2arm}	0.13							
ΔSrO_{2leg}	0.33	0.16						
$\Delta EtCO_2$	-0.28	0.33	-0.11					
ΔSV	-0.30	0.73*	-0.12	0.13				
ΔCO	0.22	-0.22	-0.15	-0.45	0.16			
ΔSVR	0.70*	0.37	-0.02	-0.05	-0.22	-0.30		
ΔSI	-0.32	0.62	-0.15	0.12	0.99***	0.21	-0.28	
ΔCI	0.13	-0.25	-0.18	-0.37	0.16	0.98***	-0.38	0.22

Table C.4: Spearman correlation test results during hypercapnia (HRC) in 50° sitting position. The levels of significance are defined as follows: *** for $p < 0.001$; ** for $p < 0.01$; * for $p < 0.05$.

C.2.3 *Hyperventilation*

Tables C.5 and C.6 represent the Spearman correlations for values obtained during hyperventilation (HV) in two different positions. Table C.5 refers to the supine and Table C.6 to the 50° position. For the details on the protocol for this challenge please refer to Figure C.5.

Figure C.5: Hyperventilation protocol. This illustration was previously shown as part of Figure 7.1.

	rCBF	$rCBFV_{sys}$	$rCBFV_{mean}$	$rCBFV_{dia}$	ΔBP_{sys}	ΔBP_{dia}	ΔMAP	ΔHR
$rCBFV_{sys}$	0.38							
$rCBFV_{mean}$	0.49	0.25						
$rCBFV_{dia}$	0.41	0.05	0.60*					
ΔBP_{sys}	0.63*	0.27	0.75**	0.69**				
ΔBP_{dia}	0.61*	0.29	0.70**	0.64*	0.95***			
ΔMAP	0.67**	0.34	0.77**	0.68**	0.99***	0.97***		
ΔHR	-0.11	-0.19	-0.38	-0.24	-0.28	-0.22	-0.33	
ΔSpO_2	0.21	-0.13	0.40	0.47	0.62*	0.64*	0.58*	0.07

	rCBF	ΔSrO_{2arm}	ΔSrO_{2leg}	$\Delta EtCO_2$	ΔSV	ΔCO	ΔSVR	ΔSI
ΔSrO_{2arm}	0.13							
ΔSrO_{2leg}	0.32	0.15						
$\Delta EtCO_2$	0.57*	0.02	0.27					
ΔSV	0.21	0.43	0.20	-0.16				
ΔCO	0.04	0.13	0.34	0.16	0.17			
ΔSVR	0.37	0.54	-0.29	0.36	-0.09	-0.59*		
ΔSI	0.21	0.46	0.16	-0.15	0.99***	0.18	-0.08	
ΔCI	0.10	0.06	0.40	0.35	0.07	0.95***	-0.46	0.07

Table C.5: Spearman correlation test results during hyperventilation (HV) in supine position. The levels of significance are defined as follows: *** for $p < 0.001$; ** for $p < 0.01$; * for $p < 0.05$.

	rCBF	$rCBFV_{sys}$	$rCBFV_{mean}$	$rCBFV_{dia}$	ΔBP_{sys}	ΔBP_{dia}	ΔMAP	ΔHR
$rCBFV_{sys}$	0.50							
$rCBFV_{mean}$	0.57*	0.66*						
$rCBFV_{dia}$	0.45	0.67**	0.77**					
ΔBP_{sys}	-0.34	-0.13	-0.36	-0.06				
ΔBP_{dia}	-0.21	-0.20	-0.32	0.00	0.87***			
ΔMAP	-0.27	-0.06	-0.30	0.04	0.94***	0.96***		
ΔHR	0.12	0.14	-0.13	-0.12	-0.49	-0.39	-0.43	
ΔSpO_2	-0.14	-0.40	0.04	-0.27	0.39	0.49	0.47	-0.58*

	rCBF	ΔSrO_{2arm}	ΔSrO_{2leg}	$\Delta EtCO_2$	ΔSV	ΔCO	ΔSVR	ΔSI
ΔSrO_{2arm}	0.26							
ΔSrO_{2leg}	0.27	0.53						
$\Delta EtCO_2$	0.50	0.72*	0.27					
ΔSV	-0.27	0.76*	0.32	0.01				
ΔCO	-0.31	0.33	0.35	-0.20	0.39			
ΔSVR	0.46	-0.21	-0.15	0.40	-0.54*	-0.85***		
ΔSI	-0.26	0.78**	0.32	0.06	0.99***	0.37	-0.49	
ΔCI	-0.10	0.35	0.41	-0.09	0.22	0.94***	-0.76***	0.21

Table C.6: Spearman correlation test results during hyperventilation (HV) in 50° sitting position. The levels of significance are defined as follows: *** for $p < 0.001$; ** for $p < 0.01$; * for $p < 0.05$.

D

ADVANTAGES OF A HYBRID DEVICE IN HEAD-OF-BED PROCEDURES

In Chapter 9, the HOB angle change 30°→ 0° (or "supine") was chosen in order to investigate the dependency of the resulting BFI values for each position between different evaluation types. The different methods used to analyse DCS data were:

Method I: fix μ_a at 0.1 cm^{-1} and μ_s' at 10 cm^{-1}

Method II: population (n = 10) average of μ_a and μ_s'

Method III: subject average of μ_a and μ_s' (entire sequence)

Method IV: subject position average of μ_a and μ_s'

Method V: subject individual μ_a and μ_s' per acquisition ("one-to-one")

Each position was kept for five minutes.

D.1 RIGHT BRAIN HEMISPHERE DATA

D.1.1 *Blood flow index data*

The BFI values calculated according to the methods explained in Section 9.2 are presented in Figure D.1. Their median (IQR) values are shown in Table D.1.

From the right hemisphere - as shown in Table D.1 - we obtain median (IQR) values for method I of $BFI_{30°,\,I}$ = 6.88 (3.96) × 10^{-9} cm^2/s and $BFI_{supine,\,I}$ = 11.37 (7.49) × 10^{-9} cm^2/s and the

Figure D.1: Comparing evaluation methods I-V against each other by looking at the BFI.

method #	position	Median BFI (IQR) [cm²/s] × 10^{-9}
I	+30°	6.88 (3.96)
	supine	11.37 (7.49)
II	+30°	6.58 (3.83)
	supine	10.87 (7.14)
III	+30°	6.23 (3.29)
	supine	9.25 (5.17)
IV	+30°	5.75 (3.44)
	supine	9.25 (5.17)
V	+30°	6.13 (3.40)
	supine	9.27 (5.14)

Table D.1: Medians (and IQR) for the absolute BFI values taken from the right brain hemisphere separated by methods and positions. Data was taken in two positions according to measurement protocol.

ones for the study averaged μ_a and μ_s' values (method II) to $\mathrm{BFI}_{30°,\,\mathrm{II}}$ = 6.58 (3.83) × 10^{-9} cm²/s and $\mathrm{BFI}_{\mathrm{supine},\,\mathrm{II}}$ = 10.87 (7.14) × 10^{-9} cm²/s.

In the case of method III, where we used the individualised μ_a and μ_s' values from each subject, the BFI median (IQR) values result in $\mathrm{BFI}_{30°,\,\mathrm{III}}$ = 6.23 (3.29) × 10^{-9} cm²/s and $\mathrm{BFI}_{\mathrm{supine},\,\mathrm{III}}$ = 9.25 (5.17) × 10^{-9} cm²/s. In methods IV and V we obtain median (IQR) values of $\mathrm{BFI}_{30°,\,\mathrm{IV}}$ = 5.75 (3.44) × 10^{-9} cm²/s and

$BFI_{supine,\,IV}$ = 9.25 (5.17) × 10^{-9} cm^2/s and $BFI_{30°,\,V}$ = 6.13 (3.40) × 10^{-9} cm^2/s and $BFI_{supine,\,V}$ = 9.27 (5.14) × 10^{-9} cm^2/s.

A LME model on method influence[1] revealed a significant difference between the first two methods (I and II) and method III-V ($p \leq 0.05$). The according p-values are presented in Table D.2. For better visibility, statistically significant differences between methods are marked by a grey background.

	30° position			
method	I	II	III	IV
II	$p > 0.05$	-		
III	$p < 0.01$	$p < 0.05$	-	
IV	$p < 0.01$	$p = 0.01$	$p > 0.05$	-
V	$p < 0.01$	$p = 0.01$	$p > 0.05$	$p > 0.05$
	supine position			
II	$p > 0.05$	-		
III	$p < 0.01$	$p < 0.01$	-	
IV	$p < 0.01$	$p < 0.01$	$p > 0.05$	-
V	$p < 0.01$	$p < 0.01$	$p > 0.05$	$p > 0.05$

Table D.2: Results (p-values) from a LME model with the method factor for the absolute BFI values. Statistically significance is marked by a grey background.

The top part of Table D.2 shows the resulting p-values for the comparison of BFI values from the 30° position between methods. The bottom part refers to the same test, but conducting it on the BFI values taken while the volunteers was in the supine position.

All values between positions differ significantly ($p < 0.001$) independently of the used analysis method. The BFIs calculated based on methods I and II differ significantly ($p < 0.05$) from the ones evaluated with method III, IV and V. Between the latter three, no significant difference was found.

D.1.2 *Relative cerebral blood flow changes*

After evaluating BFI according to the five methods presented in Section 9.2, for each volunteer the 30° position average

1 The fitted intercepts and their slopes are presented in Table D.6.

was taken as a baseline and the CBF change with the HOB angle calculated for each method individually. The resulting rCBF values are shown in Figure D.2. The graph compares all five methods (I:"fixed"; II: "study average"; III: "subject average"; IV:"subject position average" and V: "one-to-one" usage of μ_a and μ_s').

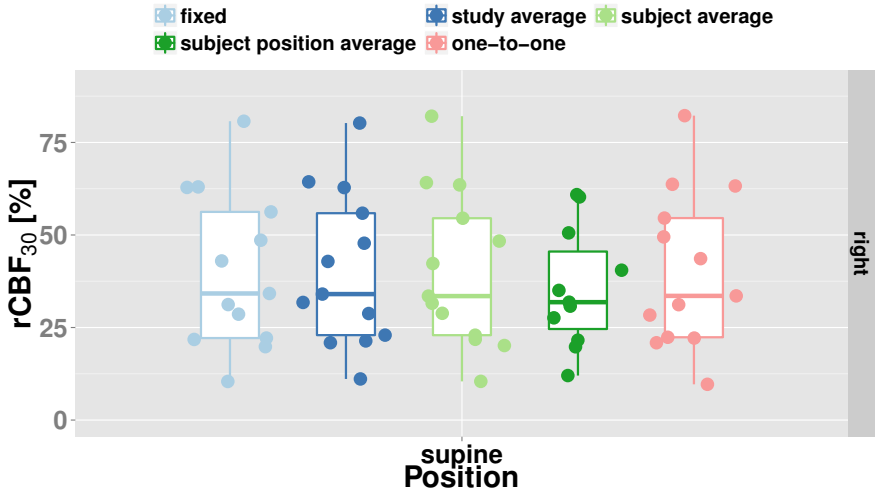

Figure D.2: Comparing evaluation methods 1-4 against each other by looking at the CBF changes with respect to the 30° position (starting position). The dashed line represents zero CBF change.

method #	Median $\mathrm{rCBF}_{30°}$ (IQR) %
I	32.70 (36.60)
II	32.90 (36.36)
III	32.52 (35.38)
IV	33.44 (39.30)
V	32.36 (34.90)

Table D.3: Medians (and IQR) for the relative CBF changes with respect to initial 30° position separated by methods.

Table D.3 shows the rCBF values in terms of a median and its respective IQR after the change from 30° to supine position for each analysis method in the right hemisphere. These values set for method I to $\mathrm{rCBF}_{\mathrm{right,\ I}}$ = 32.70 (36.60) % and the ones for the study averaged μ_a and μ_s' values (method II) to $\mathrm{rCBF}_{\mathrm{right,\ II}}$ = 32.90 (36.36) %.

In the case of method III, where we used the individualised μ_a and μ_s' values from each subject, the rCBF median (IQR) values result in $rCBF_{right,\ III}$ = 32.52 (35.38) %. In methods IV and V we obtain median (IQR) values of $rCBF_{right,\ IV}$ = 33.44 (39.30) % and $rCBF_{right,\ V}$ = 32.36 (34.90) %.

Similar to the analysis of the BFI values (Section 9.3.1), a LME model to investigate differences between rCBF values among different analysis methods[2] was employed. Here we only compare rCBF in the supine position between the above-presented different analysis methods. The p-values of this investigation are shown in Table D.4. As before, statistically significant differences between methods are marked by a grey background for better visibility.

method	I	II	III	IV
II	p > 0.05	-		
III	p > 0.05	p > 0.05	-	
IV	p < 0.01	p < 0.01	p = 0.05	-
V	p > 0.05	p > 0.05	p > 0.05	p < 0.01

Table D.4: Results (p-values) from a LME model with the method factor for the relative CBF values with respect to the initial 30° position. Statistically significance is marked by a grey background.

According to Table 9.5, the rCBF calculated based on method I-III does not differ significantly. Method IV differs significantly ($p \leq 0.05$) from all other ones in the resulting rCBF for a change from 30° to supine position. Values obtained from method V are comparable to method I-III.

D.2 COMPARISON OF DCS ANALYSIS METHODS (BFI)

A LME model employed on the BFI values taken in the study presented in Chapter 9 with the position factor every analysis method used are shown in Tables D.7 and D.7.

BFI values in the left brain hemisphere fitted with μ_a and μ_s' values of 0.1 cm^{-1} and 10 cm^{-1} (method I) set to $BFI_{30°,\ I}$ = 7.36 ± 0.82 × 10^{-9} cm^2/s and $BFI_{supine,\ I}$ = 10.33 ± 0.70 × 10^{-9} cm^2/s and the ones for the study averaged μ_a and μ_s' values (method II)

2 The fitted intercepts and their slopes are presented in Tables D.7 and D.8

method #	position	LME fitted BFI ± standard error [cm²/s] × 10^{-9}
I	+30°	7.36 ± 0.82
	supine	10.33 ± 0.70
II	+30°	7.05 ± 0.80
	supine	9.94 ± 0.68
III	+30°	5.90 ± 0.79
	supine	8.18 ± 0.56
IV	+30°	5.80 ± 0.79
	supine	8.18 ± 0.59
V	+30°	5.78 ± 0.76
	supine	8.02 ± 0.54

Table D.5: Results from a LME model with the method factor for the absolute BFI values taken from the left brain hemisphere separated by HOB position. Data was taken in two positions according to measurement protocol.

to $BFI_{30°,\,II}$ = 7.05 ± 0.80 × 10^{-9} cm²/s and $BFI_{supine,\,II}$ = 9.94 ± 0.68 × 10^{-9} cm²/s.

In the case of method III, where we used the individualised μ_a and μ_s' values from each subject, the BFI was fitted to $BFI_{30°,\,III}$ = 5.90 ± 0.79 × 10^{-9} cm²/s and $BFI_{supine,\,III}$ = 8.18 ± 0.56 × 10^{-9} cm²/s. In methods IV and V the LME models fit these values to $BFI_{30°,\,IV}$ = 5.80 ± 0.79 × 10^{-9} cm²/s and $BFI_{supine,\,IV}$ = 8.18 ± 0.59 × 10^{-9} cm²/s and $BFI_{30°,\,V}$ = 5.78 ± 0.76 × 10^{-9} cm²/s and $BFI_{supine,\,V}$ = 8.02 ± 0.54 × 10^{-9} cm²/s.

BFI values in the right brain hemisphere fitted with μ_a and μ_s' values of 0.1 cm^{-1} and 10 cm^{-1} (method I) set to $BFI_{30°,\,I}$ = 8.71 ± 1.34 × 10^{-9} cm²/s and $BFI_{supine,\,I}$ = 11.62 ± 0.65 × 10^{-9} cm²/s and the ones for the study averaged μ_a and μ_s' values (method II) to $BFI_{30°,\,II}$ = 8.33 ± 1.29 × 10^{-9} cm²/s and $BFI_{supine,\,II}$ = 11.12 ± 0.63 × 10^{-9} cm²/s.

In the case of method III, where we used the individualised μ_a and μ_s' values from each subject, the BFI was fitted to $BFI_{30°,\,III}$ = 6.70 ± 0.82 × 10^{-9} cm²/s and $BFI_{supine,\,III}$ = 9.00 ± 0.52 × 10^{-9} cm²/s. In methods IV and V the LME models fit these values to $BFI_{30°,\,IV}$ = 6.55 ± 0.83 × 10^{-9} cm²/s and $BFI_{supine,\,IV}$ = 9.00 ± 0.52 × 10^{-9} cm²/s and $BFI_{30°,\,V}$ = 6.60 ± 0.82 × 10^{-9} cm²/s and $BFI_{supine,\,V}$ = 8.88 ± 0.48 × 10^{-9} cm²/s.

method #	position	LME fitted BFI ± standard error [cm²/s] × 10^{-9}
I	+30°	8.71 ± 1.34
	supine	11.62 ± 0.65
II	+30°	8.33 ± 1.29
	supine	11.12 ± 0.63
III	+30°	6.70 ± 0.82
	supine	9.00 ± 0.48
IV	+30°	6.55 ± 0.83
	supine	9.00 ± 0.52
V	+30°	6.60 ± 0.82
	supine	8.88 ± 0.48

Table D.6: Results from a LME model with the position factor for the absolute BFI values taken from the right brain hemisphere separated by HOB position. Data was taken in two positions according to measurement protocol.

D.3 RELATIVE CBF CHANGES WITH HOB PROTOCOL FOR DIFFERENT ANALYSIS METHODS

Results of a LME model with the position factor every analysis method used are shown in Tables D.7 and D.8 for the rCBF values. The values for the initial 30° position are a result of the LME fit and therefore present a standard error.

method #	LME fitted $rCBF_{30°}$ ± standard error
I	40.10 ± 8.81
II	40.70 ± 8.93
III	40.60 ± 8.95
IV	44.87 ± 10.90
V	40.57 ± 8.92

Table D.7: Results from a LME model with the position factor for the absolute rCBF values taken from the left brain hemisphere separated by HOB position. All changes (30°→ 0°) are statistically significant ($p < 0.001$).

The rCBF values in the left brain hemisphere normalised to the initial 30° position and fitted with μ_a and μ_s' values of 0.1 cm^{-1} and 10 cm^{-1} (method I) set to $rCBF_{30°,\,I}$ = 40.10 ± 8.81 %

and the ones for the study averaged μ_a and μ_s' values (method II) to $rCBF_{30°,\,II}$ = 40.70 ± 8.93 %.

In the case of method III, where we used the individualised μ_a and μ_s' values from each subject, the BFI was fitted to $rCBF_{30°,\,III}$ = 40.60 ± 8.95 %. In methods IV and V the LME models fit these values to $rCBF_{30°,\,IV}$ = 44.87 ± 10.90 % and $rCBF_{30°,\,V}$ = 40.57 ± 8.92 %.

method #	LME fitted $rCBF_{30°}$ ± standard error
I	38.96 ± 7.33
II	39.06 ± 7.30
III	39.03 ± 7.32
IV	43.97 ± 8.90
V	39.22 ± 7.43

Table D.8: Results from a LME model with the position factor for the absolute rCBF values taken from the right brain hemisphere separated by HOB position. All changes (30°→ 0°) are statistically significant ($p < 0.001$).

The rCBF values in the right brain hemisphere normalised to the initial 30° position and fitted with μ_a and μ_s' values of 0.1 cm^{-1} and 10 cm^{-1} (method I) set to $rCBF_{30°,\,I}$ = 38.96 ± 7.33 % and the ones for the study averaged μ_a and μ_s' values (method II) to $rCBF_{30°,\,II}$ = 39.06 ± 7.30 %.

In the case of method III, where we used the individualised μ_a and μ_s' values from each subject, the BFI was fitted to $rCBF_{30°,\,III}$ = 39.03 ± 7.32 %. In methods IV and V the LME models fit these values to $rCBF_{30°,\,IV}$ = 43.97 ± 8.90 % and $rCBF_{30°,\,V}$ = 39.22 ± 7.43 %.

BIBLIOGRAPHY

[1] ASA. «Practice Advisory for Intraoperative Awareness and Brain Function Monitoring.» In: *Anesthesiology* 104.104 (2006), pp. 847–864. ISSN: 0003-3022.

[2] R Aaslid, T M Markwalder, and H Nornes. «Noninvasive transcranial Doppler ultrasound recording of flow velocity in basal cerebral arteries.» In: *J. Neurosurg.* 57.6 (1982), pp. 769–74. ISSN: 0022-3085.

[3] R Aaslid et al. «Cerebral autoregulation dynamics in humans.» In: *Stroke* 20.1 (1989), pp. 45–52. ISSN: 0039-2499.

[4] B. J. Ackerson et al. «Correlation transfer - Application of radiative transfer solution methods to photon correlation problems.» In: *J. Thermophys. Heat Transf.* 6.4 (1992), pp. 577–588. ISSN: 0887-8722.

[5] G Agarwal and S S Sikh. «Awareness during anaesthesia. A prospective study.» In: *Br. J. Anaesth.* 49.8 (1977), pp. 835–838. ISSN: 01406736.

[6] Dewesh Agrawal et al. «Bispectral index monitoring quantifies depth of sedation during emergency department procedural sedation and analgesia in children.» In: *Ann. Emerg. Med.* 43.2 (2004), pp. 247–255. ISSN: 01960644.

[7] Philip N Ainslie and James Duffin. «Integration of cerebrovascular CO2 reactivity and chemoreflex control of breathing: mechanisms of regulation, measurement, and interpretation.» In: *Am. J. Physiol. Regul. Integr. Comp. Physiol.* 296.5 (2009), R1473–95. ISSN: 0363-6119.

[8] Michael T Alkire et al. «Cerebral Metabolism during Propofol Anesthesia in Humans Studied with Positron Emission Tomography.» In: *Anesthesiology* 82.2 (1995), pp. 393–403.

[9] Michael T Alkire et al. «Positron Emission Tomography Study of Regional Cerebral Metabolism in Humans during Isoflurane Anesthesia.» In: *Anesthesiology* 86.3 (1997), pp. 549–57.

[10] M Appetecchia and F M Solivetti. «The association of colour flow Doppler sonography and conventional ultrasonography improves the diagnosis of thyroid carcinoma.» In: *Horm. Res. Paediatr.* 66.5 (2006), pp. 249–256.

[11] Marcel J H Aries et al. «Cerebral autoregulation in stroke: A review of transcranial doppler studies.» In: *Stroke* 41.11 (2010), pp. 2697–2704. ISSN: 00392499.

[12] Marcel J H Aries et al. «Cerebral blood flow velocity changes during upright positioning in bed after acute stroke: an observational study.» In: *BMJ Open* 3.8 (2013), pp. 1–8. ISSN: 2044-6055.

[13] Simon R Arridge, M Cope, and D T Delpy. «The theoretical basis for the determination of optical pathlengths in tissue: temporal and frequency analysis.» In: *Phys. Med. Biol.* 37.7 (1992), pp. 1531–60. ISSN: 0031-9155.

[14] P Astrup et al. «The Influence of Temperature and Ph on the Dissociation Curve of Oxyhemoglobin of Human Blood.» In: *Scand. J. Clin. Lab. Investig.* 17.6 (1965), pp. 515–523. ISSN: 0036-5513.

[15] L Austin and H Starke. «Ueber die Reflexion der Kathodenstrahlen und eine damit verbundene neue Erscheinung secundärer Emission.» In: *Ann. Phys.* 314.10 (1902), pp. 271–292. ISSN: 1521-3889.

[16] Michael S Avidan and George A Mashour. «Prevention of intraoperative awareness with explicit recall: making sense of the evidence.» In: *Anesthesiology* 118.2 (2013), pp. 449–456. ISSN: 1528-1175 (Electronic).

[17] Wesley Boehs Baker. «Optical Cerebral Blood Flow Monitoring of Mice To Men.» PhD thesis. University of Pennsylvania, 2015, p. 273.

[18] Wolfgang Becker. *Advanced Time-Correlated Single Photon Counting Techniques*. Ed. by A. W. Castleman, J.P. Toennies, and W. Zinth. Vol. 81. Springer Series in Chemical Physics. Berlin, Heidelberg: Springer Berlin Heidelberg, 2005, pp. 4–9. ISBN: 978-3-540-26047-9.

[19] Wolfgang Becker. *The bh TCSPC Handbook*. 6th ed. 2014, p. 768.

[20] Wolfgang Becker, Bertram Su, and Axel Bergmann. «Better FLIM and FCS data by GaAsP hybrid detectors.» In: *Sci. York* 7569 (2010), 75690S–75690S–10. ISSN: 16057422.

[21] T. Bellini et al. «Effects of finite laser coherence in quasielastic multiple scattering.» In: *Phys. Rev. A* 44.8 (1991), pp. 5215–5223. ISSN: 1050-2947.

[22] A Beloiartsev and H Theilen. «Operative Eingriffe in sitzender Position: Anästhesiologische Besonderheiten.» In: *Anaesthesist* 60.9 (2011), pp. 863–877. ISSN: 00032417.

[23] Julie Bernhardt. «Could upright posture be harmful in the early stages of stroke? - Author's reply.» In: *Lancet* 386.10005 (2015), pp. 1734–1735. ISSN: 1474547X.

[24] C C Bishop et al. «Transcranial Doppler Measurement of Middle Cerebral Artery Blood Flow Velocity : A Validation Study.» In: *Stroke* 17.5 (1986), pp. 913–916.

[25] Susan Black et al. «Preoperative and Intraoperative Echocardiography to Detect Right-to-Left Shunt in Patients Undergoing Neurosurgical Procedures in the Sitting Position.» In: *Anes* 72.3 (1990), pp. 436–438.

[26] Igor Blanco. «Diffuse optical monitoring of cerebral hemodynamics in experimental and clinical neurology.» PhD thesis. 2014.

[27] David A Boas. «Diffuse photon probes of structural and dynamical properties of turbid media: Theory and biomedical application.» PhD thesis. University of Pennsylvania, 1996, p. 260. ISBN: 9780591019735 0591019736.

[28] David A Boas, L E Campbell, and Arjun G Yodh. «Scattering and Imaging with Diffusing Temporal Field Correlations.» In: *Phys. Rev. Lett.* 75.9 (1995), pp. 1855–1858.

[29] David A Boas, Anders M Dale, and Maria Angela Franceschini. «Diffuse optical imaging of brain activation: approaches to optimizing image sensitivity, resolution, and accuracy.» In: *Neuroimage* 23 Suppl 1 (2004), S275–88. ISSN: 1053-8119.

[30] David A Boas and Arjun G Yodh. «Spatially varying dynamical properties of turbid media probed with diffusing temporal light correlation.» In: *J. Opt. Soc. Am. A* 14.1 (1997), pp. 192–215. ISSN: 1084-7529.

[31] David A Boas et al. «A vascular anatomical network model of the spatio-temporal response to brain activation.» In: *Neuroimage* 40.3 (2008), pp. 1116–1129. ISSN: 10538119. arXiv: NIHMS150003.

[32] David A Boas et al. «The accuracy of near infrared spectroscopy and imaging during focal changes in cerebral hemodynamics.» In: *Neuroimage* 13.1 (2001), pp. 76–90. ISSN: 1053-8119.

[33] David a Boas and Maria Angela Franceschini. «Haemoglobin oxygen saturation as a biomarker: the problem and a solution.» In: *Philos. Trans. R. Soc. A Math. Phys. Eng. Sci.* 369.1955 (2011), pp. 4407–4424. ISSN: 1364-503X.

[34] D S Bolar et al. «Depression of cortical gray matter CMRO2 in awake humans during hypercapnia.» In: *Proc Int Soc Magn Reson Med* 18 (2010), p. 516.

[35] Vincent Bonhomme et al. «Influence of anesthesia on cerebral blood flow, cerebral metabolic rate, and brain functional connectivity.» In: *Curr. Opin. Anaesthesiol.* 24.5 (2011), pp. 474–479. ISSN: 0952-7907.

[36] Robert S Bonser, Domenico Pagano, and Axel Haverich. *Brain protection in cardiac surgery*. Springer, 2011.

[37] Jean-Pierre Bouchard et al. «Reference optical phantoms for diffuse optical spectroscopy. Part 1–Error analysis of a time resolved transmittance characterization method.» In: *Opt. Express* 18.11 (2010), pp. 11495–507. ISSN: 1094-4087.

[38] Thomas W Bouillon et al. «Pharmacodynamic Interaction between Propofol and Remifentanil Regarding Hypnosis , Tolerance of Laryngoscopy , Bispectral Index , and Electroencephalographic Approximate Entropy.» In: *Anesthesiology* 100.6 (2004), pp. 1353–1372. ISSN: 0003-3022.

[39] A F Bradley, M. Stupfel, and John W Severinghaus. «Effect of temperature on PCO2 and PO2 of blood in vitro.» In: *J. Appl. Physiol.* 9.2 (1956), pp. 201–204.

[40] Mariana Pimenta Brandao et al. «Fluorescence lifetime of normal, benign, and malignant thyroid tissues.» In: *J. Biomed. Opt.* 20.6 (2015), p. 67003. ISSN: 1560-2281.

[41] Mariana Pimenta Brandao et al. «Optical Characterization of Normal, Benign, and Malignant Thyroid Tissue: A Pilot Study.» In: *J. Fluoresc.* 25.2 (2015), pp. 465–471. ISSN: 1053-0509.

[42] L Brass et al. «Middle cerebral artery blood velocity and cerebral blood flow in sickle cell disease.» In: *Stroke* 22.1 (1991), pp. 27–30. ISSN: 0039-2499.

[43] J Bruhn et al. «Depth of anaesthesia monitoring: What's available, what's validated and what's next?» In: *Br. J. Anaesth.* 97.1 (2006), pp. 85–94. ISSN: 00070912.

[44] Erin M Buckley et al. «Cerebral hemodynamics in preterm infants during positional intervention measured with diffuse correlation spectroscopy and transcranial Doppler ultrasound.» In: *Opt. Express* 17.15 (2009), pp. 12571–12581. ISSN: 1094-4087.

[45] Erin M Buckley et al. «Early postoperative changes in cerebral oxygen metabolism following neonatal cardiac surgery: effects of surgical duration.» In: *J. Thorac. Cardiovasc. Surg.* 145.1 (2013), 196–203, 205.e1; discussion 203–5. ISSN: 1097-685X.

[46] Erin M Buckley et al. «Validation of diffuse correlation spectroscopic measurement of cerebral blood flow using phase-encoded velocity mapping magnetic resonance imaging.» In: *J. Biomed. Opt.* 17.3 (2012), p. 037007. ISSN: 10833668.

[47] Daniel P Bulte et al. «Cerebral perfusion response to hyperoxia.» In: *J. Cereb. Blood Flow Metab.* 27.1 (2007), pp. 69–75. ISSN: 0271-678X.

[48] E A Burykh. «Interaction of hypocapnia, hypoxia, brain blood flow, and brain electrical activity in voluntary hyperventilation in humans.» In: *Neurosci Behav Physiol* 38.7 (2008), pp. 647–659. ISSN: 0097-0549.

[49] R B Buxton and L R Frank. «A model for the coupling between cerebral blood flow and oxygen metabolism during neural stimulation.» In: *J. Cereb. Blood Flow Metab.* 17 (1997), pp. 64–72. ISSN: 0271-678X.

[50] S A Carp et al. «Validation of diffuse correlation spectroscopy measurements of rodent cerebral blood flow with simultaneous arterial spin labeling MRI; towards MRI-optical continuous cerebral metabolic monitoring.» In: *Biomed. Opt. Express* 1.2 (2010), pp. 553–565. ISSN: 2156-7085.

[51] T Adrian Carpenter and John D Pickard. «Effect of hyperventilation on cerebral blood flow in traumatic head injury : Clinical relevance and monitoring correlates Effect of hyperventilation on cerebral blood flow in traumatic head injury : Clinical relevance and monitoring correlates.» In: 3493 (2008), pp. 1–11.

[52] Enrique Carrero et al. «Noninvasive monitoring of cerebral blood flow in healthy volunteers: "beach chair" and hypercapnia challenges.» In: *Eur. J. Anaesthesiol.* 31.CI (2014), p. 116.

[53] K M Case and P F Zweifel. *Linear Transport Theory*. Addison-Wesley Series in Nuclear Engineering. Addison-Wesley, 1967, p. 342.

[54] Matthew T. V. Chan and Tony Gin. «What does the bispectral EEG index monitor?» In: *Eur. J. Anaesthesiol.* 17.3 (2000), pp. 146–148. ISSN: 02650215.

[55] M. R. Checketts et al. «Recommendations for standards of monitoring during anaesthesia and recovery 2015: Association of Anaesthetists of Great Britain and Ireland.» In: *Anaesthesia* 71.1 (2016), pp. 85–93. ISSN: 13652044.

[56] Cecil Cheung et al. «In vivo cerebrovascular measurement combining diffuse near-infrared absorption and correlation spectroscopies.» In: *Phys. Med. Biol.* 46.8 (2001), p. 2053.

[57] Vidya Chidambaran, Andrew Costandi, and Ajay D'Mello. «Propofol: A Review of its Role in Pediatric Anesthesia and Sedation.» In: *CNS Drugs* 29.7 (2015), pp. 543–563. ISSN: 11791934.

[58] Silas Chikunguwo et al. «Influence of obesity and surgical weight loss on thyroid hormone levels.» In: *Surg. Obes. Relat. Dis.* 3.6 (2007), 631–5; discussion 635–6. ISSN: 1550-7289.

[59] Regine Choe and Turgut Durduran. «Diffuse optical monitoring of the neoadjuvant breast cancer therapy.» In: *Sel. Top. Quantum Electron. IEEE J.* 18.4 (2012), pp. 1367–1386.

[60] Regine Choe et al. «Optically Measured Microvascular Blood Flow Contrast of Malignant Breast Tumors.» In: *PLoS One* 9.6 (2014). Ed. by Joseph Najbauer, e99683. ISSN: 1932-6203.

[61] Kwan Y Chong et al. *Rate of change of cerebral blood flow velocity with hyperventilation during anesthesia in humans*. 2000.

[62] So Hyun Chung et al. «Macroscopic optical physiological parameters correlate with microscopic proliferation and vessel area breast cancer signatures.» In: *Breast Cancer Res.* 17.1 (2015), p. 72. ISSN: 1465-542X.

[63] Edmund S Cibas and Syed Z Ali. «The Bethesda System for Reporting Thyroid Cytopathology.» In: *Am. J. Clin. Pathol.* 132.5 (2009), pp. 658–665. ISSN: 0002-9173.

[64] Marilyn J. Cipolla. *The Cerebral Circulation*. Vol. 1. 1. 2009. Chap. 5 Control, pp. 1–59.

[65] Julie-Ann Collins et al. «Relating oxygen partial pressure, saturation and content: the haemoglobin–oxygen dissociation curve.» In: *Breathe* 11.3 (2015), pp. 194–201. ISSN: 1810-6838.

[66] Daniela Comelli et al. «In vivo time-resolved reflectance spectroscopy of the human forehead.» In: *Appl. Opt.* 46.10 (2007), pp. 1717–25. ISSN: 0003-6935.

[67] Wikimedia Commons. *Cerebral angiography, injection in the left vertebral artery, with retrograde flow in the contralateral vertebral artery, the basilar artery and the posterior communicating artery. The posterior cerebral circulation can be seen, including the posterior pa*. URL: https://upload.wikimedia.org/wikipedia/commons/3/30/Cerebral{_}angiography{\%}2C{_}arteria{_}vertebralis{_}sinister{_}injection.JPG.

[68] David S Cooper et al. «Revised American Thyroid Association management guidelines for patients with thyroid nodules and differentiated thyroid cancer.» In: *Thyroid* 19.11 (2009), pp. 1167–1214. ISSN: 1050-7256.

[69] James E Cottrell and William L Young. *Cottrell and Young's neuroanesthesia*. 5th Editio. Elsevier Health Sciences, 2010, p. 480. ISBN: 978-0-323-05908-4.

[70] Joseph P. Culver et al. «Diffuse Optical Tomography of Cerebral Blood Flow, Oxygenation, and Metabolism in Rat During Focal Ischemia.» In: *J Cereb Blood Flow Metab* 23.8 (2003), pp. 911–924. ISSN: 0271-678X.

[71] Adrian Curtin et al. «Functional near-infrared spectroscopy for the measurement of propofol effects in conscious sedation during outpatient elective colonoscopy.» In: *Neuroimage* 85 (2014), pp. 626–636. ISSN: 10538119.

[72] Armagan Dagal and Arthur M Lam. «Cerebral autoregulation and anesthesia.» In: *Curr. Opin. Anaesthesiol.* 22.5 (2009), pp. 547–52. ISSN: 1473-6500.

[73] a Dahl et al. «A comparison of transcranial Doppler and cerebral blood flow studies to assess cerebral vasoreactivity.» In: *Stroke.* 23.1 (1992), pp. 15–19. ISSN: 0039-2499.

[74] Kaustuv Das et al. «Raman spectroscopy of parathyroid tissue pathology.» In: *Lasers Med. Sci.* 21.4 (2006), pp. 192–7. ISSN: 0268-8921.

[75] B Davison, JB Sykes, and ER Cohen. *Neutron transport theory*. International series of monographs on physics. Clarendon Press, 1958, p. 450.

[76] G De Cosmo et al. «Changes in cerebral hemodynamics during laparoscopic cholecystectomy.» In: *Neurol. Res.* 21.7 (1999), pp. 658–660. ISSN: 0161-6412.

[77] P Delapille, E Verin, and C Tourny-chollet P Pasquis. «Ventilatory responses to hypercapnia in divers and non-divers : effects of posture and immersion.» In: (2001), pp. 97–103.

[78] A. E. Delfino et al. «Propofol consumption and recovery times after bispectral index or cerebral state index guidance of anaesthesia.» In: *Br. J. Anaesth.* 103.2 (2009), pp. 255–259. ISSN: 00070912.

[79] D T Delpy et al. «Estimation of optical pathlength through tissue from direct time of flight measurement.» In: *Phys. Med. Biol.* 33.12 (1988), pp. 1433–42. ISSN: 0031-9155.

[80] Christian Dippmann, Søren Winge, and Henning Bay Nielsen. «Severe cerebral desaturation during shoulder arthroscopy in the beach-chair position.» In: *Arthrosc. - J. Arthrosc. Relat. Surg.* 26.9 SUPPL. 1 (2010), S148–S150. ISSN: 07498063.

[81] Vikram S Dogra et al. «Preliminary results of ex vivo multispectral photoacoustic imaging in the management of thyroid cancer.» In: *AJR. Am. J. Roentgenol.* 202.6 (2014), W552–8. ISSN: 1546-3141.

[82] C M Domaingue. «Anaesthesia for neurosurgery in the sitting position: A practical approach.» In: *Anaesth. Intensive Care* 33.3 (2005), pp. 323–331. ISSN: 09675868.

[83] Lixin Dong et al. «Simultaneously Extracting Multiple Parameters via Fitting One Single Autocorrelation Function Curve in Diffuse Correlation Spectroscopy.» In: *IEEE Trans. Biomed. Eng.* 60.2 (2013), pp. 361–368. ISSN: 0018-9294.

[84] R. L. Dougherty et al. «Correlation transfer: Development and application.» In: *J. Quant. Spectrosc. Radiat. Transf.* 52.6 (1994), pp. 713–727. ISSN: 00224073.

[85] B. P. Drayer et al. «Xenon enhanced CT for analysis of cerebral integrity, perfusion, and blood flow.» In: *Stroke* 9.2 (1978), pp. 123–130. ISSN: 0039-2499.

[86] Derek A Duke et al. «Venous Air Embolism in Sitting and Supine Patients Undergoing Vestibular Schwannoma Resection.» In: *Neurosurgery* 42.6 (1998). ISSN: 0148-396X.

[87] Andrew K Dunn et al. «Dynamic imaging of cerebral blood flow using laser speckle.» In: *J. Cereb. Blood Flow Metab.* 21.3 (2001), pp. 195–201. ISSN: 0271-678X.

[88] Timothy Q. Duong, Costantino Iadecola, and Seong Gi Kim. «Effect of hyperoxia, hypercapnia, and hypoxia on cerebral interstitial oxygen tension and cerebral blood flow.» In: *Magn. Reson. Med.* 45.1 (2001), pp. 61–70. ISSN: 07403194.

[89] Turgut Durduran. «Noninvasive measurements of tissue hemodynamics with hybrid diffuse optical methods.» PhD thesis. University of Pennsylvania, 2004, p. 287.

[90] Turgut Durduran and Arjun G Yodh. «Diffuse correlation spectroscopy for non-invasive, micro-vascular cerebral blood flow measurement.» In: *Neuroimage* 85, Part 1.0 (2014), pp. 51–63. ISSN: 1053-8119.

[91] Turgut Durduran et al. «Bulk optical properties of healthy female breast tissue.» In: *Phys. Med. Biol.* 47.16 (2002), p. 2847. ISSN: 0031-9155.

[92] Turgut Durduran et al. «Diffuse optical measurement of blood flow, blood oxygenation, and metabolism in a human brain during sensorimotor cortex activation.» In: *Opt. Lett.* 29.15 (2004), pp. 1766–8. ISSN: 0146-9592.

[93] Turgut Durduran et al. «Diffuse optical measurement of blood flow in breast tumors.» In: *Opt. Lett.* 30.21 (2005), pp. 2915–2917.

[94] Turgut Durduran et al. «Diffuse optics for tissue monitoring and tomography.» In: *Reports Prog. Phys.* 73.7 (2010), p. 76701. ISSN: 0034-4885.

[95] Turgut Durduran et al. «Does the photon-diffusion coefficient depend on absorption?» In: *J. Opt. Soc. Am. A. Opt. Image Sci. Vis.* 14.12 (1997), pp. 3358–3365. ISSN: 1084-7529.

[96] Turgut Durduran et al. «Optical measurement of cerebral hemodynamics and oxygen metabolism in neonates with congenital heart defects.» In: *J. Biomed. Opt.* 15.3 (2010), p. 037004. ISSN: 10833668.

[97] Turgut Durduran et al. «Transcranial optical monitoring of cerebrovascular hemodynamics in acute stroke patients.» In: *Opt. Express* 17.5 (2009), pp. 3884–902. ISSN: 1094-4087.

[98] Brian L Edlow et al. «The effects of healthy aging on cerebral hemodynamic responses to posture change.» In: *Physiol. Meas.* 31.4 (2010), pp. 477–495. ISSN: 0967-3334.

[99] A. Einstein. «Über die von der molekularkinetischen Theorie der Wärme geforderte Bewegung von in ruhenden Flüssigkeiten suspendierten Teilchen.» In: *Ann. Phys.* 322.8 (1905), pp. 549–560. ISSN: 00033804.

[100] a. Einstein. «Über einen die Erzeugung und Verwandlung des Lichtes betreffenden heuristischen Gesichtspunkt.» In: *Ann. Phys.* 322.6 (1905), pp. 132–148. ISSN: 00033804.

[101] R K Ellerkmann et al. «Spectral entropy and bispectral index as measures of the electroencephalographic effects of propofol.» In: *Anesth. Analg.* 102.5 (2006), pp. 1456–1462. ISSN: 1526-7598.

[102] M Engelhardt et al. «Neurosurgical operations with the patient in sitting position: analysis of risk factors using transcranial Doppler sonography.» In: *Br. J. Anaesth.* 96.4 (2006), pp. 467–472. ISSN: 0007-0912.

[103] Sarah J Erickson and Anuradha Godavarty. «Hand-held based near-infrared optical imaging devices: A review.» In: *Med. Eng. Phys.* 31.5 (2009), pp. 495–509. ISSN: 1350-4533.

[104] Parisa Farzam and Turgut Durduran. «Multidistance diffuse correlation spectroscopy for simultaneous estimation of absolute scattering and absorption coefficient and the blood flow index.» In: *J. Biomed. Opt.* 20.5 (2015), p. 55001. ISSN: 1083-3668.

[105] Parisa Farzam et al. «Noninvasive characterization of the healthy human manubrium using diffuse optical spectroscopies.» In: *Physiol. Meas.* 35.7 (2014), p. 1469. ISSN: 1361-6579.

[106] Argyro Fassoulaki et al. «The effect of desflurane and sevoflurane on cerebral oximetry under steady-state conditions.» In: *Anesth. Analg.* 102.6 (2006), pp. 1830–1835. ISSN: 00032999.

[107] A. R. Fathi, P. Eshtehardi, and B. Meier. «Patent foramen ovale and neurosurgery in sitting position: A systematic review.» In: *Br. J. Anaesth.* 102.5 (2009), pp. 588–596. ISSN: 00070912.

[108] O K Faull, J D Cotter, and S J E Lucas. «Cerebrovascular responses during rowing: Do circadian rhythms explain morning and afternoon performance differences?» In: *Scand. J. Med. Sci. Sports* 25.4 (2014), pp. 467–475. ISSN: 1600-0838.

[109] Christopher G Favilla et al. «Optical bedside monitoring of cerebral blood flow in acute ischemic stroke patients during head-of-bed manipulation.» In: *Stroke.* 45.5 (2014), pp. 1269–74. ISSN: 1524-4628.

[110] Valery L Feigin et al. «Stroke epidemiology: A review of population-based studies of incidence, prevalence, and case-fatality in the late 20th century.» In: *Lancet Neurol.* 2.1 (2003), pp. 43–53. ISSN: 14744422.

[111] Gregory W. Fischer et al. «The Use of Cerebral Oximetry as a Monitor of the Adequacy of Cerebral Perfusion in a Patient Undergoing Shoulder Surgery in the Beach Chair Position.» In: *Pain Pract.* 9.4 (2009), pp. 304–307. ISSN: 15307085.

[112] Pierre Fiset et al. «Brain Mechanisms of Propofol-Induced Loss of Consciousness in Humans: a Positron Emission Tomographic Study.» In: *J. Neurosci.* 19.13 (1999), pp. 5506–5513. ISSN: 0270-6474.

[113] Thilo Fleck et al. «Propofol Effect on Cerebral Oxygenation in Children with Congenital Heart Disease.» In: *Pediatr. Cardiol.* 36.3 (2015), pp. 543–549. ISSN: 14321971.

[114] J Fox et al. «The Responsiveness of Cerebral Blood Flow to Changes in Arterial Carbon Dioxide Is Maintained during Propofol–Nitrous Oxide Anesthesia in Humans.» In: *Anesthesiology* 77.3 (1992), pp. 453–456.

[115] M a Franceschini, E Gratton, and S Fantini. «Noninvasive optical method of measuring tissue and arterial saturation: an application to absolute pulse oximetry of the brain.» In: *Opt. Lett.* 24.12 (1999), pp. 829–31. ISSN: 0146-9592.

[116] Maria Angela Franceschini and David A Boas. «Noninvasive measurement of neuronal activity with near-infrared optical imaging.» In: *Neuroimage* 21.1 (2004), pp. 372–386. ISSN: 10538119.

[117] Dirk Frenzel et al. «Is the bispectral index appropriate for monitoring the sedation level of mechanically ventilated surgical ICU patients?» In: *Intensive Care Med.* 28.2 (2002), pp. 178–183. ISSN: 03424642.

[118] Y Fujii et al. «Middle cerebral arterial blood flow velocity increases during laparoscopic cholecystectomy.» In: *Anesth.Analg.* 78.1 (1994), pp. 80–83.

[119] T. Gale and K. Leslie. «Anaesthesia for neurosurgery in the sitting position.» In: *J. Clin. Neurosci.* 11.7 (2004), pp. 693–696. ISSN: 09675868.

[120] Tong J Gan et al. «Bispectral index monitoring allows faster emergence and improved recovery from propofol, alfentanil, and nitrous oxide anesthesia.» In: *J. Am. Soc. Anesthesiol.* 87.4 (1997), pp. 808–815. ISSN: 0098-6151.

[121] Oliver Ganslandt et al. «The sitting position in neurosurgery: Indications, complications and results. A single institution experience of 600 cases.» In: *Acta Neurochir. (Wien).* 155.10 (2013), pp. 1887–1893. ISSN: 00016268.

[122] Jamshid Ghajar. «Traumatic brain injury.» In: *Lancet* 356.9233 (2000), pp. 923–929. ISSN: 01406736.

[123] Hossein Gharib et al. «American Association of Clinical Endocrinologists, Associazione Medici Endocrinologi, and European Thyroid Association Medical Guidelines for Clinical Practice for the Diagnosis and Management of Thyroid Nodules.» In: *Endocr. Pract.* 16 Suppl 1.June 2010 (), pp. 1–43. ISSN: 1934-2403.

[124] G Giubileo et al. «Fluorescence spectroscopy of normal and follicular cancer samples from human thyroid.» In: *Spectroscopy* 19 (2005), pp. 79–87.

[125] Peter S Glass et al. «Bispectral analysis measures sedation and memory effects of propofol, midazolam, isoflurane, and alfentanil in healthy volunteers.» In: *Am. Soc. Anesthesiol.* 86.4 (1997), pp. 836–847. ISSN: 0098-6151.

[126] J B Glen. «The development of 'Diprifusor': a TCI system for propofol.» In: *Anaesthesia* 53 Suppl 1 (1998), pp. 13–21. ISSN: 0003-2409.

[127] Daniel Agustin Godoy. *Intensive Care in Neurology and Neurosurgery*. SEEd, 2013.

[128] Henry Gray. *Anatomy of the human body*. Lea & Febiger, 1918.

[129] Juergen Gross and Uwe Ligges. *nortest: Tests for Normality*. 2015.

[130] J Grote. «Cerebral Blood Flow: Clinical and Experimental Results.» In: *Cereb. Blood Flow*. Ed. by M Brock et al. Berlin, Heidelberg: Springer Berlin Heidelberg, 1969. Chap. The Influe, pp. 75–78. ISBN: 978-3-642-85860-4.

[131] Samir H Haddad and Yaseen M Arabi. «Critical care management of severe traumatic brain injury in adults.» In: *Scand. J. Trauma. Resusc. Emerg. Med.* 20.1 (2012), p. 12. ISSN: 1757-7241.

[132] G M Hale and M R Querry. «Optical Constants of Water in the 200-nm to 200-microm Wavelength Region.» In: *Appl. Opt.* 12.3 (1973), pp. 555–563. ISSN: 0003-6935.

[133] Albrecht Harders. *Neurosurgical applications of transcranial Doppler sonography*. Springer Science & Business Media, 2012.

[134] R C Haskell et al. «Boundary conditions for the diffusion equation in radiative transfer.» In: *J. Opt. Soc. Am. A. Opt. Image Sci. Vis.* 11.10 (1994), pp. 2727–41. ISSN: 1084-7529.

[135] Donald D. Heistad and Hermes A. Kontos. «Cerebral Circulation.» In: *Compr. Physiol.* Hoboken, NJ, USA: John Wiley & Sons, Inc., 2011.

[136] Gabriela Hernandez-Meza et al. «Near-Infrared Spectroscopy for the Evaluation of Anesthetic Depth.» In: *Biomed Res. Int.* 2015 (2015). ISSN: 23146141.

[137] J Hernández-Palazón, V N de la Rosa-Carrillo, and J A Tortosa. «Anesthetic technique and development of pneumocephalus after posterior fossa surgery in the sitting position.» In: *Neurocirugia* 14.3 (2003), pp. 216–221. ISSN: 11301473.

[138] H Hertz. «Ueber einen Einfluss des ultravioletten Lichtes auf die electrische Entladung.» In: *Ann. Phys.* 267.8 (1887), pp. 983–1000. ISSN: 1521-3889.

[139] William E Hitselberger and William F House. «A warning regarding the sitting position for acoustic tumor surgery.» In: *Arch. Otolaryngol.* 106.2 (1980), p. 69.

[140] R D Hoge et al. «Simultaneous recording of task-induced changes in blood oxygenation, volume, and flow using diffuse optical imaging and arterial spin-labeling MRI.» In: *Neuroimage* 25.3 (2005), pp. 701–707. ISSN: 10538119.

[141] R Hoge et al. «Investigation of BOLD signal dependence on cerebral blood flow and oxygen consumption: The . . . » In: *Magn. Reson. Med.* 863 (1999), pp. 849–863.

[142] Zufang Huang et al. «In Vitro Imaging of Thyroid Tissues Using Two-Photon Excited Fluorescence and Second Harmonic Generation.» In: *Photomed. Laser Surg.* 28.S1 (2010), S–129–S–133. ISSN: 1549-5418.

[143] D M Hueber et al. «Non-invasive and quantitative near-infrared haemoglobin spectrometry in the piglet brain during hypoxic stress, using a frequency-domain multidistance instrument.» In: *Phys. Med. Biol.* 46.1 (2001), pp. 41–62. ISSN: 0031-9155.

[144] Egbert Huettemann et al. «Preserved CO2 reactivity and increase in middle cerebral arterial blood flow velocity during laparoscopic surgery in children.» In: *Anesth. Analg.* 94.2 (2002), 255–8, table of contents. ISSN: 0003-2999.

[145] Fahmeed Hyder, Robert G Shulman, and Douglas L Rothman. «A model for the regulation of cerebral oxygen delivery.» In: *J. Appl. Physiol.* 85 (1998), pp. 554–564. ISSN: 8750-7587.

[146] *IMPACT: International Mission for Prognosis and Analysis of Clinical Trials in TBI*.

[147] AKIRA ISHIMARU. *Wave Propagation and Scattering in Random Media*. Elsevier, 1978, pp. 175–190. ISBN: 9780123747013.

[148] Andra E Ibrahim, Julie K Taraday, and Evan D Kharasch. «Bispectral Index Monitoring during Sedation with Sevoflurane, Midazolam, and Propofol.» In: *Anesthesiology* 95.5 (2001), pp. 1151–59. ISSN: 0039-6206.

[149] Daniel Irwin et al. «Influences of tissue absorption and scattering on diffuse correlation spectroscopy blood flow measurements.» In: *Biomed. Opt. Express* 2.7 (2011), pp. 1969–1985. ISSN: 2156-7085.

[150] H. Ito, I. Kanno, and H. Fukuda. «Human cerebral circulation: positron emission tomography studies.» In: *Ann. Nucl. Med.* 19.2 (2005), pp. 65–74. ISSN: 0914-7187.

[151] Hiroshi Ito et al. «Changes in human cerebral blood flow and cerebral blood volume during hypercapnia and hypocapnia measured by positron emission tomography.» In: *J. Cereb. Blood Flow Metab.* 23.6 (2003), pp. 665–670. ISSN: 0271-678X.

[152] Kurtulus Izzetoglu et al. «The evolution of field deployable fNIR spectroscopy from bench to clinical settings.» In: *J. Innov. Opt. Health Sci.* 04.03 (2011), pp. 239–250. ISSN: 1793-5458.

[153] Steven L Jacques. «Time resolved propagation of ultrashort laser pulses within turbid tissues.» In: *Appl. Opt.* 28.12 (1989), pp. 2223–9. ISSN: 0003-6935.

[154] Matthias Jaeger and Erhard W Lang. «Cerebrovascular pressure reactivity and cerebral oxygen regulation after severe head injury.» In: *Neurocrit. Care* 19.1 (2013), pp. 69–73. ISSN: 1556-0961.

[155] Hyejin Jeong et al. «Cerebral Oxygen Saturation Measured by Near-infrared Spectroscopy and Jugular Venous Bulb Oxygen Saturation during Arthroscopic Shoulder Surgery in Beach Chair Position under Sevoflurane-Nitrous Oxide or Propofol-Remifentanil Anesthesia.» In: *Anesthesiology* 116.5 (2012), pp. 1047–1056. ISSN: 0003-3022.

[156] F F Jobsis. «Noninvasive, infrared monitoring of cerebral and myocardial oxygen sufficiency and circulatory parameters.» In: *Science (80-.).* 198.4323 (1977), pp. 1264–1267.

[157] Jay W Johansen. «Update on bispectral index monitoring.» In: *Best Pract. Res. Clin. Anaesthesiol.* 20.1 (2006), pp. 81–99. ISSN: 15216896.

[158] Kaike K Kaisti et al. «Effects of sevoflurane, propofol and adjunct nitrous oxide on regional cerebral blood flow, oxygen consumption, and blood volume in humans.» In: *Anesthesiology* 99.3 (2003), pp. 603–613. ISSN: 0003-3022.

[159] JohnGeorge Karippacheril and TamYuk Ho. «Data acquisition from S/5 GE Datex anesthesia monitor using VSCapture: An open source.NET/Mono tool.» In: *J. Anaesthesiol. Clin. Pharmacol.* 29.3 (2013), p. 423. ISSN: 0970-9185.

[160] A Kastrup et al. «Assessment of cerebrovascular reactivity with functional magnetic resonance imaging: comparison of CO(2) and breath holding.» In: *Magn. Reson. Imaging* 19.1 (2001), pp. 13–20. ISSN: 0730-725X.

[161] H L Kaul and N Bharti. «Monitoring depth of anaesthesia.» In: *Indian J. Anesth.* 46.4 (2002), pp. 323–332.

[162] G R Kelman. «Digital computer subroutine for the conversion of oxygen tension into saturation.» In: *J. Appl. Physiol.* 21.4 (1966), pp. 1375–1376.

[163] James A Kennealy et al. «Hyperventilation-Induced Cerebral Hypoxia.» In: *Am. Rev. Respir. Dis.* 122.3 (1980), pp. 407–412. ISSN: 0003-0805.

[164] Chantal Kerssens and Peter S. Sebel. «To BIS or not to BIS? That is the question.» In: *Anesth. Analg.* 102.2 (2006), pp. 380–382. ISSN: 00032999.

[165] Seymour S Kety and C F Schmidt. «The Effects of Active and Passive Hyperventilation on Cerebral Blood Flow, Cerebral Oxygen Consumption, Cardiac Output, and Blood Pressure of Normal Young Men.» In: *J. Clin. Invest.* 25.1 (1946), pp. 107–19. ISSN: 0021-9738.

[166] Seymour S Kety and C F Schmidt. «The nitrous oxide method for the quantitative determination of cerebral blood flow in man; theory, procedure and normal values.» In: *J. Clin. Invest.* 27.4 (1948), pp. 476–483. ISSN: 0021-9738.

[167] Seymour S Kety and Carl F Schmidt. «The effects of altered arterial tensions of carbon dioxide and oxygen on cerebral blood flow and cerebral oxygen consumption of normal young men.» In: *J. Clin. Invest.* 27.4 (1948), pp. 484–492. ISSN: 0021-9738.

[168] David G Kiely, Robert I Cargill, and Brian J Lipworth. «Effects of Hypercapnia on Hemodynamic, Inotropic, Lusitropic, and Electrophysiologic Indices in Humans.» In: *Chest* 109.5 (1996), pp. 1215–1221. ISSN: 00123692.

[169] A Kienle and Michael S Patterson. «Improved solutions of the steady-state and the time-resolved diffusion equations for reflectance from a semi-infinite turbid medium.» In: *J. Opt. Soc. Am. A. Opt. Image Sci. Vis.* 14.1 (1997), pp. 246–254. ISSN: 1084-7529.

[170] Meeri N Kim. «Applications of Hybrid Diffuse Optics for Clinical Management of Adults after Brain Injury.» PhD thesis. University of Pennsylvania, 2013, p. 283.

[171] Meeri N Kim et al. «Continuous Optical Monitoring of Cerebral Hemodynamics During Head-of-Bed Manipulation in Brain-Injured Adults.» In: *Neurocrit. Care* 20.3 (2014), pp. 443–453. ISSN: 1541-6933.

[172] Igor Kissin. «Depth of Anesthesia and Bispectral Index Monitoring.» In: *Anesth. Analg.* 90.5 (2000), pp. 1114–1117. ISSN: 0003-2999.

[173] Klaus Ulrich Klein et al. «Human cerebral microcirculation and oxygen saturation during propofol-induced reduction of bispectral index.» In: *Br. J. Anaesth.* 107.5 (2011), pp. 735–41. ISSN: 1471-6771.

[174] Sang Hun Ko et al. «Cerebral oxygenation monitoring of patients during arthroscopic shoulder surgery in the sitting position.» In: *Korean J. Anesthesiol.* 63.4 (2012), pp. 297–301. ISSN: 20056419.

[175] E Kochs et al. *Cerebral blood flow velocity in relation to cerebral blood flow, cerebral metabolic rate for oxygen, and electroencephalogram analysis during isoflurane anesthesia in dogs*. 1993.

[176] Christian Kolbitsch et al. «The influence of hyperoxia on regional cerebral blood flow (rCBF), regional cerebral blood volume (rCBV) and cerebral blood flow velocity in the middle cerebral artery (CBFVMCA) in human volunteers.» In: *Magn. Reson. Imaging* 20.7 (2002), pp. 535–541. ISSN: 0730-725X (Print).

[177] Arne Kovac and Bernard W. Silverman. «Extending the Scope of Wavelet Regression Methods by Coefficient-Dependent Thresholding.» In: *J. Am. Stat. Assoc.* 95.449 (2000), p. 172. ISSN: 01621459.

[178] Jacek Kupisiak et al. «Bispectral index and cerebral oximetry in low-flow and high-flow rate anaesthesia during laparoscopic cholecystectomy - a randomized controlled trial.» In: *Wideochirurgia i Inne Tech. Malo Inwazyjne* 6.4 (2011), p. 226. ISSN: 18954588.

[179] Jeffrey C. Lagarias et al. «Convergence Properties of the Nelder–Mead Simplex Method in Low Dimensions.» In: *SIAM J. Optim.* 9.1 (1998), pp. 112–147. ISSN: 1052-6234.

[180] F S Larsen et al. «Transcranial Doppler is valid for determination of the lower limit of cerebral blood flow autoregulation.» In: *Stroke* 25.10 (1994), pp. 1985–8. ISSN: 0039-2499.

[181] Niels A Lassen. «Cerebral blood flow and oxygen consumption in man.» In: *Physiol. Rev.* 39.2 (1959), pp. 183–238. ISSN: 0031-9333.

[182] Jae Hoon Lee et al. «Effects of beach-chair position and induced hypotension on cerebral oxygen saturation in patients undergoing arthroscopic shoulder surgery.» In: *Arthrosc. - J. Arthrosc. Relat. Surg.* 27.7 (2011), pp. 889–894. ISSN: 07498063.

[183] P A Lemieux and D J Durian. «Investigating non-Gaussian scattering processes by using nth-order intensity correlation functions.» In: *J. Opt. Soc. Am. A* 16.7 (1999), pp. 1651–1664. ISSN: 1084-7529.

[184] Umberto Leon-Dominguez et al. «Molecular concentration of deoxyHb in human prefrontal cortex predicts the emergence and suppression of consciousness.» In: *Neuroimage* 85 (2014), pp. 616–625. ISSN: 10538119.

[185] Irene E. Leonard and Anthony J. Cunningham. «Anaesthetic considerations for laparoscopic cholecystectomy.» In: *Best Pract. Res. Clin. Anaesthesiol.* 16.1 (2002), pp. 1–20. ISSN: 15216896.

[186] K Leslie et al. «Propofol blood concentration and the Bispectral Index predict suppression of learning during propofol/epidural anesthesia in volunteers.» In: *Anesth. Analg.* 81.6 (1995), pp. 1269–1274. ISSN: 0003-2999.

[187] Gregory A Liguori et al. «The use of metoprolol and glycopyrrolate to prevent hypotensive/bradycardic events during shoulder arthroscopy in the sitting position under interscalene block.» In: *Anesth. Analg.* 87.6 (1998), pp. 1320–5. ISSN: 0003-2999.

[188] William B. Lo and Harold Ellis. «The circle before willis: A historical account of the intracranial anastomosis.» In: *Neurosurgery* 66.1 (2010), pp. 7–17. ISSN: 0148396X.

[189] Alan D. Lopez et al. «Global and regional burden of disease and risk factors, 2001: systematic analysis of population health data.» In: *Lancet* 367.9524 (2006), pp. 1747–1757. ISSN: 01406736.

[190] N Lorenzo et al. «Pneumocephalus and tension pneumocephalus after posterior fossa surgery in the sitting position: A prospective study.» In: *Acta Neurochir. (Wien).* 83.3 (1986), pp. 112–115. ISSN: 0942-0940.

[191] At Lovell et al. «Continuous measurement of cerebral oxygenation by near infrared spectroscopy curing induction of anesthesia.» In: (1999), pp. 554–558.

[192] Guy L Ludbrook, Elizabeth Visco, and Arthur M Lam. «Relation between Brain Concentrations, Electroencephalogram, Middle Cerebral Artery Blood Flow Velocity, and Cerebral Oxygen Extraction during Induction of Anesthesia.» In: *Anesthesiology* 97.6 (2002), pp. 1363–70. ISSN: 0003-3022.

[193] Anton Lund et al. «Ultrasound tagged near infrared spectroscopy does not detect hyperventilation-induced reduction in cerebral blood flow.» In: *Scand. J. Clin. Lab. Invest.* 76.1 (2016), pp. 82–87. ISSN: 0036-5513.

[194] Heikki Luukinen et al. «Rapid Increase of Fall-Related Severe Head Injuries with Age Among Older People: A Population-Based Study.» In: *J. Am. Geriatr. Soc.* 47.12 (1999), pp. 1451–1452. ISSN: 00028614.

[195] Jennifer M Lynch et al. «Noninvasive Optical Quantification of Cerebral Venous Oxygen Saturation in Humans.» In: *Acad. Radiol.* 21.2 (2014), pp. 162–167. ISSN: 10766332.

[196] P. Maggio et al. «Does hypercapnia-induced impairment of cerebral autoregulation affect neurovascular coupling? A functional TCD study.» In: *J. Appl. Physiol.* 115.4 (2013), pp. 491–497. ISSN: 8750-7587.

[197] L S Malatino et al. «Cerebral blood flow velocity after hyperventilation-induced vasoconstriction in hypertensive patients.» In: *Stroke.* 23.12 (1992), pp. 1728–32. ISSN: 0039-2499.

[198] G. Maret and P. E. Wolf. «Multiple light scattering from disordered media. The effect of brownian motion of scatterers.» In: *Zeitschrift für Phys. B Condens. Matter* 65.4 (1987), pp. 409–413. ISSN: 0722-3277.

[199] Marinella Marinoni et al. «Technical limits in transcranial Doppler recording: Inadequate acoustic windows.» In: *Ultrasound Med. Biol.* 23.8 (1997), pp. 1275–1277. ISSN: 03015629.

[200] K R Marsden et al. «Aging blunts hyperventilation-induced hypocapnia and reduction in cerebral blood flow velocity during maximal exercise.» In: *Age (Omaha).* 34.3 (2012), pp. 725–735. ISSN: 0161-9152.

[201] Fabrizio Martelli et al. «There's plenty of light at the bottom: statistics of photon penetration depth in random media.» In: *Sci. Rep.* 6 (2016), p. 27057. ISSN: 2045-2322.

[202] John T Martin. *Neuroanesthetic adjuncts for surgery in the sitting position. I. Introduction and basic equipment*. 1970.

[203] J. Matjasko et al. «Anesthesia and surgery in the seated position: Analysis of 554 cases.» In: *Neurosurgery* 17.5 (1985), pp. 695–702. ISSN: 0148396X.

[204] B. F. Matta et al. «Cerebral pressure autoregulation and carbon dioxide reactivity during propofol-induced EEG suppression.» In: *Br. J. Anaesth.* 74.2 (1995), pp. 159–163. ISSN: 00070912.

[205] Bryan McIver. «Evaluation of the thyroid nodule.» In: *Oral Oncol.* 49.7 (2013), pp. 645–653. ISSN: 1368-8375.

[206] T J Mcmurray et al. «Propofol sedation using Diprifusor TM target-controlled infusion in adult intensive care unit patients *.» In: (2004), pp. 636–641.

[207] Lingzhong Meng and Adrian W Gelb. «Regulation of Cerebral Autoregulation by Carbon Dioxide.» In: *Anesthesiology* 122.1 (2015), pp. 196–205. ISSN: 0003-3022.

[208] Rickson C Mesquita et al. «Diffuse optical characterization of an exercising patient group with peripheral artery disease.» In: *J. Biomed. Opt.* 18.5 (2013), p. 57007. ISSN: 1560-2281.

[209] Rickson C Mesquita et al. «Direct measurement of tissue blood flow and metabolism with diffuse optics.» In: *Philos. Trans. R. Soc. A Math. Phys. Eng. Sci.* 369.1955 (2011), pp. 4390–4406. ISSN: 1364-503X.

[210] Weidong Mi et al. «The interaction between fentanyl and propofol during emergence from anesthesia: monitoring with the EEG-Bispectral index™.» In: *J. Clin. Anesth.* 15.2 (2003), pp. 103–107. ISSN: 09528180.

[211] Anastasios Milionis and Charalampos Milionis. «Correlation between Body Mass Index and Thyroid Function in Euthyroid Individuals in Greece.» In: *ISRN Biomarkers* 2013 (2013), pp. 1–7. ISSN: 2314-6265.

[212] J. Douglas Miller, Albert E. Stanek, and Thomas W. Langfitt. «Cerebral blood flow regulation during experimental brain compression.» In: *J. Neurosurg.* 39.2 (1973), pp. 186–196. ISSN: 0022-3085.

[213] M A Mirski et al. «Diagnosis and treatment of vascular air embolism.» In: *Anesthesiology* 106.1 (2007), pp. 164–177. ISSN: 0003-3022.

[214] Annelies T. Moerman et al. «Cerebral oxygen desaturation during beach chair position.» In: *Eur. J. Anaesthesiol.* 29.2 (2012), pp. 82–87. ISSN: 0265-0215.

[215] Won-Jin Moon et al. «Benign and malignant thyroid nodules: US differentiation—multicenter retrospective study 1.» In: *Radiology* 247.3 (2008), pp. 762–770.

[216] T J Morgan. «The oxyhaemoglobin dissociation curve in critical illness.» In: *Crit. Care Resusc.* 1.1 (1999), pp. 93–100. ISSN: 1441-2772.

[217] Ramez Moustafa and Jean-Claude Baron. «Clinical review: Imaging in ischaemic stroke – implications for acute management.» In: *Crit. Care* 11.5 (2007), p. 227. ISSN: 13648535.

[218] X. Muñoz et al. «Accuracy and reliability of pulse oximetry at different arterial carbon dioxide pressure levels.» In: *Eur. Respir. J.* 32.4 (2008), pp. 1053–1059. ISSN: 09031936.

[219] John M Murkin and M Arango. «Near-infrared spectroscopy as an index of brain and tissue oxygenation.» In: *Br. J. Anaesth.* 103 Suppl (2009), pp. i3–13. ISSN: 1471-6771.

[220] Glenn S Murphy et al. «Cerebral oxygen desaturation events assessed by near-infrared spectroscopy during shoulder arthroscopy in the beach chair and lateral decubitus positions.» In: *Anesth. Analg.* 111.2 (2010), pp. 496–505. ISSN: 00032999.

[221] P. S. Myles et al. «Bispectral index monitoring to prevent awareness during anaesthesia: The B-Aware randomised controlled trial.» In: *Lancet* 363.9423 (2004), pp. 1757–1763. ISSN: 01406736.

[222] Masayasu Nakayama et al. «The effect of fentanyl on hemodynamic and bispectral index changes during anesthesia induction with propofol.» In: *J. Clin. Anesth.* 14.2 (2002), pp. 146–149. ISSN: 09528180.

[223] Il Seong Nam-Goong et al. «Ultrasonography-guided fine-needle aspiration of thyroid incidentaloma: correlation with pathological findings.» In: *Clin. Endocrinol. (Oxf).* 60.1 (2004), pp. 21–28. ISSN: 0300-0664.

[224] Guy Nason. *wavethresh: Wavelets statistics and transforms.* 2013.

[225] Ricard Navarro et al. «Unexpected bilateral increase of cerebral regional saturation of oxygen as an early warning sign of air embolism.» In: *J. Clin. Anesth.* 23.5 (2011), pp. 431–432. ISSN: 09528180.

[226] J.A. Nelder et al. «A simplex method for function minimization.» In: *Comput. J.* 7.4 (1964), pp. 308–313. ISSN: 00104620.

[227] Gert E. Nilsson, Torsten Tenland, and P. Ake Öberg. «Evaluation of a laser Doppler flowmeter for measurement of tissue blood flow.» In: *IEEE Trans. Biomed. Eng.* 27.10 (1980), pp. 597–604. ISSN: 0018-9294.

[228] S Nioka, Q Luo, and B Chance. «Oxygen Transport to Tissue XIX.» In: ed. by David K Harrison and David T Delpy. Boston, MA: Springer US, 1997. Chap. Human Brai, pp. 237–242. ISBN: 978-1-4615-5399-1.

[229] Vasilis Ntziachristos and Britton Chance. «Accuracy limits in the determination of absolute optical properties using time-resolved NIR spectroscopy.» In: *Med. Phys.* 28.6 (2001), pp. 1115–1124. ISSN: 0094-2405.

[230] Vasilis Ntziachristos et al. «Multichannel photon counting instrument for spatially resolved near infrared spectroscopy.» In: *Rev. Sci. Instrum.* 70.1 (1999), pp. 193–201.

[231] P Ake Oberg. «Laser-Doppler flowmetry.» In: *Crit. Rev. Biomed. Eng.* 18.2 (1990), pp. 125–163.

[232] S Ogawa and Tm Lee. «Brain magnetic resonance imaging with contrast dependent on blood oxygenation.» In: *Proc. . . .* 87.24 (1990), pp. 9868–72. ISSN: 0027-8424.

[233] S Ogawa et al. «Functional brain mapping by blood oxygenation level-dependent contrast magnetic resonance imaging. A comparison of signal characteristics with a biophysical model.» In: *Biophys. J.* 64.3 (1993), pp. 803–812. ISSN: 0006-3495.

[234] T Oshima, F Karasawa, and T Satoh. «Effects of propofol on cerebral blood flow and the metabolic rate of oxygen in humans.» In: *Acta Anaesthesiol. Scand.* 46.7 (2002), pp. 831–835. ISSN: 0001-5172.

[235] Marius G Pakalniskis et al. «Tumor Angiogenesis Change Estimated by Using Diffuse Optical Spectroscopic Tomography: Demonstrated Correlation in Women Undergoing Neoadjuvant Chemotherapy for Invasive Breast Cancer?» In: *Radiology* 259.2 (2011), pp. 365–374.

[236] S C Palmon et al. «Venous air embolism: a review.» In: *J. Clin. Anesth.* 9.3 (1997), pp. 251–7. ISSN: 0952-8180.

[237] Anastasios Papadonikolakis et al. «Avoiding Catastrophic Complications of Stroke and Death Related to Shoulder Surgery in the Sitting Position.» In: *Arthrosc. - J. Arthrosc. Relat. Surg.* 24.4 (2008), pp. 481–482. ISSN: 07498063.

[238] Eun Young Park, Ja Young Kwon, and Ki Jun Kim. «Carbon dioxide embolism during laparoscopic surgery.» In: *Yonsei Med. J.* 53.3 (2012), pp. 459–466. ISSN: 05135796.

[239] Piyush M Patel and John C Drummond. *Miller's anesthesia*. Ed. by D Ronald et al. 8th ed. Elsevier Saunders, 2014. Chap. 21, p. 3576. ISBN: 978-0-7020-5283-5.

[240] Michael S Patterson, B Chance, and B C Wilson. «Time resolved reflectance and transmittance for the noninvasive measurement of tissue optical properties.» In: *Appl. Opt.* 28.12 (1989), pp. 2331–2336. ISSN: 0003-6935.

[241] Michael S Patterson et al. «Frequency-domain reflectance for the determination of the scattering and absorption properties of tissue.» In: *Appl. Opt.* 30.31 (1991), pp. 4474–4476. ISSN: 0003-6935.

[242] Blake G Perry et al. «The effect of hypercapnia on static cerebral autoregulation.» In: *Physiol. Rep.* 2.6 (2014), e12059. ISSN: 2051-817X.

[243] Seth W Perry, Ryan M Burke, and Edward B Brown. «Two-Photon and Second Harmonic Microscopy in Clinical and Translational Cancer Research.» In: *Ann. Biomed. Eng.* 40.2 (2012), pp. 277–291. ISSN: 0090-6964.

[244] Jose Pinheiro et al. *{nlme}: Linear and Nonlinear Mixed Effects Models*. 2015.

[245] Michael J Pitman et al. «The fluorescence of thyroid tissue.» In: *Otolaryngol. - Head Neck Surg.* 131.5 (2004), pp. 623–627. ISSN: 01945998.

[246] Roland N. Pittman. «Chapter 4 Oxygen Transport.» In: *Regul. Tissue Oxyg.* Morgan & Claypool Life Sciences, 2011.

[247] Anna M Planas. «Rodent Models of Stroke.» In: ed. by Ulrich Dirnagl. Totowa, NJ: Humana Press, 2010. Chap. Non-invasiv, pp. 139–165. ISBN: 978-1-60761-750-1.

[248] Brian W Pogue and Michael S Patterson. «Frequency-domain optical absorption spectroscopy of finite tissue volumes using diffusion theory.» In: *Phys. Med. Biol.* 39.7 (1994), pp. 1157–1180. ISSN: 0031-9155.

[249] Andrea Pohl and David J. Cullen. «Cerebral ischemia during shoulder surgery in the upright position: A case series.» In: *J. Clin. Anesth.* 17.6 (2005), pp. 463–469. ISSN: 09528180.

[250] Valerie Pollard et al. «The influence of carbon dioxide and body position on near-infrared spectroscopic assessment of cerebral hemoglobin oxygen saturation.» In: *Anesth. Analg.* 82.2 (1996), pp. 278–287.

[251] J M Porter, C Pidgeon, and A J Cunningham. «The sitting position in neurosurgery: a critical appraisal.» In: *Br J Anaesth* 82.1 (1999), pp. 117–128. ISSN: 0039-6206.

[252] Hemanshu Prabhakar. *Complications in Neuroanesthesia*. Academic Press New York, 2016, p. 500.

[253] Scott A Prahl. *Optical Absorption of Hemoglobin*.

[254] P N Pusey, J M Vaughan, and D V Willetts. «Effect of spatial incoherence of the laser in photon-correlation spectroscopy.» In: *J. Opt. Soc. Am.* 73.8 (1983), p. 1012. ISSN: 0030-3941.

[255] R Core Team. *R: A Language and Environment for Statistical Computing*. Vienna, Austria, 2013.

[256] M E Raichle and F Plum. «Hyperventilation and cerebral blood flow.» In: *Stroke.* 3.5 (1972), pp. 566–75. ISSN: 0039-2499.

[257] Peter Reinstrup et al. «Cerebral Blood Flow and Transcranial Doppler Sonography Measurements of CO(2)-Reactivity in Acute Traumatic Brain Injured Patients.» In: *Neurocrit. Care* (2012). ISSN: 1556-0961.

[258] M Reivich. «Arterial Pco2 and Cerebral Hemodynamics.» In: *Am. J. Physiol.* 206 (1964), pp. 25–35. ISSN: 0039-6206.

[259] Agnes Rigouzzo et al. «The relationship between bispectral index and propofol during target-controlled infusion anesthesia: A comparative study between children and young adults.» In: *Anesth. Analg.* 106.4 (2008), pp. 1109–1116. ISSN: 00032999.

[260] Jorge Ripoll. «Light diffusion in turbid media with biomedical application.» PhD thesis. Universidad Autonoma de Madrid, 2000.

[261] R O Robinson et al. «Positron emission tomography and the central nervous system.» In: *Arch. Dis. Child.* 81.3 (1999), pp. 263–70. ISSN: 1468-2044.

[262] Nadège Roche-Labarbe et al. «Noninvasive optical measures of CBV, StO2, CBF index, and rCMRO2 in human premature neonates' brains in the first six weeks of life.» In: *Hum. Brain Mapp.* 31.3 (2010), pp. 341–352. ISSN: 10659471.

[263] E Rostrup et al. «Regional differences in the CBF and BOLD responses to hypercapnia: a combined PET and fMRI study.» In: *Neuroimage* 11.2 (2000), pp. 87–97. ISSN: 1053-8119.

[264] C S Roy and C S Sherrington. «On the Regulation of the Blood-supply of the Brain.» In: *J. Physiol.* 11.1-2 (1890), pp. 85–158.17. ISSN: 0022-3751.

[265] Irene Rozet and Monica S. Vavilala. «Risks and Benefits of Patient Positioning During Neurosurgical Care.» In: *Anesthesiol. Clin.* 25.3 (2007), pp. 631–653. ISSN: 19322275. arXiv: NIHMS150003.

[266] Meyer Saklad. «Grading of patients for surgical procedures.» In: *Anesthesiology* 2.3 (1941), pp. 281–284. ISSN: 0003-3022.

[267] S Sancak et al. «Comparison of Color Flow Doppler Sonography (CFDS) and immunohistologic detection of microvessels for the assessment of the malignancy of thyroid nodules.» In: *Horm. Metab. Res.* 42.09 (2010), pp. 670–676.

[268] Michael Schaapveld et al. «Second Cancer Risk Up to 40 Years after Treatment for Hodgkin's Lymphoma.» In: *N. Engl. J. Med.* 373.26 (2015), pp. 2499–2511. ISSN: 0028-4793.

[269] G Schneider and Peter S Sebel. «Monitoring depth of anaesthesia.» In: *Eur. J. Anaesthesiol.* 14 (1997), pp. 21–28.

[270] T W Schnider et al. «The influence of method of administration and covariates on the pharmacokinetics of propofol in adult volunteers.» In: *Anesthesiology* 88.5 (1998), pp. 1170–82. ISSN: 0003-3022.

[271] Felix Scholkmann et al. «A review on continuous wave functional near-infrared spectroscopy and imaging instrumentation and methodology.» In: *Neuroimage* 85 (2014), pp. 6–27. ISSN: 10538119.

[272] S Schraag et al. «The performance of electroencephalogram bispectral index and auditory evoked potential index to predict loss of consciousness during propofol infusion.» In: *Anesth. Analg.* 89.5 (1999), pp. 1311–1315. ISSN: 0003-2999.

[273] Christina Schraml et al. «FAIR true-FISP perfusion imaging of the thyroid gland.» In: *J. Magn. Reson. Imaging* 26.1 (2007), pp. 66–71. ISSN: 1053-1807.

[274] S Schwarz et al. «Effects of body position on intracranial pressure and cerebral perfusion in patients with large hemispheric stroke.» In: *Stroke* 33 (2002), pp. 497–501. ISSN: 0039-2499.

[275] P S Sebel et al. «A multicenter study of bispectral electroencephalogram analysis for monitoring anesthetic effect.» In: *Anesth. Analg.* 84.4 (1997), pp. 891–899. ISSN: 0003-2999.

[276] Peter S Sebel et al. «The incidence of awareness during anesthesia: A multicenter United States study.» In: *Anesth. Analg.* 99.3 (2004), pp. 833–839. ISSN: 00032999.

[277] Sanathana Konugolu Venkata Sekar et al. «Broadband Time-Resolved Diffuse Optical Spectrometer for Clinical Diagnostics: Characterization and in-vivo Measurements in the 600-1350 nm spectral range.» In: *Diffus. Opt. Imaging V*. Optical Society of America, 2015, 95380R.

[278] Juliette Selb et al. «Sensitivity of near-infrared spectroscopy and diffuse correlation spectroscopy to brain hemodynamics: simulations and experimental findings during hypercapnia.» In: *Neurophotonics* 1.1 (2014), p. 015005. ISSN: 2329-423X.

[279] John W Severinghaus. «Blood gas calculator.» In: *J. Appl. Physiol.* 21.3 (1966), pp. 1108–16. ISSN: 0021-8987.

[280] John W Severinghaus. «Simple, accurate equations for human blood O 2 dissociation computations .» In: *J. Appl. Physiol.* 46.3 (1979), pp. 599–602.

[281] Nissar Shaikh and Firdous Ummunisa. «Acute management of vascular air embolism.» In: *J. emergencies, trauma Shock* 2.3 (2009), pp. 180–185. ISSN: 0974-2700.

[282] Yu Shang et al. «Portable optical tissue flow oximeter based on diffuse correlation spectroscopy.» In: *Opt. Lett.* 34.22 (2009), pp. 3556–3558. ISSN: 0146-9592.

[283] C. G. Sheahan and D. M. Mathews. «Monitoring and delivery of sedation.» In: *Br. J. Anaesth.* 113 (2014), pp. ii37–ii47. ISSN: 14716771.

[284] Albert P Sheperd and P Ake Oberg. *Laser-Doppler blood flowmetry*. Springer Science & Business Media, 2013.

[285] Steven I Sherman. «Thyroid carcinoma.» In: *Lancet* 361.9356 (2003), pp. 501–511.

[286] Jeffrey C Sigl and Nassib G Chamoun. «An introduction to bispectral analysis for the electroencephalogram.» In: *J. Clin. Monit.* 10.6 (1994), pp. 392–404. ISSN: 1573-2614.

[287] Jennifer A Sipos. «Advances in ultrasound for the diagnosis and management of thyroid cancer.» In: *Thyroid* 19.12 (2009), pp. 1363–1372. ISSN: 1557-9077.

[288] Scott A. Small. *Quantifying cerebral blood flow: Regional regulation with global implications*. 2004.

[289] Peter Smielewski et al. «Assessment of Cerebral Autoregulation Using Carotid Artery Compression.» In: *Stroke* 27.12 (1996), pp. 2197–2203. ISSN: 0039-2499.

[290] Martin Smith. «Monitoring intracranial pressure in traumatic brain injury.» In: *Anesth. Analg.* 106.1 (2008), pp. 240–8. ISSN: 00032999.

[291] P F Soeding et al. «The effect of the sitting upright or 'beachchair' position on cerebral blood flow during anaesthesia for shoulder surgery.» In: *Anaesth. Intensive Care* 39.3 (2011), pp. 440–448. ISSN: 0310057X.

[292] Louis Sokoloff. «Effects of carbon dioxide on the cardiovascular system.» In: *J. Am. Soc. Anesthesiol.* 21.6 (1960), pp. 664–673. ISSN: 0003-3022.

[293] Dajun Song, Girish P Joshi, and Paul F White. «Titration of volatile anesthetics using bispectral index facilitates recovery after ambulatory anesthesia.» In: *Anesthesiology* 87.4 (1997), pp. 842–848.

[294] Lorenzo Spinelli et al. «Bulk optical properties and tissue components in the female breast from multiwavelength time-resolved optical mammography.» In: *J. Biomed. Opt.* 9.6 (2004), pp. 1137–42. ISSN: 1083-3668.

[295] Subhadra Srinivasan et al. «Interpreting hemoglobin and water concentration, oxygen saturation, and scattering measured in vivo by near-infrared breast tomography.» In: *Proc. Natl. Acad. Sci. U. S. A.* 100.21 (2003), pp. 12349–12354. ISSN: 0027-8424.

[296] Nino Stocchetti et al. «Hyperventilation in head injury: A review.» In: *Chest* 127.5 (2005), pp. 1812–1827. ISSN: 00123692.

[297] S Strandgaard and O B Paulson. «Cerebral autoregulation.» In: *Stroke* 15.3 (1984), pp. 413–416. ISSN: 0039-2499.

[298] Gary Strangman, David A Boas, and Jeffrey P Sutton. «Non-invasive neuroimaging using near-infrared light.» In: *Biol. Psychiatry* 52.7 (2002), pp. 679–693. ISSN: 00063223.

[299] Gary Strangman, Maria Angela Franceschini, and David A Boas. «Factors affecting the accuracy of near-infrared spectroscopy concentration calculations for focal changes in oxygenation parameters.» In: *Neuroimage* 18.4 (2003), pp. 865–879. ISSN: 10538119.

[300] Gary Strangman et al. «A quantitative comparison of simultaneous BOLD fMRI and NIRS recordings during functional brain activation.» In: *Neuroimage* 17.2 (2002), pp. 719–731. ISSN: 10538119.

[301] Hyunsuk Suh et al. «Elastic light-scattering spectroscopy for discrimination of benign from malignant disease in thyroid nodules.» In: *Ann. Surg. Oncol.* 18.5 (2011), pp. 1300–5. ISSN: 1534-4681.

[302] Ulas Sunar et al. «Noninvasive diffuse optical measurement of blood flow and blood oxygenation for monitoring radiation therapy in patients with head and neck tumors: a pilot study.» In: *J. Biomed. Opt.* 11.6 (2006), p. 64021.

[303] C Symonds. «The circle of Willis.» In: *Br. Med. J.* 1.4906 (1955), pp. 119–24. ISSN: 0007-1447.

[304] Wendy Tanamai et al. «Diffuse optical spectroscopy measurements of healing in breast tissue after core biopsy: case study.» In: *J. Biomed. Opt.* 14.1 (2009), p. 014024. ISSN: 1083-3668.

[305] Felipe B Tancredi and Richard D Hoge. «Comparison of cerebral vascular reactivity measures obtained using breath-holding and CO2 inhalation.» In: *J. Cereb. Blood Flow Metab.* 33.7 (2013), pp. 1066–74. ISSN: 1559-7016.

[306] Paola Taroni et al. «In vivo absorption and scattering spectroscopy of biological tissues.» In: *Photochem. Photobiol. Sci.* 2.2 (2003), p. 124. ISSN: 1474-905X.

[307] Caroline S B Teixeira et al. «Thyroid tissue analysis through Raman spectroscopy.» In: *Analyst* 134.11 (2009), pp. 2361–70. ISSN: 1364-5528.

[308] The University Hospital. University of Medicine & Dentistry of New Jersey. *Stroke statistics*.

[309] Martin M Tisdall et al. «The effect on cerebral tissue oxygenation index of changes in the concentrations of inspired oxygen and end-tidal carbon dioxide in healthy adult volunteers.» In: *Anesth. Analg.* 109.3 (2009), pp. 906–13. ISSN: 1526-7598.

[310] Alessandro Torricelli et al. «In vivo optical characterization of human tissues from 610 to 1010 nm by time-resolved reflectance spectroscopy.» In: *Phys. Med. Biol.* 46.8 (2001), pp. 2227–37. ISSN: 0031-9155.

[311] Alessandro Torricelli et al. «Time domain functional NIRS imaging for human brain mapping.» In: *Neuroimage* 85 (2014), pp. 28–50.

[312] Gerard J Tortora and Bryan H Derrickson. *Principles of anatomy and physiology*. 14th Editi. Hoboken, NJ, USA: John Wiley & Sons, 2008. ISBN: 1118808436.

[313] Bruce J Tromberg et al. «Assessing the future of diffuse optical imaging technologies for breast cancer management.» In: *Med. Phys.* 35.6 (2008), pp. 2443–2451. ISSN: 00942405.

[314] L. Uhrig, S. Dehaene, and B. Jarraya. «Cerebral mechanisms of general anesthesia.» In: *Ann. Fr. Anesth. Reanim.* 33.2 (2014), pp. 72–82. ISSN: 17696623.

[315] Romain Valabrègue et al. «Relation Between Cerebral Blood Flow and Metabolism Explained by a Model of Oxygen Exchange.» In: *J. Cereb. Blood Flow Metab.* 23.5 (2003), pp. 536–545. ISSN: 0271-678X.

[316] L. Valencia et al. «Does sevoflurane preserve regional cerebral oxygen saturation measured by near-infrared spectroscopy better than propofol?» In: *Ann. Fr. Anesth. Reanim.* 33.4 (2014), pp. 59–65. ISSN: 17696623.

[317] H K Van Aken et al. *Intensivmedizin*. Georg Thieme Verlag, 2006. ISBN: 9783131511423.

[318] Nielufar Varjavand et al. *The Interactive Oxyhemoglobin Dissociation Curve*.

[319] Ioanna Vasileiou et al. «Propofol: A review of its non-anaesthetic effects.» In: *Eur. J. Pharmacol.* 605.1-3 (2009), pp. 1–8. ISSN: 00142999.

[320] Alberto L Vazquez et al. «Cerebral oxygen delivery and consumption during evoked neural activity.» In: *Front. Neuroenergetics* 2.June (2010), p. 11. ISSN: 1662-6427.

[321] Kyle Verdecchia et al. «Assessment of the best flow model to characterize diffuse correlation spectroscopy data acquired directly on the brain.» In: *Biomed. Opt. Express* 6.11 (2015), p. 4288. ISSN: 2156-7085.

[322] S. Verges et al. «Cerebral perturbations during exercise in hypoxia.» In: *AJP Regul. Integr. Comp. Physiol.* 302.8 (2012), R903–R916. ISSN: 0363-6119.

[323] Robert A Veselis et al. «A neuroanatomical construct for the amnesic effects of propofol.» In: *Anesthesiology* 97.2 (2002), pp. 329–337. ISSN: 0003-3022.

[324] E E de Waal et al. «The effects of low-pressure carbon dioxide pneumoperitoneum on cerebral oxygenation and cerebral blood volume in children.» In: *Anesth Analg* 94.3 (2002), 500–5; table of contents. ISSN: 0003-2999.

[325] Lihong V Wang and Hsin-i Wu. *Biomedical Optics*. Hoboken, NJ, USA: John Wiley & Sons, Inc., 2009, p. 376. ISBN: 9780470177013.

[326] N A Watson et al. «The effect of hyperoxia on cerebral blood flow: a study in healthy volunteers using magnetic resonance phase-contrast angiography.» In: *Eur. J. Anaesthesiol.* 17.3 (2000), pp. 152–159. ISSN: 0265-0215.

[327] Andreas Weyland et al. «Flow Velocity Measurements as an Index of Cerebral Blood Flow: Validity of Transcranial Doppler Sonographic Monitoring during Cardiac Surgery.» In: *Anesthesiology* 81.6 (1994), pp. 1401–10.

[328] D R White, H Q Woodard, and S M Hammond. «Average soft-tissue and bone models for use in radiation dosimetry.» In: *Br. J. Radiol.* 60.717 (1987), pp. 907–913.

[329] Hadley Wickham. *ggplot2: elegant graphics for data analysis*. Springer New York, 2009. ISBN: 978-0-387-98140-6.

[330] Hadley Wickham. *gtable: Arrange grobs in tables.* 2012.

[331] Hadley Wickham. *scales: Scale Functions for Visualization*. 2015.

[332] Anne W Wojner-Alexander et al. «Heads down: flat positioning improves blood flow velocity in acute ischemic stroke.» In: *Neurology* 64.8 (2005), pp. 1354–7. ISSN: 1526-632X.

[333] Martin Wolf, Marco Ferrari, and Valentina Quaresima. «Progress of near-infrared spectroscopy and topography for brain and muscle clinical applications.» In: *J. Biomed. Opt.* 12.6 (2007), p. 062104. ISSN: 1083-3668.

[334] Ronald L Wolf and John A Detre. «Clinical neuroimaging using arterial spin-labeled perfusion magnetic resonance imaging.» In: *Neurotherapeutics* 4.3 (2007), pp. 346–359. ISSN: 1933-7213.

[335] F Xu et al. «The influence of carbon dioxide on brain activity and metabolism in conscious humans.» In: *J Cereb Blood Flow Metab* 31.1 (2011), pp. 58–67. ISSN: 0271-678X.

[336] Feng Xu et al. «Effect of hypoxia and hyperoxia on cerebral blood flow, blood oxygenation, and oxidative metabolism.» In: *J. Cereb. Blood Flow Metab.* 32.10 (2012), pp. 1909–18. ISSN: 1559-7016.

[337] A Yli-Hankala et al. «EEG bispectral index monitoring in sevoflurane or propofol anaesthesia: analysis of direct costs and immediate recovery.» In: *Acta Anaesthesiol. Scand.* 43.5 (1999), pp. 545–9. ISSN: 0001-5172.

[338] Marie L. Young et al. «Comparison of surgical and anesthetic complications in neurosurgical patients experiencing venous air embolism in the sitting position.» In: *Neurosurgery* 18.2 (1986), pp. 157–161. ISSN: 0148396X.

[339] Guoqiang Yu. «Near-infrared diffuse correlation spectroscopy in cancer diagnosis and therapy monitoring.» In: *J. Biomed. Opt.* 17.1 (2012), pp. 10901–10909.

[340] Guoqiang Yu et al. «Noninvasive monitoring of murine tumor blood flow during and after photodynamic therapy provides early assessment of therapeutic efficacy.» In: *Clin. Cancer Res.* 11.9 (2005), pp. 3543–3552. ISSN: 1078-0432.

[341] Guoqiang Yu et al. «Validation of diffuse correlation spectroscopy for muscle blood flow with concurrent arterial spin labeled perfusion MRI.» In: *Opt. Express* 15.3 (2007), pp. 1064–75. ISSN: 1094-4087.

[342] Greg Zaharchuk, A. J. Martin, and W. P. Dillon. «Noninvasive imaging of quantitative cerebral blood flow changes during 100% oxygen inhalation using arterial spin-labeling MR imaging.» In: *Am. J. Neuroradiol.* 29.4 (2008), pp. 663–667. ISSN: 01956108.

[343] Alois Zauner and J Paul Muizelaar. «Brain metabolism and cerebral blood flow.» In: *Head Inj.* 1997. Chap. 5 Brain me, pp. 90–99. ISBN: 0 412 58540 5.

[344] Chao Zhou et al. «Diffuse optical monitoring of blood flow and oxygenation in human breast cancer during early stages of neoadjuvant chemotherapy.» In: *J. Biomed. Opt.* 12.5 (2007), pp. 51903–51911.

[345] Quing Zhu et al. «Benign versus malignant breast masses: optical differentiation with US-guided optical imaging reconstruction.» In: *Radiology* 237.1 (2005), p. 57.

[346] Peyman Zirak et al. «Effects of acetazolamide on the micro- and macro-vascular cerebral hemodynamics: a diffuse optical and transcranial doppler ultrasound study.» In: *Biomed. Opt. Express* 1.5 (2010), pp. 1443–1459. ISSN: 2156-7085.

COLOPHON

This document was typeset using the typographical look-and-feel `classicthesis` developed by André Miede. The style was inspired by Robert Bringhurst's seminal book on typography "*The Elements of Typographic Style*". `classicthesis` is available for both LaTeX and LyX:

https://bitbucket.org/amiede/classicthesis/

Happy users of `classicthesis` usually send a real postcard to the author, a collection of postcards received so far is featured here:

http://postcards.miede.de/

Final Version as of December 14, 2016.